2018

LANTHANIDE-BASED CORE-SHELL NANOPARTICLES AS MULTIFUNCTIONAL PLATFORMS FOR TARGETED RADIONUCLIDE THERAPY AND MULTIMODAL MOLECULAR IMAGING

Miguel Toro-Gonzalez
Virginia Commonwealth University

COPYRIGHT PAGE

LANTHANIDE-BASED CORE-SHELL NANOPARTICLES AS MULTIFUNCTIONAL PLATFORMS FOR TARGETED RADIONUCLIDE THERAPY AND MULTIMODAL MOLECULAR IMAGING

A dissertation submitted in partial fulfillment of the requirements for the degree of Doctor of Philosophy at Virginia Commonwealth University

by

Miguel Toro González

Bachelor of Science, Mechanical Engineering, National University of Colombia, CO

Director: Jessika V. Rojas, Ph.D.

Assistant Professor, Mechanical and Nuclear Engineering Department

Mechanical and Nuclear Engineering, College of Engineering

Virginia Commonwealth University

Richmond, Virginia

November, 2018

Acknowledgments

None of this would have been possible without my family, girlfriend, and friends, from my heart I really appreciate all their support, encouragement, and the sacrifices that they have made for me.

I am sincerely grateful to my advisor, Dr. Jessika V. Rojas, for supporting me throughout my graduate studies, for allowing me to make the research my own, for sharing her research interests, and for encouraging to always do my best.

I would like to thank the committee members, Dr. Massimo Bertino, Dr. Reza Mohammadi, Dr. Supathorn Phongikaroon, and Dr. Christina Tang. I will always be grateful for the knowledge you shared as my professors in materials, continuum, nonproliferation, and nanoscale physics. I really appreciate your willingness to collaborate and assist me throughout my dissertation and for furthering my knowledge of nanotechnology, material science, and nuclear engineering. I would like to thank Dr. Christina Tang since she willingly accepted to be part of my committee with such a short notice. To Dr. Sundaresan Gobalakrishnan, I wish him well and hope he recovers promptly.

I want to thank Dr. Carlos E. Castaño for always being available to support my research with significant inputs, assist with material characterization, and discuss my research results and plans.

I would like to thank Dr. Dustin M. Clifford for all the assistance and encouragement that he gave me, while being a student and after he joined our lab as a postdoc. I will always remember the good conversations, his concerts at The camel, and all the fun times. I am truly grateful for his

friendship. I want to thank Maria for her assistance and for sharing the lab with me since we started this journey in 2015. I would like to thank Dr. Joseph Turner for assisting me with trainings, discussing different components of my project, and furthering my knowledge in luminescence, elemental composition, and surface characterization.

I would like to thank the members of the Nuclear and Radiochemistry Group, Saed, Roy, Sandra, Justin, Ashley, Allison, David, Lance, Karen, Kevin, and Kathleen. They welcomed me in their group from the first day, helped me with everything they could to support my research, and made my time in Tennessee one of the best experiences that I have had. Particularly, I would like to thank Dr. Saed Mirzadeh for being my mentor, for all the knowledge he shared, and for supporting my research.

I want to thank Dr. Diana M. Lopez for considering and suggesting me to this doctoral opportunity. Her guidance as an undergraduate student, the knowledge she shared, and all the experiences we had working in the Friction Stir Welding project and with the high school girls. All those experiences contributed significantly to my growth as a person and researcher. I will always be thankful for the opportunity she gave me.

I would like to thank the Mechanical and Nuclear Engineering department for their support. In addition, I would like to recognize the U.S. Department of Energy Isotope Program within the Office of Nuclear Physics and an appointment to the Oak Ridge National Laboratory Nuclear Engineering Science Laboratory Synthesis program, sponsored by the U.S. Department of Energy and administered by the Oak Ridge Institute for Science and Education for their financial support during my work at Oak Ridge.

Table of Contents

List of Figures

List of Tables

List of Abbreviations

Abbreviation	Meaning
CN	Coordination number
CSF	Cerebrospinal fluid
CT	Charge-transfer
DI	Deionized
DLS	Dynamic light scattering
FI	Fluorescence imaging
FWHM	Full-width at half maximum
HPGe	High-purity germanium
ICP-OES	Inductively coupled plasma–optical emission spectroscopy
mAbs	Monoclonal antibodies
MRI	Magnetic resonance imaging
Na-TPP	Sodium tripolyphosphate
NIR	Near-infrared
NPs	Nanoparticles
ORNL	Oak Ridge National Laboratory
PBS	Phosphate buffer saline
PET	Positron emission tomography

PI	Polydispersity index
PMT	Photomultiplier tube
PVP	Poly(vinylpyrrolidone)
ROS	Reactive oxygen species
SAED	Selected area electron diffraction
SPECT	Single photon emission computer tomography
TEM	Transmission electron microscope
TRT	Targeted radionuclide therapy
TTC	Targeted thorium conjugates
UV	Ultraviolet
VCU	Virginia Commonwealth University
XRD	X-ray diffraction

Abstract

LANTHANIDE-BASED CORE-SHELL NANOPARTICLES AS MULTIFUNCTIONAL PLATFORMS FOR TARGETED RADIONUCLIDE THERAPY AND MULTIMODAL MOLECULAR IMAGING

By Miguel Toro González

A dissertation submitted in partial fulfillment of the requirements for the degree of Doctor of Philosophy at Virginia Commonwealth University.

Virginia Commonwealth University, 2018

Director: Jessika V. Rojas, Ph.D.

Assistant Professor, Mechanical and Nuclear Engineering Department

Lanthanide phosphate ($LnPO_4$) and lanthanide vanadate ($LnVO_4$) nanoparticles (NPs) are promising platforms for theranostic applications because of their chemical stability, low solubility, low toxicity, and unique luminescence and magnetic properties. Motivated by the high radiation resistance and ability to host actinides of naturally occurring lanthanide-based compounds, $LnPO_4$ and $LnVO_4$ NPs were studied as radionuclide carriers for targeted radionuclide therapy using *in vivo* α-generators, ^{223}Ra, ^{225}Ac, and ^{227}Th. The implementation of these radionuclides has shown potential for the treatment of micrometastases and solid tumors as well as challenges in the retention of decay daughters at the target site to minimize unwanted radiotoxicity. $LnPO_4$ and $LnVO_4$ core-shell NPs doped with either ^{156}Eu, a "cocktail" of $^{85, 89}Sr$ and ^{156}Eu, or *in vivo* α-generators ^{223}Ra, ^{225}Ac, and ^{227}Th were synthesized in aqueous media. *In vitro* retention of

radionuclides was investigated by dialyzing the radionuclide-doped NPs suspensions against deionized water and quantifying the activity in dialysate aliquots over time. The crystal structure, morphology, physical stability, luminescence and magnetic properties were evaluated. Partial retention of ^{156}Eu (~70–95%) and $^{85, 89}$Sr (>80%) was evidenced in $LnPO_4$ core NPs, while ^{227}Th and decay daughters were quantitatively retained in $LaPO_4$ core + 2 shells NPs (>99%). $Gd_{0.8}Eu_{0.2}VO_4$ and $GdVO_4$ core-shell NPs showed partial retention of ^{223}Ra (~75%), ^{225}Ac (75–95%), ^{227}Th (>96%), and decay daughters. Radionuclide retention was influenced by the lanthanide concentration, crystal structure, and number of shells. The partial retention of radionuclides in both $LnPO_4$ and $LnVO_4$ core-shell NPs may enhance the treatment efficacy while minimizing unwanted toxicity. $LnVO_4$ core and core-shell NPs have potential as carriers of short-lived radionuclides for both diagnostic and therapeutic applications. Emission intensities were higher for $LnVO_4$ with respect to $LnPO_4$ NPs, whereas no significant difference was observed in the magnetic susceptibilities. $GdVO_4$ core NPs displayed enhancement of the signal intensity in T_1-weighted images. This work evidences the promising application of both $LnPO_4$ and $LnVO_4$ NPs as platforms for targeted radionuclide therapy and multimodal molecular imaging.

1 Introduction

1.1 Motivation

Nanotechnology is contributing to achieve a major goal in medicine through the development of platforms that allow for an early detection and efficient treatment of clinical conditions with minimum side effects [1]. Multifunctional lanthanide-based nanoparticles (NPs) such as lanthanide phosphate ($LnPO_4$) and lanthanide vanadate ($LnVO_4$) are expected to have a key impact in nanomedicine because of the unique luminescence and magnetic properties of lanthanide ions [2], [3]. This is supported by the extensive number of studies that have reported the synthesis, characterization, and development of lanthanide-based NPs for biomedical applications [4]–[21]. A significant fraction of these studies has focused on exploiting lanthanide-based NPs as contrast agents for fluorescence imaging (FI) and/or magnetic resonance imaging (MRI). For FI, the adjustment of the elemental composition and concentration of Ln^{3+} ions can result in either downshifting, downconversion, or upconversion luminescence, where the latter is preferable for *in vivo* biomedical applications due to the penetration depth of infrared light in tissue (~5 mm) and minimal photodamage to cells [22]–[24]. For MRI, Gd^{3+} is the lanthanide of choice for the development of positive-T_1 contrast agents because of its large spin magnetic moment ($r_1 \propto \mu_s^2$), while either Dy^{3+} or Ho^{3+} may be used as negative-T_2 contrast agents thanks to their large magnetic moment ($r_2 \propto \mu^2$) [25].

The radiation resistance and ability to host actinides of naturally occurring lanthanide-based compounds [26]–[28] have encouraged the development of synthetic lanthanide-based NPs

as radionuclide carriers for either nuclear imaging or targeted radionuclide therapy (TRT). The addition of radionuclides as dopants in lanthanide-based NPs has the potential of combining the sensitivity of either single photon emission computed tomography (SPECT) or positron emission tomography (PET) with the spatial resolution of MRI within a single platform [29]–[31]. Although multimodal PET/SPECT/FI/MRI platforms may improve the diagnostic and monitoring of multiple diseases, only a limited number of studies have reported the synthesis, characterization, and evaluation of radionuclide-doped lanthanide-based NPs [32]–[37]. The development of lanthanide-based NPs for TRT has focused primarily on using $LnPO_4$ core-shell NPs doped with *in vivo* α-generators ^{223}Ra and ^{225}Ac [38]–[42] or β^--emitter ^{177}Lu [43]. Both ^{225}Ac and ^{223}Ra have evidenced promising efficacy as *in vivo* α-generators for the treatment of metastatic castration-resistant prostate cancer [44], [45]. Nonetheless, the leakage of decay daughters from the radioimmunoconjugate and the affinity of $RaCl_2$ to bone tissues may limit the application of ^{225}Ac and ^{223}Ra to different types of cancer. Thus, the partial retention of decay daughters and high radiochemical yield of α-generators shown by $LnPO_4$ NPs is contributing towards the spread of TRT [38]–[42].

$LnVO_4$ NPs are alternative platforms for the retention of therapeutically relevant radionuclides based on the radiation resistance evidenced by their crystal structure [26], [46]. In addition, the fact that $LnVO_4$ NPs can be prepared by simple aqueous synthesis routes makes them suitable for radiochemical settings [47]. $LnVO_4$ NPs are likely to have comparable radionuclide retention capabilities to that of $LnPO_4$ NPs, while the ability to synthesize them in a fraction of the time required for $LnPO_4$ NPs may open the possibility to use short half-lived radionuclides. The encouraging characteristics of $LnVO_4$ NPs, the promising use of ^{225}Ac, ^{223}Ra, and ^{227}Th as *in vivo* α-generators for TRT, and the limited studies that have been carried out with radionuclide-doped lanthanide-based NPs provide a motivation to explore and study lanthanide-based NPs as

multifunctional platforms for both molecular imaging and TRT applications. Furthermore, the retention of ^{227}Th and its first decay daughter ^{223}Ra has not been assessed yet in $LaPO_4$ core and core + 2 shells NPs, which have shown partial retention of $^{223, 225}$Ra, ^{225}Ac, and decay daughters [38]–[42]. The successful completion of this study will contribute to the development of radionuclide-doped $LnPO_4$ and $LnVO_4$ NPs as theranostic platforms for an early detection, a better treatment planning, and an efficient treatment of tumors [48].

1.2 Purpose

The purpose of this dissertation is to develop and investigate $LnPO_4$ and $LnVO_4$ core-shell NPs as multifunctional platforms for TRT and multimodal molecular imaging. The *in vitro* retention of *in vivo* α-generators ^{223}Ra, ^{225}Ac, ^{227}Th, and decay daughters was assessed in $LnPO_4$ and $LnVO_4$ core-shell NPs. Additional isotopes such as ^{156}Eu and $^{85, 89}$Sr were also used to demonstrate the versatility of $LnPO_4$ and $LnVO_4$ NPs to host and retain radionuclides for diagnostic and therapeutic applications. The influence of the crystal structure, lanthanide concentration, and core-shell structure in the retention of radionuclides was studied in both $LnPO_4$ and $LnVO_4$ core and core-shell NPs. Particularly, the lanthanide concentration in $LnPO_4$ and $LnVO_4$ NPs was tailored to provide luminescence and/or magnetic properties for their application as contrast agents in FI and/or MRI, while core-shell structures were developed to enhance the retention of radionuclides.

1.3 Approach

Four phases were proposed and explored to assess the *in vitro* retention of *in vivo* α-generators and decay daughters in $LnVO_4$ and $LnPO_4$ core-shell NPs synthesized with either luminescence and/or magnetic functionalities. In phase I, $LnPO_4$ core-shell NPs were synthesized via an aqueous route that have been previously used to prepare radionuclide-doped NPs. The

influence of temperature and heating time on the growth kinetics and core-shell formation of $LnPO_4$ NPs was evaluated to reduce the time consumed during synthesis toward the implementation of short-lived radionuclides. The dependence of luminescence and magnetic properties on the lanthanide concentration was also studied to provide functionalities for FI and/or MRI. A similar approach was followed in phase II for $LnVO_4$ core-shell NPs, which were synthesized by two precipitation routes in water. Each route is suitable for radiochemical settings and yielded NPs with distinctive morphology, physical stability, and surface chemistry. Characterization of the crystal structure, morphology, luminescence properties, magnetic susceptibility, surface chemistry, physical stability, among others, was carried out for both $LnPO_4$ and $LnVO_4$ NPs. Particular attention was given to the development of core-shell structures in $LnVO_4$ NPs to enhance the retention of radionuclides, whereas the adjustment of the lanthanide concentration within $LnPO_4$ and $LnVO_4$ NPs was done to provide luminescence and magnetic properties.

In phase III, the experiments and characterization carried out in phases I and II were used as a reference to define the optimal synthesis conditions and concentration of lanthanide ions for the synthesis of radionuclide-doped $LnVO_4$ and $LnPO_4$ core-shell NPs. The *in vitro* retention of ^{223}Ra, ^{225}Ac, ^{227}Th, and decay daughters was studied for $LnVO_4$, whereas ^{227}Th and $^{85, 89}Sr$, ^{156}Eu were tested in $LnPO_4$ NPs. The purification of radionuclides, radiochemical synthesis, and evaluation of the *in vitro* retention were carried out at Oak Ridge National Laboratory (ORNL). Lastly in phase IV, current efforts are being focused on the surface characterization and assessment of the physical stability of $LnVO_4$ and $LnPO_4$ core-shell NPs. Phases I, II, and IV were completed at Virginia Commonwealth University (VCU).

1.4 Organization of the Dissertation

This dissertation consists of 7 chapters in total. Chapter 2 starts with a general description of the synthesis methods that have been used to produce $LnVO_4$ and $LnPO_4$ NPs and their multifunctional properties for nanomedicine. An overview of TRT and the carriers that have been tested, particularly for *in vivo* α-generators and decay daughters, is also presented in this chapter. In Chapter 3, the chemicals, radionuclides, materials, and synthesis routes used to prepare $LnPO_4$ and $LnVO_4$ NPs are described. In addition, the sample preparation, techniques, and equipment used for the characterization of both nonradioactive and radionuclide-doped NPs are presented. The characterization of nonradioactive $LnPO_4$ and $LnVO_4$ core-shell NPs, after varying synthesis parameters such as temperature, heating time, lanthanide concentration, among others, is summarized in Chapters 4 and 5, respectively. Chapter 6 describes the *in vitro* retention of radionuclides in $LnPO_4$ and $LnVO_4$ core-shell NPs synthesized with either luminescence and/or magnetic functionalities. The last chapter (Chapter 7) summarizes the conclusions of this dissertation and suggests future steps for testing the multifunctional capabilities of $LnPO_4$ and $LnVO_4$ NPs.

2 Literature Review

2.1 Multifunctional $LnPO_4$ and $LnVO_4$ NPs

The unique optical and magnetic properties of lanthanide-based NPs, arising from the *4f* electronic configuration of Ln^{3+} ions, as well as their low toxicity have prompted their development for biomedical applications [49]. The ability of lanthanide-based NPs to have both diagnostic and therapeutic functionalities within a single platform is contributing to the development of non-invasive, specific, and individualized therapies [50], [51]. These functionalities may be tailored based on the choice of host matrix, concentration of Ln^{3+} ions, surface functionalization, or morphology [52], [53]. This versatility has made of lanthanide-based NPs one of the most engineered materials for biomedical applications [2]. Among matrices, oxides such as orthophosphate (PO_4) and orthovanatate (VO_4) have shown high chemical and thermal stability [54], [55], low toxicity [5], [56], and adaptable functionalization strategies [9], [52], [57]–[59]. Furthermore, the existence of multiple synthesis methods that could be used for pharmaceutical preparations of $LnVO_4$ and $LnPO_4$ NPs have encouraged their application in nanomedicine [55]. Different synthesis methods, those that may be suitable for either biomedical applications or radiochemical settings are presented in **Table 2-1** with their advantages and disadvantages.

Table 2-1 Summary of synthesis methods used for $LnPO_4$ and $LnVO_4$ NPs with their advantages and disadvantages for either biomedical or radiochemical applications (adapted from [2]).

Method	Advantages	Disadvantages
Precipitation	▪ Tunable morphology ▪ Narrow size distribution ▪ Simple procedure ▪ Low costs	▪ Low crystallinity ▪ Calcination or annealing may be required
Hydrothermal, solvothermal	▪ Tunable morphology ▪ Highly crystalline NPs	▪ Specialized reaction vessels ▪ Long reaction times
Sol-gel	▪ Simple procedure ▪ Tunable morphology	▪ Broad particle size distribution ▪ Calcination or annealing may be required ▪ Long reaction times
Microwave assisted	▪ Clean, fast, and energy efficient ▪ Tunable morphology	▪ Specialized microwave reactors
Sonochemical	▪ Tunable morphology ▪ Simple setup	▪ Specialized high-intensity ultrasonic probe

The application of lanthanide-based NPs for diagnostics has been focused primarily on fluorescence, magnetic resonance, and/or computed tomography imaging [60], [61]. The large Stoke's shifts, an absence of blinking, narrow emission bands, and a high resistance to photobleaching of lanthanide-based NPs have made them an alternative to fluorescence dyes or quantum dots [49], [52], [60]. The fluorescence or emission wavelength of lanthanide-based NPs is independent of their size and either downconversion or upconversion luminescence can be obtained by tailoring the composition and concentration of Ln^{3+} ions [62]–[64]. Application of lanthanide-based NPs as MRI contrast agents is related to the unpaired electrons of Gd^{3+} and the large magnetic moments of Dy^{3+} and Ho^{3+} ions [25], [65]. Although Gd-chelates are extensively used as MRI contrast agents, a higher image contrast can be obtained using gadolinium-based NPs with only a fraction of the applied dose required for commercial contrast agents [21]. Moreover, the toxicity associated to the transmetallation of Gd^{3+} ions with endogenous cations can be minimized using Gd-based NPs, where the Gd cations are bound within an inorganic crystal [22],

[66]. Dysprosium- or holmium-based NPs have proven to be promising contrast agents for applications at high magnetic field strengths since saturation of their magnetic moment is not achieved as in the case of superparamagnetic iron oxide NPs [25], [61], [65]. Lastly, lanthanide-based NPs have been proposed as contrast agents for x-ray computed tomography because of their atomic number and low toxicity with respect to barium and iodine-based compounds [61], [67].

As therapeutic agents, lanthanide-based NPs may be used for photodynamic therapy, radiation therapy, and/or drug delivery [49]. The luminescence properties, absorption and emission, of lanthanide-based NPs allow the excitation of a photosensitizer using either ultraviolet (UV) or near-infrared (NIR) radiation to produce reactive oxygen species (ROS) intended to kill cancer cells [68]. X-rays can also be used as a source of excitation thanks to the atomic number of Ln^{3+} ions, while providing a greater penetration depth to that of UV or NIR [69]. A similar rationale is used for radiation therapy, where lanthanide-based NPs interact with x-rays inducing a localize dose enhancement [70]. Lanthanide-based NPs have also been investigated as carriers of either anticancer drugs or radionuclides [9], [13], [15], [38]–[43], [71]. Surface modification of lanthanide-based NPs has been carried out by adding a shell of mesoporous silica, whose large surface area and porous structure will ensure a high adsorption of anticancer drugs [9], [15]. The mesoporous shell not only provides drug carrier capabilities, but it also enhances the physical and chemical stability, reduces the toxicity, and facilitates the functionalization and bioconjugation of lanthanide-based NPs [61], [72]. The interest of lanthanide-based NPs as radionuclide carriers has been encouraged by the radiation resistance and ability to host multivalent ions, particularly actinides, of naturally occurring lanthanide-based compounds [26]–[28]. The encapsulation of radionuclides has been carried out by substituting a Ln^{3+} ion with a radioactive isotope within the crystal structure of lanthanide-based NPs [38]–[43]. The performance of lanthanide-based NPs as radionuclide carriers for TRT applications will be introduced in section 2.2 and discussed in detail

in Chapter 6. It is important to highlight that lanthanide-based compounds have been suggested as alternative nuclear waste forms for the conditioning of radioactive waste streams based on their ability to contain high waste load, their high thermal and chemical stability, and the radiation resistance evidenced by their crystal structure [26], [27], [46], [73], [74].

Multifunctional lanthanide-based NPs with diagnostic and therapeutic functionalities can be developed to recognize cancer cells, deliver therapeutic drugs, and visualize the evolution of the tumor [75]. Lanthanide-based NPs may also include nuclear imaging capabilities by incorporating radionuclides within their crystal structure or having them adsorbed on their surface. The high sensitivity of either computed tomography, SPECT, or PET, the excellent spatial resolution of MRI, and the low-cost and easy operation of near-infrared fluorescence can be combined by designing multimodal imaging platforms [31]. A similar approach could be followed for therapeutic purposes, where lanthanide-based NPs can be used as a platform to enhance the dose at the target site as well as to deliver anticancer drugs and radionuclides to increase the destruction of cancer cells that may have showed either resistance to chemotherapy or radiation [76].

2.2 Targeted Radionuclide Therapy

In TRT, radionuclides are used for the specific targeting of cancer cells to reduce the toxicity and side effects associated with current treatment procedures [77], [78]. The rationale behind TRT is to use the radiation generated during the decay of radionuclides in-situ to destroy the nuclear DNA strands via either radiation-induced ionization, chemical transmutation, or generation of ROS [77]. The types of radiation that are of main interest for biological applications are α-particles, β^--particles, and Auger electrons because of their short range in tissue and high linear energy transfer [79]. The range is an essential parameter to identify the tumor size that can be treated with each type of radiation, where α- and β^--particles may be suitable for micrometastatic tumors and

solid tumors of large size, respectively [77], [79]. Radiopharmaceuticals such as Zevalin® (^{90}Y-ibritumomab tiuxetan), Bexxar® (^{131}I-tositumomab), and Xofigo® ($^{223}RaCl_2$), based on both α- and β^--emitting radionuclides, have been approved by the United States Food and Drug Administration for medical treatment [44], [80].

The clinical efficacy of Xofigo® as well as the high linear energy transfer and relative biological effectiveness of α-particles has increased the interest in developing new radiopharmaceuticals based on α-emitting radionuclides [81], [82]. Using α-emitting radionuclides can lead to a large fraction of DNA double-strand breaks, which are hard to repair by the cells, thanks to the high linear energy transfer of α-particles and the similar distance between two ionizations events of α-particles in water to that of two strands of DNA [83]–[85]. Although there is not known resistance mechanism against the highly cytotoxic α-particles, their use in clinical settings has been limited by (i) the availability of radionuclides with proper physical and chemical characteristics, (ii) the production of radionuclides in clinical quantities, and (iii) the design of carriers to minimize the leakage of radionuclides *in vivo* [86], [87]. Among α-emitting radionuclides, the leakage of *in vivo* α-generators such as ^{223}Ra, ^{225}Ac, ^{227}Th, and decay daughters from the tumor site represents a significant risk in biological settings since free radionuclides can deliver substantial dose to normal tissue and decrease the efficacy of the treatment [81]. To prevent the leakage of α-emitting radionuclides, various approaches have been proposed such as a local administration to the target site, a fast uptake by tumor cells by selecting a proper targeting agent, and/or the use of a carrier [81]. The development of carriers is not only the most promising alternative to minimize the side effects caused by the leakage of α-emitting radionuclides when using large activities, but it also allows the addition of multiple functionalities. The retention of α-emitting radionuclides at the target site will be influenced by the highly energetic decay daughter nucleus as well as the *in vivo* stability and the resistance to radiation damage of the carrier [77].

The simplest carriers that have been used for either α-emitting or other therapeutically relevant radionuclides are monoclonal antibodies (mAbs), chelating agents, and peptides [80], [83], [88], [89]. Monoclonal antibodies are characterized by their ability to be easily bound to the radionuclide, their high specificity towards predominant antigens in the tumor, and their superior diversity and affinity compared to peptides [90], [91]. The main disadvantage of either mAbs, peptides, or chelating agents is the fact that they cannot sustain the recoil energy of decay daughters resulting in their release [92]. More complex alternatives for the retention of *in vivo* α-generators have been proposed including liposomes, zeolites, polymersomes, lanthanide- and metal-based NPs [81]. Although these carriers may provide additional functionalities and the ability to deliver large activities, the α-particle recoil energy (100–200 keV) will always result in chemical bond breaking [92], [93]. The partial retention of α-emitting radionuclides and decay daughters in these structures has been associated to either (i) the conversion of a fraction of the recoil energy to translational energy of the structure, (ii) the intrinsic attenuation of the decay daughter by the structure, (iii) the implantation of the decay daughter in adjacent structures, or (iv) the reloading/adsorption of decay daughters by structure and/or surface groups [92], [94]–[96]. The structures that have been studied for the retention of *in vivo* α-generators such as ^{223}Ra, ^{225}Ac, ^{227}Th, and decay daughters will be described for each radionuclide in the following paragraphs.

Although ^{223}Ra is the first *in vivo* α-generator that has been approved for treatment of prostate cancer [44], the lack of suitable chelating agents and the rapid dissociation in biological media of radium isotopes have restricted their application for treatment of other cancers [97]. Various platforms have been proposed for the encapsulation and retention of radium isotopes and decay daughters (**Table 2-2**). Nanozeolites have been doped with radium isotopes via an exchange reaction with Na^+ ions that are located within the channels and interstices of the NPs [98], [99]. These NPs have shown high retention of radium isotopes in multiple media and partial retention

of decay daughters (**Table 2-2**). The partial retention of decay daughters has been related to a translation of their recoil energy to the whole NP as well as to re-adsorption in the NPs because of their characteristics as ion exchanger [98], [99]. Despite the promising retention capabilities of nanozeolites, their large size (~100 nm), tendency to aggregate, and high hydrophilicity may limit their *in vivo* application [99]. Although liposomes have high retention of radium isotopes in multiple biological media, the retention of decay daughters is dependent on the liposome size [100], [101]. The application of liposomes in biological settings may be restricted by the difficulties associated to their synthesis and preparation, their large size (>100 nm), and polydispersity. Fe_3O_4 NPs are a promising multifunctional platform for theranostic applications where MRI and TRT are combined thanks to the sorption of ^{223}Ra. However, low retention of decay daughters may be expected since the radionuclide is adsorbed on the NP surface [102]. Both hydroxyapatite and $CaCO_3$ particles have shown high retention of radium isotopes (>90%) and have been used in a number of biomedical applications due to their biocompatibility, nonetheless, their main drawback is the lack of functionalities for molecular imaging and their affinity to bone tissue [103]–[105]. Lastly, the quantitative retention of ^{223}Ra and decay daughter ^{211}Pb in $LaPO_4$ core + 2 shells NPs is promising for TRT since it will reduce the dose deliver to healthy tissue and enhance the efficacy of the treatment [38]. Surface modification with targeting moieties of La(^{223}Ra)PO_4 NPs must be done to assess their biodistribution, biocompatibility, and *in vivo* response.

Table 2-2 Nano-platform carriers that have been studied for the retention of Ra isotopes and decay daughters towards TRT.

Platform	Isotope	Radiolabeling	Parent/daughter retention	Reference
Nanozeolite (50–80 nm)	^{223}Ra	Ion exchange Na ↔ Ra	>99.5% for ^{223}Ra 90–95 % for decay products	[99]

Liposome (mean Ø 120 nm)	^{223}Ra, ^{224}Ra, ^{228}Ac	Ionophore mediated loading	^{223}Ra: 96 ± 1% in water 93 ± 2% in serum No daughter retention reported	[101]
NaA nanozeolite (30–70 nm)	^{224}Ra, ^{225}Ra	Ion exchange Na ⟷ Ra	>99.5% for ^{223}Ra in multiple media, Partial retention of decay products	[98]
Fe_3O_4 NPs (12–16 nm)	^{223}Ra	Sorption or precipitation on surface	Quantitative in PBS and PVP >95% in plasma, serum, albumin, Geloplasma® No daughter retention reported	[102]
$LaPO_4$ core and core + 2 shell NPs (3.8–7.1 nm)	^{223}Ra, ^{225}Ra	Replacement of La for Ra in the crystal structure	**Core:** ~88% of ^{223}Ra ^{211}Pb in equilibrium with ^{223}Ra **Core + 2 shells:** >99.6% of ^{223}Ra quantitative retention of ^{211}Pb >99.98% of ^{225}Ra, 80% of ^{221}Fr	[38]
Hydroxyapatite nano- and microparticles	^{223}Ra	Sorption or incorporation into structure	**For NPs:** >85% of ^{223}Ra for incorporation while >90% for sorption, ~95% for incorporation and annealed No daughter retention reported	[103]
Hydroxyapatite nanoparticles	^{223}Ra	Surface and intrinsic labelling	>95% of ^{223}Ra after 24 hours in physiological saline. Depends on labeling yield	[104]
$CaCO_3$ microparticles (1–3 µm, 3–15 µm)	^{224}Ra	Precipitation on particle surface	>95% for ^{224}Ra and ^{212}Pb	[105]

PBS: phosphate buffer saline, PVP: poly(vinylpyrrolidone)

Contrary to radium, actinium isotopes can be readily attached to either chelating agents, complexes, or antibodies [87], [106], [107]. Biodistribution and toxicity studies using these carriers have shown rapid association of free ^{225}Ac cations to serum proteins and significant accumulation of decay daughters, ^{221}Fr and ^{213}Bi, in the kidneys since no retention is expected at the target site [81]. Despite the anticipated toxicity of decay daughters when using chelating agents or mAbs, the interest in ^{225}Ac for TRT has increased thanks to the remarkable therapeutic efficacy of ^{225}Ac-PSMA-617 for large-stage metastatic castration-resistance prostate cancer [45], [108]. Liposomes, polymersomes, $LnPO_4$ core-shell NPs, and TiO_2 NPs have been studied as carriers of ^{225}Ac and decay daughters for application in TRT to minimize the leakage of radionuclides (**Table 2-3**). The main challenge of using either liposomes or polymersomes as carriers is their size

dependent retention of decay daughters, which can be enhanced significantly when designing large liposomes (>1 μm) [101], [109], [110]. The large size of liposomes and polymersomes limits their stability, affects their intra- and inter-cellular uptake, and may result in the clogging of microcapillary vessels [94], [109]. Polymersomes loaded with ^{225}Ac showed no uptake by the cell nucleus because of their large size [111]. Smaller carriers such as $LnPO_4$ or TiO_2 NPs have shown partial retention of radionuclides. The retention of radionuclides in $LnPO_4$ NPs is dependent on the number of shells and their elemental composition [42]. Surface-modified $LaPO_4$ core NPs with mAb 201B showed rapid accumulation in mouse lung and >80% *in vivo* retention of ^{213}Bi [39]. Following a multi-step procedure to synthesize $LnPO_4$ core-shell NPs, having four shells of $GdPO_4$ and a gold layer, an increase in the *in vitro* retention of ^{221}Fr to 90% was achieved [42]. The high sorption affinity of TiO_2 NPs was exploited to labeled ^{225}Ac cations via a simple and fast procedure [94]. The high retention of decay daughters, >68.5% of ^{221}Fr in PBS, physiological salt, and cerebrospinal fluid (CSF), was attributed to the reloading of decay daughters thanks to the cation exchange properties of TiO_2 NPs [94]. Their relatively large size (~100 nm) after surface functionalization may impose limitations to their application in biological settings due to their slow clearance [81], [94].

Table 2-3 Nano-platform carriers that have been assessed for the retention of Ac isotopes and decay daughters towards TRT.

Platform	Isotope	Radiolabeling	Parent/daughter retention	Ref.
Zwitterionic and cationic liposomes (100–800 nm)	^{225}Ac	Passive entrapment	>88% of ^{225}Ac in zwitterionic >54% of ^{225}Ac in cationic <12% of ^{213}Bi, retention was dependent on size and composition	[100]
Multivesicular liposomes (758 ± 287 nm)	^{225}Ac	Passive entrapment	>95% of ^{225}Ac <20% of ^{213}Bi	[109]
Liposomes (mean Ø 120 nm)	^{223}Ra, ^{224}Ra, ^{228}Ac	Ionophore mediated loading	^{228}Ac: 95 ± 2% No daughter retention reported	[101]

PEGylated liposomes (121 ±6 nm)	^{225}Ac	Ionophore mediated loading	54–81% of ^{225}Ac in PBS 35–56% of ^{225}Ac in serum media No daughter retention reported	[112]
Polymersomes (800 nm)	^{225}Ac	Ionophore mediated loading	~93% of ^{225}Ac 69 ± 1.5% of ^{221}Fr 53 ± 4.0% of ^{213}Bi	[113]
$InPO_4$ containing polymersomes (100–800 nm)	^{225}Ac	Co-encapsulation with $InPO_4$	92 ± 3% of ^{225}Ac <60% of ^{221}Fr, <40% of ^{213}Bi in 100 nm polymersomes	[95]
$LaPO_4$ core NPs (<10 nm)	^{225}Ac	Replacement of La for Ac in the crystal structure	~99.9% for ^{225}Ac ~40% for ^{221}Fr and ^{213}Bi	[39]
$La_{(1-x)}Gd_xPO_4$ core, core + 2, and core + 4 shell NPs (<22 nm)	^{225}Ac	Replacement of La for Ac in the crystal structure	**Core:** ~99% of ^{225}Ac, 60.2 ± 3.0% of ^{221}Fr **Core + 2 shells:** 99.42 ± 0.02% of ^{225}Ac, 69.2 ± 1.7% of ^{221}Fr **Core + 4 shells:** >99.96% of ^{225}Ac, >79.4% of ^{221}Fr	[42]
TiO_2 NPs (25 nm)	^{225}Ac	Ion exchange reaction on OH groups	>95% of ^{225}Ac and ^{221}Fr in PBS >9% of ^{225}Ac, <70% of ^{221}Fr in CSF	[94]

Differing from its first decay daughter, ^{227}Th is able to form stable chelator complexes for its application in TRT [82], [86]. Several studies have shown the potential application of targeted thorium conjugates (TTC) for B-cell lymphomas, solid cancers, acute myeloid leukemia, among others [82], [114]–[116]. The half-life of ^{227}Th ($T_{1/2}$ = 18.7 days) is comparable to the blood half-life of antibodies [115] and is suitable for radiopharmaceutical production, drug distribution, and patient treatment [117]. The long half-life of ^{227}Th may also increase the dose delivered to the tumor while minimizing that to normal tissue [101]. The generation of ^{227}Th from thermal neutron irradiation of a ^{226}Ra target may allow its production in relevant quantities to promote the spread of TRT clinically [86]. Although TTCs have shown promising *in vitro* and *in vivo* results, these conjugates cannot retain decay daughters at the target site. It has been reported that TTCs can

induce myelosuppression because of the bone seeker characteristics of ^{223}Ra, which can be reversible depending on the administered dose [82]. The leakage of decay daughters may also decrease the efficacy of the treatment and hence large activities will be required to achieve the desired dose. Therefore, the development and evaluation of nano-platforms doped with ^{227}Th is of utmost importance to continue its spread as *in vivo* α-generator in TRT.

Targeted radionuclide therapy using α- and β^--emitting radionuclides can reduce the collateral damage to healthy tissue compare to external beam radiation therapy [90]. Application of α-emitting radionuclides has the advantage that α-particles can overcome the resistance of cells to β^--radiation, γ-radiation, chemotherapeutic drugs, and apoptosis [118]. Although the application of α-emitting radionuclides has been suggested for small tumors, metastasized cells, and cellular clusters because of the short range of α-particles, the treatment of solid tumors may also be possible [108]. A low amount of activity is required to deliver therapeutically relevant doses for cancer treatment when using *in vivo* α-generators [101]. However, the treatment efficacy depends on a reduction of the radionuclide leakage from the target site to maximize the dose deliver and minimize the toxicity to healthy organs. The design of nano-platforms aims to minimize the leakage of both parent and daughter radionuclides as well as to provide multiple functionalities to assess the evolution of the tumors and to develop personalized cancer treatments [119]. These nano-platforms can be modified with antibody fragments to achieve a specific and fast uptake by the tumor as well as to minimize their toxicity [87]. The partial retention of decay daughters and a fast uptake by the tumor of functionalized nano-platforms may be the solution to the collateral damage caused to healthy tissue [81].

3 Experimental Procedure

This chapter gives a general description of the chemical precursors and synthesis methods used for the preparation of nonradioactive $LnPO_4$ and $LnVO_4$ NPs. More details regarding the concentration of reagents, temperature, heating time, among others, will be presented in Chapters 4 and 5. The preparation of the radioisotopes of interest for the synthesis of radionuclide-doped NPs is also described in this section. Lastly, the techniques, equipment, and sample preparation used for the characterization of both nonradioactive and radionuclide-doped NPs are presented.

3.1 Chemical Precursors, Radionuclides, and Materials

3.1.1 Chemical Precursors

The chemical precursors used for the synthesis of both $LnPO_4$ and $LnVO_4$ NPs are presented in **Table 3-1**.

Table 3-1 Description, chemical formula, manufacturer, and purity of chemical precursors used for the synthesis of lanthanide-based NPs.

Description	Manufacturer	Purity
Lanthanum(III) chloride heptahydrate ($LaCl_3 \cdot 7H_2O$)	Sigma-Aldrich	ACS reagent
Cerium(III) chloride heptahydrate ($CeCl_3 \cdot 7H_2O$)	Sigma-Aldrich	99.9%
Neodymium(III) chloride hydrate ($NdCl_3 \cdot xH_2O$)	Alfa Aesar®	99.9%
Europium(III) chloride hexahydrate ($EuCl_3 \cdot 6H_2O$)	Sigma-Aldrich	99.9%
Gadolinium(III) chloride hexahydrate ($GdCl_3 \cdot 6H_2O$)	Alfa Aesar®	99.9%

Terbium(III) chloride hexahydrate ($TbCl_3 \cdot 6H_2O$)	Alfa Aesar®	99.9%
Dysprosium(III) chloride hydrate ($DyCl_3 \cdot xH_2O$)	Alfa Aesar®	99.9%
Holmium(III) chloride hexahydrate ($HoCl_3 \cdot 6H_2O$)	Alfa Aesar®	99.9%
Ytterbium(III) nitrate hydrate ($Yb(NO_3)_3 \cdot xH_2O$)	Alfa Aesar®	99.9%
Lutetium(III) chloride hexahydrate ($LuCl_3 \cdot 6H_2O$)	Alfa Aesar®	99.9%
Sodium tripolyphosphate pentabasic ($Na_5P_3O_{10}$)	Sigma-Aldrich	≥98%
Sodium orthovanadate (Na_3VO_4)	Acros Organics	99%
Sodium citrate dihydrate ($Na_3C_6H_5O_7 \cdot 2H_2O$)	Sigma-Aldrich	Ultrapure reagent

3.1.2 Radionuclides

A brief description of the production and purification of radionuclides based on established routines at ORNL is given below:

- **^{156}Eu**

A solution consisting mainly of ^{156}Eu ($T_{1/2}$ = 15.2 days) with negligible quantities of ^{154}Eu and ^{155}Eu in a 0.1 M HCl was obtained as a by-product of routine strontium-89 ($T_{1/2}$ = 50.5 days) production at the High Flux Isotope Reactor at ORNL. The highly enriched ^{88}Sr target contained <10 ppm of natural europium (^{151}Eu and ^{153}Eu), as impurities. During a 24-day irradiation of ~2 g of ^{88}Sr target at a thermal neutron flux of 2×10^{15} n s^{-1} cm^{-1}, ~20 μCi of ^{156}Eu and <1 μCi of ^{154}Eu and ^{155}Eu, are co-produced with ~2 Ci of ^{89}Sr. Various isotopes of europium such as ^{154}Eu, ^{155}Eu, and ^{156}Eu as well as ^{89}Sr were produced through neutron capture during the irradiation. Following irradiation, the target was processed in a hot cell facility, and the Eu isotopes were separated from Sr by ion exchange and extraction chromatography methods.

- **$^{85, 89}$Sr and ^{156}Eu cocktail**

A radioactive cocktail solution consisting of ^{85}Sr ($T_{1/2}$ = 64.8 days), ^{89}Sr, and ^{156}Eu in a 0.1 M HCl was obtained from routine strontium-89 production at the High Flux Isotope Reactor at ORNL as described above. The radioactive solution had a high concentration of strontium ions (~ 15 mg/mL).

- **^{225}Ac**

A carrier-free ^{225}Ac ($T_{1/2}$ = 9.9 days) stock was acquired from a mixture of ^{228}Th, ^{229}Th, and ^{232}Th by anion and cation exchange chromatography at ORNL [120]. Briefly, thorium-229 stock from either pre-existing waste material stored for over 30 years at ORNL or recovered from chemical separation of ^{233}U is dissolved in 8 M HNO_3. Ra and Ac are separated from the Th, U, and Fe cations using an anion exchange resin. Final purification and separation of ^{225}Ac from Ra, Pb, and Bi cations is carried out using a cation exchange resin [120]. Production and separation of ^{225}Ac via spallation of Th targets has also been reported [121]–[123]. The separation process only comprises solid-support sorption, which implies a significant reduction of organic radioactive waste [121]. A two-step sequence involving cation exchange and extraction chromatography has also been proposed for purification of Ac from Th targets [123]. Overall, the separation and purification of Ac isotopes is dependent on their method of production [123]. The decay scheme of ^{225}Ac is shown in **Fig. 3-1**.

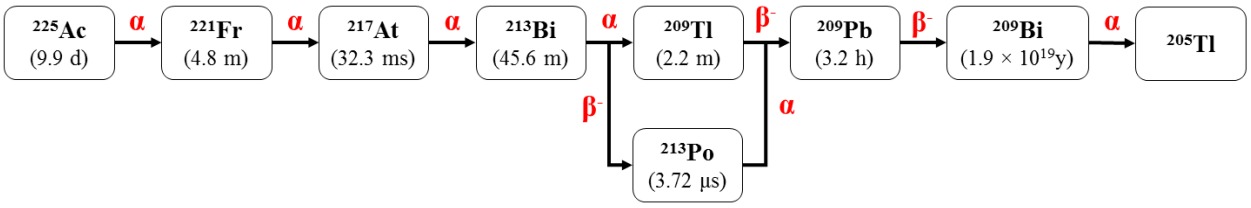

Fig. 3-1 Nuclear decay scheme of ^{225}Ac.

- **^{227}Th and ^{223}Ra**

Production of ^{227}Ac/^{227}Th/^{223}Ra generator may be carried out by several methods such as ^{227}Ac originating from natural sources of ^{235}U, proton spallation of ^{232}Th, or neutron irradiation of ^{226}Ra [^{226}Ra(n,γ)^{227}Ra → ^{227}Ac] [121], [124]. The latter is the most feasible method for the production of ^{227}Th and ^{223}Ra in clinically relevant quantities. Purification and separation of either

^{227}Th or ^{223}Ra was carried out in a hot cell facility via ion exchange and extraction chromatography methods. The decay scheme of ^{227}Th is shown in **Fig. 3-2Fig. *3-1***.

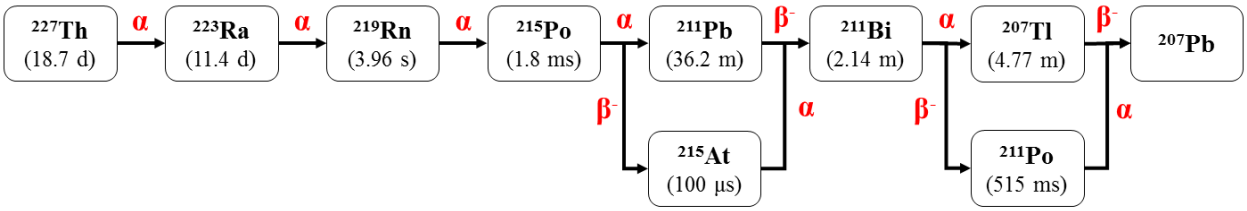

Fig. 3-2 Nuclear decay scheme of ^{227}Th.

3.1.3 Materials

Deionized (DI) water (18 MΩ) used for the preparation of aqueous solutions was obtained from a MilliQ® water purification system (Millipore Sigma, Burlington, MA). The purification of the NPs suspensions after synthesis was done by using dialysis against DI water. Biotech regenerated cellulose dialysis membranes with a molecular weight cutoff of 8–10 kDa were purchased from Spectrum Labs® (Repligen Corporation, Waltham, MA). The regenerated cellulose membrane was washed several times with DI water before being used to remove preservatives.

3.2 Synthesis of $LnPO_4$ core and core-shell NPs

$LnPO_4$ core NPs were synthesized by precipitation of Ln^{3+} and $[PO_4]^{3-}$ ions from lanthanide salts ($LnCl_3{\cdot}xH_2O$) and sodium tripolyphosphate ($Na_5P_3O_{10}$, Na-TPP) [125]. Both $LnCl_3{\cdot}xH_2O$ and $Na_5P_3O_{10}$ were prepared at 0.1 M in DI water. Lanthanide salts were mixed at specific volume ratios to achieve the desired molar concentrations of Ln^{3+} ions. The Ln-solution was mixed with the solution containing Na-TPP at volume ratios of 1:1 and 1:2, depending on the Ln^{3+} ions used, to obtain a clear solution (**Fig. 3-3** and **Fig. 3-4**). The mixture of $LnCl_3$/Na-TPP was heated at 90 °C for 3 hours to promote the hydrolysis of the tripolyphosphate ($[P_3O_{10}]^{5-}$) ions into

pyrophosphate ($[P_2O_7]^{4-}$) and orthophosphate ($[PO_4]^{3-}$) ions [125]. The interaction between the $[PO_4]^{3-}$ and Ln^{3+} contributes to the nucleation and growth of the $LnPO_4$ core NPs, while a fraction of the tripolyphosphate and pyrophosphate groups helps to restrict the growth and acts as stabilizer [125]. The formation and growth of $LnPO_4$ core NPs resulted in a change of the solution appearance from clear to turbid (**Fig. 3-5**). The as-prepared $LnPO_4$ core NPs suspensions were dialyzed against DI water to remove unreacted species. After dialysis, the NPs suspension changed appearance, becoming more translucent (**Fig. 3-6**).

For the synthesis of $LnPO_4$ core-shell NPs, a mixture of $LnCl_3$ and Na-TPP was prepared at a 1:2 volume ratio. The fresh $LnCl_3$/Na-TPP mixture was added to the as-prepared or dialyzed core NPs suspensions in a 1:1 volume ratio and mixed using a vortex mixer. The resulting suspension was heated at 90 °C for 3 hours to synthesized $LnPO_4$ core + 1 shell NPs. Deposition of additional shells was completed by repeating this procedure while keeping the 1:2 volume ratio between $LnCl_3$ and Na-TPP and the 1:1 volume ratio between the fresh $LnCl_3$/Na-TPP solution and core NPs suspension. The as-prepared $LnPO_4$ core-shell NPs suspensions were also dialyzed against DI water to remove unreacted species.

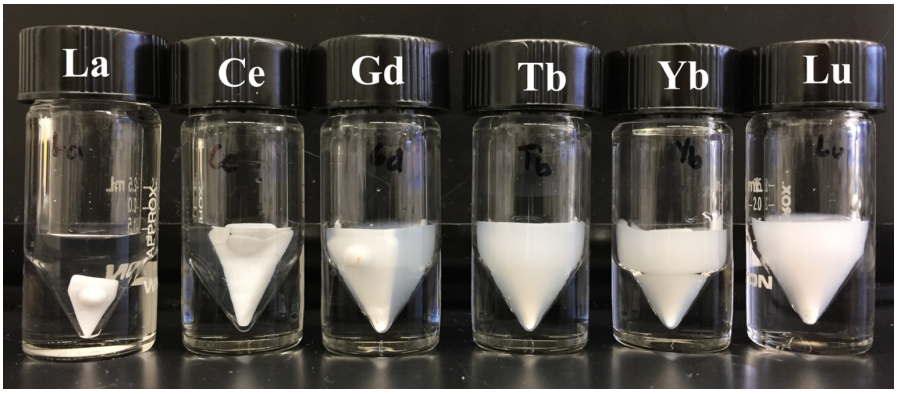

Fig. 3-3 Ln-TPP solution appearance at 1:1 Ln:Na-TPP volume ratio before synthesis.

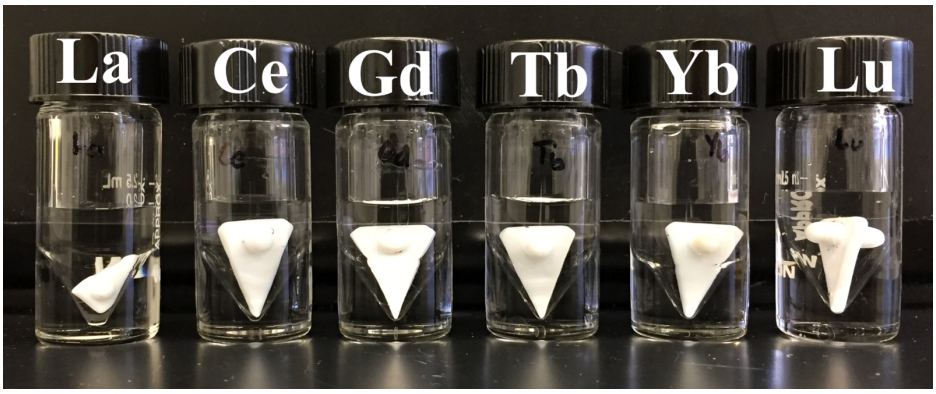

Fig. 3-4 Ln-TPP solution appearance at 1:2 Ln:Na-TPP volume ratio before synthesis.

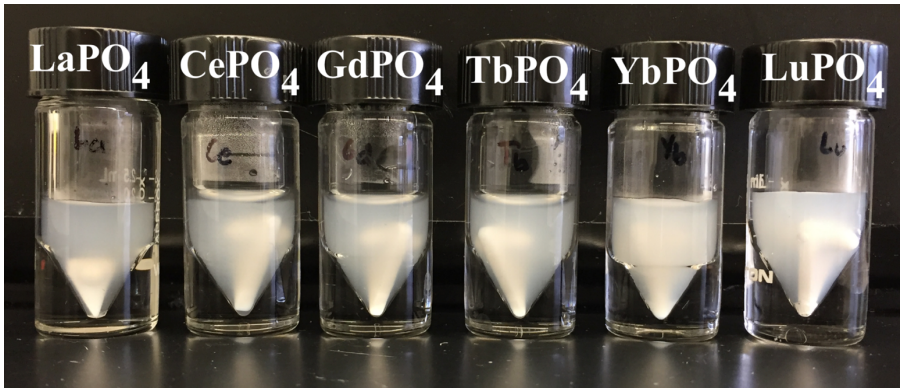

Fig. 3-5 $LnPO_4$ (Ln^{3+} = La, Ce, Gd, Tb, Yb, Lu) core NPs suspension appearance at 1:2 Ln:Na-TPP volume ratio after synthesis at 90 °C for 3 hours.

Fig. 3-6 Comparison between the appearance of as-prepared and dialyzed $LaPO_4$ core NPs suspensions.

3.3 Synthesis of $LnVO_4$ core and core-shell NPs

3.3.1 Citrate Route Synthesis

$LnVO_4$ core NPs were synthesized by an aqueous route from a mixture of lanthanide chloride salts, sodium citrate, and sodium orthovanadate [47]. The synthesis of $LnVO_4$ core NPs started by mixing 0.1 M $LnCl_3 \cdot xH_2O$ salts at specific volume ratios [**Fig. 3-7(a)**]. Next, a 0.75 volume equivalent of 0.1 M $Na_3C_6H_5O_7 \cdot 2H_2O$ was added to a 1 volume equivalent of the lanthanide salts solution under constant stirring. The resulting mixture was homogenized using a vortex mixer until a white turbid solution, corresponding to Ln-cit complexes, was obtained [**Fig. 3-7(b)**]. Lastly, a 0.75 volume equivalent of 0.1 M Na_3VO_4 (pH adjusted to 12.5 using NaOH) was added and the solution was stirred until it was clear and colorless [**Fig. 3-7(c)**]. The solution containing lanthanide-citrate-vanadate oligomeric species was heated at 60 °C for 30 minutes to synthesize $LnVO_4$ core NPs. Afterwards, the suspension was cooled, transferred into the regenerated cellulose membrane, and dialyzed against DI water to remove unreacted species.

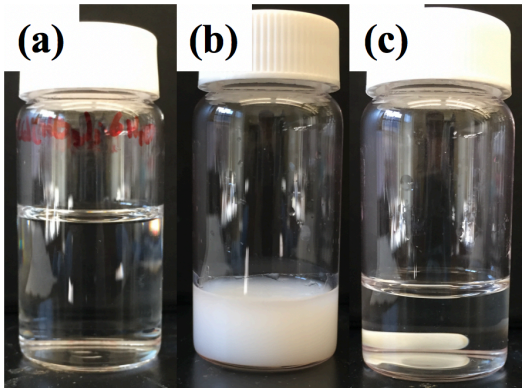

Fig. 3-7 Solution appearance of (a) $LnCl_3$, (b) Ln-cit, and (c) Ln-cit-VO_4 used for the synthesis of $LnVO_4$ NPs.

$LnVO_4$ core-shell NPs synthesis was carried out by preparing a solution containing lanthanide-citrate-vanadate oligomeric species having the same molar concentration to that used for the

$LnVO_4$ core NPs. This solution was then added in a volume ratio of 1.5:1 or 2:1 to the $LnVO_4$ core NPs suspension and mixed thoroughly using a vortex mixer. The resulting clear and colorless suspension was heated at 60 °C for 30 minutes to synthesize $LnVO_4$ core + 1 shell NPs. Deposition of additional shells was carried out by repeating this procedure while keeping the volume ratio of 1.5:1 or 2:1 between the fresh lanthanide-citrate-vanadate oligomeric species solution and the $LnVO_4$ core NPs suspension.

3.3.2 Flow Synthesis

$LnVO_4$ core NPs were prepared in aqueous media by precipitation of Ln^{3+} and $[VO_4]^{3-}$ ions at room temperature [126]. This synthesis method consists in the addition at a 1:1 volume ratio of an aqueous solution of 0.1 M $LnCl_3 \cdot xH_2O$ salts into a 0.1 M Na_3VO_4 solution, which pH was adjusted to 12.5 using NaOH [126]. The addition of the lanthanide salt was done at ~1 mL min^{-1} using a peristaltic pump, while vigorously stirring the Na_3VO_4 solution. The pH of the mixture was monitored continuously during the addition of $LnCl_3$ and stabilized ~11 using 1 M NaOH. After adding $LnCl_3$, the turbid suspension was stirred for 30 minutes before the NPs suspension was precipitated by centrifugation and cleaned to remove the excess of unreacted species. The set-up used for the synthesis of $LnVO_4$ core NPs before and after adding $LnCl_3$ is shown in **Fig. 3-8**.

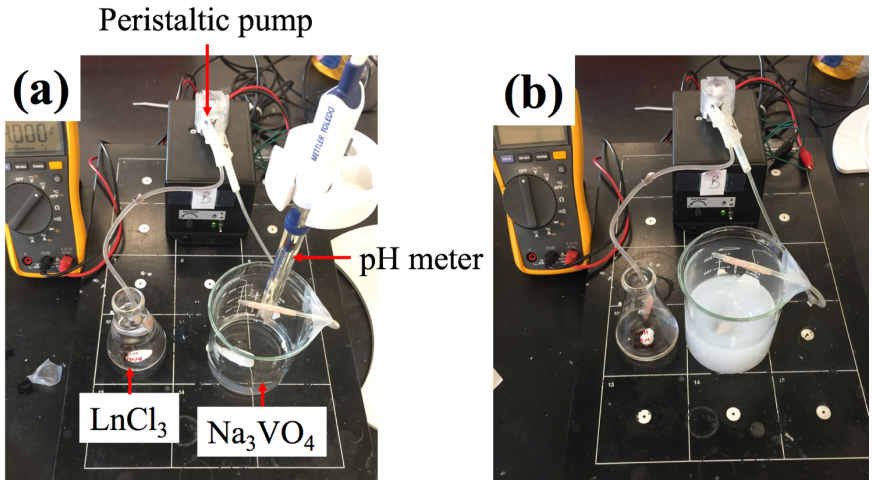

Fig. 3-8 Experimental setup for flow synthesis of $LnVO_4$ NPs (a) before and (b) after preparation.

3.4 Nanoparticles Characterization

3.4.1 Crystal Structure and Crystallite Size

The crystal structure of $LnPO_4$ and $LnVO_4$ core-shell NPs was characterized by powder x-ray diffraction (XRD) using a PANanalytical X'Pert Pro x-ray diffractometer (Malvern Panalytical, Malvern, United Kindom) operated at 45 kV and 40 mA with a Cu anode (Cu k_α, λ = 1.504 Å). For the sample preparation, $LnPO_4$ core-shell and $LnVO_4$ core NPs suspensions prepared as described in sections 3.2 and 3.3.2, respectively, were precipitated by centrifugation and then dried in an oven at 60–90 °C overnight. $LnVO_4$ core-shell NPs suspensions, prepared as described in section 3.3.1, were mixed with ethanol in a 3:2 volume ratio to facilitate their precipitation by centrifugation and then dried in an oven at 60–90 °C overnight. The dried samples were ground using a mortar and pestle until a fine powder was obtained.

Room temperature diffraction patterns were collected using a reflection transmission spinner PW3064/60 stage while spun at 30 revolutions per minute. Analysis of the crystal structure was done using a HighScore Plus software equipped with an International Centre of Diffraction Data

database. The crystallite size of $LnPO_4$ and $LnVO_4$ NPs was calculated using the Scherrer equation [127]:

$$D = \frac{K\lambda}{\beta \cos\theta} \quad \textbf{3-1}$$

where D is the crystallite size, λ is the wavelength of the Cu-K_α radiation, β is the full-width at half maximum (FWHM) of the selected reflection, θ is the Bragg angle, and K is a shape factor set as 0.9.

3.4.2 Morphology

Morphology of the $LnPO_4$ and $LnVO_4$ NPs was characterized transmission electron microscopy (TEM). TEM characterization was done using a Zeiss Libra 120 (Zeiss, Oberkochen, Germany) with a LaB_6 filament operating at 120 kV and a FEI Titan operating at 300 kV. For sample preparation, the as-prepared or dialyzed $LnPO_4$ NPs suspensions were diluted (×100 in DI water), followed by sonication for 30 minutes. The diluted sample was then drop-casted onto a carbon-coated copper grid (Mesh 300). $LnVO_4$ NPs suspensions, prepared as described in section 3.3.1, were diluted (×50–100 in DI water), dispersed by sonication, and drop-casted onto a carbon-coated copper grid (Mesh 300). The dried $LnVO_4$ NPs, prepared by both methods, were dispersed in acetone, sonicated for 10–30 minutes, and drop-casted onto a carbon-coated grid (300 mesh). The particle size of $LnPO_4$ and $LnVO_4$ NPs was measured manually using the software ImageJ v1.5i.

3.4.3 Hydrodynamic Size and Zeta Potential

The hydrodynamic size, particle size distribution, and ζ-potential of both as-prepared and dialyzed $LnPO_4$ and $LnVO_4$ NPs suspensions were obtained using a NanoPlus HD (Micromeritics®, Norcross, GA). This equipment uses a laser diode operated at 30 mW and 660

nm wavelength. Characterization of the hydrodynamic size and particle size distribution was done by dynamic light scattering (DLS) at room temperature using a quartz cuvette (1 cm path length). Both normalized intensity and number distributions were obtained for each sample. The intensity distribution is related to the intensity of light scattered by particles of different sizes and hence it is expected to highlight the contribution of larger particles based on Mie theory, whereas the number distribution provides a representation of the number of particles based on their size. Data collection for all samples was done using the same standard operating procedure. Briefly, the solvent was defined as water with a refractive index, viscosity, and dielectric constant of 1.3328, 0.8878 cP, and 78.3, respectively. The regularization method, known as CONTIN, was used to obtain the size distribution of the NPs suspensions from the dynamic light scattering data. Three repetitions, each of them consisting of 25 accumulation times, were averaged to obtain the mean and standard deviation of the hydrodynamic size and particle size distributions.

The mean ζ-potential of both as-prepared and dialyzed $LnPO_4$ and $LnVO_4$ NPs suspensions was obtained from 3 repetitions consisting of 5 accumulation times. Measurements were collected at a constant voltage and current of 60 V and 51 mA, respectively. The conversion equation used corresponds to the Smoluchowski equation, which relates the mobility of the NPs with the ζ-potential at the interface [128].

3.4.4 Luminescence Properties

The as-prepared and dialyzed $LnPO_4$ and $LnVO_4$ NPs suspensions were diluted (×20–50 in DI water) to characterize their absorption, emission, and excitation spectra. The absorption spectra were recorded on a GENESYS™ 10S UV-vis spectrophotometer (Thermo Fisher Scientific, Waltham, MA). The excitation and emission spectra were acquired on a Cary Eclipse fluorescence spectrophotometer (Agilent, Santa Clara, CA). All suspensions were characterized using a UV Fused Quartz cuvette (ThorLabs, Newton, NJ) with four polished sides and 1 cm path length. A

detailed description of the program, optics, and conditions used to record the emission and excitation spectra of the NPs suspensions will be given in Chapters 4, 5, and 6 for each sample. Time-resolved luminescence lifetimes were recorded using a QuantMaster-3 spetrofluorometer with a Xenon Flash lamp excitation source and a photomultiplier tube (PMT) detector.

3.4.5 Magnetic Susceptibility

The magnetic susceptibilities of $LnPO_4$ and $LnVO_4$ NPs were characterized in a VersaLab™ 3 Tesla (Quantum Design Inc., San Diego, CA) vibrating sample magnetometer. Each powder sample was massed into a polypropylene capsule, centered, and measured in a field from 0–3 T at 300 K to record the magnetic moment.

3.4.6 Elemental Composition

The relative concentration of elements, particularly of lanthanide ions, was assessed by energy-dispersive x-ray spectroscopy using a Hitachi SU-70 analytical field emission scanning electron microscope (Hitachi, Tokyo, Japan) and a Phenom ProX Desktop scanning electron microscope from Phenom-world (Thermo Fisher Scientific, Waltham, MA). For sample preparation, dried $LnPO_4$ and $LnVO_4$ NPs were mounted on a carbon tape in an aluminum sample holder.

Inductively coupled plasma–optical emission spectroscopy (ICP–OES) was used to estimate the elemental content of $LnPO_4$ and $LnVO_4$ NPs suspensions. Characterization was done using an Agilent 5110 ICP-OES (Agilent, Santa Clara, CA), which detection limit for multiple elements is summarized in **Table 3-2**. ICP standards for Cs, Ba, La, Gd, Pb, and Bi were purchased from Inorganic Ventures™ (Christiansburg, VA). A 1000 ppm was diluted serially to standard solutions ranging in concentration from 0.1–150 ppm to construct a calibration curve for each element.

Table 3-2 Detection limit of various elements in Agilent 5110 ICP-OES.

Element	Detection limit (ppb)
Cesium	3200
Barium	0.07
Lanthanum	0.02
Gadolinium	2.5
Lead	14
Bismuth	12

3.4.7 Radioactivity

Radioactivity measurements were carried out using a high-purity germanium (HPGe) detector (Ortec, Oak Ridge, TN) with a crystal active volume ~100 cm^3 and a beryllium window that was coupled to a PC-based multichannel analyzer (Canberra Industries, Meriden, CT). Energy and efficiency calibrations were determined by γ-ray sources traceable to the National Institute of Standards and Technology. The γ-energy and intensities used to determine the activity of multiple isotopes are summarized in **Table 3-3**.

Table 3-3 Gamma energy and intensity of various isotopes. Data obtained from interactive charts of nuclides, National Nuclear Data Center, Brookhaven National Laboratory [129].

Isotope	Gamma energy (keV)	Intensity (%)
^{85}Sr	514.0	96.0
^{89}Sr	908.96	0.0095
^{156}Eu	88.97	8.4
	811.77	9.7
^{211}Pb	404.85	3.78
^{213}Bi	440.4	25.94
^{221}Fr	218.1	11.4
^{223}Ra	154.2	5.7

	269.46	13.9
^{225}Ac	150.1	0.6
^{227}Th	235.96	12.9
	256.23	7.0

Radiochemical yield and *in vitro* retention of radionuclides were evaluated using a similar set-up as reported previously for $LnPO_4$ NPs [38], [39], [41]–[43]. Briefly, the as-prepared radionuclide-doped $LnPO_4$ and $LnVO_4$ NPs were transferred into a dialysis membrane and dialyzed against DI water for 20 hours. The conical vial, spin vane, and pipette tip used during synthesis were assayed to determine the activity lost. A 5 mL aliquot from the dialysate was analyzed to quantify the activity associated with unreacted radionuclides from the first dialysis. The dialysate was changed with clean DI water to assess the retention of radionuclides in $LnPO_4$ and $LnVO_4$ NPs over time. Subsequent 5 mL aliquots were taken periodically every 3–4 days and assayed in the HPGe detector. Aliquots from ^{225}Ac-doped NPs were immediately counted after withdrawal in the HPGe detector to assess the activity of ^{221}Fr due to its short half-life. Each aliquot was assayed for 20 consecutive 1-minute intervals that were used to build the decay curve of ^{221}Fr. The same aliquot was assayed after a couple of hours to determine the activity of ^{225}Ac based on the activity of ^{221}Fr now in secular equilibrium with ^{225}Ac. Dialysate aliquots from either ^{156}Eu-, $^{85, 89}$Sr-, ^{227}Th-, or ^{223}Ra-doped NPs were assayed for longer intervals (>10 minutes) based on their long half-lives.

4 $LnPO_4$ core and core-shell NPs

This chapter provides a description of the synthesis and characterization of $LnPO_4$ core and core-shell NPs. The general synthesis route described in section 3.2 was used as a reference, however some modifications were made to study the influence of synthesis parameters such as temperature, heating time, lanthanide concentration, and reagents concentration, in both core and core-shell NPs. The crystal structure, morphology, luminescence and magnetic properties, as well as the physical stability of $LnPO_4$ core and core-shell NPs were characterized. The results presented in this chapter were used as reference towards the development of radionuclide-doped $LnPO_4$ NPs for applications in multimodal molecular imaging and TRT.

4.1 Influence of Temperature and Heating Time

In this section, the influence of temperature and heating time in the growth kinetics and formation of $La_{0.4}Ce_{0.45}Tb_{0.15}PO_4$ core and $LaPO_4$ core-shell NPs was evaluated. The synthesis of $LnPO_4$ NPs is based on the precipitation of Ln^{3+} and $[PO_4]^{3-}$ using $[P_3O_{10}]^{5-}$ as orthophosphate source and complexing agent [125]. The hydrolysis of triphosphate upon heating results in pyrophosphate and orthophosphate species, hence variation of both temperature and heating time may provide the tools to control the yield and size of $LnPO_4$ core-shell NPs. Buissette et *al.* reported that a significant fraction of the lanthanide phosphate phase was formed after 90 minutes at 90 ºC [125]. Having these conditions as reference, lower temperatures (75 ºC, 80 ºC, 85 ºC, and 90 ºC) and shorter heating times (30–180 minutes) were studied to assess the formation of $La_{0.4}Ce_{0.45}Tb_{0.15}PO_4$ core NPs. $LaPO_4$ core, core + 2 shells, and core + 4 shells NPs were synthesized at 80 ºC and 90 ºC after heating for either 2 or 3 hours. Overall, increasing the

temperature caused the formation of both $La_{0.4}Ce_{0.45}Tb_{0.15}PO_4$ core and $LaPO_4$ core-shell NPs at shorter heating times (<3 hours). These results suggest that during radiochemical synthesis, the activity loss because of radioactive decay could be reduced by synthesizing $LnPO_4$ core-shell NPs at high temperature (90 °C) and short heating time (<3 hours) without significantly affecting the formation of $LnPO_4$ NPs. The results presented in this section have been adapted from [130].

4.1.1 Growth Kinetics of $La_{0.4}Ce_{0.45}Tb_{0.15}PO_4$ core NPs

$La_{0.4}Ce_{0.45}Tb_{0.15}PO_4$ core NPs were synthesized using a 1:1 volume ratio of $LnCl_3$ to Na-TPP. The synthesis was performed at either 75 ºC, 80 ºC, 85 ºC, or 90 ºC for 3 hours, while taking aliquots of the NPs suspensions every 30 minutes to study the growth kinetics of $LnPO_4$ NPs. The absorption spectra of diluted solutions and NPs suspensions were used to evaluate the formation of $LnPO_4$ NPs based on the evolution of the absorption bands of cerium-tripolyphosphate complexes (248 nm and 302 nm) and cerium in a crystalline lanthanide phosphate phase (272 nm) [125], [131]. Although the absorption band at 272 nm was seen at 75 ºC after 3 hours of heating, the presence of the absorption band at 302 nm suggests that a fraction of cerium-tripolyphosphate complexes did not result in NPs formation [**Fig. 4-1(a)**]. Increasing the temperature to 80 ºC resulted in the vanishing of the cerium-tripolyphosphate complexes bands after 2.5 hours of heating [**Fig. 4-1(b)**]. Additionally, the greater absorbance at 272 nm implies that a significant fraction of Ce^{3+} ions are in a lanthanide phosphate phase. A further increase in temperature to 85 ºC or 90 ºC had as a consequence the disappearance of the cerium-tripolyphosphate bands after 1.5 hours [**Fig. 4-1(c)**] and 1 hour [**Fig. 4-1(d)**] of heating, respectively. At these temperatures, the band at 272 nm reaches its maximum after 3 hours of heating, which implies a greater fraction of $LnPO_4$ NPs in suspension with respect to shorter heating times (**Fig. 4-1**). In summary, the synthesis of $LnPO_4$ NPs can be carried out at temperatures as low as 75 ºC with the disadvantage

that long heating times (>3 hours) are required to achieve a high yield of NPs. Increasing the temperature to >80 ºC allows for a reduction of the heating time to ~2 hours based on the disappearance of cerium-tripolyphosphate bands (**Fig. 4-1**). A reduction of the heating time may contribute to the development of $LnPO_4$ NPs with small size and high physical stability since a lower fraction of polyphosphate species is hydrolyzed into orthophosphate groups, however this may also compromise the NPs yield [125].

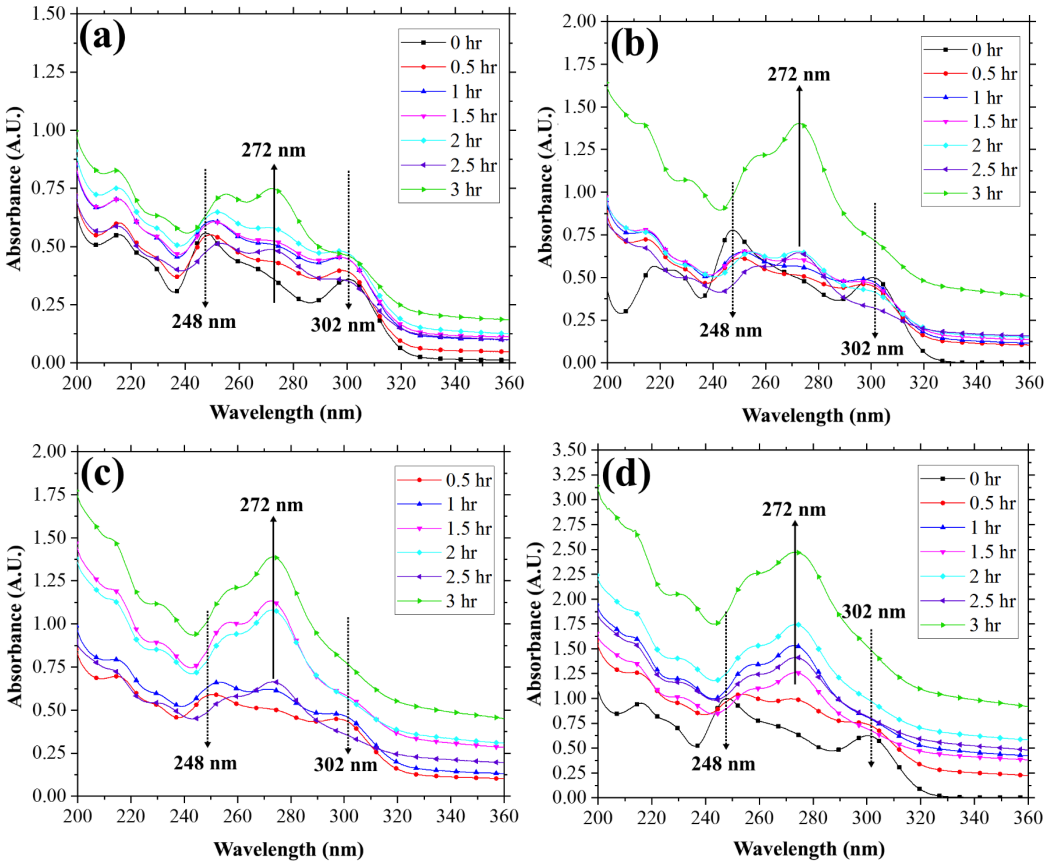

Fig. 4-1 Absorption spectra evolution with heating time of $La_{0.4}Ce_{0.45}Tb_{0.15}PO_4$ core NPs synthesized at (a) 75 ºC, (b) 80 ºC, (c) 85 ºC, and (d) 90 ºC using 1:1 Ln:Na-TPP volume ratio.

4.1.2 Crystal Structure of $LaPO_4$ core-shell NPs

The crystal structure and crystallite size of $LaPO_4$ core, core + 2 shells, and core + 4 shells NPs synthesized as described in section 3.2 were evaluated at 80 ºC and 90 ºC after 2 hours and 3

hours of heating. A rhabdophane-type structure with a hexagonal crystal system and a space group $P6_222$ (pdf: 01-075-1881) corresponding to $LaPO_4$ was obtained for all the samples. The diffraction patterns of $LaPO_4$ core NPs synthesized after 2 hours of heating at both temperatures showed broader and less intense Bragg reflections to that observed after 3 hours (**Fig. 4-2**). The broader Bragg reflections can be attributed to the small crystallite size of $LaPO_4$ core NPs synthesized after 2 hours of heating.

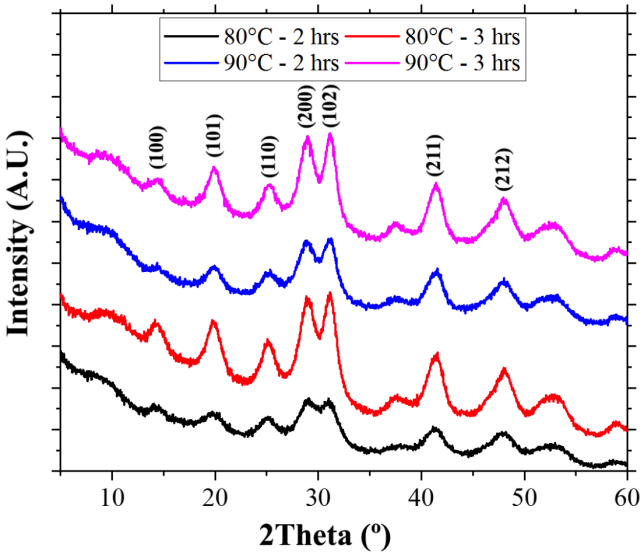

Fig. 4-2 Diffraction patterns of $LaPO_4$ core NPs synthesized at 80 ºC and 90 ºC for either 2 or 3 hours using a 1:1 La:Na-TPP volume ratio (section 3.2).

The deposition of two $LaPO_4$ shells, which will follow an epitaxial growth mechanism [131], resulted in a decrease of the FWHM and an increase of the Bragg reflection intensities for all synthesis conditions (**Fig. 4-3**). A similar trend, consisting in narrow and intense peaks, was observed after adding two more $LaPO_4$ shells (**Fig. 4-4**).

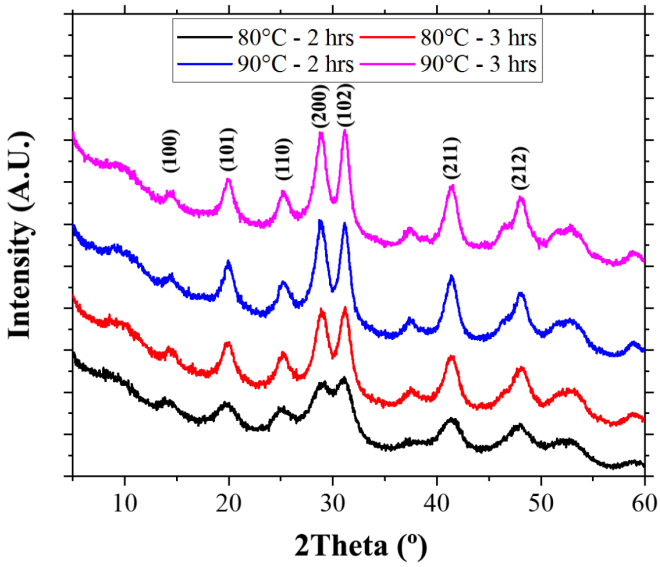

Fig. 4-3 Diffraction patterns of $LaPO_4$ core + 2 shells NPs synthesized by mixing a solution of La/Na-TPP (1:2 La:Na-TPP volume ratio) with $LaPO_4$ core NPs suspension at a 1:1 volume ratio, while heating at 80 ºC and 90 ºC for either 2 or 3 hours (section 3.2).

The epitaxial growth of two and four shells on $LaPO_4$ core NPs was evidenced by a continuous increase of the crystallite size for both temperatures and heating times as shown in **Fig. 4-5**. The crystallite size and error bars reported correspond to the average and standard deviation obtained from multiple Bragg reflections. $LaPO_4$ core and core-shell NPs prepared at 80 ºC for 2 hours had the broader Bragg reflection peaks and hence the smaller crystallite size among the synthesis conditions evaluated. Nonetheless, the obtained diffraction patterns demonstrated that short heating times (2 hours) and low temperatures (80 °C) can be used to prepare $LnPO_4$ core and core-shell NPs with a small crystallite size (<4.5 nm).

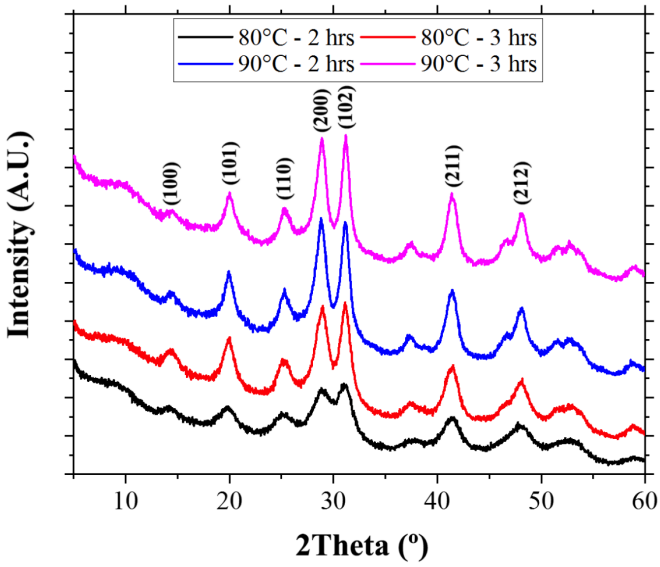

Fig. 4-4 Diffraction patterns of $LaPO_4$ core + 4 shells NPs synthesized by mixing a solution of La/Na-TPP (1:2 La:Na-TPP volume ratio) with $LaPO_4$ core NPs suspension at a 1:1 volume ratio, while heating at 80 ºC and 90 ºC for either 2 or 3 hours (section 3.2).

For $LaPO_4$ core-shell NPs synthesized at 80 ºC, the increase in crystallite size after the deposition of shells was not as significant as observed for the samples prepared at 90 ºC (**Fig. 4-5**). These results are consistent with the growth kinetics of $LnPO_4$ core NPs, where an increase in temperature caused the vanishing of the cerium-tripolyphosphate complexes absorption bands in shorter (<2 hours) heating times (section 4.1.1). Furthermore, there is no significant difference between the mean crystallite size of $LaPO_4$ core and core-shell NPs synthesized at 90 ºC for either 2 or 3 hours (**Fig. 4-5**), which implies that shorter heating times (~2 hours) could be implemented for radiochemical synthesis.

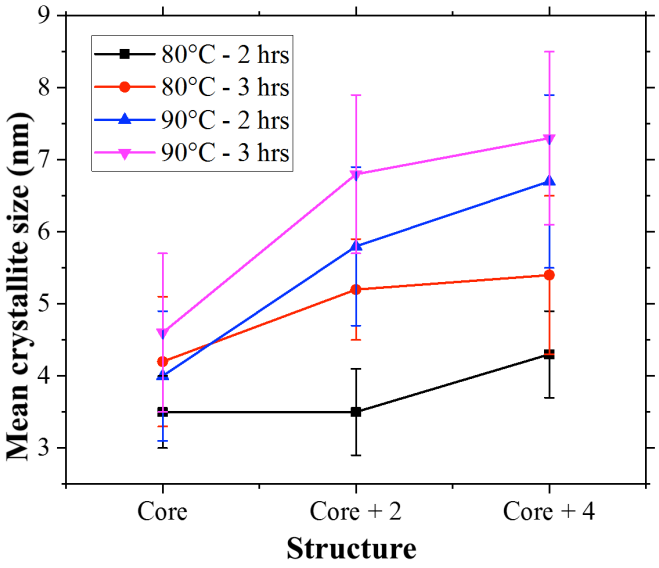

Fig. 4-5 Mean crystallite size of $LaPO_4$ core, core + 2 shells, and core + 4 shells synthesized following the procedure described in section 3.2, while heating at 80 ºC and 90 ºC for either 2 or 3 hours.

4.2 Influence of Reagents Concentration

In this section, the role of sodium tripolyphosphate as complexing agent and source of orthophosphate species was studied. The concentration of tripolyphosphate species was varied at either 1:0.5, 1:1, 1:1.5, 1:2, or 1:3 Ln:Na-TPP volume ratio for the synthesis of $La_{0.8}Ce_{0.2}PO_4$ core NPs, while temperature and heating time were kept at 90 ºC and 3 hours. The formation of $La_{0.8}Ce_{0.2}PO_4$ core NPs was determined based on the absorption spectra of as-prepared NPs suspensions. The crystal structure, luminescence properties, particle size distribution, and ζ-potential of $La_{0.8}Ce_{0.2}PO_4$ core NPs suspensions were characterized for each Ln:Na-TPP. Increasing the concentration of Na-TPP caused the formation of smaller $La_{0.8}Ce_{0.2}PO_4$ core NPs which displayed greater luminescence properties and physical stability compared to that of lower Na-TPP concentrations.

4.2.1 Absorption Spectra

To study the influence of reagents concentration, the Ln:Na-TPP volume ratio was set at either 1:0.5, 1:1, 1:1.5, 1:2, or 1:3 for the synthesis of $La_{0.8}Ce_{0.2}PO_4$ core NPs at 90 ºC for 3 hours. Formation of $La_{0.8}Ce_{0.2}PO_4$ core NPs was assessed as described in section 4.1.1. As shown in **Fig. 4-6**, synthesis of $La_{0.8}Ce_{0.2}PO_4$ core NPs using a 1:3 Ln:Na-TPP did not result in NP formation since only the bands of cerium-tripolyphosphate complexes were observed. Lower Ln:Na-TPP ratios (1:0.5–2) resulted in the formation of $La_{0.8}Ce_{0.2}PO_4$ core NPs based on the absorption band at 272 nm. This behavior could be attributed to the role of the polyphosphate species as complexing agent and source of orthophosphate groups [125].

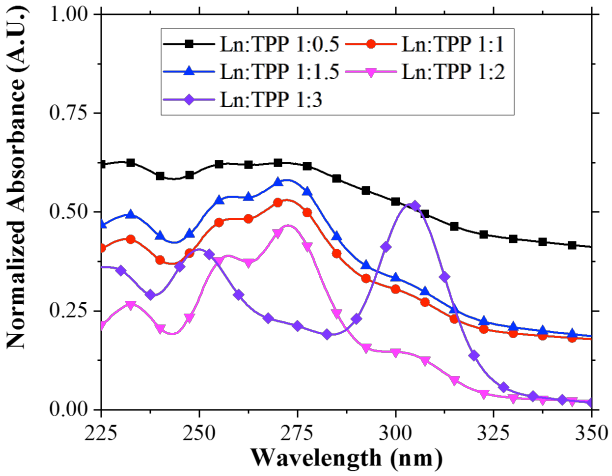

Fig. 4-6 Normalized absorption spectra of $La_{0.8}Ce_{0.2}PO_4$ core NPs synthesized at 90 ºC for 3 hours using different Ln:Na-TPP volume ratio.

Higher concentrations of polyphosphate species, such as 1:3 Ln:Na-TPP, restricts significantly the formation of $LnPO_4$ nuclei and hence the growth of $LnPO_4$ NPs. Lower concentrations (1:0.5) may result in a large growth or aggregation of $LnPO_4$ NPs since the fraction of polyphosphate species required to control the size and stabilize the NPs is relatively low. It is assumed that the shape of the absorption spectrum from $La_{0.8}Ce_{0.2}PO_4$ (1:0.5) core NPs, where the

absorption band at 272 nm is not well defined, is attributed to a lack of physical stability and hence aggregation of NPs that causes significant light scattering (Rayleigh scattering). Thus, a concentration of tripolyphosphate species lower than 3 times the concentration of Ln ions is desired for the synthesis of $LnPO_4$ core and core-shell NPs.

4.2.2 Crystal Structure

$La_{0.8}Ce_{0.2}PO_4$ core NPs synthesized using 1:0.5, 1:1, 1:1.5, and 1:2 Ln:Na-TPP have a rhabdophane-type structure with a hexagonal crystal system and a space group $P6_222$ (pdf: 01-075-1881, $LaPO_4$). The diffraction pattern for the sample with the lowest concentration of tripolyphosphate species (1:0.5) evidenced sharper peaks with respect to the rest of the patterns (**Fig. 4-7**). Higher concentrations of tripolyphosphate species (>1:1 Ln:Na-TPP) lead to the formation of smaller crystallites and hence broader Bragg reflections of $La_{0.8}Ce_{0.2}PO_4$ core NPs that resulted in significant overlapping of the peaks.

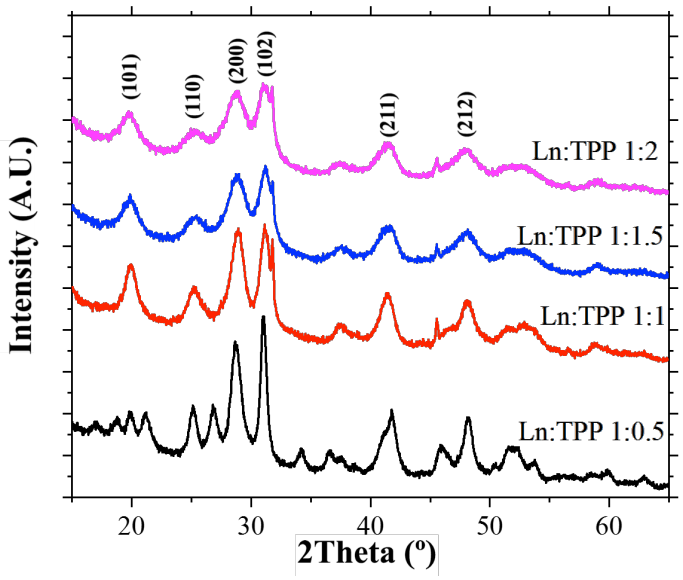

Fig. 4-7 Diffraction patterns of $La_{0.8}Ce_{0.2}PO_4$ core NPs synthesized at 90 ºC for 3 hours using different Ln:Na-TPP volume ratio.

Despite the overlapping of the Bragg reflections, the diffraction patterns obtained for $La_{0.8}Ce_{0.2}PO_4$ core NPs are consistent with the hexagonal crystal structure of $LaPO_4$. The crystallite size of $La_{0.8}Ce_{0.2}PO_4$ core NPs decreased from 9.5 ± 3.1 nm to 4.0 ± 1.1 nm after increasing the concentration of tripolyphosphate species in solution by four times (**Error! Not a valid bookmark self-reference.**).

Table 4-1 Crystallite size of $La_{0.8}Ce_{0.2}PO_4$ core NPs synthesized at 90 ºC for 3 hours using different Ln:Na-TPP volume ratio.

Ln:Na-TPP	Crystallite size (nm)
1:0.5	9.5 ± 3.1
1:1	6.1 ± 0.6
1:1.5	4.3 ± 1.1
1:2	4.0 ± 1.1

4.2.3 Excitation and Emission Spectra

The excitation and emission spectra of diluted $La_{0.8}Ce_{0.2}PO_4$ core NPs suspensions are shown in **Fig. 4-8**. The excitation spectrum was recorded using an emission wavelength of 350 nm, an excitation filter at 250–395 nm, and a PMT voltage of 500 V. It can be observed the similarity between the absorption (**Fig. 4-6**) and the excitation (**Fig. 4-8**) spectra of $La_{0.8}Ce_{0.2}PO_4$ core NPs, where the maximum intensity is at 272 nm. The highest excitation intensity corresponded to $La_{0.8}Ce_{0.2}PO_4$ core NPs synthesized with 1:2 Ln:Na-TPP, whereas the lowest was observed for 1:0.5 [**Fig. 4-8(a)**]. The emission spectrum of $La_{0.8}Ce_{0.2}PO_4$ core NPs was acquired with a PMT voltage of 500 V, an emission filter at 295–1,100 nm, and an excitation wavelength of 272 nm [**Fig. 4-8(b)**]. The emission spectra is characterized by a broad and an intense band at ~350 nm related to transitions of Ce^{3+} ions from the lowest component of ^2D state to the spin-orbit components $^2F_{7/2}$ and $^2F_{5/2}$ of the ground state, which luminescence is not completely quenched

[125], [132]–[135]. The lowest emission of $La_{0.8}Ce_{0.2}PO_4$ core NPs (1:0.5) may be attributed to the lower excitation intensity as well as to a self-quenching effect caused by their aggregation [136].

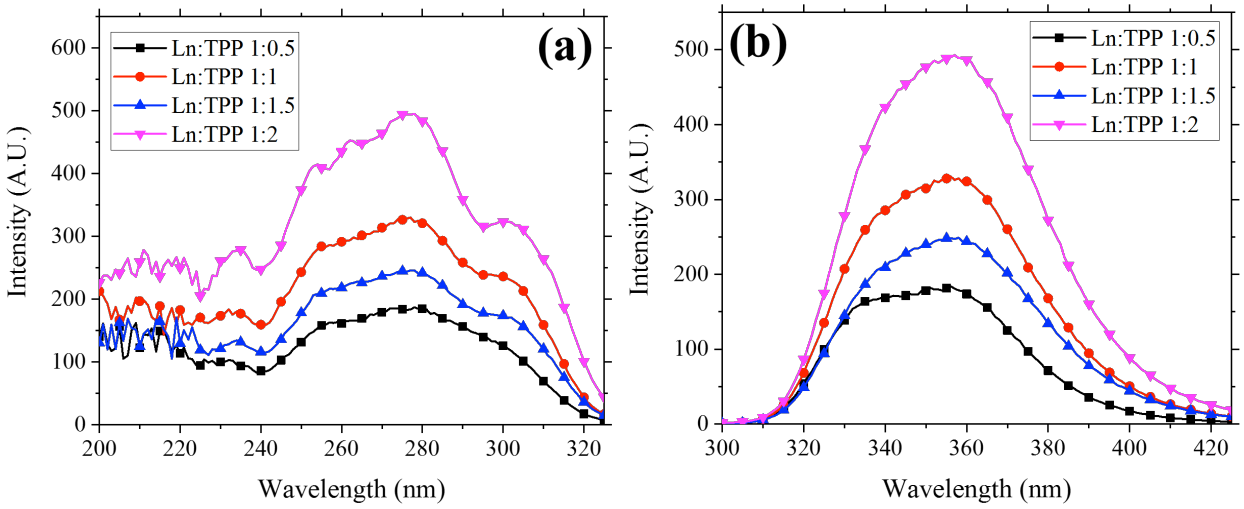

Fig. 4-8 (a) Excitation and (b) emission spectra of $La_{0.8}Ce_{0.2}PO_4$ core NPs synthesized at 90 ºC for 3 hours using different Ln:Na-TPP volume ratio.

4.2.4 Hydrodynamic Size and Zeta Potential

DLS was used to determine the hydrodynamic size, particle size distribution, and ζ-potential of the as-prepared $La_{0.8}Ce_{0.2}PO_4$ core NPs. **Table 4-2** shows the mean and standard deviation of the cumulant size, polydispersity index (PI), number size, and ζ-potential obtained for $La_{0.8}Ce_{0.2}PO_4$ core NPs suspensions. An increase in tripolyphosphate concentration is accompanied by a decrease in the cumulant size, PI, and number size (**Table 4-2**). These results indicate significant aggregation of $La_{0.8}Ce_{0.2}PO_4$ core NPs upon a decrease in the concentration of tripolyphosphate species, which is consistent with the discussion presented in section 4.2.1 regarding the shape of the absorption spectra (**Fig. 4-6**) as well as with the lower intensity of the excitation and emission spectra (**Fig. 4-8**). The lower concentration of polyphosphate species available for complexation with Ln cations causes the aggregation of $La_{0.8}Ce_{0.2}PO_4$ core NPs.

Although the mean PI, cumulant and number size were reported for $La_{0.8}Ce_{0.2}PO_4$ core NPs synthesized using a 1:0.5 Ln:Na-TPP volume ratio, these values are not reliable since the NPs were not stable in suspension (precipitated at the bottom of the cuvette) during data acquisition. Based on the PI and particle size distribution, the optimum Ln:Na-TPP volume ratio to synthesize $La_{0.8}Ce_{0.2}PO_4$ core NPs with homogenous particle size and high physical stability is 1:2. Almost all the as-prepared $La_{0.8}Ce_{0.2}PO_4$ core NPs had a negative ζ-potential, which is consistent with the presence of polyphosphate species with negative charge at the NP surface, except for the sample synthesized with 1:0.5 Ln:Na-TPP that had a positive ζ-potential (**Table 4-2**). The difference in ζ-potential for the latter is caused by the lower concentration of tripolyphosphate species, which may have transformed completely into orthophosphate groups and hence the fraction of polyphosphate species available for complexation is not enough to stabilize the NPs. The magnitude of the ζ-potential indicates that $La_{0.8}Ce_{0.2}PO_4$ core NPs prepared with 1:1 and 1:1.5 Ln:Na-TPP volume ratio are strongly anionic since their magnitude is greater than -30 mV [137]. The negative surface charge of the as-prepared $La_{0.8}Ce_{0.2}PO_4$ core NPs may contribute to lower toxicity with respect to cationic NPs, where cell wall disruption is expected since most of the cell membranes are negatively charged [137].

Table 4-2 Cumulant size, PI, number size, and ζ-potential of $La_{0.8}Ce_{0.2}PO_4$ core NPs synthesized at 90 ºC for 3 hours using different Ln:Na-TPP volume ratio.

Ln:Na-TPP	Cumulant size (nm)	PI	Number size (nm)	ζ-potential (mV)
1:0.5	$(37.5 \pm 4.1) \times 10^2$	1.04 ± 0.38	$(3.9 \pm 1.8) \times 10^4$	13.6 ± 0.6
1:1	$(33.1 \pm 3.2) \times 10^2$	0.54 ± 0.09	$(6.0 \pm 4.4) \times 10^2$	-31.9 ± 0.9
1:1.5	383.8 ± 0.7	0.29 ± 0.01	91.7 ± 16.5	-35.5 ± 0.2
1:2	32.0 ± 0.4	0.19 ± 0.01	16.1 ± 0.3	-16.9 ± 0.7

4.3 Influence of Lanthanide Concentration

In this section, $LnPO_4$ (Ln^{3+} = GdCeTb and GdEu) core NPs possessing a wide concentration of lanthanide ions (**Table 4-3**) were synthesized using a 1:2 Ln:Na-TPP at 90 °C for 3 hours. The core NPs were characterized to assess their potential application as multimodal platforms for molecular imaging. The influence of lanthanide concentration in $LnPO_4$ core NPs morphology, crystal structure, absorption, emission, excitation, and magnetic susceptibility (χ) was studied. The luminescence properties were assessed for the application of $LnPO_4$ core NPs as contrasts agents for FI based on the emission of light from Ce^{3+}, Eu^{3+}, and Tb^{3+} ions. The magnetic susceptibility was characterized to evaluate the response of $LnPO_4$ core NPs as MRI contrast agents. It is expected that $LnPO_4$ core NPs will behave as positive-T_1 contrast agents depending on the Gd^{3+} concentration because of its large spin magnetic moment ($\mu_s = S(S+1)\hbar^2$) and its relation with the longitudinal relaxivity ($r_1 \propto \mu_s^2$) [25]. $LnPO_4$ core NPs could also be used as negative-T_2 contrast agents depending on the transversal relaxivity, which is related the magnetic moment associated to each Ln^{3+} ($r_2 \propto \mu^2$) [25]. Variations of χ are expected based on the Curie formula which relates χ with the concentration and magnitude of the magnetic moment associated to each Ln^{3+} ($\mu_{Ce} = 2.4\ \mu_B$, $\mu_{Eu} = 3.4\ \mu_B$, $\mu_{Gd} = 7.95\ \mu_B$, and $\mu_{Tb} = 9.5\ \mu_B$) [138], [139]. The results presented in this section have been adapted from [140].

Table 4-3 Description, concentration, and sample abbreviation for $LnPO_4$ core NPs.

Description	**30 at.% Gd^{3+} and Ce^{3+}:Tb^{3+} molar ratio**	**Abbreviation**

$GdCeTbPO_4$	1:1	$Gd_{0.3}Ce_{0.35}Tb_{0.35}$
	2:1	$Gd_{0.3}Ce_{0.467}Tb_{0.233}$
	1:2	$Gd_{0.3}Ce_{0.233}Tb_{0.467}$
	3:1	$Gd_{0.3}Ce_{0.525}Tb_{0.175}$
	1:3	$Gd_{0.3}Ce_{0.175}Tb_{0.525}$
	6:1	$Gd_{0.3}Ce_{0.6}Tb_{0.1}$
	1:6	$Gd_{0.3}Ce_{0.1}Tb_{0.6}$
Description	**x at.% Gd^{3+} and 3:1 Ce^{3+}:Tb^{3+} molar ratio**	**Abbreviation**
$GdCeTbPO_4$	95	$Gd_{0.95}Ce_{0.0375}Tb_{0.0125}$
	90	$Gd_{0.9}Ce_{0.075}Tb_{0.025}$
	80	$Gd_{0.8}Ce_{0.15}Tb_{0.05}$
	70	$Gd_{0.7}Ce_{0.225}Tb_{0.075}$
	60	$Gd_{0.6}Ce_{0.3}Tb_{0.1}$
	50	$Gd_{0.5}Ce_{0.375}Tb_{0.125}$
Description	**x at.% Eu^{3+}**	**Abbreviation**
$GdEuPO_4$	10	$Gd_{0.9}Eu_{0.1}$
	20	$Gd_{0.8}Eu_{0.2}$
	30	$Gd_{0.7}Eu_{0.3}$
	40	$Gd_{0.6}Eu_{0.4}$
	50	$Gd_{0.5}Eu_{0.5}$

4.3.1 Elemental Composition

Energy-dispersive x-ray spectroscopy was used to confirm the concentration of lanthanide ions in the as-prepared $LnPO_4$ core NPs with respect to the nominal concentrations (**Table 4-3**). The lanthanide concentration was calculated based on the weight percent of each lanthanide ion with respect to the total weight percent of lanthanide ions as reported by the EDAX system incorporated into the microscope. The results showed significant agreement between the nominal and experimental concentration of lanthanide ions for almost all the samples (**Table 4-4**). The discrepancies observed for Tb and Eu cations in a couple of samples were significant because of

the low concentrations used and the similarity in energy between the Lα and M lines of these lanthanides with respect to Gd.

Table 4-4 Calculated relative molar concentration of lanthanide ions and error percent with respect to nominal concentrations.

Abbreviation		**Gd**	**Ce**	**Tb**
$Gd_{0.3}Ce_{0.35}Tb_{0.35}$	**Calculated (%)**	31.4	33.2	35.4
	Error (%)	*4.6*	*5.2*	*1.2*
$Gd_{0.3}Ce_{0.525}Tb_{0.175}$	**Calculated (%)**	32.2	49.6	18.2
	Error (%)	*7.8*	*5.5*	*4.0*
$Gd_{0.3}Ce_{0.6}Tb_{0.1}$	**Calculated (%)**	30.8	59.2	10.0
	Error (%)	*2.8*	*1.4*	*0.2*
$Gd_{0.3}Ce_{0.1}Tb_{0.6}$	**Calculated (%)**	30.7	9.5	59.8
	Error (%)	*2.3*	*4.8*	*0.4*
$Gd_{0.95}Ce_{0.0375}Tb_{0.0125}$	**Calculated (%)**	93.2	3.5	3.3
	Error (%)	*1.9*	*6.5*	*162.4*
$Gd_{0.8}Ce_{0.15}Tb_{0.05}$	**Calculated (%)**	78.8	15.4	5.8
	Error (%)	*1.4*	*2.4*	*15.9*
$Gd_{0.6}Ce_{0.3}Tb_{0.1}$	**Calculated (%)**	58.8	30.3	10.9
	Error (%)	*2.0*	*1.0*	*8.7*
		Gd	**Eu**	
$Gd_{0.9}Eu_{0.1}$	**Calculated (%)**	88.1	11.9	
	Error (%)	*2.2*	*19.4*	
$Gd_{0.7}Eu_{0.3}$	**Calculated (%)**	70	30	
	Error (%)	*0.1*	*0.04*	
$Gd_{0.5}Eu_{0.5}$	**Calculated (%)**	50.5	49.5	
	Error (%)	*1.0*	*1.0*	

4.3.2 Crystal Structure

The diffraction patterns of $LnPO_4$ core NPs (**Table 4-3**) are shown in **Fig. 4-9**, **Fig. 4-10**, and **Fig. 4-11**. Significant peak broadening and hence overlapping of Bragg reflections, characteristic of nanoscale crystallites, were observed in all diffraction patterns.

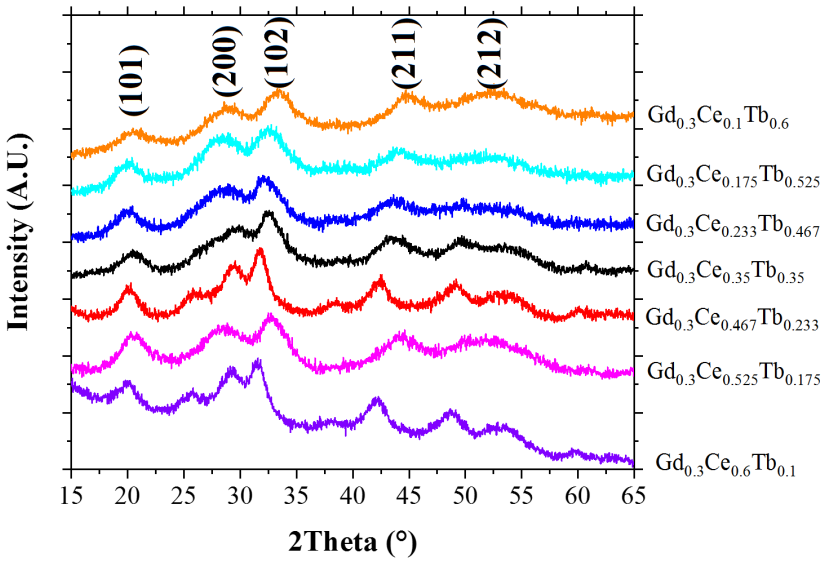

Fig. 4-9 Diffraction patterns of $LnPO_4$ core NPs synthesized at 90 ºC for 3 hours using 1:2 Ln:Na-TPP volume ratio, while having 30 at.% Gd^{3+} and different Ce^{3+}:Tb^{3+} molar ratios.

The Bragg reflections of $LnPO_4$ core NPs are shifted with respect to the reference patterns of pure $CePO_4$, $EuPO_4$, $GdPO_4$, and $TbPO_4$ due to the presence of substitutional lanthanide atoms in their crystal structure. This shifting of the 2θ angles implies a change in the d-spacing due to elastic strains imposed by the difference in size between the ionic radius of the lanthanide ions used (*i.e.* Tb^{3+} ≈ 1.18 Å, Gd^{3+} ≈ 1.20 Å, Eu^{3+} ≈ 1.21 Å, Ce^{3+} ≈ 1.27 Å) [141]. The as-prepared $LnPO_4$ core NPs matched with the crystal structure of cerium phosphate (pdf: 01-074-1889, $CePO_4$) and hydrated gadolinium phosphate (pdf: 00-039-0232, $GdPO_4 \cdot xH_2O$) having a hexagonal crystal system and a space group $P3_121$.

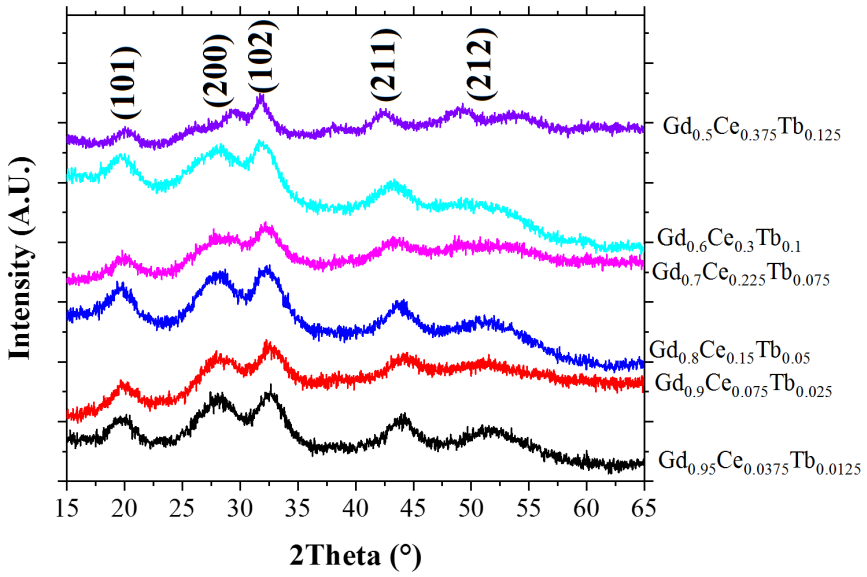

Fig. 4-10 Diffraction patterns of $LnPO_4$ core NPs synthesized at 90 ºC for 3 hours using 1:2 Ln:Na-TPP volume ratio, while having a 3:1 Ce^{3+}:Tb^{3+} molar ratio and different Gd^{3+} at.%.

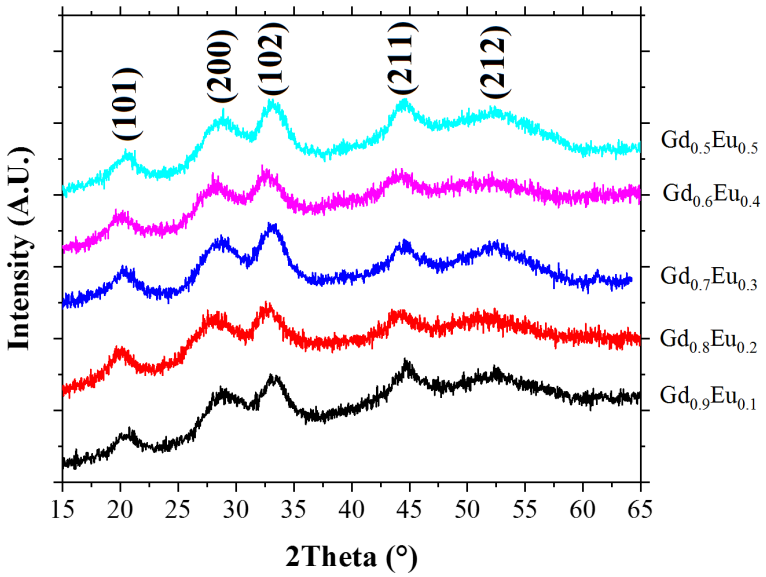

Fig. 4-11 Diffraction patterns of $GdEuPO_4$ core NPs synthesized at 90 ºC for 3 hours using 1:2 Ln:Na-TPP volume ratio, while having different Eu^{3+} at.%.

The mean crystallite size and standard deviation of $LnPO_4$ core NPs are presented in **Table 4-5**. The small crystallite size (<5.1 nm) of $LnPO_4$ core NPs is consistent with the higher

concentration of tripolyphosphate species used for synthesis (section 4.2.2). Moreover, the crystallite size was not influenced significantly by the concentration of lanthanide ions used.

Table 4-5 Mean crystallite size for $LnPO_4$ core NPs synthesized at 90 ºC for 3 hours using 1:2 Ln:Na-TPP volume ratio.

Abbreviation	Crystallite size (nm)
$Gd_{0.3}Ce_{0.35}Tb_{0.35}$	3.3 ± 0.1
$Gd_{0.3}Ce_{0.467}Tb_{0.233}$	4.0 ± 0.8
$Gd_{0.3}Ce_{0.233}Tb_{0.467}$	2.8 ± 0.7
$Gd_{0.3}Ce_{0.525}Tb_{0.175}$	3.8 ± 0.9
$Gd_{0.3}Ce_{0.175}Tb_{0.525}$	2.9 ± 0.3
$Gd_{0.3}Ce_{0.6}Tb_{0.1}$	4.3 ± 0.5
$Gd_{0.3}Ce_{0.1}Tb_{0.6}$	2.9 ± 0.4
$Gd_{0.95}Ce_{0.0375}Tb_{0.0125}$	5.1 ± 0.8
$Gd_{0.9}Ce_{0.075}Tb_{0.025}$	3.1 ± 0.6
$Gd_{0.8}Ce_{0.15}Tb_{0.05}$	5.1 ± 1.9
$Gd_{0.7}Ce_{0.225}Tb_{0.075}$	2.5 ± 0.4
$Gd_{0.6}Ce_{0.3}Tb_{0.1}$	4.7 ± 1.2
$Gd_{0.5}Ce_{0.375}Tb_{0.125}$	3.7 ± 0.8
$Gd_{0.9}Eu_{0.1}$	4.9 ± 1.2
$Gd_{0.8}Eu_{0.2}$	2.9 ± 0.4
$Gd_{0.7}Eu_{0.3}$	3.3 ± 0.9
$Gd_{0.6}Eu_{0.4}$	3.2 ± 0.5
$Gd_{0.5}Eu_{0.5}$	4.8 ± 1.2

4.3.3 Morphology

TEM micrographs of $LnPO_4$ core NPs are shown in **Fig. 4-12**, **Fig. 4-13**, **Fig. 4-14**, and **Fig. 4-15**. Branched structures can be observed at low magnifications for all $LnPO_4$ core NPs, while at higher magnifications these branched structures are formed by $LnPO_4$ core NPs with spherical and ellipsoidal morphologies surrounded by a low-density matrix **Fig. 4-13** and **Fig.**

4-14. The formation of these structures is assumed to be related to the polymerization of unreacted polyphosphate oligomers, $[P_3O_{10}]^{5-}$ and $[P_2O_7]^{4-}$, that have a higher concentration in solution given by the initial volume ratio of Ln^{3+} to $[P_3O_{10}]^{5-}$ ions [125]. Thus, P_3O_{10} and P_2O_7 anions promote the formation of a polymeric shell encompassing the $LnPO_4$ core NPs as observed in the micrographs.

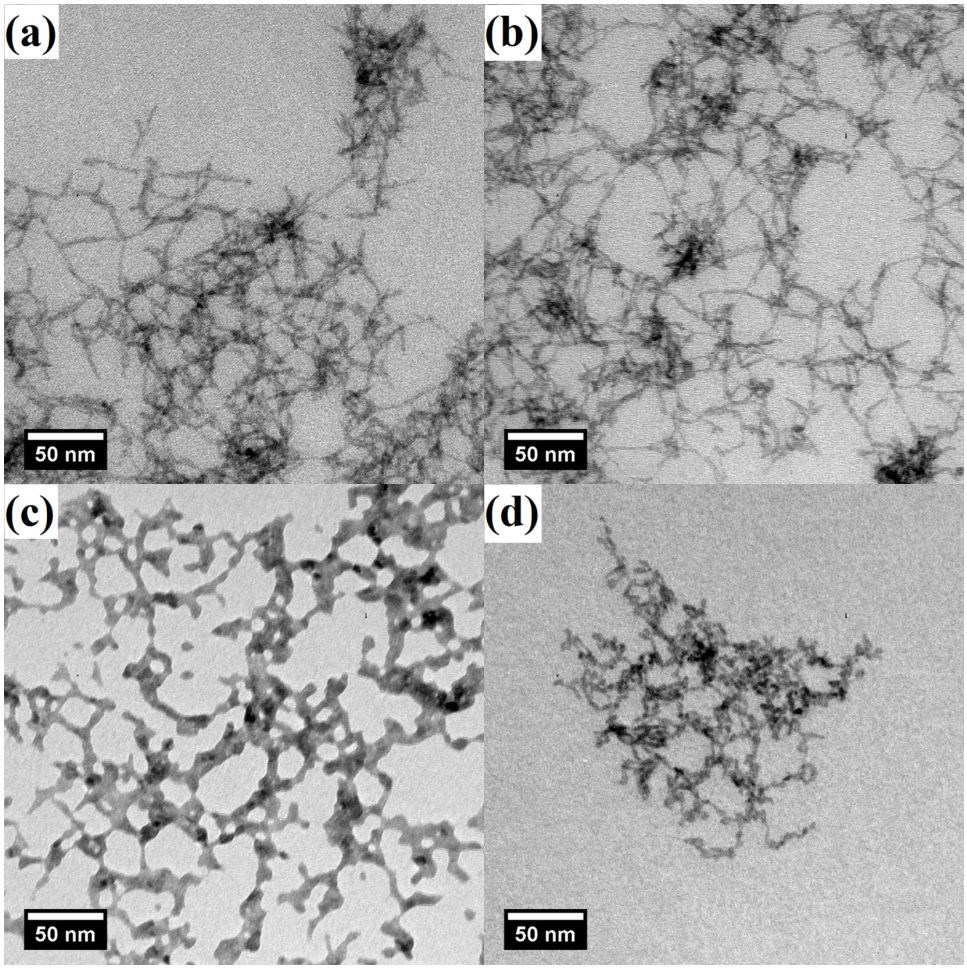

Fig. 4-12 TEM micrographs of (a, b) $Gd_{0.3}Ce_{0.233}Tb_{0.467}PO_4$ and (c, d) $Gd_{0.3}Ce_{0.6}Tb_{0.1}PO_4$ NPs synthesized at 90 ºC for 3 hours using 1:2 Ln:Na-TPP volume ratio.

These unreacted phosphate oligomers were intended to be removed by dialysis, however, as seen from the images their removal was partially successful. Particle size distributions of

$Gd_{0.95}Ce_{0.0375}Tb_{0.0125}PO_4$ (**Fig. 4-13**) and $Gd_{0.6}Ce_{0.3}Tb_{0.1}PO_4$ (**Fig. 4-14**) NPs follow a lognormal distribution with mean sizes of 5.0 ± 1.3 nm (n = 112) and 3.5 ± 0.7 nm (n = 122), respectively.

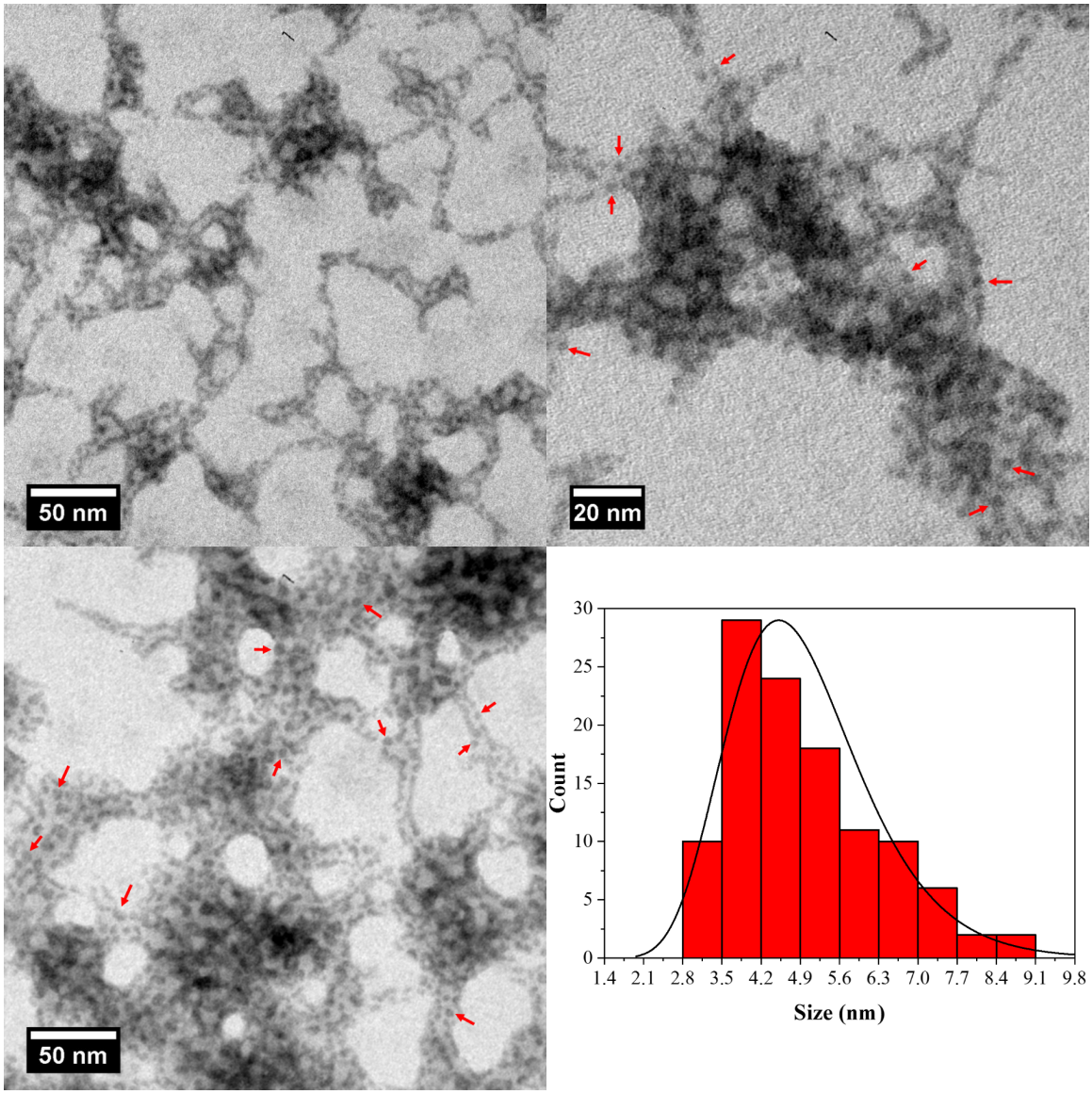

Fig. 4-13 TEM micrographs and particle size distribution of $Gd_{0.95}Ce_{0.0375}Tb_{0.0125}PO_4$ NPs [indicated by arrows] synthesized at 90 ºC for 3 hours using 1:2 Ln:Na-TPP volume ratio.

The remaining $LnPO_4$ core NPs are expected to have comparable morphologies and particle size distributions with respect to $Gd_{0.95}Ce_{0.0375}Tb_{0.0125}PO_4$ and $Gd_{0.6}Ce_{0.3}Tb_{0.1}PO_4$. The

$LnPO_4$ core NPs correspond to single crystals based on the similarity between the mean particle size and the mean crystallite size.

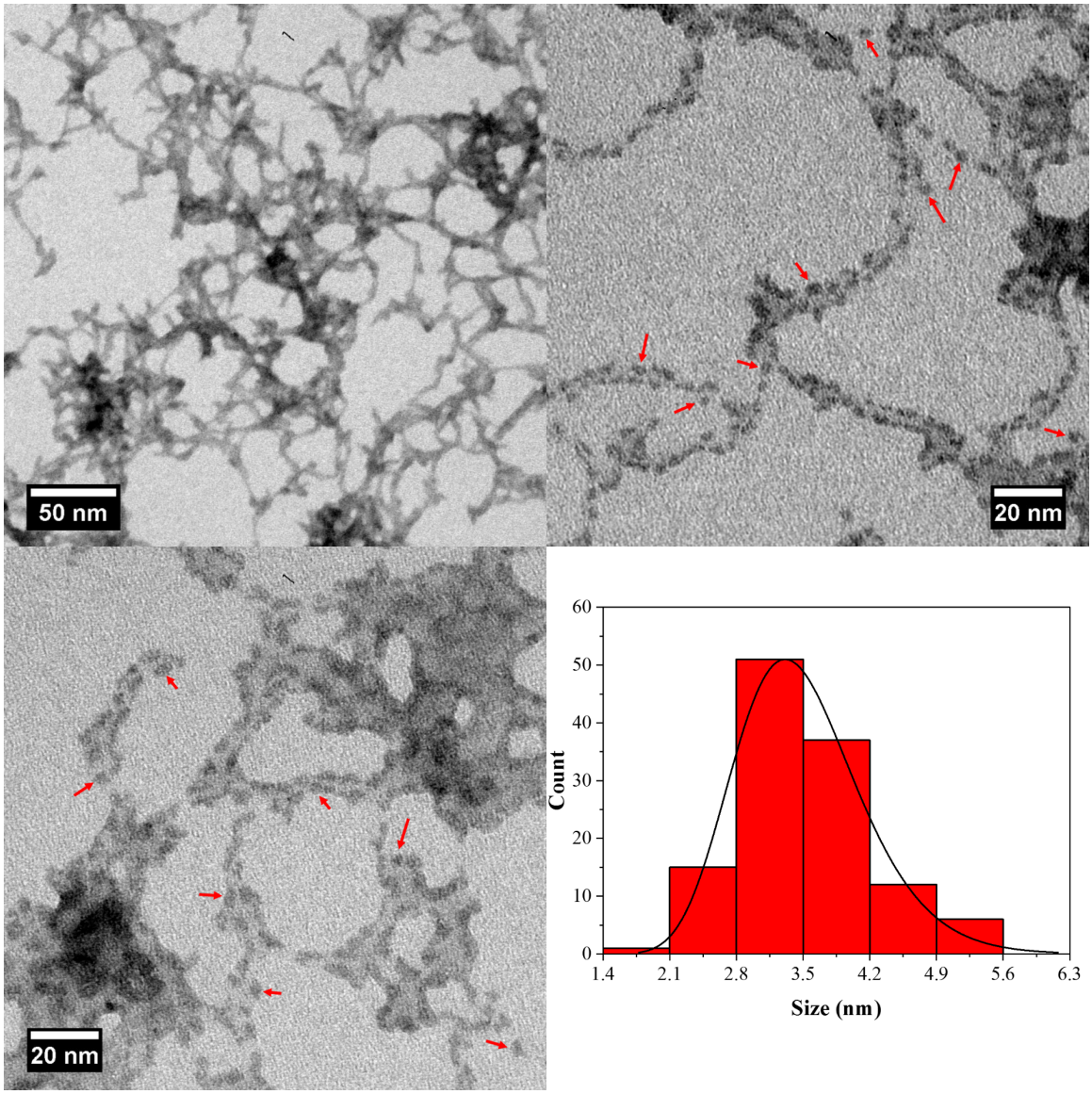

Fig. 4-14 TEM micrographs and particle size distribution of $Gd_{0.6}Ce_{0.3}Tb_{0.1}PO_4$ NPs [indicated by arrows] synthesized at 90 ºC for 3 hours using 1:2 Ln:Na-TPP volume ratio.

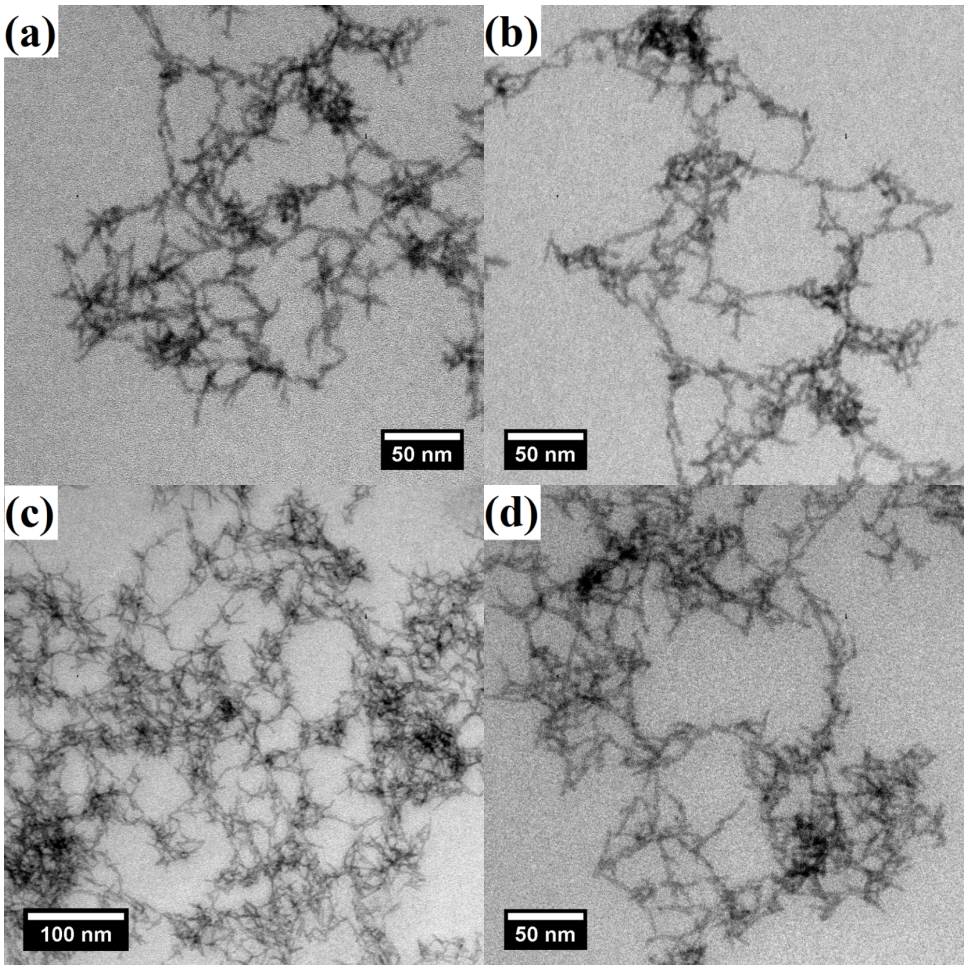

Fig. 4-15 TEM micrographs of (a, b) $Gd_{0.7}Eu_{0.3}PO_4$ and (c, d) $Gd_{0.5}Eu_{0.5}PO_4$ NPs synthesized at 90 ºC for 3 hours using 1:2 Ln:Na-TPP volume ratio.

4.3.4 Absorption, Excitation, and Emission Spectra

The absorption spectra of $LnPO_4$ core NPs with concentrations outlined in **Table 4-3** are presented in **Fig. 4-16** and **Fig. 4-17**. The absorption spectra of $LnPO_4$ (Ln^{3+} = Ce, Gd, and Tb) core NPs showed the characteristic peak at 272 nm attributed to the Ce^{3+} ions in the lanthanide phosphate phase (**Fig. 4-16**) [125]. The absorbance of the peak at 272 nm is directly related to the relative Ce^{3+} concentration within the NPs. For example, the highest absorbance corresponded to $Gd_{0.3}Ce_{0.6}Tb_{0.1}PO_4$, while $Gd_{0.3}Ce_{0.1}Tb_{0.6}PO_4$ had the lowest [**Fig. 4-16(a)**].

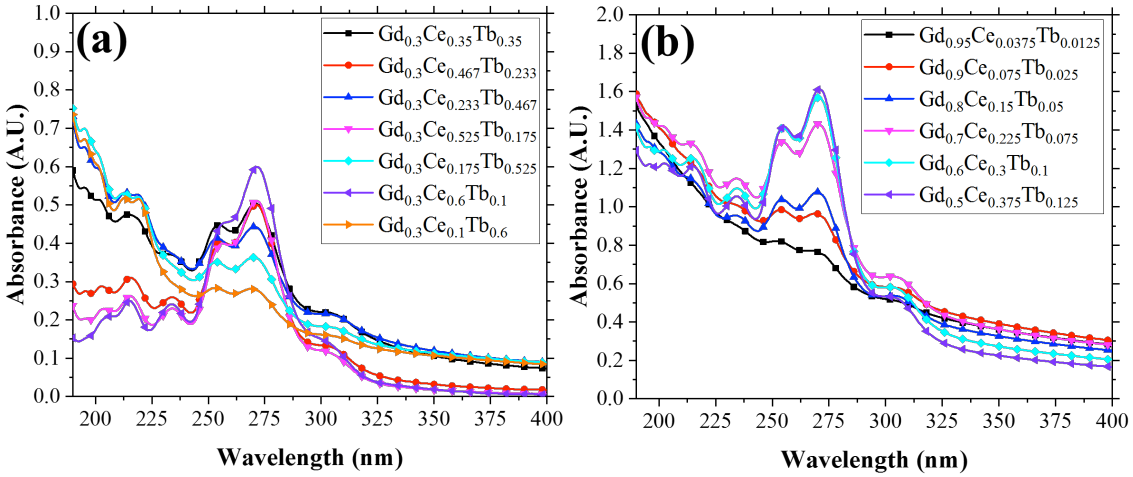

Fig. 4-16 Absorption spectra of $LnPO_4$ core NPs synthesized at 90 ºC for 3 hours using 1:2 Ln:Na-TPP volume ratio, while having different (a) Ce^{3+}:Tb^{3+} molar ratio and (b) Gd^{3+} concentration.

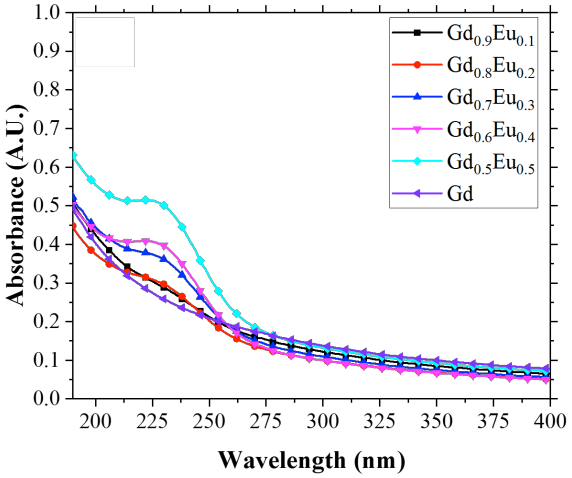

Fig. 4-17 Absorption spectra of $GdEuPO_4$ core NPs synthesized at 90 ºC for 3 hours using 1:2 Ln:Na-TPP volume ratio, while having different Eu^{3+} at.%.

The same trend was observed in **Fig. 4-16(b)**, where decreasing the concentration of Gd^{3+} ions caused an increase in the absorbance at 272 nm. The additional absorption bands observed at 214, 235, 255, and 272 nm correspond to the spin-orbit components of the excited *5d* state of Ce^{3+} ions, $^2D_{5/2}$ and $^2D_{3/2}$, which are split by the crystal field [133]. The absorption spectra of $Gd_xEu_{(1-x)}PO_4$ NPs is characterized by an absorption band below 300 nm that represents the charge-transfer

(CT) transition between Eu-O [142] and which absorbance increased with higher Eu^{3+} concentration (**Fig. 4-17**).

The excitation spectra of $LnPO_4$ (Ln^{3+} = Ce, Gd, and Tb) core NPs were recorded using an emission wavelength of 352 nm, an excitation filter at 250–395 nm, and a PMT voltage of 600 V. The similarity between the absorption (**Fig. 4-16**) and excitation (**Fig. 4-18**) spectra of $LnPO_4$ (Ln^{3+} = Ce, Gd, and Tb) core NPs is a validation of the energy transfer from Ce^{3+} to Tb^{3+} ions [133]. The excitation spectrum for $LnPO_4$ (Ln^{3+} = Ce, Gd, and Tb) core NPs has its maximum intensity at 272 nm and the magnitude is particularly dependent on the concentration of Ce^{3+} ions for the samples prepared with different Ce^{3+}:Tb^{3+} molar ratio [**Fig. 4-18(a)**].

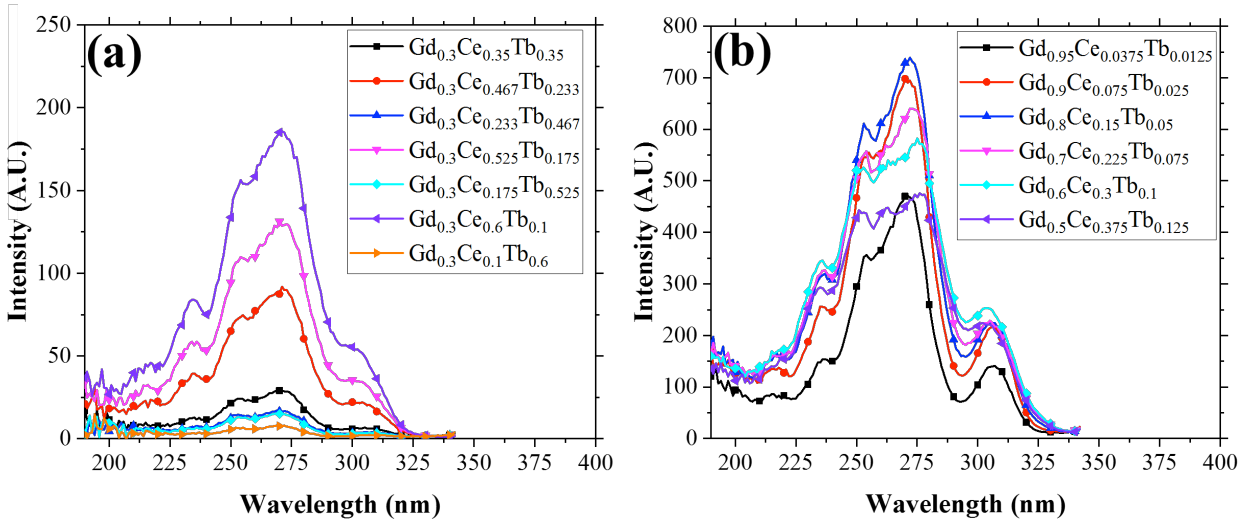

Fig. 4-18 Excitation spectra of $LnPO_4$ core NPs synthesized at 90 ºC for 3 hours using 1:2 Ln:Na-TPP volume ratio, while having different (a) Ce^{3+}:Tb^{3+} molar ratio and (b) Gd^{3+} concentration.

The excitation spectra of $Gd_{(1-x)}Eu_xPO_4$ core NPs were collected using an emission wavelength of 590 nm, an excitation filter at 250–395 nm, and a PMT voltage of 800 V. None of the spectra shown in **Fig. 4-19** exhibited the characteristic CT from the O^{2-} 2*p* orbital to the Eu^{3+} 4*f* orbital represented by a broad band around 260 nm [143]. The lack of this band is assumed to be related to the high concentration of Eu^{3+} ions used for synthesis of $Gd_{(1-x)}Eu_xPO_4$ core NPs,

where it has been shown that europium-doped $GdPO_4$ NPs having 10 at.% and 30 at.% of Eu^{3+} are missing this excitation band [142].

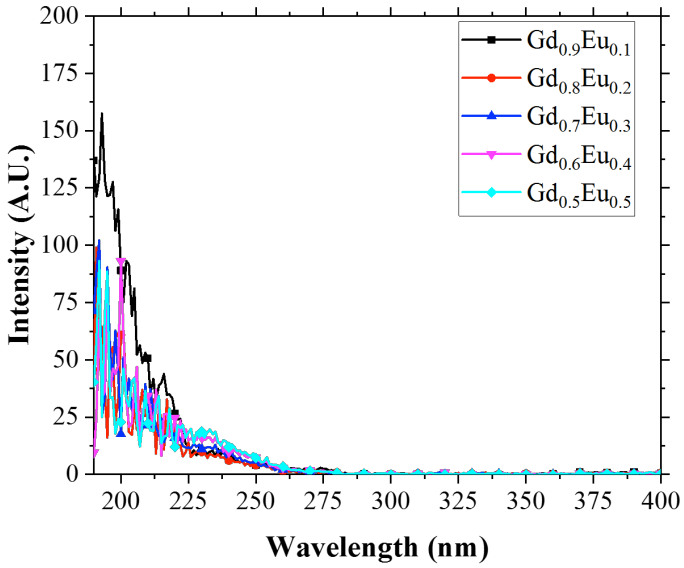

Fig. 4-19 Excitation spectra of $GdEuPO_4$ core NPs synthesized at 90 ºC for 3 hours using 1:2 Ln:Na-TPP volume ratio, while having different Eu^{3+} at.%.

Emission filters at 295–1,100 nm and 550–1,100 nm were used to collect the emission spectra of $GdCeTbPO_4$ and $Gd_{(1-x)}Eu_xPO_4$ core NPs to prevent secondary order transmissions [144]. The emission spectra of $GdCeTbPO_4$ core NPs was acquired with a PMT voltage of 600 V and an excitation wavelength of 272 nm. The spectra is characterized by a broad and an intense emission band at ~350 nm (**Fig. 4-20**) related to transitions of Ce^{3+} ions from the lowest component of the ^2D state to the spin-orbit components $^2F_{7/2}$ and $^2F_{5/2}$ of the ground state, which luminescence is not completely quenched [125], [132]–[135]. The high intensity of this emission band caused the appearance of a second harmonic in the visible range [600–800 nm] (**Fig. 4-20**). The emission intensity of both Ce^{3+} bands is dependent on the concentration of this lanthanide within $LnPO_4$ core NPs [**Fig. 4-20(a)**]. The characteristic $^5D_4$-^7F_J (J = 4, 5, and 6) Tb^{3+} transitions were also observed in the emission spectra of $GdCeTbPO_4$ core NPs [145]. In **Fig. 4-20(a)**, the intensity of

the $^5D_4$-^7F_J transitions increased with higher concentration of Tb^{3+} ions, where the highest intensity corresponded to $Gd_{0.3}Ce_{0.1}Tb_{0.6}PO_4$ core NPs. For $GdCeTbPO_4$ core NPs synthesized with different Gd^{3+} at.%, the emission bands from Ce^{3+} ions are more intense than that of the $^5D_4$-^7F_J Tb^{3+} transitions [**Fig. 4-20(b)**], suggesting an inefficient energy transfer between Ce^{3+} to Tb^{3+} ions [146]. It has been shown that low concentrations of Ce^{3+} and Tb^{3+} ions, such as the ones used for $GdCeTbPO_4$ core NPs, result in a higher emission from Ce^{3+} ions with respect to that from Tb^{3+} ions [147]. A continuous increase in the concentration of both Ce^{3+} and Tb^{3+} ions resulted in a significant increase in the intensity of the Tb^{3+} emission [**Fig. 4-20(b)**]. It is expected that by dropping the concentration of Ce^{3+} ions within $LnPO_4$ core NPs, the emission of Tb^{3+} ions will increase at the expense of the Ce^{3+} emission [135], [147].

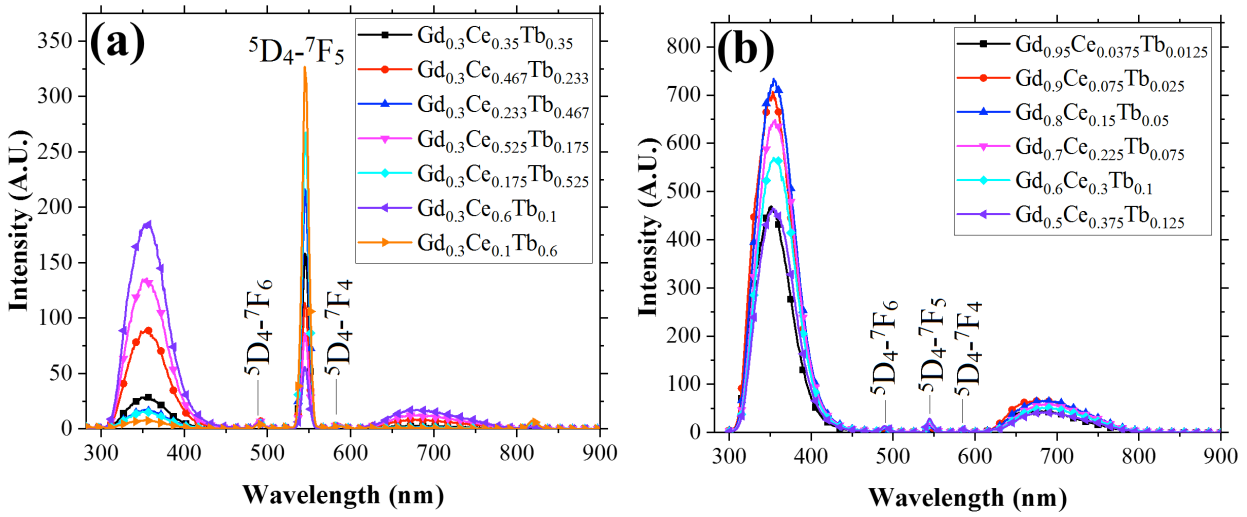

Fig. 4-20 Emission spectra of $LnPO_4$ core NPs synthesized at 90 ºC for 3 hours using 1:2 Ln:Na-TPP volume ratio, while having different (a) Ce^{3+}:Tb^{3+} molar ratio and (b) Gd^{3+} concentration.

The emission spectra of $GdEuPO_4$ NPs was recorded using a PMT voltage of 800 V and an excitation wavelength of 225 nm. The spectra showed the characteristic $^5D_0$–^7F_J (J = 1–4) Eu^{3+} transitions (**Fig. 4-21**) [53], [148]. The most intense peak located at 594 nm is attributed to the magnetic-dipole ($^5D_0$–$^7F_1$) transition [149]. The relative intensity between the magnetic-dipole

($^5D_0$–$^7F_1$) and electric-dipole ($^5D_0$–$^7F_2$) transitions is influenced by the local symmetry of Eu^{3+} ions within $LnPO_4$ NPs [150]. Hence, the higher intensity of the magnetic-dipole transition in $Gd_{(1-x)}Eu_xPO_4$ NPs suggests the higher occupancy of Eu^{3+} ions with inversion symmetry in the $GdPO_4$ hexagonal lattice [149].

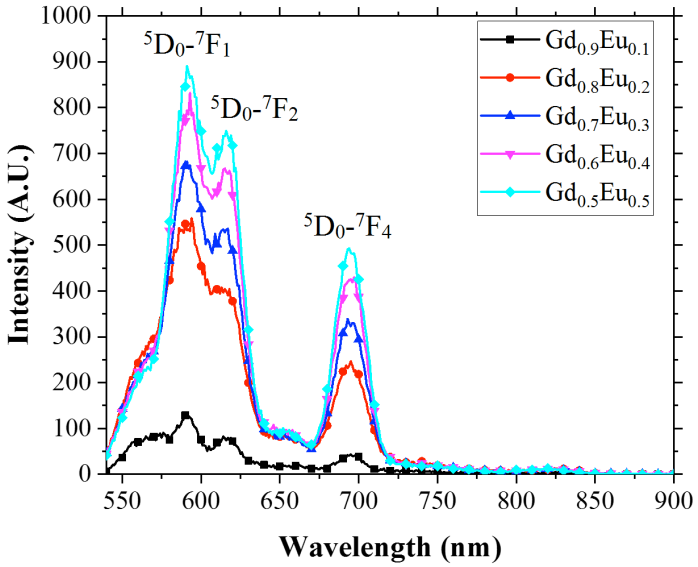

Fig. 4-21 Emission spectra of $GdEuPO_4$ core NPs synthesized at 90 ºC for 3 hours using 1:2 Ln:Na-TPP volume ratio, while having different Eu^{3+} at.%.

The fluorescence emission of $LnPO_4$ core NPs doped with either Ce^{3+}:Tb^{3+} or Eu^{3+} ions under UV light radiation is shown in **Fig. 4-22**. $LnPO_4$ core NPs doped with Ce^{3+}:Tb^{3+} are characterized by a bright green emission (~550 nm), while the Eu^{3+}-doped NPs displayed a light red color (594 nm) (**Fig. 4-22**). It is well known that the fluorescence emission of $LnPO_4$ core NPs is influenced by their nanocrystalline nature [151], the high concentration of Ln^{3+} ions [142], and the P/Ln ratio [152]. Particularly, the high [P/(Gd+Eu)] ratio used in $GdEuPO_4$ core NPs may have caused a decrease of the luminescence emission due to the low intensity of the excitation band [152], [153].

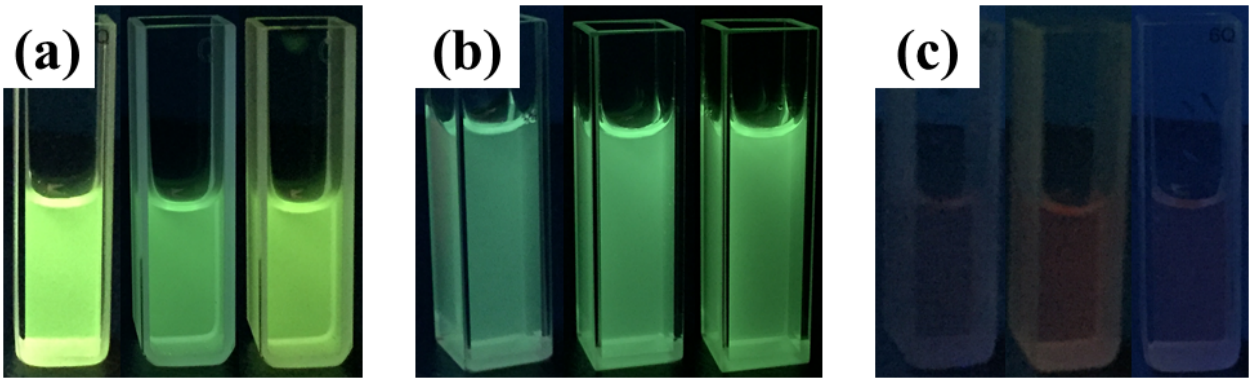

Fig. 4-22 Fluorescence of $LnPO_4$ core NPs synthesized at 90 ºC for 3 hours using 1:2 Ln:Na-TPP volume ratio, while having different (a) Ce^{3+}:Tb^{3+} molar ratio, (b) Gd^{3+} concentration, and (c) Eu^{3+} concentration.

4.3.5 Magnetic Susceptibility

The paramagnetic behavior of Ln^{3+} ions is characterized by a linear increase of the mass magnetization with the magnetic field (**Fig. 4-23** and **Fig. 4-24**). The magnetic susceptibility (χ) was computed from the mass magnetization and magnetic field curves to compare the magnetic properties of the $LnPO_4$ core NPs (**GdEuPO4 core** NPs synthesized at 90 ºC for 3 hours using 1:2 Ln:Na-TPP volume ratio, while having different Eu3+ at.%.

Table *4-6*). It is important to mention the correction that must be done to determine the contribution of the diamagnetic susceptibility. Based on Pascal constants for the $-PO_4$ group, it is expected that for all samples this group will have a diamagnetic susceptibility of -0.5×10^{-6} emu Oe^{-1} g^{-1} [154], which was subtracted from the paramagnetic susceptibility of the $LnPO_4$ core NPs. $Gd_{0.3}Ce_{0.1}Tb_{0.6}PO_4$ core NPs displayed the highest susceptibility (94.50×10^{-6} emu Oe^{-1} g^{-1}), whereas $Gd_{0.3}Ce_{0.6}Tb_{0.1}PO_4$ core NPs had the lowest (36.55×10^{-6} emu Oe^{-1} g^{-1}). This trend is associated with the magnetic moment (μ) of each Ln^{3+} ion and its relationship to the magnetic susceptibility based on the Curie formula, where χ is directly proportional to the square of μ [138]:

$$\chi = \frac{N\mu^2}{3k_BT} \qquad \textbf{4-1}$$

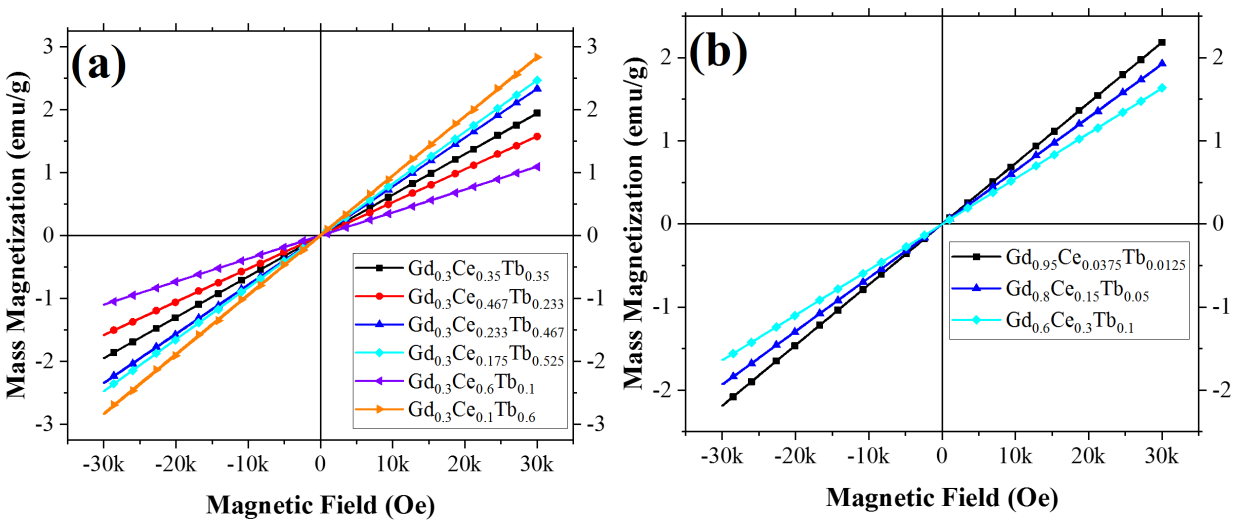

Fig. 4-23 Mass magnetization (emu/g) versus field (Oe) loop for $LnPO_4$ core NPs synthesized at 90 ºC for 3 hours using 1:2 Ln:Na-TPP volume ratio, while having different (a) Ce^{3+}:Tb^{3+} molar ratio and (b) Gd^{3+} concentration.

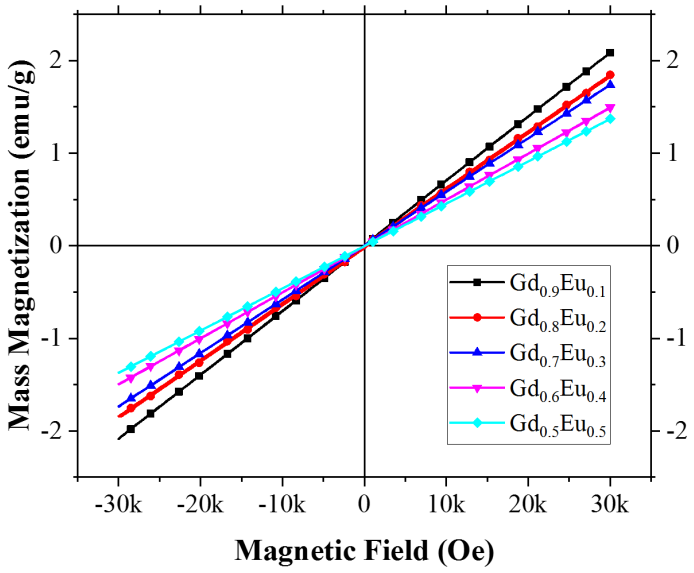

Fig. 4-24 Mass magnetization (emu/g) versus field (Oe) loop for $GdEuPO_4$ core NPs synthesized at 90 ºC for 3 hours using 1:2 Ln:Na-TPP volume ratio, while having different Eu^{3+} at.%.

Table 4-6 Magnetic susceptibilities $LnPO_4$ core NPs synthesized at 90 ºC for 3 hours using 1:2 Ln:Na-TPP volume ratio.

Abbreviation	Magnetic Susceptibility ($\times 10^{-6}$ emu Oe^{-1} g^{-1})
$Gd_{0.3}Ce_{0.35}Tb_{0.35}$	64.79
$Gd_{0.3}Ce_{0.467}Tb_{0.233}$	52.59
$Gd_{0.3}Ce_{0.233}Tb_{0.467}$	77.86
$Gd_{0.3}Ce_{0.175}Tb_{0.525}$	82.22
$Gd_{0.3}Ce_{0.6}Tb_{0.1}$	36.55
$Gd_{0.3}Ce_{0.1}Tb_{0.6}$	94.50
$Gd_{0.95}Ce_{0.0375}Tb_{0.0125}$	72.79
$Gd_{0.8}Ce_{0.15}Tb_{0.05}$	64.26
$Gd_{0.6}Ce_{0.3}Tb_{0.1}$	54.57
$Gd_{0.9}Eu_{0.1}$	69.49
$Gd_{0.8}Eu_{0.2}$	61.52
$Gd_{0.7}Eu_{0.3}$	57.88
$Gd_{0.6}Eu_{0.4}$	49.80
$Gd_{0.5}Eu_{0.5}$	45.72

4.4 Influence of Annealing Temperature

In this section, the influence of annealing temperature on the crystal structure, absorption, excitation, and emission of $LaPO_4$, $Gd_{0.3}Ce_{0.6}Tb_{0.1}PO_4$, and $Gd_{0.3}Ce_{0.1}Tb_{0.6}PO_4$ core NPs was evaluated. Lanthanide phosphate compounds can be synthesized in hexagonal, monoclinic, or tetragonal crystal structures depending on the lanthanide concentration, the synthesis route, and the annealing treatment post-synthesis [155], [156]. The hexagonal crystal structure is associated with hydrated lanthanide phosphate ($LnPO_4 \cdot xH_2O$), whereas the anhydrous form crystallizes in monoclinic structure [155]. The tetragonal crystal structure is only expected for heavy lanthanide ions (Ln^{3+} = Tb, Dy, Ho, Er, Tm, Yb, Lu) [157]. Luminescence properties are improved after annealing because of an enhancement of the NPs crystallinity and a reduction of surface defects

[158], [159]. Therefore, performing an annealing treatment to the as-prepared $LnPO_4$ NPs may improve their response as FI contrast agents. Nonetheless, the application of annealed $LnPO_4$ NPs for biomedical applications may be restricted because of the broad particle size distribution obtained after treatment [61]. Synthesis of $LnPO_4$ core NPs was carried out using either 1:1 or 1:2 Ln:Na-TPP, depending on the lanthanides used (section 3.2), at 90 °C for 3 hours. To study the influence of annealing, the as-prepared $LnPO_4$ core NPs were dried initially at 100 ºC overnight and then annealed for 3 hours at either 400 or 800 ºC. The characterization of the absorption, emission, and excitation spectra was done by dispersing the powder material in DI water.

4.4.1 Crystal Structure

The diffraction patterns of as-prepared and annealed $LaPO_4$, $Gd_{0.3}Ce_{0.6}Tb_{0.1}PO_4$, and $Gd_{0.3}Ce_{0.1}Tb_{0.6}PO_4$ core NPs are shown in **Fig. 4-25**, **Fig. 4-26**, and **Fig. 4-27**, respectively. A hexagonal crystal structure corresponding to $LaPO_4$ with space group $P6_222$ (pdf: 01-075-1881), $CePO_4$ with space group $P3_121$ (pdf: 01-074-1889), and $GdPO_4 \cdot xH_2O$ with space group $P3_121$ (pdf: 00-039-0232) was obtained for $LaPO_4$, $Gd_{0.3}Ce_{0.6}Tb_{0.1}PO_4$, and $Gd_{0.3}Ce_{0.1}Tb_{0.6}PO_4$ core NPs dried at 100 ºC overnight, respectively. These results are consistent with the hexagonal crystal structure reported for $LnPO_4$ nanophosphors [160]. The sharp Bragg reflections observed at ~32º and 46º for $Gd_{0.3}Ce_{0.6}Tb_{0.1}PO_4$ and $Gd_{0.3}Ce_{0.1}Tb_{0.6}PO_4$ core NPs correspond to sodium chloride that precipitated from unreacted species after synthesis. After annealing at 400 ºC for 3 hours, a phase transition from hexagonal to monoclinic was observed for $LaPO_4$ and $Gd_{0.3}Ce_{0.6}Tb_{0.1}PO_4$ core NPs (**Fig. 4-25** and **Fig. 4-26**), which can be indexed as $LaPO_4$ (pdf: 00-032-0493) and $CePO_4$ (pdf: 00-026-0355) having a monoclinic structure with space group $P2_1/n$, respectively. Although the transition of $LnPO_4 \cdot xH_2O$ from hexagonal to monoclinic has been reported to occur around 300 ºC [155], the crystal structure of $Gd_{0.3}Ce_{0.1}Tb_{0.6}PO_4$ core NPs remained hexagonal after annealing at 400 ºC for 3 hours (**Fig. 4-27**). It is assumed that the high concentration of Tb^{3+} ions contributed to a delay in the phase transformation. Overall, there was a slight decrease in the FWHM of the Bragg reflections after annealing at 400 ºC which was observed as an increase of the crystallite size for almost all the samples (**synthesized at** 90 ºC for 3 hours using 1:2 Ln:Na-TPP volume ratio and annealed at different temperature for 3 hours.

Lastly, Gd0.3Ce0.1Tb0.6PO4 core NPs have a tetragonal crystal structure with space group I41/amd (pdf: 00-032-1292) and few Bragg reflections peaks matched the monoclinic crystal structure of GdPO4 with space group of P21/n (pdf: 00-032-0386) (**Fig. 4-27**). These results indicate that the annealing of LnPO4 core NPs caused a refinement of the crystal structure, an

increase of the crystallite size, and a phase transition from hexagonal to either monoclinic or monoclinic/tetragonal depending on the lanthanide concentration.

Table *4-7*). The annealing of $LnPO_4$ core NPs at 800 ºC for 3 hours caused a significant decrease of the FWHM of all Bragg reflections and a phase transition from hexagonal to either monoclinic or monoclinic/tetragonal crystal structures. The decrease of the FWHM is reflected by an increase in one order of magnitude of the crystallite size for all the samples (**synthesized at** 90 ºC for 3 hours using 1:2 Ln:Na-TPP volume ratio and annealed at different temperature for 3 hours.

Lastly, Gd0.3Ce0.1Tb0.6PO4 core NPs have a tetragonal crystal structure with space group I41/amd (pdf: 00-032-1292) and few Bragg reflections peaks matched the monoclinic crystal structure of GdPO4 with space group of P21/n (pdf: 00-032-0386) (**Fig. 4-27**). These results indicate that the annealing of LnPO4 core NPs caused a refinement of the crystal structure, an increase of the crystallite size, and a phase transition from hexagonal to either monoclinic or monoclinic/tetragonal depending on the lanthanide concentration.

Table *4-7*).

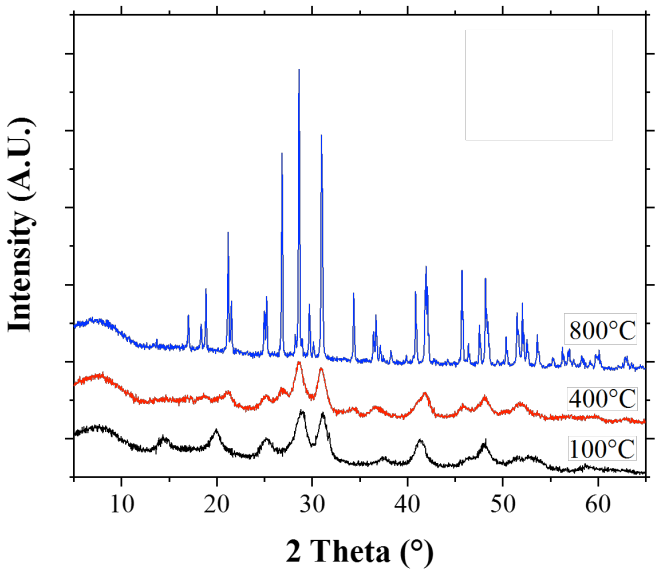

Fig. 4-25 Diffraction patterns of $LaPO_4$ core NPs synthesized at 90 ºC for 3 hours using 1:1 La:Na-TPP volume ratio and annealed at different temperature for 3 hours.

The crystal structure of $LaPO_4$ core NPs corresponds to monoclinic with space group $P2_1/n$ (pdf: 00-032-0493) (**Fig. 4-25**). For $Gd_{0.3}Ce_{0.6}Tb_{0.1}PO_4$ core NPs almost all the Bragg reflections matched with pure $CePO_4$ having a monoclinic crystal structure and space group $P2_1/n$ (pdf: 00-026-0355). However, the Bragg reflections highlighted with * in **Fig. 4-26** correspond to $TbPO_4$ with tetragonal structure and space group $I4_1/amd$ (pdf: 00-032-1292).

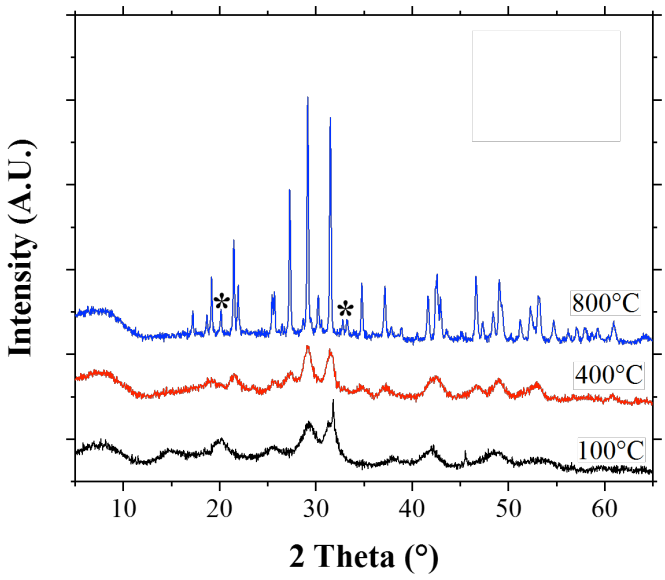

Fig. 4-26 Diffraction patterns of $Gd_{0.3}Ce_{0.6}Tb_{0.1}PO_4$ core NPs synthesized at 90 ºC for 3 hours using 1:2 Ln:Na-TPP volume ratio and annealed at different temperature for 3 hours.

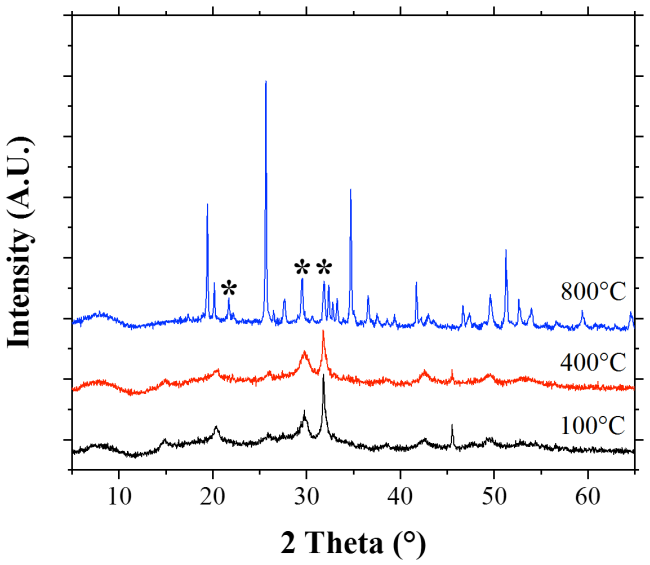

Fig. 4-27 Diffraction patterns of $Gd_{0.3}Ce_{0.1}Tb_{0.6}PO_4$ core NPs synthesized at 90 ºC for 3 hours using 1:2 Ln:Na-TPP volume ratio and annealed at different temperature for 3 hours.

Lastly, $Gd_{0.3}Ce_{0.1}Tb_{0.6}PO_4$ core NPs have a tetragonal crystal structure with space group $I4_1/amd$ (pdf: 00-032-1292) and few Bragg reflections peaks matched the monoclinic crystal structure of $GdPO_4$ with space group of $P2_1/n$ (pdf: 00-032-0386) (**Fig. 4-27**). These results indicate that the annealing of $LnPO_4$ core NPs caused a refinement of the crystal structure, an increase of the crystallite size, and a phase transition from hexagonal to either monoclinic or monoclinic/tetragonal depending on the lanthanide concentration.

Table 4-7 Mean crystallite size of $LnPO_4$ core NPs synthesized at 90 ºC for 3 hours and annealed at different temperature for 3 hours.

	Crystallite size (nm)		
Temperature / **Sample**	**100 ºC**	**400 ºC**	**800 ºC**
$LaPO_4$	6.0 ± 0.4	6.6 ± 1.1	73.5 ± 12.9

$Gd_{0.3}Ce_{0.6}Tb_{0.1}PO_4$	4.8 ± 2.2	7.5 ± 1.4	63.8 ± 1.1
$Gd_{0.3}Ce_{0.1}Tb_{0.6}PO_4$	5.5 ± 2.3	5.5 ± 0.8	76.8 ± 4.4

4.4.2 Absorption, Excitation, and Emission Spectra

The absorption spectra of $Gd_{0.3}Ce_{0.6}Tb_{0.1}PO_4$ core NPs is characterized by two absorption bands at 253 nm and 272 nm [**Fig. 4-28(a)**] corresponding to *4f* → *5d* electronic transitions of Ce^{3+} ions [161]. These bands are clearly observed for $Gd_{0.3}Ce_{0.6}Tb_{0.1}PO_4$ core NPs annealed at 400 ºC for 3 hours, whereas the absorption spectra at 100 ºC and 800 ºC displayed two broad bands [**Fig. 4-28(a)**]. The higher normalized absorbance of $Gd_{0.3}Ce_{0.6}Tb_{0.1}PO_4$ core NPs annealed at 800 ºC may be related to a greater interaction of light with the NPs, Rayleigh scattering, due to a significant increase of the particle size and NP aggregation (**synthesized at** 90 ºC for 3 hours using 1:2 Ln:Na-TPP volume ratio and annealed at different temperature for 3 hours.

Lastly, Gd0.3Ce0.1Tb0.6PO4 core NPs have a tetragonal crystal structure with space group I41/amd (pdf: 00-032-1292) and few Bragg reflections peaks matched the monoclinic crystal structure of GdPO4 with space group of P21/n (pdf: 00-032-0386) (**Fig. 4-27**). These results indicate that the annealing of LnPO4 core NPs caused a refinement of the crystal structure, an increase of the crystallite size, and a phase transition from hexagonal to either monoclinic or monoclinic/tetragonal depending on the lanthanide concentration.

Table *4-7*). A similar behavior was observed for $Gd_{0.3}Ce_{0.1}Tb_{0.6}PO_4$ core NPs, where the sample annealed at 800 ºC had a higher absorbance to that of the other samples because of light scattering [**Fig. 4-28(b)**]. For $Gd_{0.3}Ce_{0.1}Tb_{0.6}PO_4$ core NPs, the absorption spectra were characterized by an absorption band ~220 nm originating from the spin allowed *f* → *d* transitions of Tb^{3+}, which relative intensity and shape was not affected by annealing. The excitation spectra of $Gd_{0.3}Ce_{0.6}Tb_{0.1}PO_4$ and $Gd_{0.3}Ce_{0.1}Tb_{0.6}PO_4$ core NPs were recorded using a PMT voltage of 600 V and an emission wavelength of 352 nm. For $Gd_{0.3}Ce_{0.6}Tb_{0.1}PO_4$ core NPs, the excitation spectra showed resemblance with the absorption spectra since the *4f* → *5d* electronic transitions from Ce^{3+} ions can be observed, however, there was no significant difference in intensity between the

samples [**Fig. 4-29(a)**]. In **Fig. 4-29(b)**, the excitation spectra of $Gd_{0.3}Ce_{0.1}Tb_{0.6}PO_4$ core NPs did not show the $f \rightarrow d$ transition band of Tb^{3+} (~218 nm) [162]. Although broad bands corresponding to Ce^{3+} ions were observed for $Gd_{0.3}Ce_{0.1}Tb_{0.6}PO_4$ core NPs annealed at 400 ºC, their intensity is relatively low because of the concentration of Ce cations in the sample.

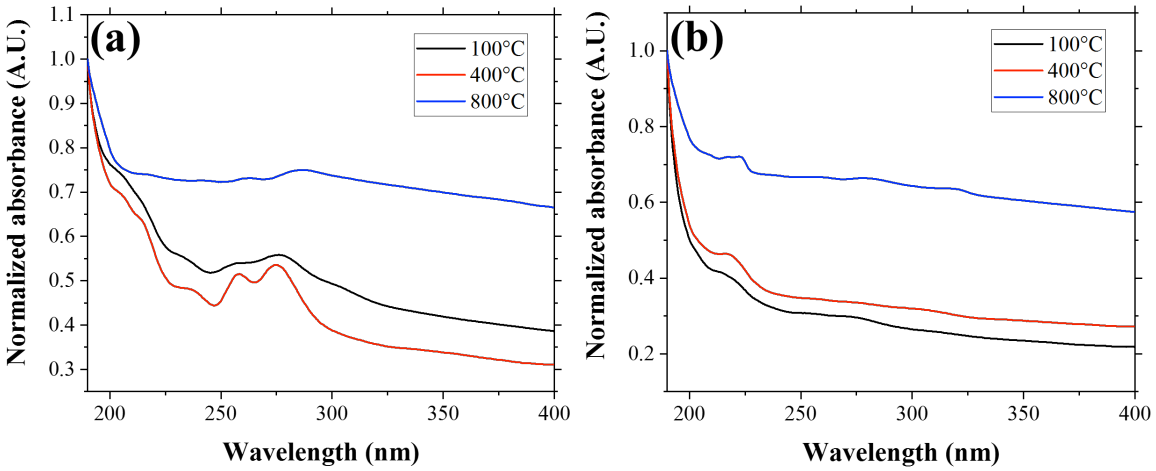

Fig. 4-28 Absorption spectra of (a) $Gd_{0.3}Ce_{0.6}Tb_{0.1}PO_4$ and (b) $Gd_{0.3}Ce_{0.1}Tb_{0.6}PO_4$ core NPs synthesized at 90 ºC for 3 hours using a 1:2 Ln:Na-TPP volume ratio and annealed at different temperature for 3 hours.

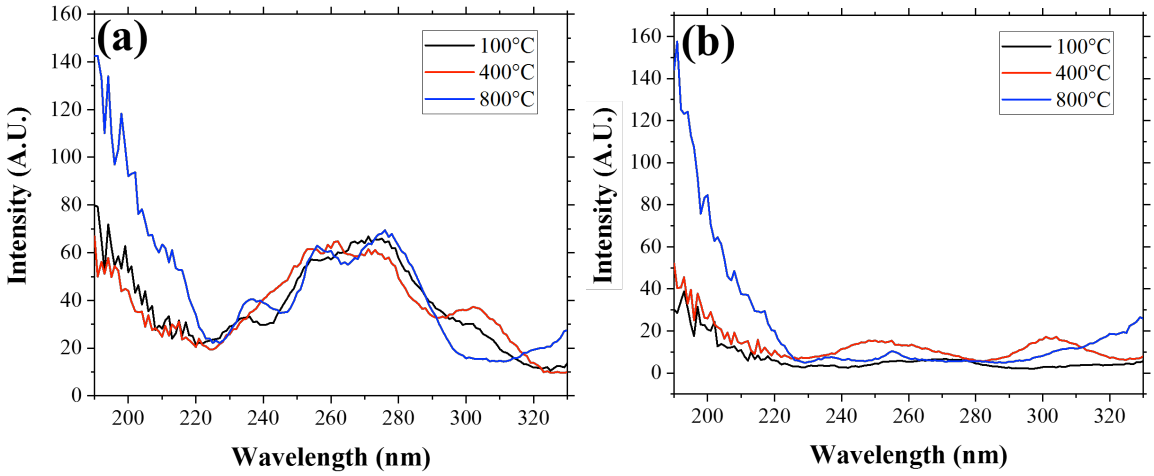

Fig. 4-29 Excitation spectra of (a) $Gd_{0.3}Ce_{0.6}Tb_{0.1}PO_4$ and (b) $Gd_{0.3}Ce_{0.1}Tb_{0.6}PO_4$ core NPs synthesized at 90 ºC for 3 hours using a 1:2 Ln:Na-TPP volume ratio and annealed at different temperature for 3 hours.

The emission spectra of $Gd_{0.3}Ce_{0.6}Tb_{0.1}PO_4$ and $Gd_{0.3}Ce_{0.1}Tb_{0.6}PO_4$ core NPs were recorded using an emission filter at 295–1,100 nm, a PMT voltage of 600 V, and an excitation wavelength of 272 nm. For $Gd_{0.3}Ce_{0.6}Tb_{0.1}PO_4$ core NPs, there was not a significant difference between the emission spectra of the as-prepared NPs and the sample annealed at 400 ºC [**Fig. 4-30(a)**]. Both spectra displayed a broad emission band ~350 nm related to the transition from the $5d^1$ configuration to the $^2F_{5/2}$ and $^2F_{7/2}$ levels of Ce^{3+} ions [161]. The characteristic $^5D_4$-$^7F_6$ (490 nm), $^5D_4$-$^7F_5$ (540 nm), and $^5D_4$-$^7F_4$ (560 nm) Tb^{3+} transitions [62] were observed in all emission spectra [**Fig. 4-30(a)**]. At 800 ºC, the emission spectra displayed higher intensity bands for both Ce^{3+} and Tb^{3+} ions with respect to the other two samples. Moreover, the emission of Ce^{3+} ions is characterized by two bands at ~348 nm and 385 nm corresponding to the direct emission from the $^2D(5d^1)$ state to the $^2F_{5/2}$ and $^2F_{7/2}$ caused by spin-orbit coupling, respectively [163]. The additional bands, between 400–450 nm, are associated to the emission of Tb^{3+} ions. A similar behavior was observed for $Gd_{0.3}Ce_{0.1}Tb_{0.6}PO_4$ core NPs, where the highest intensity was observed after annealing at 800 ºC for 3 hours [**Fig. 4-30(b)**]. The intensity of the $^5D_4$-^7F_J Tb^{3+} transitions is

comparable to the intensity of the Ce^{3+} band despite the difference in concentration between both Ln^{3+} ions. These results suggest that the emission of Tb^{3+} is significantly affected by concentration quenching. Additionally, the presence of two phases, monoclinic and tetragonal, in $LnPO_4$ core NPs annealed at 800 ºC may result in segregation of Ln cations and hence lower energy transfer between Ce^{3+} to Tb^{3+} because of the large distance between ions [164].

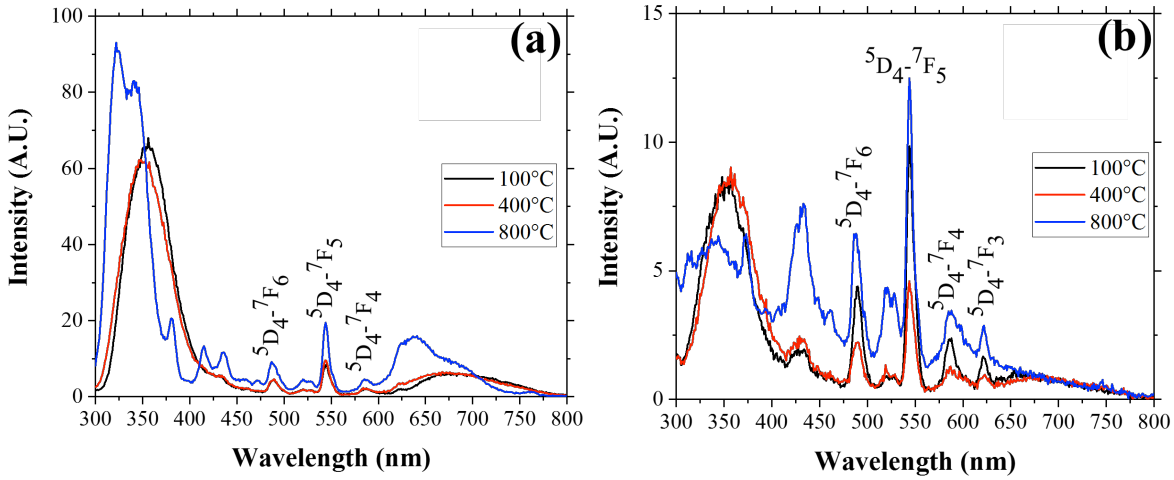

Fig. 4-30 Emission spectra of (a) $Gd_{0.3}Ce_{0.6}Tb_{0.1}PO_4$ and (b) $Gd_{0.3}Ce_{0.1}Tb_{0.6}PO_4$ core NPs synthesized at 90 ºC for 3 hours using a 1:2 Ln:Na-TPP volume ratio and annealed at different temperature for 3 hours.

4.5 Summary

$LnPO_4$ core and core-shell NPs having characteristic luminescence and/or magnetic properties were synthesized in aqueous media by precipitation of Ln^{3+} and $[PO_4]^{3-}$ ions. The proposed synthesis route, used for the precipitation of $LnPO_4$ core and core-shell NPs from $LnCl_3$ and Na-TPP at 90 °C for 3 hours, has been tested in radiochemical synthesis because of its simplicity and the fact that nonspecialized equipment (*i.e.* hot plate-stirrer) is implemented. The influence of synthesis parameters on the crystal structure, morphology, physical stability, luminescence and magnetic properties of $LnPO_4$ core, core + 2 shells, and core + 4 shells NPs was

assessed in this chapter. Modification of synthesis parameters may allow the formation of $LnPO_4$ NPs in shorter synthesis times (<3 hours), whereas tailoring the composition and concentration of lanthanide ions will provide multifunctional properties. The main results obtained in this chapter regarding the synthesis and characterization of $LnPO_4$ core and core-shell NPs towards the development of multifunctional platforms for TRT and molecular imaging are described below:

- No significant difference in the crystallite size of $LaPO_4$ core and core-shell NPs was observed for samples synthesized at 90 °C for either 2 or 3 hours of heating. The time-consuming multi-step procedure followed for the synthesis of radionuclide-doped $LnPO_4$ core-shell NPs can take advantage of shorter heating times (<3 hours) to minimize the activity loss without compromising the particle formation. The optimal synthesis parameters include a heating time greater than 2 hours at 90 °C, when using a 1:1 Ln:Na-TPP volume ratio.
- Increasing the concentration of Na-TPP during synthesis resulted in the formation of smaller $LnPO_4$ core NPs with good physical stability in water and enhanced luminescence properties. The optimum Ln:Na-TPP ratio will depend on the lanthanide(s) ions used during synthesis and their relative concentrations. Monodisperse and stable $LnPO_4$ NPs are more attractive for biological applications than particles that have broad size distributions such as the ones observed in $La_{0.8}Ce_{0.2}PO_4$ core NPs synthesized with a concentration of Na-TPP below 1.5 times the concentration of $LnCl_3$.
- Luminescence and magnetic properties can be tailored by adjusting the composition and concentration of lanthanide ions in $LnPO_4$ NPs. The characteristic green (554 nm) and red (594 nm) fluorescence of Tb^{3+} and Eu^{3+} ions was observed for $LnPO_4$ NPs, respectively. An inefficient energy transfer between Eu cations and O anions may have caused the low fluorescence intensity observed for Eu^{3+} with respect to that of Tb^{3+} ions.

- Post-annealing treatment of $LnPO_4$ NPs caused a phase transition, an increase in the crystallite size, and a modification of the luminescence properties. Although high temperature annealing treatment is intended to enhance the crystallinity and luminescence properties of $LnPO_4$ NPs, the resulting particle size distribution may not be suitable for biological applications.

5 $LnVO_4$ core and core-shell NPs

This chapter summarizes the experiments and characterization carried out for $LnVO_4$ core and core-shell NPs. The procedures described in section 3.3.1 and 3.3.2 were used as a reference for the synthesis of $LnVO_4$ NPs using the citrate and flow route, respectively. Modifications to both synthesis routes were made to assess the influence of synthesis parameters and reagents concentration, among others, during the formation of $LnVO_4$ core and core-shell NPs. The particle size, crystal structure, NPs yield, magnetic susceptibility, luminescence properties, and the ζ-potential were characterized. Understanding the influence of each synthesis parameter on the formation of $LnVO_4$ core and core-shell NPs contributed towards the development of multifunctional platforms for biomedical applications.

5.1 Citrate Route Synthesis

In this section, the influence of temperature, heating time, and reagents concentration in the synthesis of $LnVO_4$ core and core-shell NPs was evaluated since additional studies are necessary for the development of multifunctional platforms for TRT and molecular imaging. Particularly, the development of core-shell structures is essential to increase the retention of decay daughters when using *in vivo* radionuclide generators [42]. Hence, a procedure for the synthesis of $LnVO_4$ core-shell NPs was proposed and tested in this section. The work of Huignard et *al.* consisted in the synthesis of europium-doped YVO_4 core NPs at 60 ºC for 30 minutes using a specific concentration of reagents [47]. Additional lanthanide ions and their combination within $LnVO_4$ NPs may provide multifunctional capabilities for various applications. Having this in mind, the

evolution of the hydrodynamic size of $LnVO_4$ (Ln^{3+} = Nd, Eu, Gd, Tb, Dy, Ho) core NPs, based on the intensity distribution, was followed over time using DLS after synthesis at either 60 ºC, 75 ºC, or 90 ºC. Studying the particle size growth of $LnVO_4$ core NPs at various temperatures and heating times will contribute to understand the role of these parameters during NPs formation when using different lanthanide ions. The crystal structure and magnetic susceptibility of $LnVO_4$ core NPs, synthesized at either 60 ºC for 10 minutes or 90 ºC for 30 minutes, were characterized. These synthesis conditions represent two contrasting cases to assess the formation of $LnVO_4$ core NPs at the lowest temperature (60 °C) and a short heating time (10 minutes). Moreover, the interest in $LnVO_4$ core NPs synthesized at 90 °C for 30 minutes is related to the expected formation of larger particles, which can be used to enhance the retention of radionuclides. The yield and ζ-potential of $GdVO_4$ core NPs synthesized at 60 °C and 90 °C for different heating times were compared to relate the growth kinetics with the fraction of NPs formed and their physical stability in suspension. The results showed that increasing the temperature and heating time causes the growth of larger particles as well as a greater fraction of them. There was no significant difference between the crystallite size and magnetic susceptibility of $LnVO_4$ core NPs synthesized at either 60 ºC for 10 minutes or 90 ºC for 30 minutes, which suggests aggregation of NPs for the latter synthesis conditions. Finally, the variability of the ζ-potential for $GdVO_4$ core NPs synthesized at 60 °C and 90 °C could be associated with the fraction of NPs in suspension.

$GdVO_4$ was used as reference compound to test the proposed procedure for the synthesis of core-shell NPs. During synthesis, various reagents concentrations were used while the heating time and temperature were kept at 30 minutes and 60 °C. The concentrations of sodium citrate and sodium orthovanadate were varied to assess their influence on the particle size, formation of core-shell structures, and NPs yield. Reducing the concentration of sodium citrate contributed to the formation of large particles and/or aggregation of NPs because of its role as complexing agent

[47]. In contrast, a significant increase in the particle size was observed when using high concentrations of sodium orthovanadate because of NPs aggregation. There was no significant difference on the particle size growth of core-shell structures when using a 1:1, 1:1.5, and 1:2 volume ratio between $LnVO_4$ core NPs suspension and lanthanide-citrate-vanadate solution. An increase in $LnVO_4$ NPs yield was obtained after decreasing the concentration of sodium citrate during synthesis.

5.1.1 Influence of Temperature and Heating Time

$LnVO_4$ core NPs were synthesized as described in section 3.3.1, the volume ratio between reagents was kept at 1:0.75:0.75 for $LnCl_3$, sodium citrate, and Na_3VO_4, while the heating time and temperature were varied. The particle size growth was followed for $LnVO_4$ (Ln^{3+} = Nd, Eu, Gd, Tb, Dy, Ho) core NPs synthesized at either 60 ºC, 75 ºC, or 90 ºC for heating times ranging between 5 to 60 minutes. The hydrodynamic size of the $LnVO_4$ core NPs was obtained from the normalized intensity distribution using DLS. The crystal structure, crystallite size, and magnetic susceptibility of $LnVO_4$ core NPs synthesized at either 60 ºC for 10 minutes or 90 ºC for 30 minutes were also reported.

5.1.1.1 Hydrodynamic Size

The mean hydrodynamic size of $LnVO_4$ core NPs synthesized at 60 ºC, 75 ºC, and 90 ºC for multiple heating times is shown in **Fig. 5-1**, **Fig. 5-2**, and **Fig. 5-3**, respectively. The hydrodynamic size increased at each temperature after synthesizing $LnVO_4$ core NPs for longer heating times. This increase in particle size with time is associated with the progressive consumption of free molecular species that contribute to $LnVO_4$ NPs formation [47]. A similar behavior was obtained after increasing the temperature for the same heating time. The largest particle size for each $LnVO_4$ core NPs was obtained after heating at 90 ºC. At this temperature, the

rate at which the oligomeric species are consumed is expected to be higher with respect to lower temperatures (60 °C or 75 °C). This trend suggests that NPs formation can be achieved at shorter heating times (<30 minutes) by increasing the temperature, which could be of interest for the synthesis of radionuclide-doped $LnVO_4$ core NPs, particularly when using short-lived radionuclides.

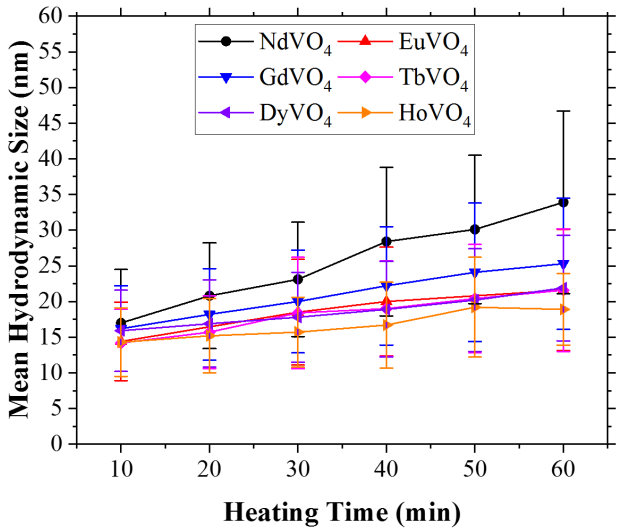

Fig. 5-1 Mean hydrodynamic size (intensity distribution) of $LnVO_4$ NPs synthesized at 60 °C for different heating times using a 1:0.75:0.75 Ln:cit:VO_4 volume ratio.

Although all samples were synthesized at the same conditions, the rate of particle growth was higher for $NdVO_4$ core NPs, while there was not significant difference between the remaining samples based on the reported standard deviations. In summary, the increase of temperature and heating time resulted in larger particle size and also broader size distributions, which could be associated with particle growth, NP aggregation, or both.

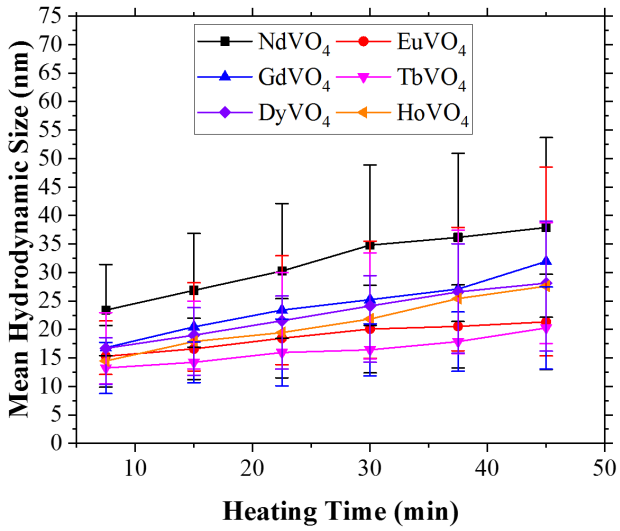

Fig. 5-2 Mean hydrodynamic size (intensity distribution) of $LnVO_4$ NPs synthesized at 75 °C for different heating times using a 1:0.75:0.75 Ln:cit:VO_4 volume ratio.

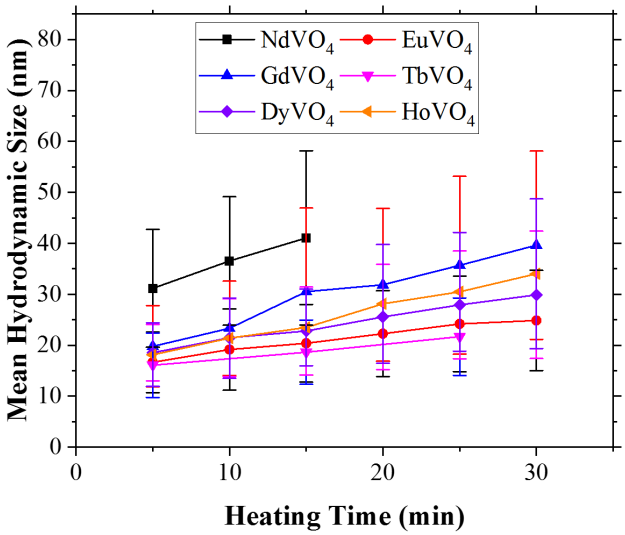

Fig. 5-3 Mean hydrodynamic size (intensity distribution) of $LnVO_4$ NPs synthesized at 90 °C for different heating times using a 1:0.75:0.75 Ln:cit:VO_4 volume ratio.

5.1.1.2 Crystal Structure

The diffraction patterns of $LnVO_4$ core NPs synthesized at either 60 °C for 10 minutes or 90 °C for 30 minutes are shown in **Fig. 5-4**. The crystal structure of $LnVO_4$ core NPs matches with

a tetragonal system with space group $I4_1/amd$. The Bragg reflections highlighted with * correspond to sodium chloride that was precipitated after synthesis [**Fig. 5-4(a)**]. In **Table 5-1**, the reference pattern and crystallite size for each $LnVO_4$ core NPs are presented. As expected from the diffraction patterns, where broad Bragg reflections were observed, $LnVO_4$ core NPs have a crystallite size below 10 nm. Although two contrasting conditions were used for the synthesis of $LnVO_4$ core NPs, no significant difference was observed between their crystallite sizes. These results suggest that $LnVO_4$ core NPs are formed by crystallites, which size is independent of the temperature and heating time used during synthesis, but that may be affected by the reagents concentration ($LnCl_3$, sodium citrate, and Na_3VO_4). Therefore, the increase in particle size evidenced from DLS upon an increase in heating time and temperature may correspond to NP aggregation rather than growth. This hypothesis is consistent with the influence of heating time and temperature on the consumption of oligomeric species.

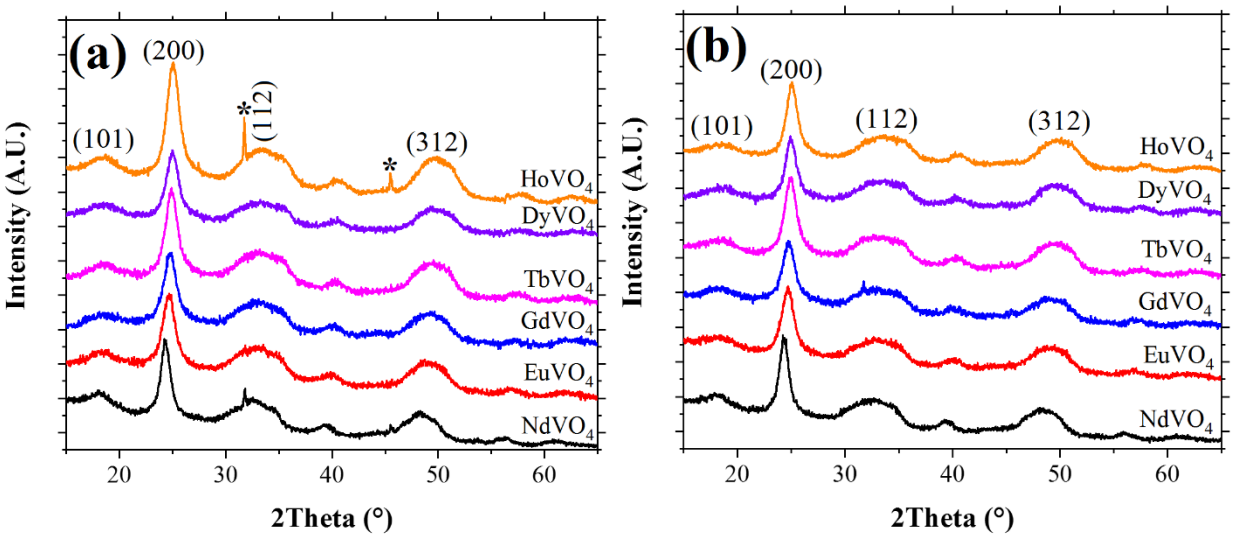

Fig. 5-4 Diffraction patterns of $LnVO_4$ core NPs synthesized at (a) 60 °C for 10 minutes and (b) 90 °C for 30 minutes using a 1:0.75:0.75 Ln:cit:VO_4 volume ratio.

Table 5-1 Crystallite size and reference pattern of $LnVO_4$ core NPs synthesized at different conditions using a 1:0.75:0.75 Ln:cit:VO_4 volume ratio.

Sample	60 °C – 10 minutes	90 °C – 30 minutes	Reference
$NdVO_4$	7.4	7.7	pdf: 01-072-0859
$EuVO_4$	5.8	5.9	pdf: 01-072-0278
$GdVO_4$	5.7	5.7	pdf: 00-017-0260
$TbVO_4$	5.7	5.9	pdf: 01-072-0276
$DyVO_4$	5.9	6.7	pdf: 01-072-0275
$HoVO_4$	5.8	6.5	pdf: 00-015-0764

5.1.1.3 Magnetic Susceptibility

In **Fig. 5-5**, the mass magnetization versus magnetic field loops of $LnVO_4$ core NPs synthesized at 60 °C for 10 minutes and 90 °C for 30 minutes are shown. The trend observed for the mass magnetization of $LnVO_4$ core NPs agrees with the Curie formula [equation$\chi = \frac{N\mu^2}{3k_BT}$ **4-1**$\chi = \frac{N\mu^2}{3k_BT}$ **4-1**], which relates the magnetic susceptibility to magnetic moment of each Ln^{3+} ion. The magnetic susceptibility was calculated from the slope of each curve (**The highest** magnitude was obtained for DyVO4, whereas the lowest corresponds to EuVO4. No significant difference between the magnetic susceptibility of LnVO4 core NPs synthesized at both set of conditions was observed. The high magnetic moment of Tb3+, Dy3+, and Ho3+ ions and hence large magnetic susceptibility may be exploited for the development of negative-T2 contrast agents for application in high magnetic fields [25], [165].

Table *5-2*).

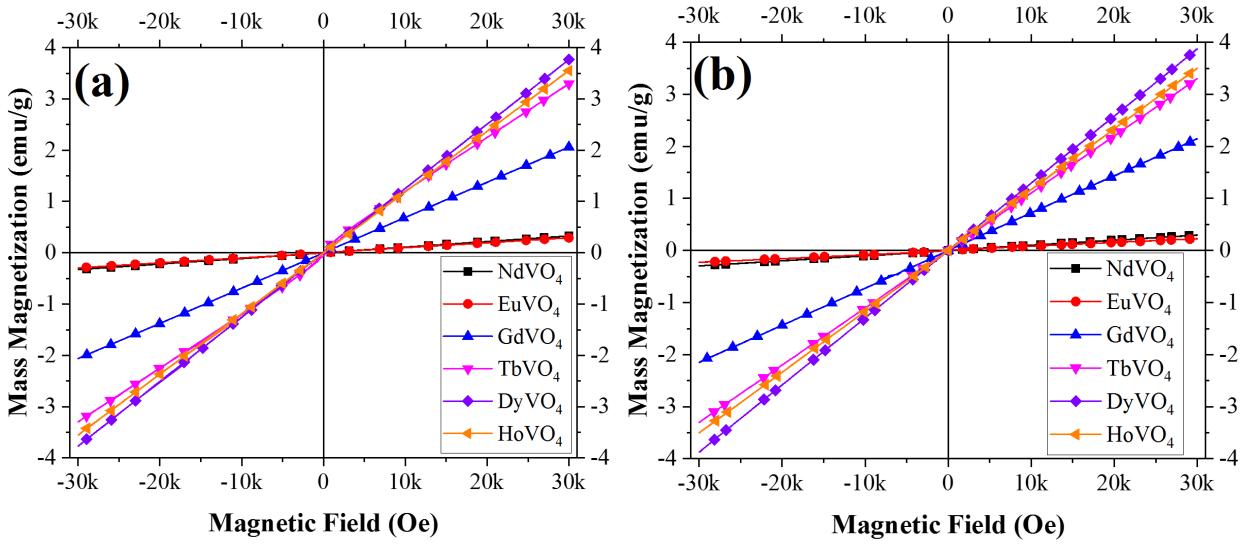

Fig. 5-5 Mass magnetization (emu/g) versus field (Oe) loop for $LnVO_4$ core NPs synthesized at (a) 60 °C for 10 minutes and (b) 90 °C for 30 minutes using a 1:0.75:0.75 Ln:cit:VO_4 volume ratio.

The highest magnitude was obtained for $DyVO_4$, whereas the lowest corresponds to $EuVO_4$. No significant difference between the magnetic susceptibility of $LnVO_4$ core NPs synthesized at both set of conditions was observed. The high magnetic moment of Tb^{3+}, Dy^{3+}, and Ho^{3+} ions and hence large magnetic susceptibility may be exploited for the development of negative-T_2 contrast agents for application in high magnetic fields [25], [165].

Table 5-2 Magnetic susceptibility of $LnVO_4$ core NPs synthesized at different conditions using a 1:0.75:0.75 Ln:cit:VO_4 volume ratio.

	Magnetic Susceptibility ($\times 10^{-6}$ emu Oe^{-1} g^{-1})	
Sample	**60 °C – 10 minutes**	**90 °C – 30 minutes**
$NdVO_4$	11.0	9.92
$EuVO_4$	9.79	7.74
$GdVO_4$	68.8	71.7
$TbVO_4$	112.2	110.1
$DyVO_4$	125.6	129.1
$HoVO_4$	118.5	116.9

5.1.1.4 Nanoparticle Yield

The yield of $GdVO_4$ core NPs synthesized at 60 ºC and 90 ºC for various heating times was calculated based on the concentration of Gd cations measured using ICP-OES. The as-prepared $GdVO_4$ core NPs suspensions were dialyzed against DI water for 20 hours and the Gd concentration of both dialysate and dialyzed NPs suspension was compared to the nominal concentration of Gd cations. In **Table 5-3**, the mean yield and standard deviation for $GdVO_4$ core NPs synthesized at various heating times and temperatures are presented. Although no significant difference was observed between the yield of $GdVO_4$ synthesized for 10 minutes and 30 minutes at 60 ºC, a higher yield was observed upon increase in heating time at a specific temperature. An increase in temperature to 90 ºC caused a higher $GdVO_4$ core NPs yield with respect to those obtained at 60 ºC (**Table 5-3**). The fact that a greater fraction of $LnVO_4$ core NPs could be synthesized at higher temperatures (90 °C) and shorter heating times (<30 minutes) is appealing for radiochemical settings, particularly when using short-lived radionuclides.

Table 5-3 Yield of $GdVO_4$ core NPs synthesized at different conditions using a 1:0.75:0.75 Ln:cit:VO_4 volume ratio.

Temperature (°C)	Heating time (min)	Yield (%)
60	10	68.8 ± 5.7
	30	65.8 ± 5.8
	60	73.0 ± 8.4
90	5	74.2 ± 9.7
	15	80.1 ± 6.6
	30	85.0 ± 8.2

5.1.1.5 Zeta Potential

The physical stability of as-prepared $GdVO_4$ core NPs synthesized at 60 °C and 90 °C was assessed based on the ζ-potential. In **Table 5-4**, the mean ζ-potential and standard deviation of $GdVO_4$ core NPs synthesized at various conditions are summarized. The magnitude of the zeta potential was below -10 mV for $GdVO_4$ core NPs synthesized at 60 °C for heating times shorter than 40 minutes. The sudden increase in the absolute magnitude of the zeta potential at heating times equal or longer than 50 minutes could be related to a larger fraction of NPs in suspension. It is assumed that the variability and low ζ-potential of $GdVO_4$ NPs synthesized at heating times between 10 to 40 minutes is caused by a low fraction of NPs and a high concentration of unreacted species. This behavior was not observed at 90 °C, where the absolute magnitude of the mean ζ-potential was greater than 25 mV for almost all the samples. The consistent ζ-potential of $GdVO_4$ core NPs synthesized at 90 °C is assumed to be related to a higher yield of NPs (**Table 5-3**). The negative magnitude of the ζ-potential obtained for all samples is consistent with the presence of citrate groups that are complexed to Ln^{3+} ions on the NP surface [47].

Table 5-4 Mean ζ-potential of $GdVO_4$ core NPs synthesized at different conditions using a 1:0.75:0.75 Ln:cit:VO_4 volume ratio.

ζ-potential (mV)						
Time (m) Temp.	**10**	**20**	**30**	**40**	**50**	**60**
60 °C	-4.7 ± 6.6	-0.1 ± 0.5	-8.9 ± 2.3	-5.1 ± 4.4	-12.5 ± 0.4	-35.7 ± 0.6
90 °C	-28.4 ± 7.5	-18.7 ± 2.1	-30.3 ± 3.6	-27.4 ± 6.8	-33.4 ± 3.2	-27.2 ± 4.8

5.1.2 Influence of Reagents Concentration

The concentration of sodium citrate and sodium orthovanadate was varied to assess their influence on particle growth for $GdVO_4$ core and core-shell NPs. Synthesis of $GdVO_4$ core NPs

was carried out at 60 °C for 30 minutes, while the volume ratio between sodium citrate and sodium orthovanadate was adjusted at 0.55–0.75 and 0.75–0.95 with respect to $GdCl_3$, respectively. The hydrodynamic size from the intensity and number distributions was reported at each concentration as well as the PI. The crystallite size and yield of $GdVO_4$ core NPs obtained for multiple citrate concentrations were also compared. The synthesis procedure proposed for the development of $GdVO_4$ core-shell NPs was tested at various reagents concentrations and volume ratios between the core NPs suspension and the fresh oligomeric species solution. The hydrodynamic size, particle size distribution, and crystallite size were used to assess the formation of core-shell structures.

5.1.2.1 Hydrodynamic Size

In **Table 5-5**, the mean hydrodynamic size and standard deviation are reported for different volume ratios of sodium citrate and Na_3VO_4 with respect to that of $GdCl_3$. The hydrodynamic size of $GdVO_4$ core NPs synthesized with 0.55, 0.65, and 0.75 volume equivalent of sodium citrate for a fixed 0.75 volume equivalent of Na_3VO_4 did not show significant difference (**Table 5-5**). Larger hydrodynamic size and size distributions were observed upon an increase in concentration of Na_3VO_4 for the same concentrations of sodium citrate. This trend is related to a decrease in the fraction of surface Gd cations available for complexation with citrate groups as well as a reduction of citrate groups to stabilize the $GdVO_4$ core NPs. It is expected that decreasing the concentration of sodium citrate while increasing the concentration of Na_3VO_4 will result in significant NP aggregation rather than NP growth.

Table 5-5 Mean intensity and number particle size of $GdVO_4$ core NPs synthesized 60 °C for 30 minutes using different chemical volume ratios.

Ln	Cit	VO_4	PI	Size [intensity] (nm)	Size [number] (nm)
1	0.75	0.75	0.112	15.1 ± 8.4	8.8 ± 2.0
		0.85	0.202	34.5 ± 14.4	14.6 ± 3.9

		0.95	0.280	258.0 ± 122.3	38.7 ± 19.0
	0.65	0.75	0.159	15.8 ± 5.8	8.8 ± 2.2
		0.85	0.181	56.6 ± 27.6	21.9 ± 6.2
		0.95	0.311	326.4 ± 230.3	40.4 ± 14.7
	0.55	0.75	0.072	16.8 ± 6.6	8.8 ± 2.2
		0.85	0.231	69.7 ± 40.6	22.7 ± 6.4
		0.95	0.322	497.4 ± 342.5	122.2 ± 62.8

A procedure for the synthesis of $GdVO_4$ core-shell NPs based on mixing the core NPs suspension with a solution containing Ln-cit-VO_4 oligomeric species was proposed. The volume ratio between the core NPs suspension and the oligomeric species solution was varied at either 1:1, 1:1.5, or 1:2. To study the influence of the concentration of fresh oligomeric species in the particle growth of $GdVO_4$ core-shell NPs, the volume ratio between Ln:cit:VO_4 was kept at 1:0.75:0.75 while the synthesis was carried out at 60 °C for 30 minutes. In **Fig. 5-6**, the particle size of $GdVO_4$ core, core + 1 shell, and core + 2 shells NPs is compared with respect to the volume ratio between the core NPs suspension and the oligomeric species solution. These results showed that there is no significant difference between the particle size of core and core-shell structures based on the volume ratios used. However, it is observed that the mean core-shell particle size is larger when synthesized using volume ratios of 1:1.5 and 1:2 with respect to 1:1 of core NPs suspension to oligomeric species solution. The deposition of shells for all the volume ratios studied was accompanied by an increase in the mean particle size and standard deviation (**Fig. 5-6**).

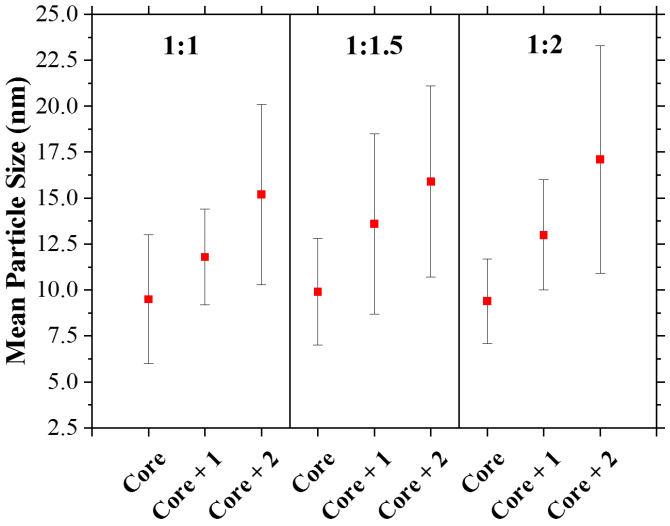

Fig. 5-6 Mean particle size (number distribution) of $GdVO_4$ core-shell NPs synthesized at 60 °C for 30 minutes using a 1:0.75:0.75 Ln:cit:VO_4 volume ratio, while increasing the volume ratio of oligomeric species solution to core NPs suspension.

The evolution of the intensity and number distribution of $GdVO_4$ core-shell NPs is shown in **Fig. 5-7**. The deposition of shells caused broader particle size distributions suggesting that the mechanism behind core-shell structure formation may be Ostwald ripening, where the smaller nuclei dissolve while the larger nuclei and/or core NPs coarsen [166]. Hence, the synthesis of core-

shell structures could result in the formation of new core NPs depending on the concentration of oligomeric species and the synthesis parameters used.

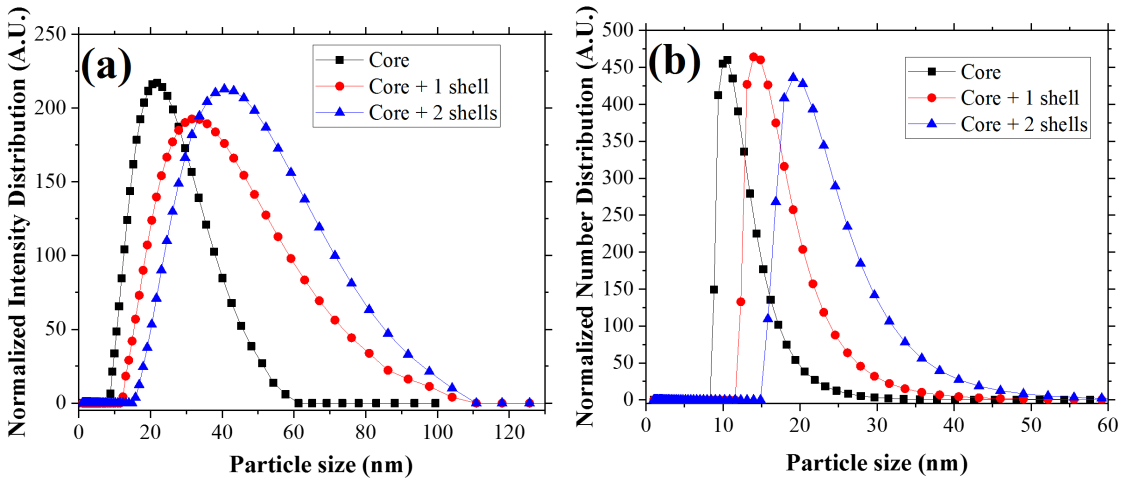

Fig. 5-7 Normalized (a) intensity and (b) number particle size distributions of $GdVO_4$ core-shell NPs synthesized at 60 °C for 30 minutes using a 1:0.75:0.75 Ln:cit:VO_4 volume ratio, while keeping a 1:1.5 volume ratio of core NPs suspension to oligomeric species solution.

The formation of $GdVO_4$ core-shell NPs was also studied using lower concentration of sodium citrate to promote the deposition of thicker shells, while keeping a constant concentration of Na_3VO_4. The mean hydrodynamic size and standard deviation of $GdVO_4$ core, core + 1 shell, and core + 2 shells for 1:1.5 and 1:2 volume ratio of core NPs suspension to fresh oligomeric solution are shown in **Table 5-6** and **Table 5-7**, respectively. The fresh oligomeric solution was prepared using the same concentration of chemical reagents proposed for the core NPs. Despite the assumption that decreasing the concentration of sodium citrate would result in a thicker shell deposition, the results showed that there is no significant difference in particle size between the proposed chemical concentrations.

Table 5-6 Mean intensity and number particle size of $GdVO_4$ core and core-shell NPs synthesized at 60 °C for 30 minutes using at various chemical ratios, while keeping the volume ratio of core NPs suspension to fresh oligomeric solution 1:1.5.

Ln	Cit	VO_4	Structure	PI	Size [intensity] (nm)	Size [number] (nm)
1	0.75	0.75	Core	0.156	13.9 ± 17.5	6.6 ± 1.2
			Core + 1 shell	0.209	15.5 ± 3.7	9.3 ± 2.0
			Core + 2 shells	0.236	17.5 ± 3.8	13.6 ± 2.3
1	0.65	0.75	Core	0.097	12.8 ± 4.3	7.8 ± 1.8
			Core + 1 shell	0.132	16.5 ± 4.8	9.3 ± 2.1
			Core + 2 shells	0.152	18.3 ± 5.1	12.8 ± 2.4
1	0.55	0.75	Core	0.036	13.4 ± 4.5	8.1 ± 1.9
			Core + 1 shell	0.092	17.3 ± 5.7	10.5 ± 2.5
			Core + 2 shells	0.110	19.8 ± 6.8	11.6 ± 2.8

Table 5-7 Mean intensity and number particle size of $GdVO_4$ core and core-shell NPs synthesized at 60 °C for 30 minutes using at various chemical ratios, while keeping the volume ratio of core NPs suspension to fresh oligomeric solution 1:2.

Ln	Cit	VO_4	Structure	PI	Size [intensity] (nm)	Size [number] (nm)
1	0.75	0.75	Core	0.095	12.8 ± 20.2	8.1 ± 1.5
			Core + 1 shell	0.146	14.6 ± 2.7	12.2 ± 1.8
			Core + 2 shells	0.132	16.7 ± 3.0	14.0 ± 1.8
1	0.65	0.75	Core	0.058	12.2 ± 4.0	6.3 ± 1.4
			Core + 1 shell	0.064	16.0 ± 4.4	11.0 ± 2.1
			Core + 2 shells	0.076	19.1 ± 6.4	11.4 ± 2.7
1	0.55	0.75	Core	0.054	13.2 ± 4.4	8.1 ± 1.8
			Core + 1 shell	0.075	17.6 ± 5.9	10.6 ± 2.5
			Core + 2 shells	0.132	19.8 ± 6.7	11.8 ± 2.8

It is expected that a larger fraction of citrate groups on the NPs surface may hinder the deposition and growth of shells. Additionally, an increase in the concentration of oligomeric species did not promote the formation of thicker shells. This behavior could be attributed to the

fact that a high concentration of oligomeric species may promote the formation of new core NPs rather than the deposition of shells under the temperature and heating time used.

5.1.2.2 Crystal Structure

The diffraction patterns of $GdVO_4$ core and core + 2 shells NPs synthesized at 60 °C for 30 minutes while using either 0.75, 0.65, or 0.55 volume equivalent of sodium citrate are shown in **Fig. 5-8**. The crystal structure of both core and core + 2 shells NPs corresponds to a tetragonal system with space group $I4_1/amd$ (pdf: 00-017-0260). A decrease in the concentration of sodium citrate did not result in a significant difference in the crystallite size of $GdVO_4$ core NPs, which magnitude was between 4.8 to 5.2 nm. Although the citrate groups control the size of the $GdVO_4$ core NPs, the similarity in crystallite size may be attributed to the citrate concentrations studied. A further decrease of citrate concentration was not explored because significant aggregation of NPs has been reported [47]. The deposition of two shells of $GdVO_4$ was carried out using a 1:1.5 volume ratio of core NPs suspension to fresh oligomeric solution. The deposition of two $GdVO_4$ shells caused an increase in the crystallite size to 5.8–6.4 nm. As observed from the $GdVO_4$ core NPs, the difference in crystallite size for core + 2 shells NPs synthesized using various citrate concentrations is not significant. It is expected that the formation of core-shells structures and hence increase in crystallite size are related to an epitaxial grow mechanism of $GdVO_4$ shells on the core NPs surface. An additional set of experiments to test the deposition of shells at different heating time and temperature was performed. In this case, $GdVO_4$ core-shell NPs were synthesized at 90 °C for 10 minutes while keeping the volume ratio of chemicals at 1:0.75:0.75 and a 1:1.5 volume ratio of core NPs suspension to fresh oligomeric solution. The deposition of shells decreased the FWHM of the Bragg reflections and therefore resulted in an increase of the crystallite size (**Fig. 5-9**). The crystallite size was 6.6 nm, 8.6 nm, and 9.5 nm for $GdVO_4$ core, core + 1 shell, and core + 2 shells, respectively. The crystallite size of $GdVO_4$ core + 2 shells (9.5

nm), synthesized at 90 °C for 10 minutes, is larger than the one obtained for $GdVO_4$ core NPs (5.7 nm), synthesized at 90 ºC for 30 minutes. This difference of 3.8 nm in crystallite size between two NPs suspensions that were synthesized at the same temperature (90 °C) and equivalent heating time (30 minutes) supports the hypothesis that the addition of fresh oligomeric solutions contributed to the deposition of shells on the core surface. In summary, the development of core-shell structures is dependent on the heating time, temperature, and reagents concentration. The continuous increase in crystallite size validates the successful growth of $GdVO_4$ shells by using the proposed method under various synthesis conditions.

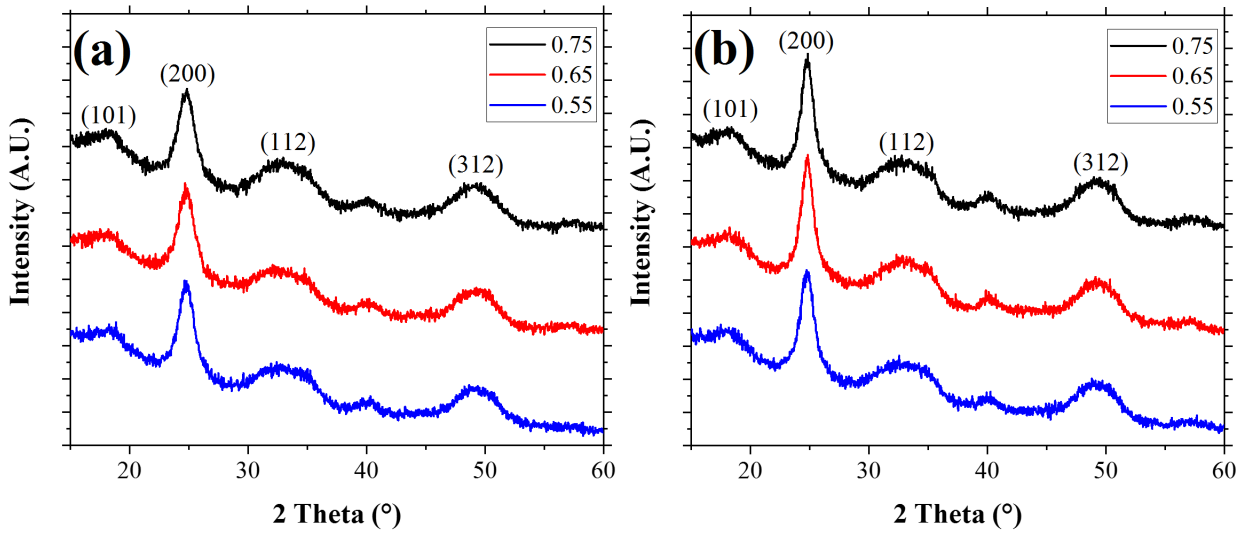

Fig. 5-8 Diffraction patterns of $GdVO_4$ (a) core and (b) core + 2 shells NPs synthesized at 60 °C for 30 minutes using different citrate concentrations (Ln:cit = 1:0.75, 1:0.65, 1:0.55), while keeping a 1:1.5 volume ratio of core NPs suspension to oligomeric species solution.

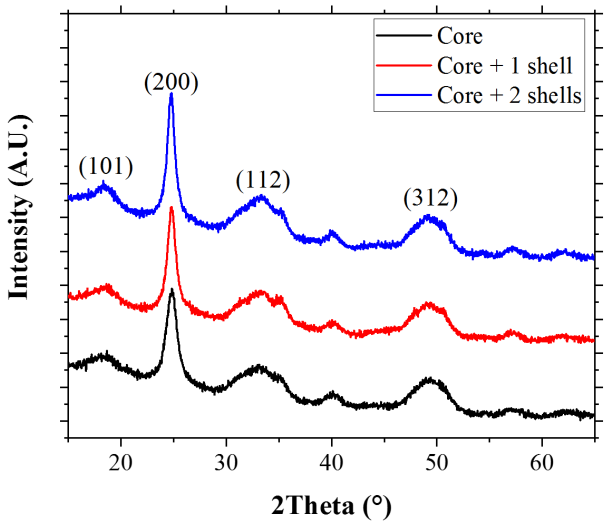

Fig. 5-9 Diffraction patterns of $GdVO_4$ core, core + 1 shell, and core + 2 shells NPs synthesized at 90 °C for 10 minutes using 1:0.75:0.75 Ln:cit:VO_4 and 1:1.5 core NPs suspension to oligomeric species solution volume ratios.

5.1.2.3 Nanoparticle Yield

The fraction of $GdVO_4$ core NPs synthesized at 60 °C for 30 minutes was assessed based on the concentration of Gd cations. $GdVO_4$ core NPs suspensions synthesized with either 0.75, 0.65, or 0.55 volume equivalent of sodium citrate were dialyzed against DI water for 20 hours. The Gd concentration of both dialysate and dialyzed NPs suspension was measured by ICP-OES and compared to the nominal concentration of Gd cations. A decrease in sodium citrate concentration did not result in a significant difference in the NPs yield (**Table 5-8**). However, it can be observed that the mean value increases ~10% for lower concentrations of sodium citrate (0.65 and 0.55). The higher yield obtained when using lower concentrations of sodium citrate (0.65 and 0.55) could be explained by its role as complexing agent, where it may also hinder the formation of NPs since a fraction of lanthanide ions can remain as Ln-cit complexes in solution.

Therefore, a decrease in sodium citrate concentration will contribute to the formation of a larger fraction of NPs with negligible influence on the particle size distribution and crystallite size.

Table 5-8 $GdVO_4$ core NPs yield synthesized at 60 °C for 30 minutes using different citrate concentrations, while keeping a 1:0.75 Ln:VO_4 volume ratio.

Reagents concentration [Ln:cit:VO_4]	Yield (%)
1:0.75:0.75	65.8 ± 5.8
1:0.65:0.75	78.6 ± 9.9
1:0.55:0.75	76.9 ± 1.2

5.1.2.4 Magnetic Susceptibility

The mass magnetization versus magnetic field loops of $GdVO_4$ core, core + 1 shell, and core + 2 shells NPs synthesized at 90 °C for 10 minutes while keeping the volume ratio of chemicals at 1:0.75:0.75 and a 1:1.5 volume ratio of core NPs suspension to fresh oligomeric solution are shown in **Fig. 5-10**.

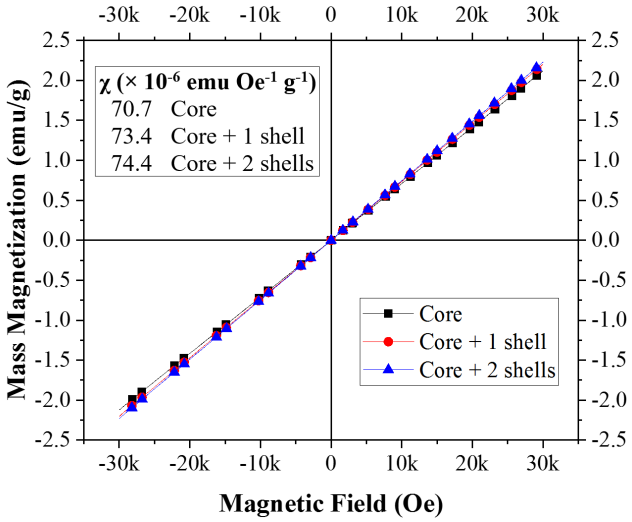

Fig. 5-10 Mass magnetization (emu/g) versus field (Oe) loop for $GdVO_4$ core, core + 1 shell, and core + 2 shells NPs synthesized at 90 °C for 10 minutes using 1:0.75:0.75 Ln:cit:VO_4 and 1:1.5 core NPs suspension to fresh oligomeric solution volume ratios.

The deposition of shells resulted in an increase of magnetic susceptibility with respect to the $GdVO_4$ core NPs. Although the increase in magnetic susceptibility is not significant, the larger magnitude could be related to a higher yield of $GdVO_4$ core-shell NPs with respect to core. This assumption is based on the dependence of the magnetic susceptibility on the number of ions (N) as shown in equation $\chi = \frac{N\mu^2}{3k_BT}$ **4-1**, where temperature and the magnetic moment were kept constant. In core-shell structures, a lower fraction of unreacted species that are diamagnetic will contribute toward a higher magnetic susceptibility.

5.1.3 Synthesis of $Gd_{(1-x)}Eu_xVO_4$ core NPs

Europium-doped gadolinium vanadate ($Gd_{(1-x)}Eu_xVO_4$) core NPs were synthesized by mixing 0.1 M $GdCl_3$ and 0.1 M $EuCl_3$ at specific volume ratios [Eu/(Gd+Eu) = 0.05, 0.1, 0.2, and 0.4] while using the concentration of reagents, temperature, and heating time described in section 3.3.1. The diffraction patterns, time-resolved luminescence decay lifetimes, absorption, excitation, and emission spectra were collected for the different samples to assess the influence of Eu^{3+} concentration. Particular interest was placed on the minimum Eu^{3+} concentration that will provide the highest emission intensity with negligible concentration quenching for the development of multimodal contrast agents for FI and MRI. The absorption, excitation, and emission spectra as well as the luminescence decay lifetimes were influenced by the Eu^{3+} concentration, whereas no significant difference was observed in the crystal structure and crystallite size of $Gd_{(1-x)}Eu_xVO_4$ core NPs. The results presented in this section have been adapted from a manuscript accepted at Journal of Materials Chemistry B.

5.1.3.1 Crystal Structure

Diffraction patterns of $Gd_{(1-x)}Eu_xVO_4$ core NPs matched with a tetragonal system having a zircon-type structure and space group $I4_1/amd$ (pdf: 00-017-0260, $GdVO_4$). The increase in Eu^{3+} concentration results in a slight shifting of 2θ, which implies a change in the d-spacing due to elastic strains imposed by the difference in size between the ionic radii of Gd^{3+} and Eu^{3+} ions (**Fig. 5-11**) [141]. The crystallite size of $Gd_{(1-x)}Eu_xVO_4$ core NPs seems to be independent of the Eu^{3+} concentration since no significant differences were observed between samples (**Error! Reference s ource not found.**).

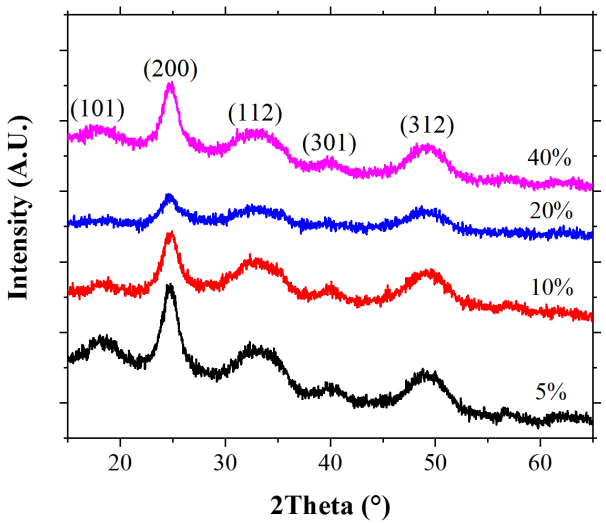

Fig. 5-11 Diffraction patterns of $Gd_{(1-x)}Eu_xVO_4$ core NPs synthesized at 60 °C for 30 minutes using 1:0.75:0.75 Ln:cit:VO_4 volume ratio.

Table 5-9 Crystallite size of $Gd_{(1-x)}Eu_xVO_4$ core NPs synthesized at 60 °C for 30 minutes using 1:0.75:0.75 Ln:cit:VO_4 volume ratio.

Sample	Crystallite size (nm)
$Gd_{0.95}Eu_{0.05}VO_4$	4.5
$Gd_{0.9}Eu_{0.1}VO_4$	4.4
$Gd_{0.8}Eu_{0.2}VO_4$	4.7
$Gd_{0.6}Eu_{0.4}VO_4$	4.7

5.1.3.2 Luminescence Properties

The absorption, excitation, and emission spectra of $Gd_{(1-x)}Eu_xVO_4$ core NPs having Eu^{3+} concentration from 5–40 at.% are shown in **Fig. 5-12**, **Fig. 5-13**, and **Fig. 5-14**, respectively. The concentration of lanthanide ions in $Gd_{(1-x)}Eu_xVO_4$ core NPs is consistent with the nominal Eu^{3+} concentrations (**Table 5-10**).The absorption spectrum is characterized by an absorption band around 280 nm, which corresponds to the O^{2-}-V^{5+} CT band [167]. An increase in Eu^{3+} concentration resulted in a slight rise in the absorbance, which may be related to the O^{2-}-Eu^{3+} CT (250–260 nm), which could not be observed due to overlapping with O^{2-}-V^{5+} CT band (**Fig. 5-12**). The excitation spectrum was recorded using an emission wavelength of 618 nm, an excitation filter between 250–395 nm, and a PMT voltage of 600 V. As shown in **Fig. 5-13**, the excitation spectrum is characterized by two CT bands corresponding to O^{2-}-Eu^{3+} (~280 nm) and O^{2-}-V^{5+} (~305 nm), where the latter is related to the symmetry-allowed absorption $^1A_1 \rightarrow {}^1T_2$ of the $[VO_4]^{3-}$ unit [168]–[170]. An increase of Eu^{3+} concentration was accompanied by a higher intensity of the O^{2-}-Eu^{3+} band, while the O^{2-}-V^{5+} band becomes unnoticeable due to overlapping (**Fig. 5-13**).

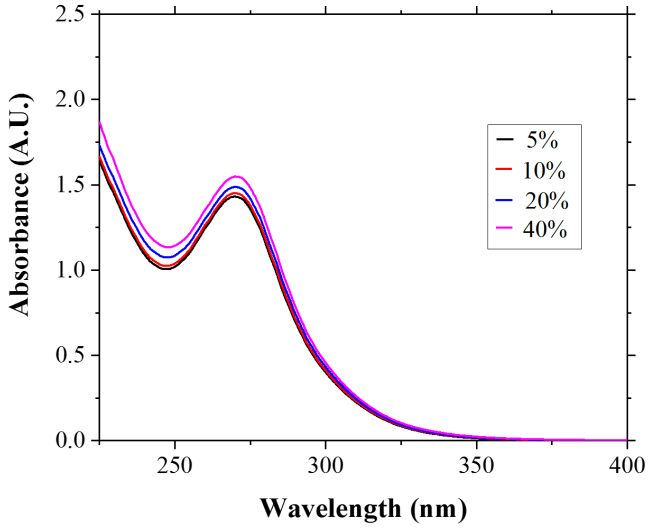

Fig. 5-12 Absorption spectra of $Gd_{(1-x)}Eu_xVO_4$ core NPs synthesized at 60 °C for 30 minutes using 1:0.75:0.75 Ln:cit:VO_4 volume ratio.

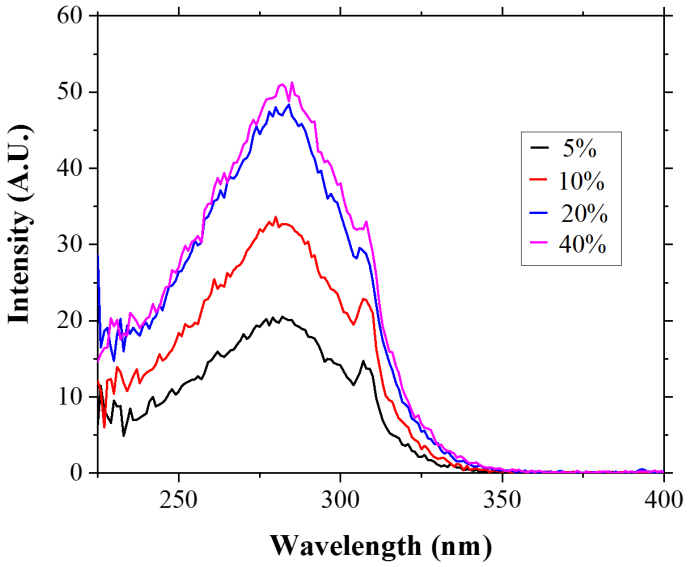

Fig. 5-13 Excitation spectra of $Gd_{(1-x)}Eu_xVO_4$ core NPs synthesized at 60 °C for 30 minutes using 1:0.75:0.75 Ln:cit:VO_4 volume ratio.

The emission spectrum of each sample was recorded using an excitation wavelength of 280 nm, a PMT voltage of 600 V, and an emission filter from 295–1,100 nm. All emission spectra displayed the characteristic $^5D_0 \rightarrow {}^7F_J$ (J = 1–4) Eu^{3+} transitions originating from low energy transfer (**Fig. 5-14**) [171]. It has been evidenced that the dopant concentration has to be optimized for each Ln^{3+} ion based on the properties of the host lattice [8]. Although increasing the Eu^{3+} concentration to 40 at.% caused the highest emission intensity at $^5D_0 \rightarrow {}^7F_2$ transition, the difference with 20 at.% was not significant evidencing concentration quenching. Time-resolved luminescence decay curves of $Gd_{(1-x)}Eu_xVO_4$ core NPs displayed a better fit (higher R^2) when using a biexponential function with respect to that obtained with an exponential (**Fig. 5-15**). An increase of Eu^{3+} concentration from 5% to 40% caused a decrease in the average luminescence decay lifetime from 1.33 µs to 0.89 µs, respectively. Increasing the concentration of Eu^{3+} ions caused a decrease in the distance between dopant ions, which promoted Eu-Eu interactions resulting in cross relaxation processes [59], [126], [172]. The higher the concentration of dopant

ions, the greater is the probability of non-radiative de-excitation, which is observed as a decrease in the average luminescence decay lifetime [8]. Additionally, the nonexponential behavior of the time-resolved luminescence decay curves may suggest the energy transfer of Eu^{3+} to impurities [169]. Although the average luminescence decay life time of $Gd_{0.8}Eu_{0.2}VO_4$ core NPs was 17.9% lower with respect to that of $Gd_{0.95}Eu_{0.05}VO_4$, an increase of 89% in emission intensity encouraged the use of 20% Eu^{3+} as an optimal concentration for fluoresence applications.

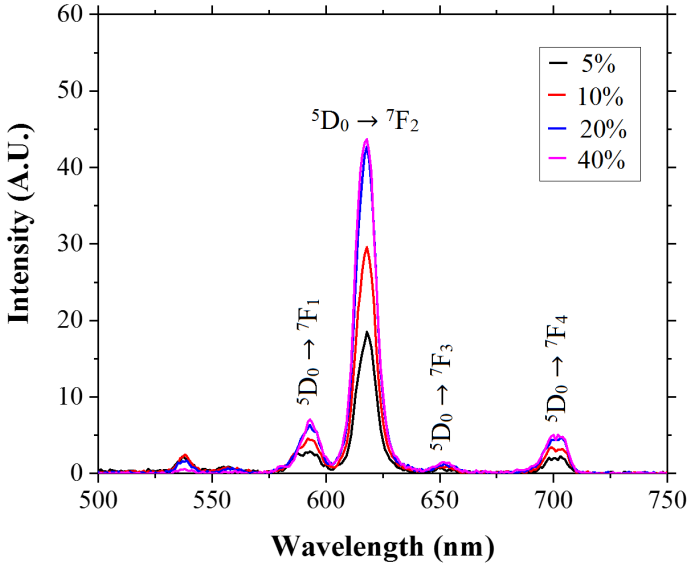

Fig. 5-14 Emission spectra of $Gd_{(1-x)}Eu_xVO_4$ core NPs synthesized at 60 °C for 30 minutes using 1:0.75:0.75 Ln:cit:VO_4 volume ratio.

Table 5-10 Lanthanide weight percentage results for $Gd_{(1-x)}Eu_xVO_4$ core NPs synthesized at 60 °C for 30 minutes using 1:0.75:0.75 Ln:cit:VO_4 volume ratio.

	Weight percentage (%)	
Sample	**Eu**	**Gd**
$Gd_{0.95}Eu_{0.05}VO_4$	5.6	94.4
$Gd_{0.9}Eu_{0.1}VO_4$	10.6	89.4
$Gd_{0.8}Eu_{0.2}VO_4$	20.9	79.1
$Gd_{0.6}Eu_{0.4}VO_4$	40.4	59.6

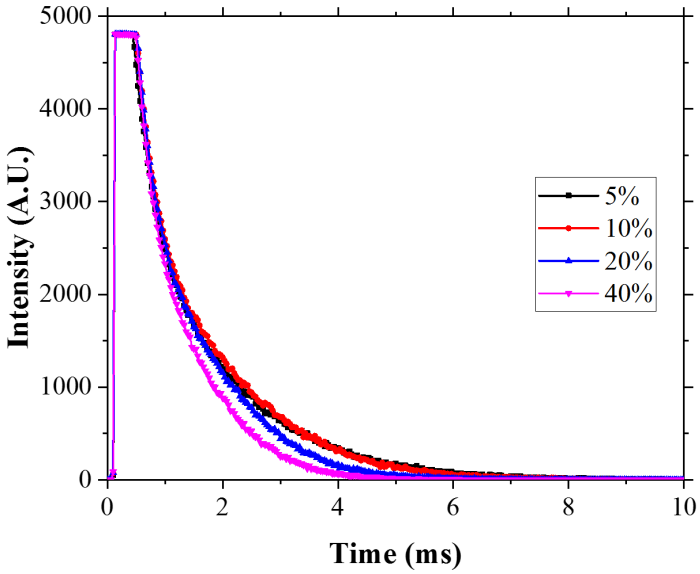

Fig. 5-15 Time-resolved luminescence decay curves of $Gd_{(1-x)}Eu_xVO_4$ core NPs synthesized at 60 °C for 30 minutes using 1:0.75:0.75 Ln:cit:VO_4 volume ratio.

5.2 Flow Synthesis

In this section, the formation of $LnVO_4$ NPs by precipitation at room temperature was studied because of its attractiveness for radiochemical synthesis and the promising application of these NPs as MRI contrast agents. A detailed study of the influence of pH, reagents ($LnCl_3$ and Na_3VO_4) concentration, and lanthanide composition is presented for $LnVO_4$ NPs prepared using flow synthesis. Huignard et *al*. reported that the pH of the solution must not be either too alkaline (pH > 13) to prevent the irreversible precipitation of $Ln(OH)_3$ species or too acidic (pH < 8) since polyvanadate species will be formed [126]. Based on these results, it was concluded that additional studies were necessary for the development of multifunctional platforms for biomedical applications. The synthesis of $LnVO_4$ NPs was completed as reported in section 3.3.2. The pH was monitored continuously during the addition of $LnCl_3$ solutions and adjusted at either 8, 10, 11, or 12 using NaOH (1 M). The reagents concentration, $LnCl_3$ and Na_3VO_4, was set at either 0.01 M, 0.05 M, 0.1 M, or 0.2 M while the pH was kept at 12. Pure $LnVO_4$ (Ln^{3+} = La, Gd, Tb, Dy, and

Ho) and Dy-doped $LnVO_4$ (Ln^{3+} = La, Gd, and Lu) NPs were prepared using 0.1 M solutions of both $LnCl_3$ and Na_3VO_4, while keeping the pH at ~11 to assess their potential application as radionuclides carriers and molecular imaging contrast agents. It was observed that the pH, reagents concentration, and crystal structure influenced the morphology of $LnVO_4$ NPs. The results presented in this section have been adapted from a manuscript that is under preparation.

5.2.1 Influence of Synthesis Parameters

$GdVO_4$ NPs were synthesized using 0.1 M $GdCl_3$ and 0.1 M Na_3VO_4 by adding $GdCl_3$ at ~1 mL min^{-1} and adjusting the pH at either 8, 10, 11, or 12 using 1 M NaOH. Synthesis parameters such as flow rate, stirring speed, and stirring time were also studied, however, the results are not shown since no significant influence on the morphology and crystallite size of $GdVO_4$ NPs was observed. The concentration of both $GdCl_3$ and Na_3VO_4 was also varied at either 0.01, 0.05, 0.1, or 0.2 M while keeping the flow rate and pH at ~1 mL min^{-1} and 12, respectively. The crystallite size and morphology of the as-prepared $GdVO_4$ NPs were characterized.

5.2.1.1 Crystal Structure

The crystal structure of $GdVO_4$ NPs synthesized at various pH corresponds to a tetragonal system with zircon-type structure having a space group of $I4_1/amd$ (pdf: 00-017-0260). As shown in **Fig. 5-16**, no second phases were observed in the diffraction patterns suggesting that gadolinium hydroxide and polyvanadate species were not precipitated under the synthesis conditions and pH range used throughout the experiments. The Bragg reflections become broader with a decrease in the pH indicating a reduction of the crystallite size (**Table 5-11**). The crystallite size was almost three times larger for $GdVO_4$ NPs when the pH was adjusted from 12 to 8, 23.4 nm versus 8.3 nm, respectively. It is assumed that a decrease of the pH may contribute to a slower formation and

precipitation of NPs because of the simultaneous and competing process where orthovanadate groups change into polyvanadate species.

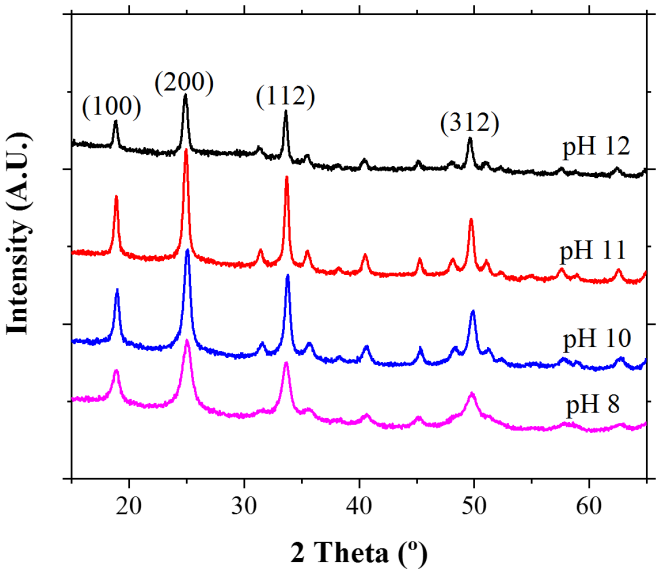

Fig. 5-16 Diffraction patterns of $GdVO_4$ NPs synthesized using 0.1 M $GdCl_3$ and 0.1 M Na_3VO_4, a flow rate ~1 mL min^{-1}, while adjusting the pH at different values.

Table 5-11 Crystallite size of $GdVO_4$ NPs synthesized using 0.1 M $GdCl_3$ and 0.1 M Na_3VO_4, a flow rate ~1 mL min^{-1}, while adjusting the pH at different values.

pH	Crystallite size (nm)
12	23.2
11	17.2
10	13
8	8.4

In **Fig. 5-17**, $GdVO_4$ NPs synthesized using both $GdCl_3$ and Na_3VO_4 at concentrations from 0.01 M to 0.2 M in a 1:1 volume ratio have diffraction patterns that match with a tetragonal structure with space group of $I4_1/amd$ of pure $GdVO_4$ (pdf: 00-017-0260). The crystallite size of $GdVO_4$ NPs synthesized using both $GdCl_3$ and Na_3VO_4 at either 0.01 M or 0.05 M is ~44 nm, while for higher concentrations (≥0.1 M) the crystallite size is almost half this magnitude (**Table**

5-12). The difference in crystallite size may be associated to the concentration of Gd^{3+} and $[VO_4]^{3-}$ species available for nuclei formation. At lower $GdCl_3$ and Na_3VO_4 concentrations, either 0.01 M or 0.05 M, the fraction of stable nuclei formed after mixing both chemicals may be lower with respect to high reagents concentrations. Therefore, a lower fraction of stable nuclei will promote the formation and growth of large particles. Another hypothesis is related to the precipitation of $Gd(OH)_3$, which interaction with Na_3VO_4 is slow causing the formation of few particles of large size [126]. Particularly, at lower reagents concentration (<0.1 M), the pH of the solution remained ~12.5 for a significant fraction of time, which may have prompted the precipitation of gadolinium hydroxide species.

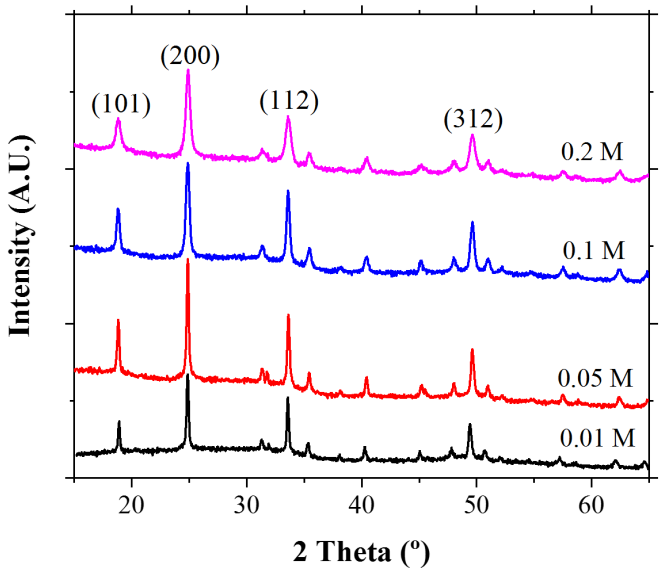

Fig. 5-17 Diffraction patterns of $GdVO_4$ NPs synthesized using different $GdCl_3$ and Na_3VO_4 concentrations, a flow rate ~1 mL min^{-1}, and keeping the pH ~12.

Table 5-12 Crystallite size of $GdVO_4$ NPs synthesized using different $GdCl_3$ and Na_3VO_4 concentrations, a flow rate ~1 mL min^{-1}, and keeping the pH ~12.

Reagents concentration (mol/L)	Crystallite size (nm)
0.01	43.0
0.05	44.5
0.1	23.2
0.2	18.9

5.2.1.2 Morphology and Particle Size Distribution

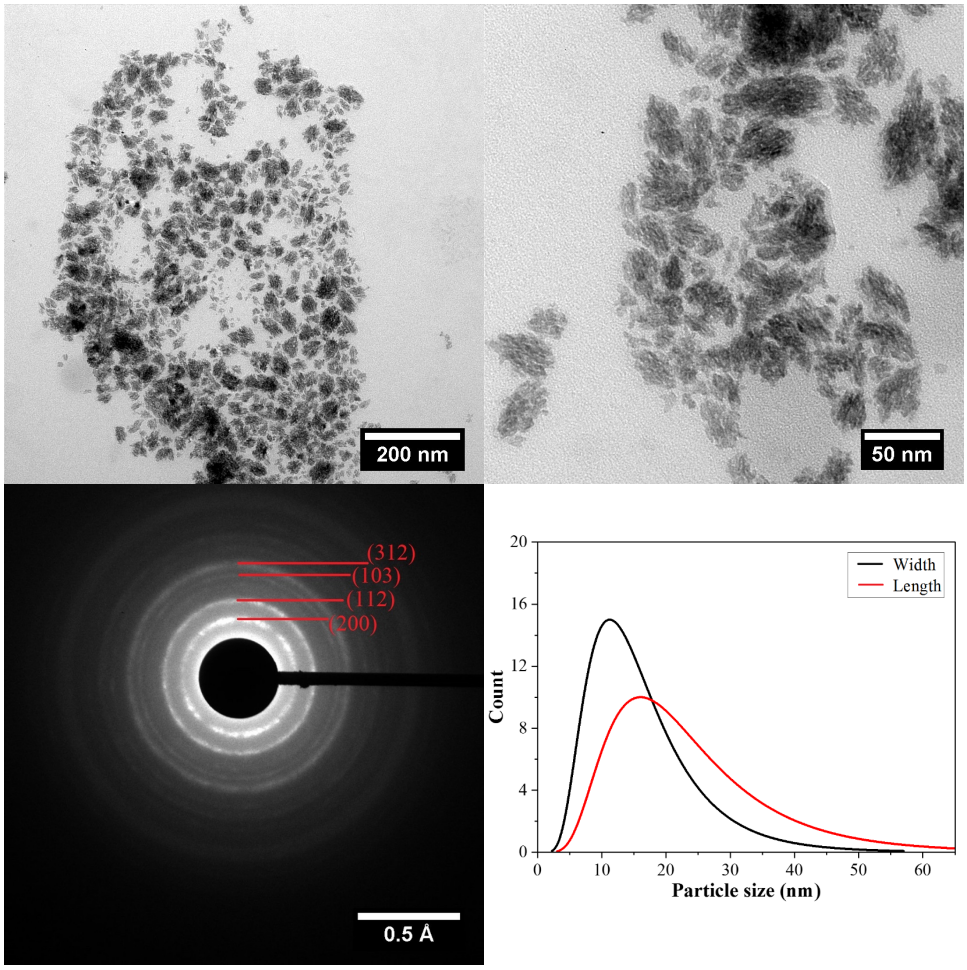

Fig. 5-18 TEM micrographs, SAED pattern, and particle size distribution of $GdVO_4$ NPs synthesized using 0.1 M $GdCl_3$ and 0.1 M Na_3VO_4, a flow rate ~1 mL min^{-1}, while adjusting the pH at 8.

TEM micrographs, selected area electron diffraction (SAED) patterns, and particle size distributions of $GdVO_4$ NPs prepared at a pH of 8, 10, 11, and 12 are shown in **Fig. 5-18**, **Fig. 5-19**, **Fig. 5-20**, and **Fig. 5-21**, respectively. The particle size distribution of each sample is represented by two characteristic dimensions, width and length, with mean sizes and distributions reported in **Table 5-13**. Anisotropic $GdVO_4$ NPs of various sizes were observed after keeping the pH ~8 (**Fig. 5-18**).

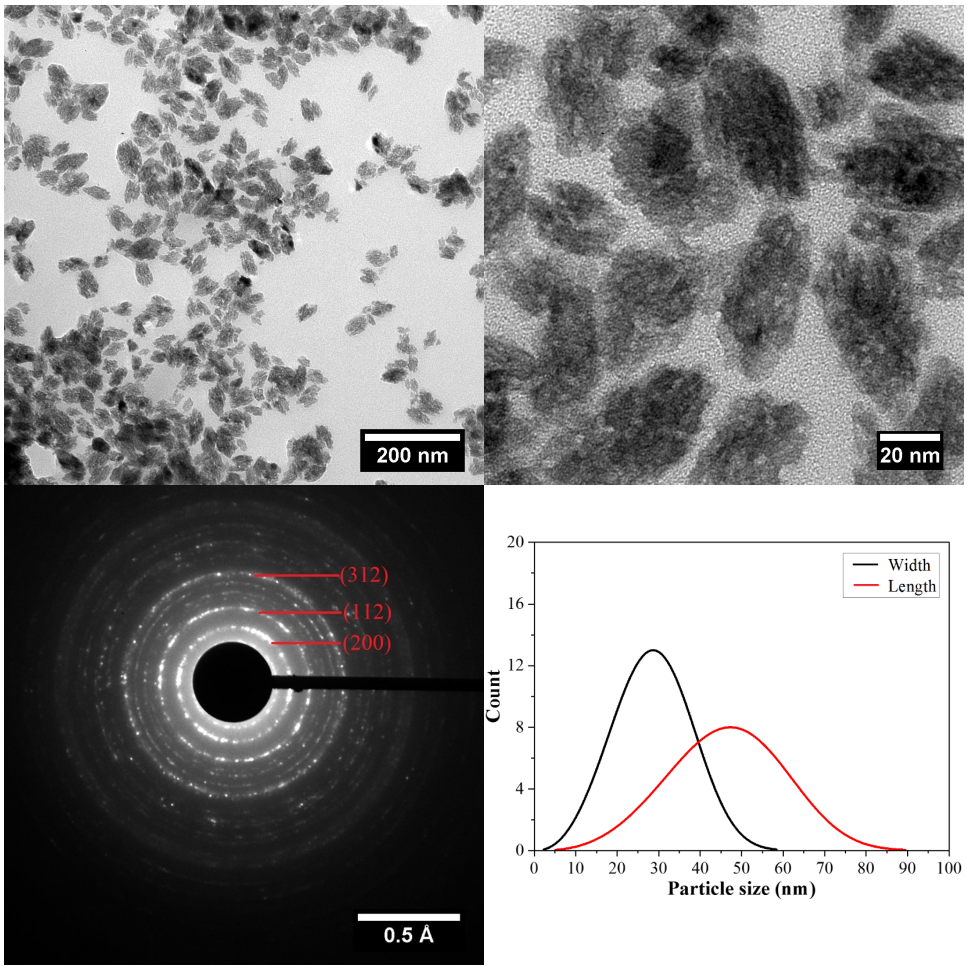

Fig. 5-19 TEM micrographs, SAED pattern, and particle size distribution of $GdVO_4$ NPs synthesized using 0.1 M $GdCl_3$ and 0.1 M Na_3VO_4, a flow rate ~1 mL min^{-1}, while adjusting the pH at 10.

In **Fig. 5-18**, it is observed a contrast change through the particles that could be associated to either aggregation of small crystallites, defects on the NPs surface, or porosity. The assumption that the contrast change is related to aggregation of crystallites is consistent with the difference between the crystallite (**Table 5-11**) and particle size (**Table 5-13**). Keeping the pH ~10 resulted in NPs with ellipsoidal shape in which the contrast change through the particle was observed (**Fig. 5-19**). As discussed above, small crystallites could aggregate resulting in larger particles based on the difference between the crystallite size (**Table 5-11**) and the mean particle size (**Table 5-13**).

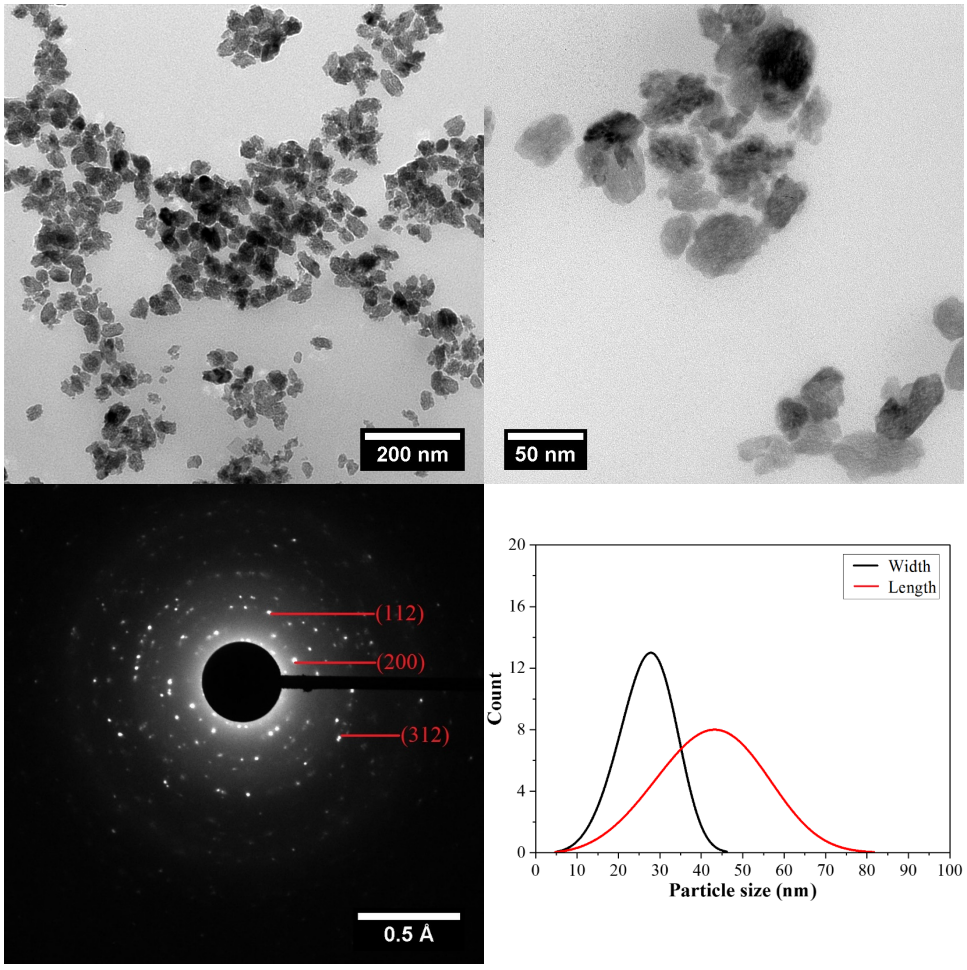

Fig. 5-20 TEM micrographs, SAED pattern, and particle size distribution of $GdVO_4$ NPs synthesized using 0.1 M $GdCl_3$ and 0.1 M Na_3VO_4, a flow rate ~1 mL min^{-1}, while adjusting the pH at 11.

Increasing the pH to ~11 caused the formation of $GdVO_4$ NPs with ellipsoidal and trapezoidal shape (**Fig. 5-20**). The contrast difference within each NP was not as noticeable as observed for $GdVO_4$ NPs synthesized at pH of 8 and 10, which may be related to the larger crystallite size obtained at a pH of 11 (**Table 5-11**). However, polycrystalline particles are expected based on the disparity between the crystallite size and the measured width and length, having mean values of 26.8 ± 6.7 nm and 42.4 ± 12.9 nm, respectively.

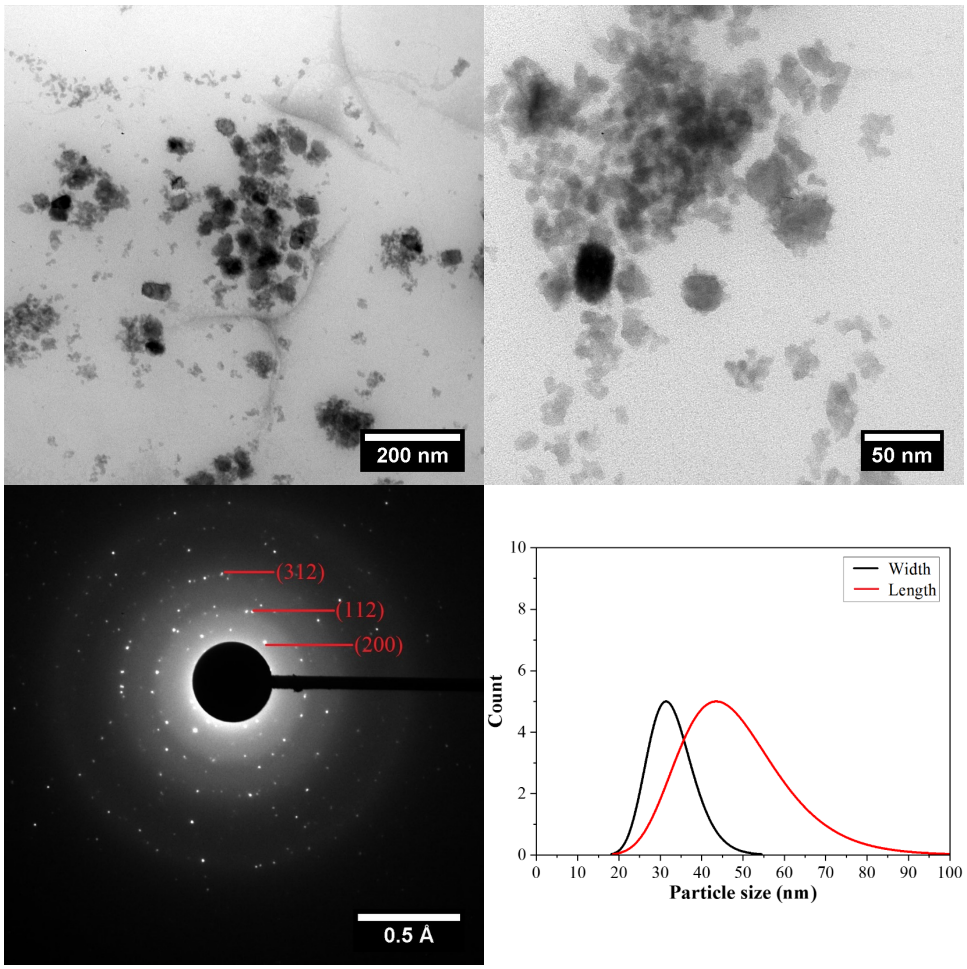

Fig. 5-21 TEM micrographs, SAED pattern, and particle size distribution of $GdVO_4$ NPs synthesized using 0.1 M $GdCl_3$ and 0.1 M Na_3VO_4, a flow rate ~1 mL min^{-1}, while adjusting the pH at 12.

Lastly, two distinct features were observed for $GdVO_4$ NPs synthesized at a pH ~12, the presence of large ellipsoidal and trapezoidal particles and aggregates of small crystallites (**Fig. 5-21**). The formation of large particles is consistent with the magnitude of the crystallite size (**Table 5-11**). The homogeneous contrast observed within each particle may imply the formation of single crystals or a reduction of surface defects. The formation of aggregates and dispersion of small particles could be caused by the rapid precipitation of $Gd(OH)_3$ which interacts slowly with $[VO_4]$ anions due to the high pH used during synthesis (**Fig. 5-21**). This hypothesis is consistent with the diffraction results, where the intensity of the Bragg reflections of $GdVO_4$ NPs synthesized at a pH of 12 was lower to that of samples prepared at a pH of 10 and 11 (**Fig. 5-16**). The lower intensity may be related to a low fraction of crystalline $GdVO_4$ NPs. The SAED patterns of all $GdVO_4$ matched with the Bragg reflections of a tetragonal crystal structure. A decrease in the pH caused the appearance of rings rather than brighter dots because of the precipitation of polycrystalline $GdVO_4$ NPs with small crystallite size (**Table 5-11**). In summary, polycrystalline particles with anisotropic morphology, which may have a significant concentration of defects or porosity, were obtained after decreasing the pH towards acidic conditions during synthesis. The presence of surface defects may affect the retention of radionuclides and the response as contrast agents. The pH of the solution should not be kept above 12 since a larger fraction small crystallites and aggregates of lanthanide hydroxide species may be precipitated.

Table 5-13 Mean particle size, standard deviation, and distribution of $GdVO_4$ NPs synthesized synthesized using 0.1 M $GdCl_3$ and 0.1 M Na_3VO_4, a flow rate ~1 mL min^{-1}, while adjusting the pH at different values.

pH	Length (nm)	Width (nm)	Distributions (length, width)

12	48.2 ± 12.7	32.7 ± 5.7	Lognormal, lognormal
11	42.4 ± 12.9	26.8 ± 6.7	Weibull, normal
10	46.4 ± 14.2	28.7 ± 8.7	Weibull, lognormal
8	23.2 ± 11.2	16.1 ± 7.2	Lognormal, lognormal

TEM micrographs of $GdVO_4$ NPs synthesized using both $GdCl_3$ and Na_3VO_4 at 0.2 M, 0.1 M, 0.05 M, and 0.01 M are shown in **Fig. 5-22**, **Fig. 5-23**, **Fig. 5-24**, and **Fig. 5-25**, respectively. $GdVO_4$ NPs synthesized using both $GdCl_3$ and Na_3VO_4 at 0.1 M correspond to the reference conditions (section 3.3.2). At 0.1 M reagents concentration and a pH of 12, the TEM micrographs are characterized by large $GdVO_4$ NPs surrounded by aggregates of small crystallites (**Fig. 5-23**). Increasing the reagents concentration to 0.2 M caused the formation large aggregates corresponding to particles ~20 nm in size with trapezoidal shape (**Fig. 5-22**). Although the pH was kept at 12, the formation of aggregates of small crystallites was not observed. $GdVO_4$ NPs prepared using both $GdCl_3$ and Na_3VO_4 at 0.05 M are characterized by large particles accompanied by a low fraction of small crystallites at their surface (**Fig. 5-24**). The presence of these crystallites could be related to the irreversible precipitation of gadolinium hydroxide species or to the mechanism of formation of $GdVO_4$ NPs. The latter may involve the coarsening of small crystallites, which resulted in large $GdVO_4$ NPs. Similar results were obtained using both $GdCl_3$ and Na_3VO_4 at 0.01 M, however, a larger fraction of small crystallites with respect to higher reagents concentrations (0.05 or 0.1 M) was observed near the $GdVO_4$ NP surface (**Fig. 5-25**). As discussed previously, the lower concentration of reagents caused the formation of a smaller fraction of stable nuclei and hence the growth of large particles because of the rapid precipitation

of $Gd(OH)_3$. Overall, the as-prepared $GdVO_4$ NPs correspond to single crystals based on the similarity between their particle size and crystallite size (**Table 5-12**).

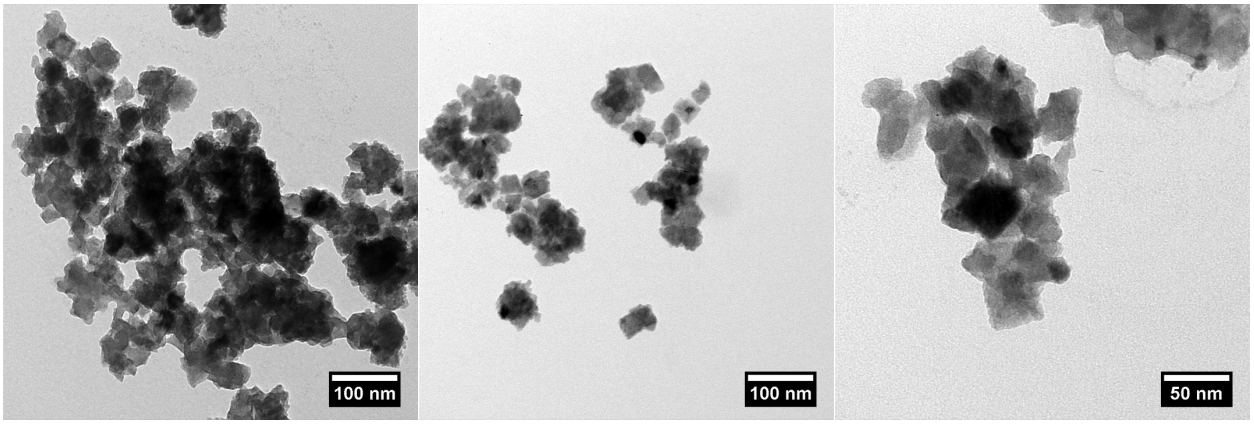

Fig. 5-22 TEM micrographs of $GdVO_4$ NPs synthesized using 0.2 M $GdCl_3$ and 0.2 M Na_3VO_4, a flow rate ~1 mL min^{-1}, while adjusting the pH at 12.

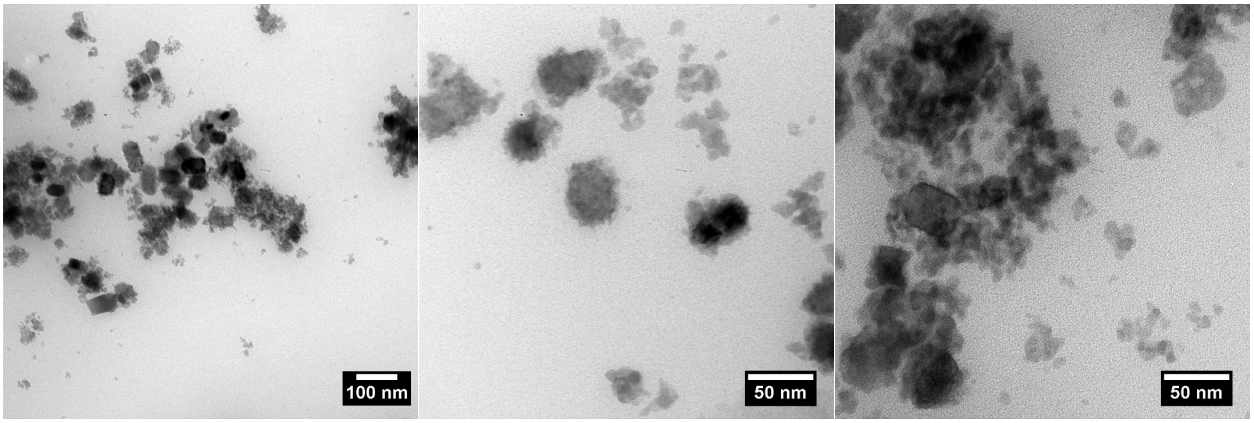

Fig. 5-23 TEM micrographs of $GdVO_4$ NPs synthesized using 0.1 M $GdCl_3$ and 0.1 M Na_3VO_4, a flow rate ~1 mL min^{-1}, while adjusting the pH at 12.

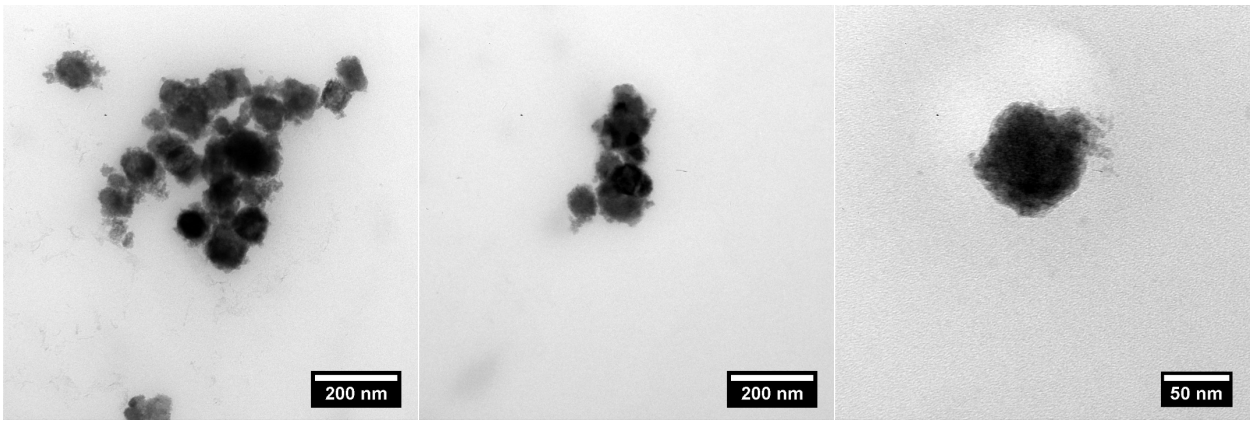

Fig. 5-24 TEM micrographs of $GdVO_4$ NPs synthesized using 0.05 M $GdCl_3$ and 0.05 M Na_3VO_4, a flow rate ~1 mL min^{-1}, while adjusting the pH at 12.

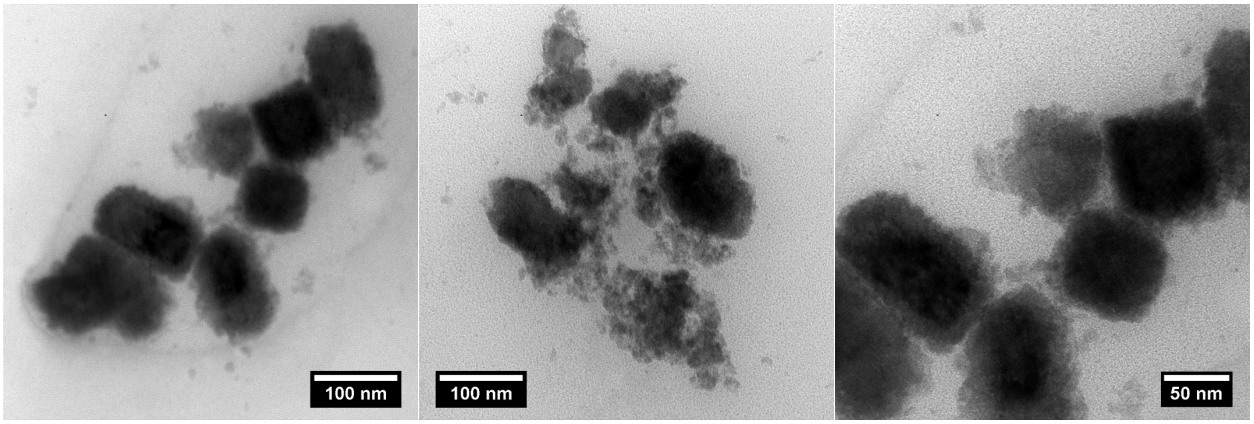

Fig. 5-25 TEM micrographs of $GdVO_4$ NPs synthesized using 0.01 M $GdCl_3$ and 0.01 M Na_3VO_4, a flow rate ~1 mL min^{-1}, while adjusting the pH at 12.

5.2.2 Synthesis of $LnVO_4$ (Ln^{3+} = La, Gd, Tb, Dy, and Ho) NPs

$LnVO_4$ (Ln^{3+} = La, Gd, Tb, Dy, and Ho) were synthesized by adding 0.1 M $LnCl_3$ into 0.1 M Na_3VO_4 at a flow rate ~1 mL min^{-1} while keeping the pH ~11. The crystal structure, morphology, and magnetic susceptibility of $LnVO_4$ NPs were characterized. The crystal structure was influenced by the tendency of each Ln^{3+} ion to crystallize in either monoclinic or tetragonal structure [173]. The particle shape seems to be related to the crystal structure of $LnVO_4$ NPs since

no significant difference was observed between $GdVO_4$, $TbVO_4$, $DyVO_4$, and $HoVO_4$. The magnetic susceptibilities were consistent with the magnetic moment of each Ln^{3+} ion.

5.2.2.1 Crystal Structure

The diffraction patterns of $LnVO_4$ NPs are shown in **Fig. 5-26**. A tetragonal system with a space group of $I4_1/amd$ was obtained for $GdVO_4$ (pdf: 00-017-0260), $TbVO_4$ (pdf: 01-072-0276), $DyVO_4$ (pdf: 01-072-0275), and $HoVO_4$ (pdf: 00-015-0764) NPs. A shifting of the Bragg reflections towards higher 2θ in tetragonal structures is caused by a decrease in the d-spacing and hence cell volume related to a reduction of the ionic radii of Ln^{3+} [174]. $LaVO_4$ NPs have a monoclinic structure with space group of $P2_1/n$ (pdf: 00-023-0324). The crystal structure of $LaVO_4$ NPs is consistent with that of bulk $LaVO_4$ [175].

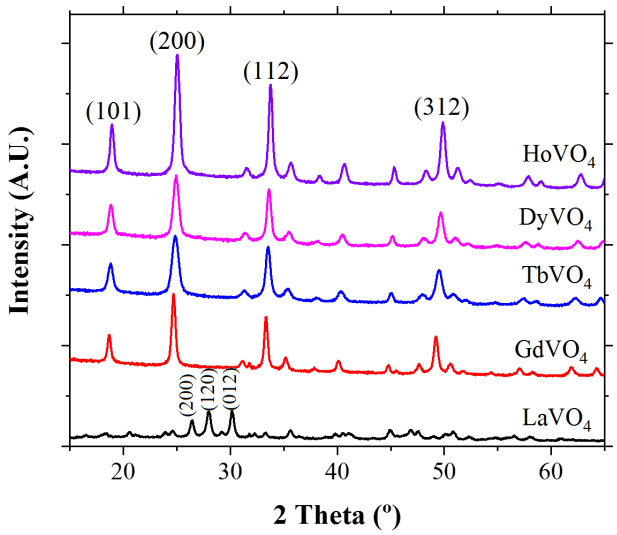

Fig. 5-26 Diffraction patterns of $LnVO_4$ NPs synthesized using 0.1 M $LnCl_3$ and 0.1 M Na_3VO_4, a flow rate ~1 mL min^{-1}, while adjusting the pH at 11.

The crystallite size of $LaVO_4$, $GdVO_4$, $TbVO_4$, $DyVO_4$, and $HoVO_4$ was 18.9 nm, 20.2 nm, 11.4 nm, 13.6 nm, and 15.7 nm, respectively. The increase in crystallite size with the decrease of the ionic radii of Ln^{3+} (Tb, Dy, and Ho) ions is consistent with the results presented in [176].

5.2.2.2 Morphology and Particle Size Distribution

TEM micrographs showed that $LaVO_4$ NPs corresponds to particles with anisotropic morphology (**Fig. 5-27**), whereas $GdVO_4$ (**Fig. 5-28**), $TbVO_4$ (**Fig. 5-29**), $DyVO_4$ (**Fig. 5-30**), and $HoVO_4$ (**Fig. 5-31**) NPs are characterized by particles with trapezoidal shape.

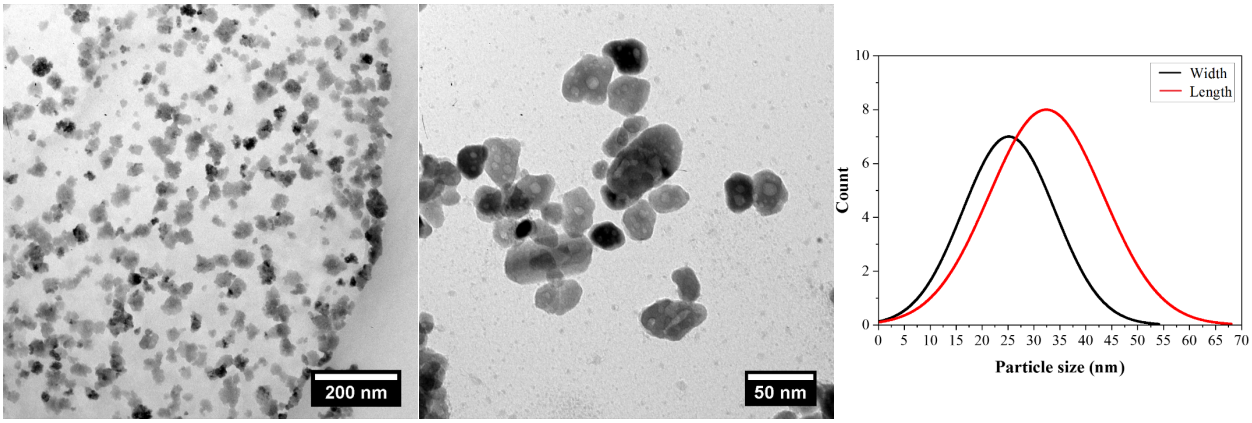

Fig. 5-27 TEM micrographs and particle size distribution of $LaVO_4$ NPs synthesized using 0.1 M $LaCl_3$ and 0.1 M Na_3VO_4, a flow rate ~1 mL min^{-1}, while adjusting the pH at 11.

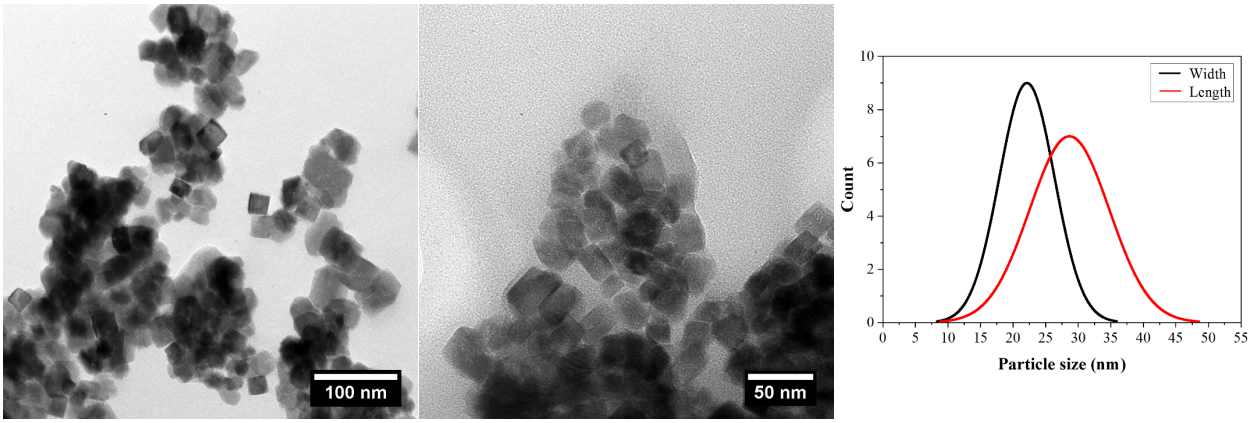

Fig. 5-28 TEM micrographs and particle size distribution of $GdVO_4$ NPs synthesized using 0.1 M $GdCl_3$ and 0.1 M Na_3VO_4, a flow rate ~1 mL min^{-1}, while adjusting the pH at 11.

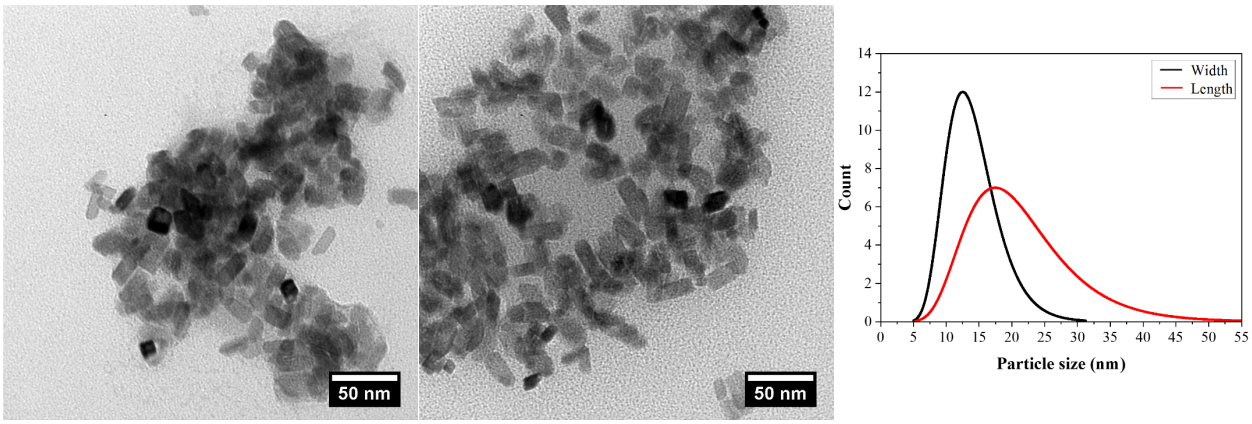

Fig. 5-29 TEM micrographs and particle size distribution of $TbVO_4$ NPs synthesized using 0.1 M $TbCl_3$ and 0.1 M Na_3VO_4, a flow rate ~1 mL min^{-1}, while adjusting the pH at 11.

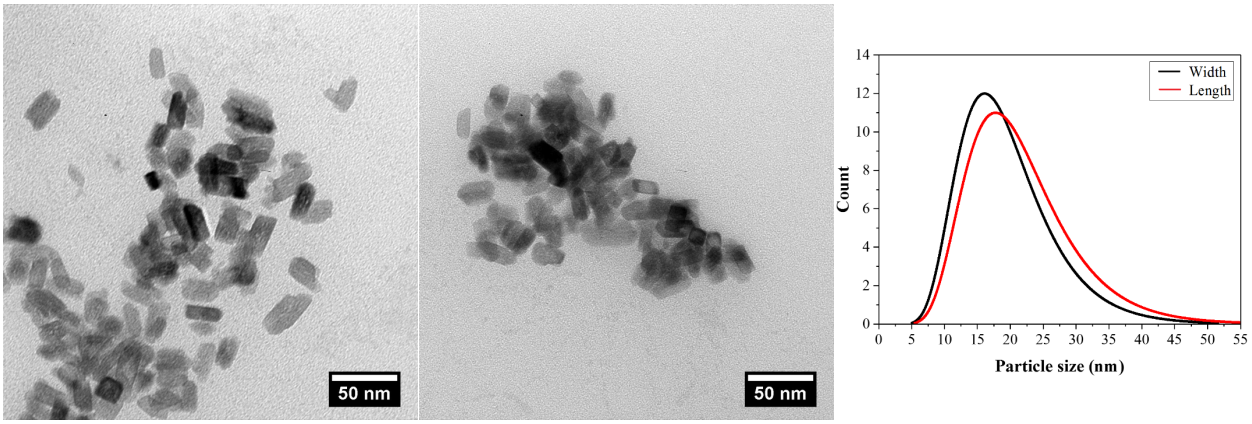

Fig. 5-30 TEM micrographs and particle size distribution of $DyVO_4$ NPs synthesized using 0.1 M $DyCl_3$ and 0.1 M Na_3VO_4, a flow rate ~1 mL min^{-1}, while adjusting the pH at 11.

This difference in morphology between $LaVO_4$ and the rest of the samples seems to be related to its crystal structure (monoclinic). The mean values for the width and length of all $LnVO_4$ NPs as well as their respective distributions are summarized in **Table 5-14**. It is assumed that the $LnVO_4$ NPs may correspond to polycrystalline particles based on the difference observed between the crystallite and particle size (**Table 5-14**).

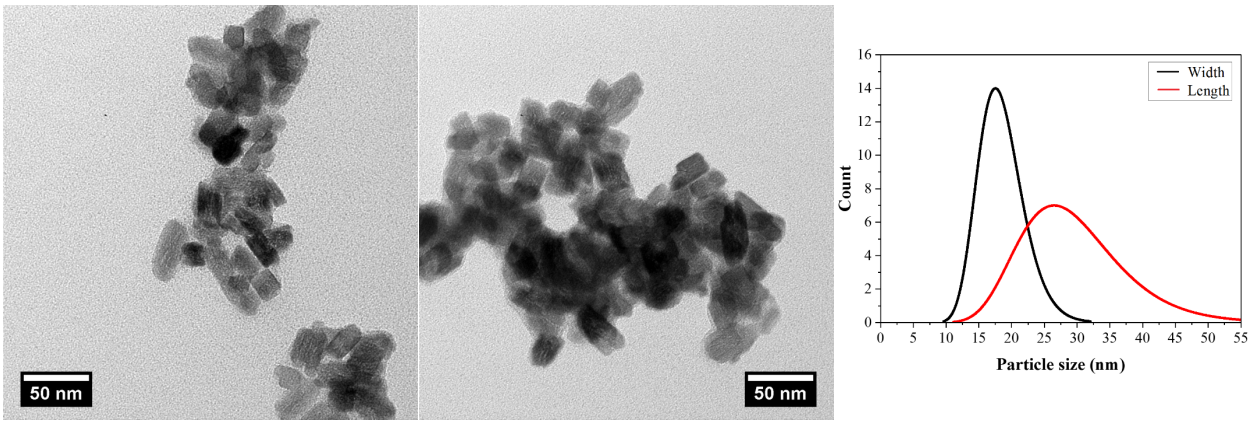

Fig. 5-31 TEM micrographs and particle size distribution of $HoVO_4$ NPs synthesized using 0.1 M $HoCl_3$ and 0.1 M Na_3VO_4, a flow rate ~1 mL min^{-1}, while adjusting the pH at 11.

Table 5-14 Mean particle size and standard deviation of $LnVO_4$ NPs synthesized using 0.1 M $LnCl_3$ and 0.1 M Na_3VO_4, a flow rate ~1 mL min^{-1}, while adjusting the pH at 11.

Sample	Length (nm)	Width (nm)	Distribution (length, width)
$LaVO_4$	32.4 ± 11.0	25.2 ± 8.9	Normal, normal
$GdVO_4$	28.7 ± 6.1	22.1 ± 4.2	
$TbVO_4$	21.3 ± 7.5	14.1 ± 4.8	Lognormal, lognormal
$DyVO_4$	21.5 ± 7.6	19.5 ± 7.7	
$HoVO_4$	29.4 ± 7.7	18.4 ± 3.3	

5.2.2.3 Magnetic Susceptibility

The mass magnetization versus magnetic field loops of $GdVO_4$, $TbVO_4$, $DyVO_4$, and $HoVO_4$ NPs (**Fig. 5-32**) are consistent with the Curie formula [equation$\chi = \frac{N\mu^2}{3k_BT}$ **4-1**] and the results presented in section 5.1.1.3. Despite the similar magnetic behavior between $LnVO_4$ NPs synthesized using the citrate and flow routes, $LnVO_4$ NPs prepared using flow have a higher magnetic susceptibility. The magnetic susceptibility of $GdVO_4$, $TbVO_4$, $DyVO_4$, and $HoVO_4$ NPs is 78.1, 133.3, 157.5, and 156.4 × 10^{-6} emu Oe^{-1} g^{-1}, respectively. These values correspond to a 13.5%, 18.8%, 25.4%, and 32.0% increase in magnitude with respect to the magnetic susceptibility

of $LnVO_4$ NPs prepared by the citrate route. This increase may be related to either a lower fraction of unreacted species which have a diamagnetic susceptibility, a higher yield of NPs, or to the fact that larger particles have a higher magnetization [165]. $TbVO_4$, $DyVO_4$, and $HoVO_4$ NPs may have potential application as negative-T_2 contrast agents since large particles have proven to have higher transversal relaxivities (r_2) to that of small particles [25], [165].

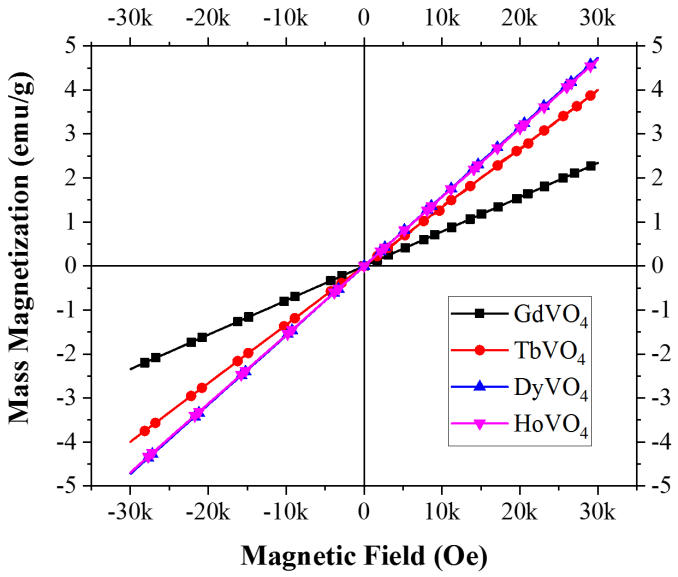

Fig. 5-32 Mass magnetization (emu/g) versus field (Oe) loop for $LnVO_4$ NPs synthesized using 0.1 M $LnCl_3$ and 0.1 M Na_3VO_4, a flow rate ~1 mL min^{-1}, while adjusting the pH at 11.

5.2.3 Synthesis of Dy-doped $LnVO_4$ (Ln^{3+} = La, Gd, and Lu) NPs

To assess the potential application of $LnVO_4$ NPs as FI contrast agents, $LaVO_4$, $GdVO_4$, and $LuVO_4$ NPs were doped with Dy^{3+} ions. The concentration of Dy^{3+} was set to 2 at.% to prevent concentration quenching. $LnVO_4$ NPs were prepared with 0.1 M $LnCl_3$ and 0.1 M Na_3VO_4 while keeping the pH of the solution at ~11. The influence of the crystal structure in the emission properties of Dy^{3+} was also studied by synthesizing $LnVO_4$ NPs with either monoclinic or

tetragonal structure. Differences in both excitation and emission spectra of $LnVO_4$ NPs are attributed to their crystal structure.

5.2.3.1 Crystal Structure

$GdVO_4$ and $LuVO_4$ NPs have a tetragonal system with a space group of $I4_1/amd$ (pdf: 00-017-0260 and 00-017-0260, respectively), while $LaVO_4$ NPs have a monoclinic structure with space group of $P2_1/n$ (pdf: 00-023-0324, $LaVO_4$) (**Fig. 5-33**). Doping $LnVO_4$ NPs with 2 at.% did not cause a shifting in the position of the Bragg reflections with respect to the reference patterns of pure $LnVO_4$. The crystallite size was 16.4 nm, 21.1 nm, and 21.1 nm for Dy-doped $LaVO_4$, $GdVO_4$, and $LuVO_4$ NPs, respectively.

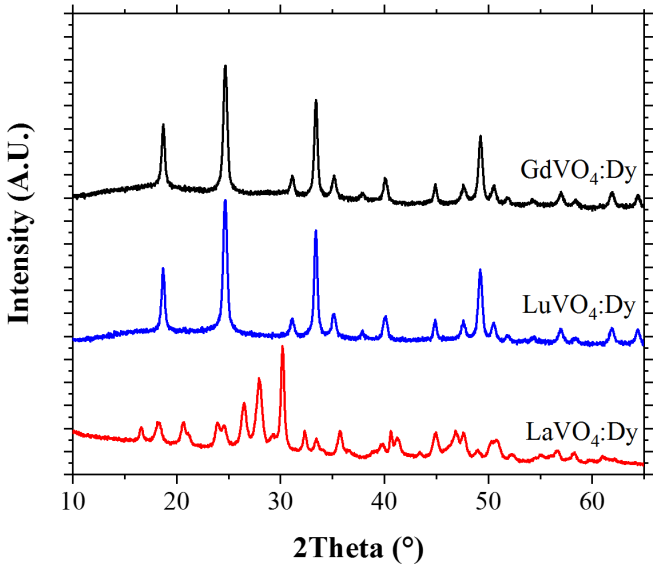

Fig. 5-33 Diffraction patterns of $LnVO_4$ NPs doped with 2 at.% Dy synthesized using 0.1 M $LnCl_3$ and 0.1 M Na_3VO_4, a flow rate ~1 mL min^{-1}, while adjusting the pH at 11.

5.2.3.2 Excitation and Emission Spectra

The excitation spectra of Dy-doped $LnVO_4$ NPs were recorded using an excitation filter at 250–395 nm, a PMT voltage of 600 V, and an emission wavelength of 574 nm. Although all spectra were recorded at the same concentration of $LnVO_4$ NPs (~0.5 mg/mL), the excitation

intensity of $LuVO_4$ NPs was higher to that of $LaVO_4$ and $GdVO_4$, respectively [**Fig. 5-34(a)**]. The difference in excitation intensity between $LnVO_4$ NPs may be related to a more efficient and favorable energy transfer between O^{2-} and V^{5+} ions [176]. The excitation spectrum is characterized by a broad band in the range of 220–340 nm which maxima is ~280 nm for $GdVO_4$ and $LuVO_4$, while for $LaVO_4$ the highest intensity is shifted to higher wavelengths (290–300 nm) [**Fig. 5-34(a)**]. The broad excitation band is related to (i) the O^{2-}-Dy^{3+} CT from the oxygen *2p* excited state to the *4f* state of dysprosium (~280 nm) and (ii) the O^{2-}-V^{5+} CT from the oxygen *2p* excited state to the empty *d* states of the central vanadium atom in the $[VO_4]^{3-}$ group (~310 nm) [177]. The wavelength at which the excitation band has its maxima may be influenced by the coordination number (CN) of V^{5+} and Ln^{3+} ions in tetragonal (CN = 8) and monoclinic (CN = 9) structures [14]. The emission spectra of Dy-doped $LnVO_4$ was recorded at excitation wavelengths of 280 nm, 310 nm, and 321 nm based on the differences observed in the excitation spectra, while using an emission filter at 295–1,100 nm and a PMT voltage of 600 V. Dy-doped $LnVO_4$ NPs exhibited blue (483 nm) and yellow (572 nm) emissions corresponding to $^4F_{9/2} \rightarrow {}^6H_{15/2}$ and $^4F_{9/2} \rightarrow {}^6H_{13/2}$ transitions, respectively [167], [177]–[179]. The intensity of the $^4F_{9/2} \rightarrow {}^6H_{15/2}$ and $^4F_{9/2} \rightarrow {}^6H_{13/2}$ transitions was higher for all $LnVO_4$ NPs when using an excitation wavelength of 280 nm (**Fig. 5-34**). Increasing the excitation wavelength to either 310 nm or 321 nm caused a reduction of the emission intensity for all the samples. The decrease in emission intensity was significant for Dy-doped $GdVO_4$ NPs [**Fig. 5-34(c)**], whereas for Dy-doped $LaVO_4$ [**Fig. 5-34(b)**] and $LuVO_4$ [**Fig. 5-34(d)**] the drop in intensity was lower due to their characteristic excitation spectrum [**Fig. 5-34(a)**]. Moreover, variation of the excitation wavelength influenced the intensity ratio of $^4F_{9/2} \rightarrow {}^6H_{13/2}$ to $^4F_{9/2} \rightarrow {}^6H_{15/2}$ transitions [**Fig. 5-35**]. The ratio between both transitions will determine the chromaticity of $LnVO_4$ NPs after excitation at various wavelengths [177]. At λ_{exc} = 280 nm, the emission of Dy-doped $LnVO_4$ NPs will be predominantly yellow, while increasing the

excitation wavelength may result in green emission because of the similar intensity between both transitions [**Fig. 5-35**].

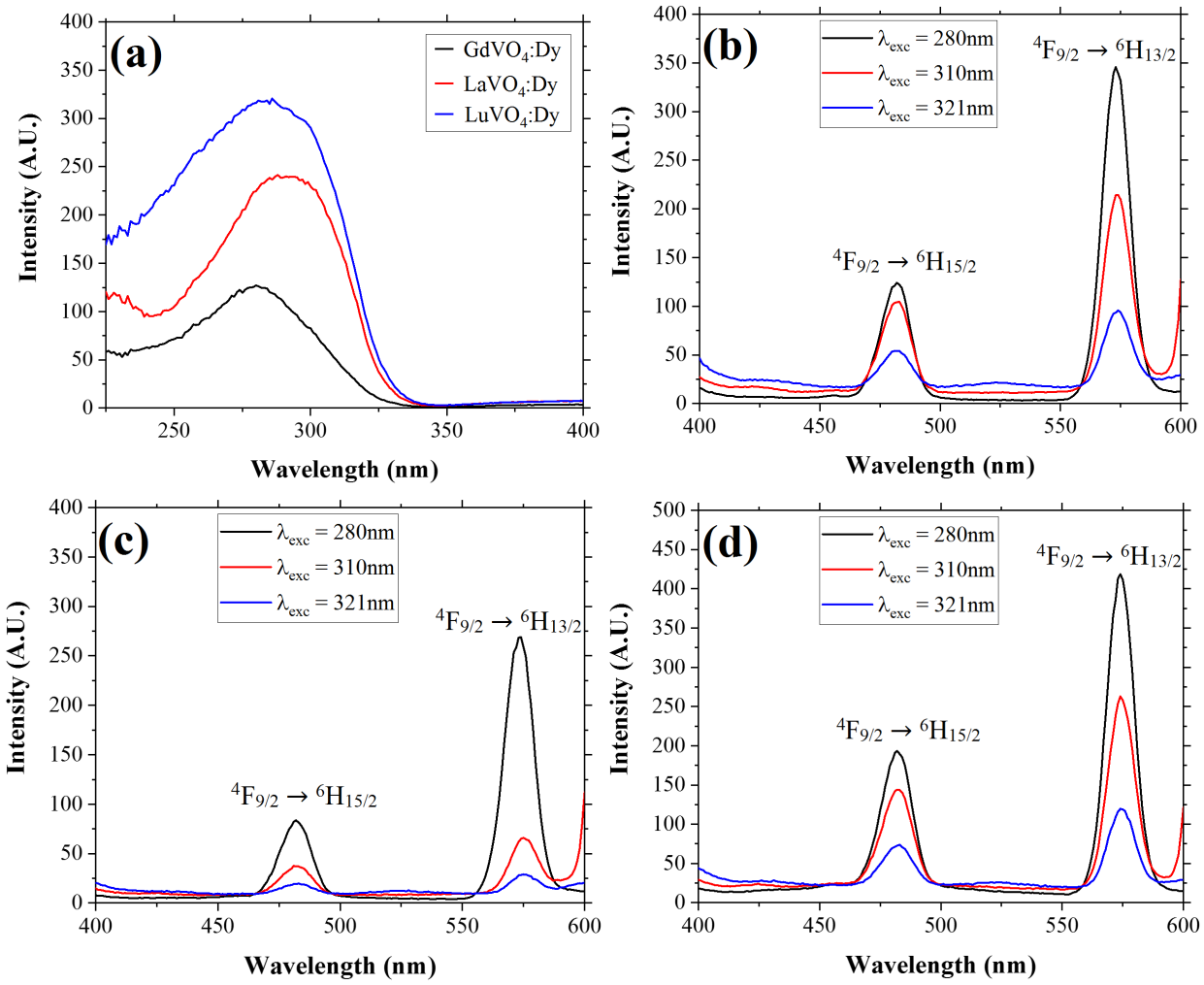

Fig. 5-34 $LnVO_4$ NPs doped with 2 at.% Dy (a) excitation spectra (λ_{em} = 574 nm) and emission spectra of (b) $LaVO_4$, (c) $GdVO_4$, and (d) $LuVO_4$ synthesized using 0.1 M $LnCl_3$ and 0.1 M Na_3VO_4, a flow rate ~1 mL min^{-1}, while adjusting the pH at 11.

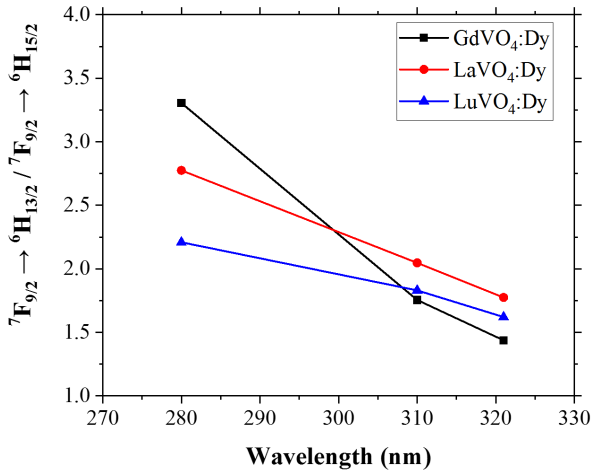

Fig. 5-35 Dependence of the $^4F_{9/2} \rightarrow {}^6H_{13/2}$ (blue) to $^4F_{9/2} \rightarrow {}^6H_{15/2}$ (yellow) ratio on the excitation wavelength of Dy-doped $LnVO_4$ NPs synthesized using 0.1 M $LnCl_3$ and 0.1 M Na_3VO_4, a flow rate ~1 mL min^{-1}, while adjusting the pH at 11.

5.3 Summary

In this chapter, $LnVO_4$ core and core-shell NPs were prepared by two synthesis routes in aqueous media that require only a fraction of the time need it for $LnPO_4$ NPs (30 minutes versus 3 hours). $LnVO_4$ NPs with characteristic morphology, stability, and surface chemistry can be obtained with each synthesis route. The short synthesis time required for each route and their simplicity could be exploited for radiochemical settings involving short-lived radionuclides. A procedure for the synthesis of $LnVO_4$ core-shell structures was proposed for the citrate route, while the deposition of shells was tested based on the increase in crystallite size and particle size distribution. Synthesis parameters such as temperature, heating time, reagents concentration, among others were varied and their influence on the particle size distribution, physical stability, luminescence and magnetic properties of $LnVO_4$ core-shell NPs was studied. The key outcomes from this chapter are summarized below:

Citrate route

- Heating time and temperature have a significant influence in the growth of $LnVO_4$ NPs based on the consumption of oligomeric species. Although short heating times resulted in $LnVO_4$ NPs formation, the NPs yield and physical stability are lower with respect to longer heating times (>10 minutes). A balance between heating time and temperature must be evaluated in each case based on the desired particle size distribution, NPs yield, and physical stability. Despite the fact that increasing the temperature to 90 °C resulted in higher NPs yield, the formation of aggregates could affect their application in biological settings. Considering the potential application of $LnVO_4$ NPs for biomedical applications, a moderate temperature (60 °C) and heating times ~30 minutes would give the optimum balance between NPs yield, particle size distribution, and physical stability.
- Synthesis of $LnVO_4$ core-shell NPs was confirmed by an increase in the crystallite size and particle size distribution. The reagents concentrations and concentration of oligomeric species solution added to the core NPs suspension can be adjusted to achieve the desired shell thickness. Although the development of $LnVO_4$ core-shell NPs is a multi-step synthesis procedure, it requires significantly less time (~1.5 hours for core + 2 shells) compared to that of $LnPO_4$ core + 2 shells NPs (~9 hours). The decrease in heating time could be exploited for the development of $LnVO_4$ core and core-shell NPs doped with short-lived radionuclides.
- Europium-doped $GdVO_4$ core NPs displayed more intense fluorescence or emission intensity upon excitation with UV light (λ = 254 nm) compared to that of $Gd_{(1-x)}Eu_xPO_4$ core NPs. This suggests that $LnVO_4$ NPs are suitable contrast agents for FI as well as MRI contrast agents. Additional advantages of $LnVO_4$ NPs involved their uniform size distribution and physical stability, which could be valuable for their application in biological settings.

Flow synthesis

- The formation of $LnVO_4$ NPs using flow synthesis is a single step and fast synthesis procedure that has potential for radiochemical settings toward the development of radionuclide carriers for TRT and nuclear waste forms.
- The morphology and crystallite size of $GdVO_4$ NPs is mainly affected by the pH and reagents concentration ($LnCl_3$ and Na_3VO_4). Particles with uniform shape can be obtained when the pH is kept between 10.5 and 11.5, whereas polycrystalline $GdVO_4$ NPs with either ellipsoidal or anisotropic shape were precipitated at lower pH.
- The morphology of $LnVO_4$ (Ln^{3+} = La, Gd, Tb, Dy, Ho) NPs seems to be related to their crystal structure, since tetragonal-like and anisotropic particles were obtained for tetragonal and monoclinic systems, respectively. $LnVO_4$ (Ln^{3+} = Tb, Dy, Ho) NPs may have application as negative-T_2 MRI contrast agents based on their high magnetic susceptibility and uniform particle size distribution.
- Luminescence properties of dysprosium-doped $LnVO_4$ (Ln^{3+} = La, Gd, Lu) NPs were influenced by the crystal structure and lanthanide ion used as a host. The chromaticity of dysprosium-doped $LnVO_4$, defined by the ratio of $^4F_{9/2} \rightarrow {}^6H_{13/2}$ to $^4F_{9/2} \rightarrow {}^6H_{15/2}$ transitions, was dependent on the host ion (Ln^{3+} = La, Gd, Lu) as well as the excitation wavelength used.

6 Radionuclide-doped $LnPO_4$ and $LnVO_4$ NPs

This chapter reviews the synthesis and characterization of radionuclide-doped lanthanide-based core and core-shell NPs. $LnPO_4$ NPs were doped with $^{85,\ 89}Sr$, ^{156}Eu, and ^{227}Th, whereas only *in vivo* α-generators ^{223}Ra, ^{225}Ac, and ^{227}Th were used for $LnVO_4$ NPs. The synthesis conditions such as temperature, heating time, and reagents concentration were chosen based on the results obtained for nonradioactive $LnPO_4$ and $LnVO_4$ NPs in Chapters 4 and 5, respectively. Additional details regarding the synthesis conditions used and complementary characterization of nonradioactive NPs are also presented in this chapter. Focus has been placed on assessing the *in vitro* retention of radionuclides in both $LnPO_4$ and $LnVO_4$ NPs as described in section 3.4.7. The partial retention of radionuclides within both $LnPO_4$ and $LnVO_4$ core-shell NPs has proven to be suitable for biomedical and engineering applications.

6.1 Retention of $^{85,\ 89}Sr$, and ^{156}Eu

In this section, $LnPO_4$ core NPs doped with either ^{156}Eu or a cocktail of $^{85,\ 89}Sr$ and ^{156}Eu are proposed as platforms where the luminescence and magnetic properties of Ln^{3+} ions are combined with radioisotopes. Although the high energy γ-rays emitted by ^{156}Eu (>1000 keV) restricts its use for biomedical applications [36], its successful incorporation and retention in $LnPO_4$ NPs evidences the potential implementation of lanthanide radioisotopes with lower energy γ-rays such as ^{141}Ce, ^{153}Gd, ^{177}Lu, and ^{166}Ho, among others, for diagnostic and therapeutic applications [180], [181]. The ability to host other radionuclides used for medical applications within the $LnPO_4$ crystal structure was evidenced by the partial retention of strontium radionuclides ($^{85,\ 89}Sr$), which

are used for the detection and treatment of bone diseases [182], [183]. The results presented in this section add to the current trend where $LnPO_4$ nanomaterials are contributing to the development of noninvasive techniques for the identification, visualization, and treatment of tumors by combining imaging and therapeutic functionalities within a single platform [50], [51].

6.1.1 $GdPO_4$ and $GdPO_4$:Ln^{3+} core NPs doped with ^{156}Eu

Synthesis of ^{156}Eu-doped $GdPO_4$, $Gd_{0.7}Eu_{0.3}PO_4$, and $Gd_{0.6}Ce_{0.3}Tb_{0.1}PO_4$ core NPs began by drying a 0.1 M HCl solution containing ~2 μCi of ^{156}Eu in a conical vial at 80 °C. Then, lanthanide chloride solutions were added and stirred for 20 minutes to ensure a complete dispersion of $^{156}Eu^{3+}$ ions. Sodium tripolyphosphate was added to the Ln solution under constant stirring in a 2:1 volume ratio to obtain a translucent solution (section 3.2). The final solution containing Ln^{3+}-$^{156}Eu^{3+}$-TPP complexes was heated to 90 °C for 3 hours to synthesize $Ln(^{156}Eu)PO_4$ core NPs. The turbid suspensions containing the ^{156}Eu-doped $LnPO_4$ core NPs were transferred into a dialysis membrane and dialyzed overnight in DI water. The first dialysate was changed after 20 hours and an aliquot was taken to quantify the activity associated with $^{156}Eu^{3+}$ ions that were not incorporated within the NPs. Afterward, aliquots from the dialysate were taken periodically (every 3−4 days) to assess the retention of ^{156}Eu over a 3-week period. The crystal structure, morphology, luminescence and magnetic properties of $Gd_{0.7}Eu_{0.3}PO_4$ and $Gd_{0.6}Ce_{0.3}Tb_{0.1}PO_4$ core NPs were presented in section 4.3. The particle size distribution and ζ-potential of as-prepared and dialyzed $LnPO_4$ core NPs were evaluated and the results are shown in section 6.1.1.1. In addition, the release of Gd^{3+} ions during dialysis was determined to estimate the potential *in vivo* toxicity of using bare $LnPO_4$ core NPs. The results presented in this section have been adapted from [140].

6.1.1.1 Particle Size Distribution, Physical Stability, and Release of Gd^{3+} ions

$GdPO_4$, $Gd_{0.6}Ce_{0.3}Tb_{0.1}PO_4$, and $Gd_{0.7}Eu_{0.3}PO_4$ core NPs suspensions were dialyzed against DI water for 48 hours to remove unreacted species. The particle size distribution and ζ-potential of as-prepared and dialyzed suspensions were compared to assess the physical stability of $LnPO_4$ NPs. $LnPO_4$ core NPs suspensions at a concentration of 0.033 M showed broad normalized intensity distributions, suggesting significant aggregation of NPs (**Fig. 6-1**). After dialysis, the particle size distribution and mean hydrodynamic size decrease for almost all the NPs suspensions with respect to the as-prepared suspensions (**Fig. 6-1**). The decrease in hydrodynamic size may be associated to the removal of unreacted species which cause aggregation of NPs.

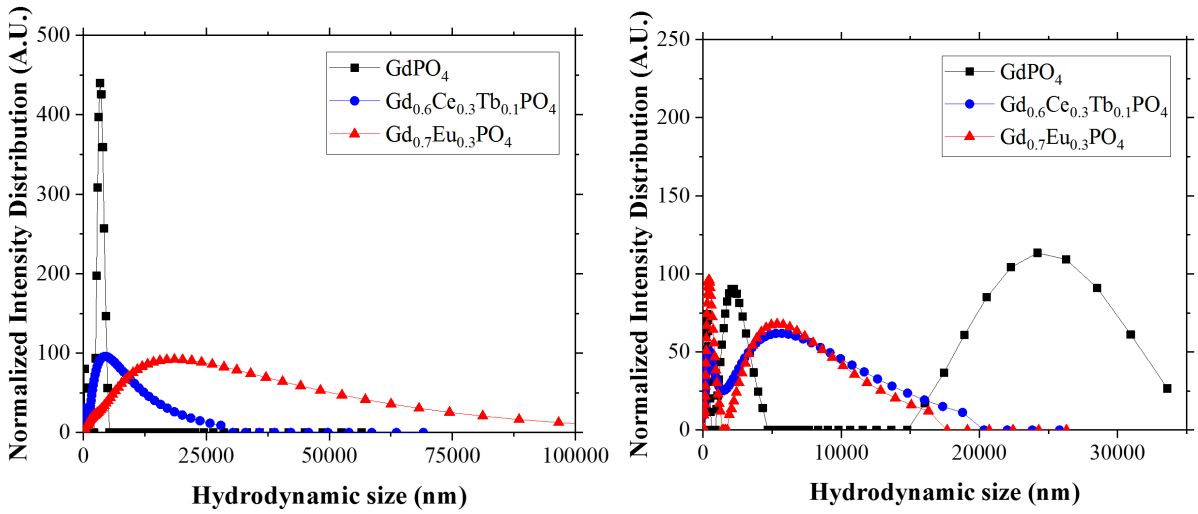

Fig. 6-1 Normalized intensity distribution of as prepared (left) and dialyzed (right) $LnPO_4$ (0.033 M) core NPs suspensions synthesized at 90 °C for 3 hours using a 1:2 Ln:Na-TPP volume ratio.

In **Fig. 6-2**, the mean hydrodynamic size of the dialyzed NPs suspensions is 1–2 orders of magnitude lower than that of the as-prepared suspensions based on the normalized number distributions. The number particle size distribution is consistent with the branched structures observed in the TEM micrographs with sizes between 20–100 nm (**Fig. 4-14** and **Fig. 4-15**).

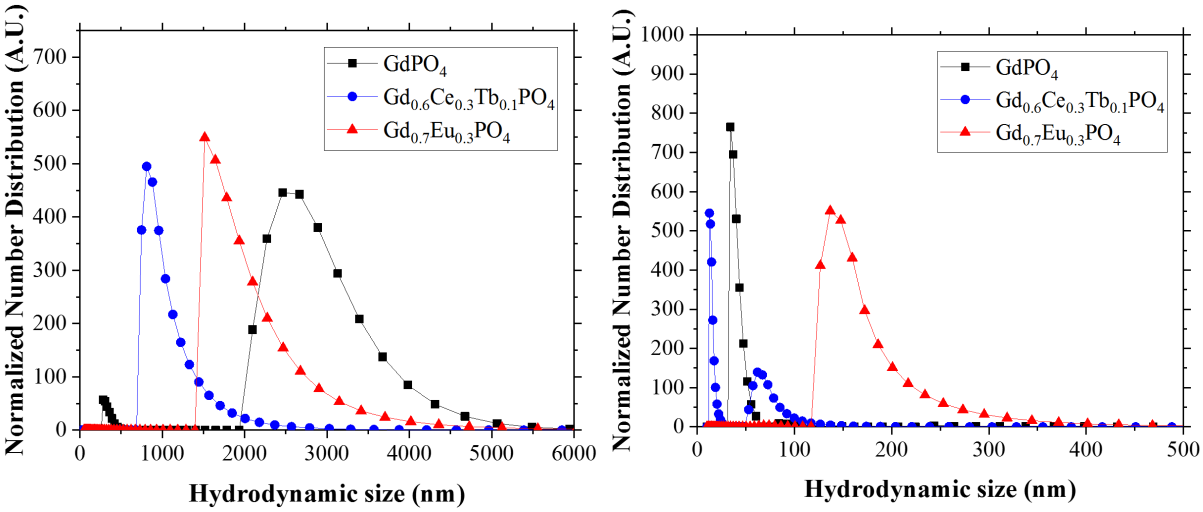

Fig. 6-2 Normalized number distribution of as prepared (left) and dialyzed (right) $LnPO_4$ (0.033 M) core NPs suspensions synthesized at 90 °C for 3 hours using a 1:2 Ln:Na-TPP volume ratio.

The as-prepared and dialyzed NPs suspensions were diluted to 1.33 mM to also assess their particle size at this condition. The dilution of both suspensions caused a significant decrease of the mean hydrodynamic size and particle size distribution as shown in **Fig. 6-3** and **Fig. 6-4**.

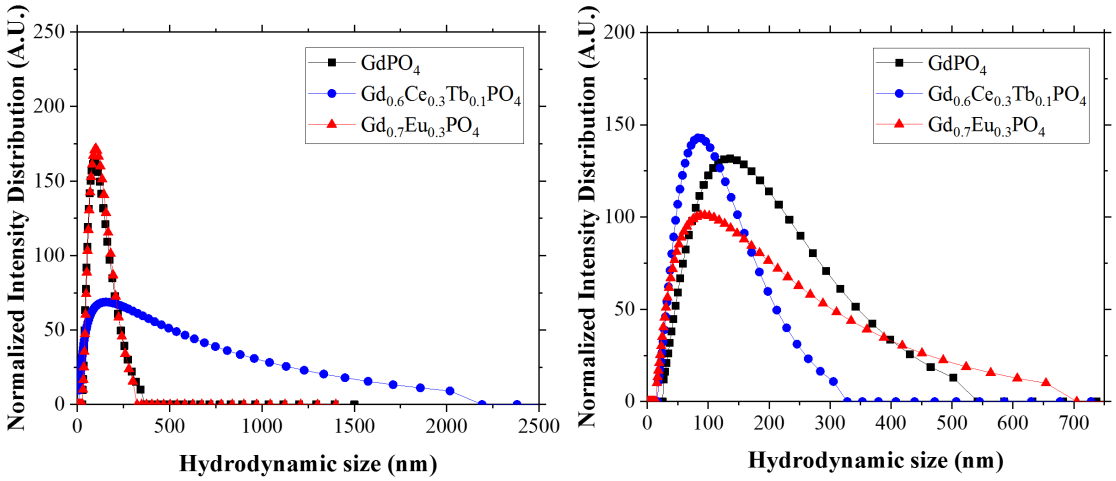

Fig. 6-3 Normalized intensity distribution of as prepared (left) and dialyzed (right) $LnPO_4$ (1.33 mM) core NPs suspensions synthesized at 90 °C for 3 hours using a 1:2 Ln:Na-TPP volume ratio.

The normalized intensity distribution shows that both as-prepared and dialyzed suspensions have a broad hydrodynamic size in the range of few tens to hundreds of nanometers

(**Fig. 6-3**), which may be related to the branched structures observed in the TEM micrographs. As shown in **Fig. 6-4**, there is no significant difference between the normalized number distributions of both suspensions suggesting that the branched structures formed during synthesis are not affected by dialysis.

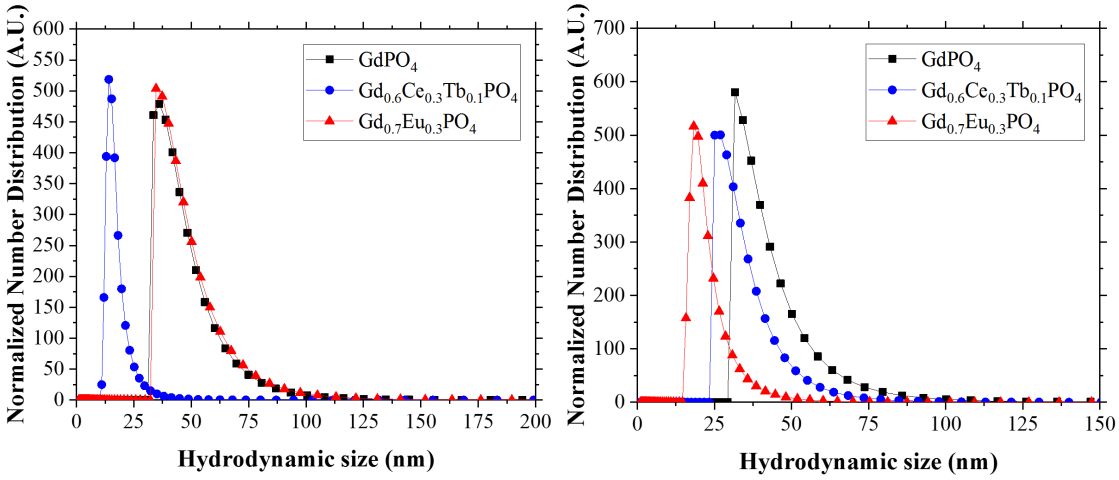

Fig. 6-4 Normalized number distribution of as prepared (left) and dialyzed (right) $LnPO_4$ (1.33 mM) core NPs suspensions synthesized at 90 °C for 3 hours using a 1:2 Ln:Na-TPP volume ratio.

Both as-prepared and dialyzed NPs suspensions had a negative ζ-potential (**Table 6-1**), which is attributed to the polymeric shell formed by polyphosphate species [125]. After dialysis, the absolute zeta potential of dialyzed $LnPO_4$ core NPs suspensions decreased relative to as-prepared suspensions (**Table 6-1**). The decrease of ~10 mV in the absolute zeta potential may be related to the removal of the polyphosphate species from the NP's surface.

Table 6-1 Mean ζ-potential and standard deviation of $LnPO_4$ (0.033 M) core NPs suspensions synthesized at 90 °C for 3 hours using a 1:2 Ln:Na-TPP volume ratio.

	Mean ζ-potential (mV)

	As prepared	Dialyzed
$GdPO_4$	-23.88 ± 1.92	-13.03 ± 0.08
$Gd_{0.6}Ce_{0.3}Tb_{0.1}PO_4$	-23.36 ± 1.57	-13.59 ± 0.27
$Gd_{0.7}Eu_{0.3}PO_4$	-28.52 ± 7.78	-18.50 ± 1.15

To assess the release of Gd cations over time, the as-prepared $GdPO_4$, $Gd_{0.6}Ce_{0.3}Tb_{0.1}PO_4$, and $Gd_{0.7}Eu_{0.3}PO_4$ core NPs suspensions were dialyzed for 4 days and a 10 mL aliquot was taken daily from each dialysate and analyzed for Gd using ICP-OES. As shown in **Fig. 6-5**, the maximum concentration of Gd cations in the dialysate is ~1.2 ppm, 1 ppm, and 0.1 ppm for $GdPO_4$, $Gd_{0.6}Ce_{0.3}Tb_{0.1}PO_4$, and $Gd_{0.7}Eu_{0.3}PO_4$ NPs, respectively. The presence of Gd cations in the dialysate may be related to the fraction of lanthanide ions that did not result in NPs formation but was retained within the polymeric shell formed around the NP's surface [125].

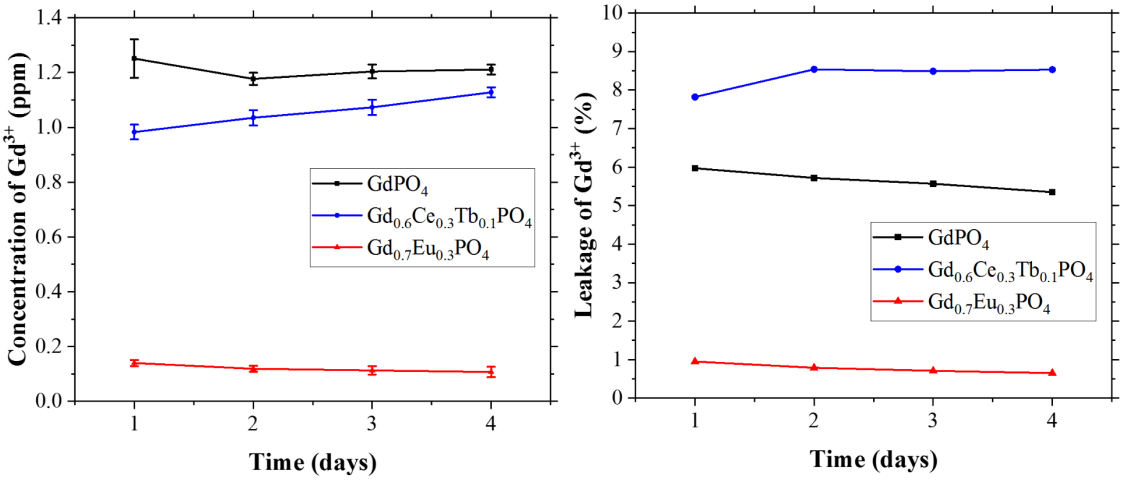

Fig. 6-5 Concentration (left) and leakage percentage (right) of Gd^{3+} in the dialysate over time from bare $LnPO_4$ core NPs synthesized at 90 °C for 3 hours using a 1:2 Ln:Na-TPP volume ratio.

The concentration of Gd cations measured in the dialysate is equivalent to a leakage of ~5.5 at.%, 8.5 at.%, and 0.9 at.% for $GdPO_4$, $Gd_{0.6}Ce_{0.3}Tb_{0.1}PO_4$, and $Gd_{0.7}Eu_{0.3}PO_4$ core NPs, respectively. As shown in **Fig. 6-5**, the leakage of Gd cations to the dialysate remains constant over time, which suggests that the NPs are chemically stable in DI water at the set conditions.

6.1.1.2 Radiochemical Yield and Retention of ^{156}Eu

The initial activity of the as-prepared Ln(^{156}Eu)PO_4 core NPs determined by γ-ray analysis was ~1.8, 2.4, and 2.2 μCi for $GdPO_4$, $Gd_{0.6}Ce_{0.3}Tb_{0.1}PO_4$, and $Gd_{0.7}Eu_{0.3}PO_4$, respectively. The activity lost in the vial, spin vane, and pipette tip used during the synthesis and transfer of the NPs suspensions into the dialysis membrane was <2% of the initial activity. After 20 hours in dialysis, an aliquot from the dialysate was taken to assess the percentage of activity associated to unreacted $^{156}Eu^{3+}$ ions. Unreacted species are expected to pass through the membrane and stay in the dialysate based on a concentration gradient. The fraction of activity measured in the dialysate was 5.2%, 5.6%, and 16.0% for $GdPO_4$, $Gd_{0.6}Ce_{0.3}Tb_{0.1}PO_4$, and $Gd_{0.7}Eu_{0.3}PO_4$, respectively. It is assumed that the activity found in the dialysate was due to $^{156}Eu^{3+}$ ions that were not incorporated within the NPs but adsorbed on their surface by polyphosphate species. However, in the case of $Gd_{0.7}Eu_{0.3}PO_4$ NPs the activity found in the 1st dialysate was about three times higher than that observed for the other two samples. In this case, it is hypothesized that a competing process between Eu^{3+} and $^{156}Eu^{3+}$ ions may contribute to a larger fraction of unreacted species from the latter, which resulted in a lower retention of $^{156}Eu^{3+}$ within $Gd_{0.7}Eu_{0.3}PO_4$ core NPs. A similar behavior was observed with $Lu_{0.5}Gd_{0.5}PO_4$ core NPs doped with ^{177}Lu, where an excess of $LuCl_3$ solution added during synthesis caused an activity loss of 21% after 24 hours [43]. The authors suggested that the increase in activity loss was due to surface bound ^{177}Lu and an exchange between stable and radioactive isotopes [43]. Nevertheless, subsequent aliquots were taken periodically and demonstrated the successful retention of ^{156}Eu in $GdPO_4$ over 3 weeks, where the activity measured was less than 0.2% of the initial activity. Similarly, $Gd_{0.6}Ce_{0.3}Tb_{0.1}PO_4$ NPs had a maximum leakage of 0.3% over the same period of time. The leakage of ^{156}Eu from both $GdPO_4$ and $Gd_{0.6}Ce_{0.3}Tb_{0.1}PO_4$ is comparable to that of ^{225}Ac from La(^{225}Ac)PO_4 and $La_{0.5}Gd_{0.5}$(^{225}Ac)PO_4 core NPs, ~0.1% and ~0.9%, respectively [42]. Instead, the maximum leakage observed for

$Gd_{0.7}Eu_{0.3}PO_4$ was ~3.5% the initial activity. The higher leakage observed for $Gd_{0.7}Eu_{0.3}PO_4$ with respect to $GdPO_4$ and $Gd_{0.6}Ce_{0.3}Tb_{0.1}PO_4$ may be related to the competing processes previously discussed and a higher fraction of surface bound ^{156}Eu cations that were not removed in the first or initial dialysate. The radiochemical yield of ^{156}Eu was 93.5%, 92.8%, and 79.6% for $GdPO_4$, $Gd_{0.6}Ce_{0.3}Tb_{0.1}PO_4$, and $Gd_{0.7}Eu_{0.3}PO_4$ core NPs, respectively. The reported yield considers the activity loss during synthesis and the initial dialysate as well as corrections for radioactive decay and volume change in dialysate due to the aliquots withdrawn. These results demonstrate the successful incorporation of $^{156}Eu^{3+}$ within the $LnPO_4$ crystal structure. Moreover, the values obtained for the radiochemical yields of $GdPO_4$ and $Gd_{0.6}Ce_{0.3}Tb_{0.1}PO_4$ are comparable to the yields reported for $LaPO_4$ core NPs doped with ^{223}Ra (~91%), ^{225}Ra (94%), and ^{225}Ac (95%) [38] as well as the yield of intrinsically radiolabeled cerium oxide NPs using ^{141}Ce (97%) [33]. Consequently, the synthesized $LnPO_4$ core NPs have the potential to retain radioactive lanthanide ions such as ^{141}Ce, ^{153}Gd, ^{177}Lu, ^{166}Ho, in addition to ^{225}Ac and ^{223}Ra, within their crystal structure.

6.1.2 $La_{(1-x)}Eu_xPO_4$ and $LnPO_4$ core NPs doped with $^{85,\ 89}Sr$ and ^{156}Eu

$La_{(1-x)}Eu_xPO_4$ and $LnPO_4$ (Ln^{3+} = La, Ce, Eu, Gd, Tb, Yb, and Lu) core NPs were doped with a cocktail of $^{85,\ 89}Sr$ and ^{156}Eu to assess the influence of lanthanide concentration in the retention of these radionuclides. The results presented in 6.1.1 implied that the retention of ^{156}Eu and hence other radionuclides may be dependent on the lanthanide concentration of $LnPO_4$ core NPs. A 0.1 M HCl solution containing ~0.188 µCi, 187.1 µCi, and 0.322 µCi of ^{85}Sr, ^{89}Sr, and ^{156}Eu, respectively, was dried in a conical glass vial at 80 °C for the synthesis of $La_{(1-x)}Eu_xPO_4$ core NPs, whereas for $LnPO_4$ core NPs ~0.197 µCi, 226.7 µCi, and 0.218 µCi of ^{85}Sr, ^{89}Sr, and ^{156}Eu were used. Lanthanide chloride solutions were added and stirred for 10 minutes to ensure a complete dispersion of radionuclides. Then, sodium tripolyphosphate was added to the lanthanide

solution in a 2:1 volume ratio under constant stirring to obtain a clear solution. Synthesis of $La_{(1-x)}Eu_xPO_4$ and $LnPO_4$ core NPs was carried out at 90 °C for 3 hours, after which the radionuclide-doped core NPs suspensions were transferred into a dialysis membrane and dialyzed against DI water for 5 days. The activity of ^{85}Sr and ^{156}Eu was quantified daily by measuring the whole radionuclide-doped $LnPO_4$ core NPs suspension inside the membrane. Additionally, a 5 mL dialysate aliquot was taken at the fourth and third day in dialysis for $La_{(1-x)}Eu_xPO_4$ and $LnPO_4$ core NPs, respectively. The crystal structure of $La_{(1-x)}Eu_xPO_4$ and $LnPO_4$ core NPs was characterized as a reference to compare the retention properties. It is expected that both $La_{(1-x)}Eu_xPO_4$ and $LnPO_4$ core NPs will have potential application as multifunctional platforms for molecular imaging based on the discussion presented in Chapter 4.

6.1.2.1 Crystal Structure

The diffraction patterns of $La_{(1-x)}Eu_xPO_4$ core NPs can be indexed as a hexagonal crystal system [**Fig. 6-6(a)**]. Narrow and intense Bragg reflections at ~32º and 45º suggest the presence of impurities, which in this case corresponds to sodium chloride that was precipitated because of the high Ln:Na-TPP volume ratio. A shifting of the Bragg reflections towards higher 2θ angles is consistent with a decrease of the d-spacing due to the difference in size between the ionic radius of La^{3+} (1.29 Å) and Eu^{3+} (1.21 Å) ions [141]. Higher Eu^{3+} concentrations caused an increase in crystallite size where the largest magnitude was obtained for $EuPO_4$ with 9.0 ± 2.0 nm, whereas $LaPO_4$ had the smallest with 4.1 ± 0.8 nm. In **Fig. 6-6(b)**, the diffraction patterns of $LaPO_4$, $CePO_4$, $GdPO_4$, and $TbPO_4$ core NPs matched with the crystal structure of hydrated $LnPO_4$ having a hexagonal crystal system and a space group $P3_121$ [184], [185]. The presence of NaCl is clearly observed for $LaPO_4$, $GdPO_4$, and $TbPO_4$ [**Fig. 6-6(b)**]. In **Fig. 6-6(b)**, the diffraction patterns of $YbPO_4$ and $LuPO_4$ core NPs are characterized by broad Bragg reflections indicating either the formation of small crystallites or the precipitation of poorly crystalline NPs [186]. It is assumed

that $YbPO_4$ and $LuPO_4$ core NPs may have a hexagonal crystal system based on the position of the Bragg reflections since the substantial peak broadening difficult the phase identification.

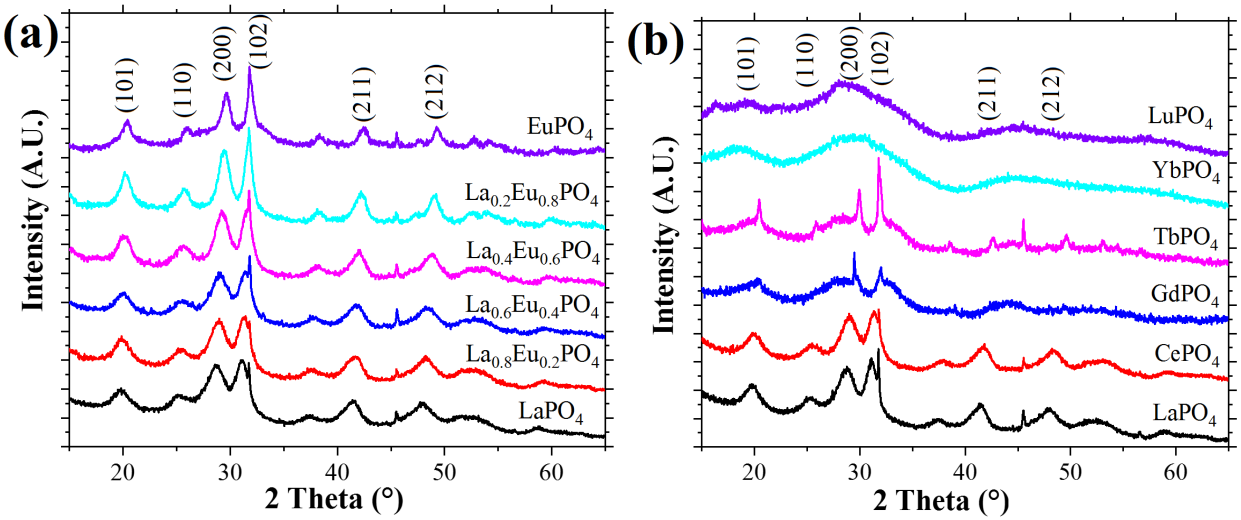

Fig. 6-6 Diffraction patterns of (a) $La_{(1-x)}Eu_xPO_4$ and (b) $LnPO_4$ core NPs synthesized at 90 °C for 3 hours using a 1:2 Ln:Na-TPP volume ratio.

6.1.2.2 Retention of $^{85,\ 89}Sr$, and ^{156}Eu

The leakage of ^{85}Sr and ^{156}Eu from $La_{(1-x)}Eu_xPO_4$ and $LnPO_4$ core NPs was determined by measuring the activity in (i) the whole radionuclide-doped core NPs suspension inside the membrane daily for a 5-day period and (ii) in a dialysate aliquot. Both approaches to quantify the leakage of radionuclides gave similar results. Although the leakage of ^{89}Sr was not explicitly reported, it is expected to follow the same behavior observed for ^{85}Sr. As shown in **Fig. 6-7**, the leakage of ^{85}Sr was relatively constant among $La_{(1-x)}Eu_xPO_4$ core NPs, where the fraction of ^{85}Sr in the dialysate was between 12.9 ± 1.3% and 18.1 ± 2.1% for $La_{0.4}Eu_{0.6}PO_4$ and $La_{0.6}Eu_{0.4}PO_4$, respectively. These results imply that the incorporation of ^{85}Sr and ^{89}Sr within $La_{(1-x)}Eu_xPO_4$ core NPs is not influenced significantly by the lanthanide concentration. The contrary effect was observed for ^{156}Eu where the leakage of either $La_{0.8}Eu_{0.2}PO_4$ or $La_{0.6}Eu_{0.4}PO_4$ was ~5 times larger than that of $EuPO_4$ (**Fig. 6-7**).

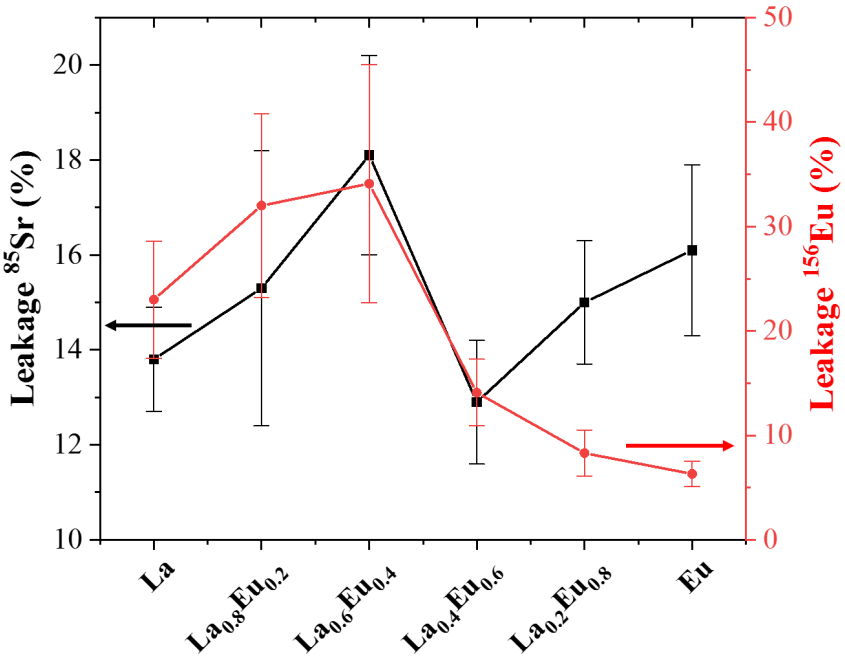

Fig. 6-7 Leakage of ^{85}Sr and ^{156}Eu from $La_{(1-x)}Eu_xPO_4$ core NPs synthesized at 90 °C for 3 hours using a 1:2 Ln:Na-TPP volume ratio.

The substantial difference in ^{156}Eu leakage among $La_{(1-x)}Eu_xPO_4$ core NPs supports the hypothesis that the lanthanide concentration influences the retention of lanthanide radionuclides. As discussed in section 6.1.1.2, the higher leakage observed for $Gd_{0.7}Eu_{0.3}PO_4$ core NPs to that of $GdPO_4$ and $Gd_{0.6}Ce_{0.3}Tb_{0.1}PO_4$ is assumed to be related to a competing process between Eu and ^{156}Eu cations. This hypothesis seems to be relevant only when the concentration of Eu^{3+} ions is lower (<50%) with respect to the remaining lanthanide ions. A continuous rise in ^{156}Eu leakage was observed when the concentration of Eu^{3+} ions increased from 0 at.% to 40 at.% in $La_{(1-x)}Eu_xPO_4$ core NPs, whereas at higher Eu^{3+} concentrations (>50%) there was a significant decrease in leakage (**Fig. 6-7**). Both Eu and ^{156}Eu are incorporated as substitutional atoms in the La^{3+} site in $LaPO_4$ causing a contraction in the unit cell as the Eu concentration increases [186]. It is assumed that $LaPO_4$ matrix will accommodate up to certain fraction of substitutional atoms before significant changes in the unit cell occur causing a higher leakage of ^{156}Eu. At higher Eu^{3+}

concentrations (>50%) in $La_{(1-x)}Eu_xPO_4$, ^{156}Eu can be easily accommodated in the $EuPO_4$ crystal structure and hence its leakage decreased.

The leakage of both ^{85}Sr and ^{156}Eu from pure $LnPO_4$ (Ln^{3+} = La, Ce, Eu, Gd, Tb, Yb, and Lu) core NPs is shown in **Fig. 6-8**. Almost all $LnPO_4$ core NPs had a similar leakage of ^{85}Sr (12.1–16.9%), except for $GdPO_4$ which had a 28.2 ± 2.3% (**Fig. 6-8**). Three distinctive behaviors regarding the leakage of ^{156}Eu were observed in $LnPO_4$ core NPs. The fraction of ^{156}Eu that leaked from $CePO_4$, $EuPO_4$, and $TbPO_4$ core NPs was below 7%. An increase to 23.2 ± 2.0% and 19 ± 4.1% was observed for $LaPO_4$ and $GdPO_4$ core NPs, while the ^{156}Eu leakage from $YbPO_4$ and $LuPO_4$ was greater than 40%. It is expected that the difference in ionic radii between ^{156}Eu, Yb^{3+}, and Lu^{3+} is the main cause behind the lower incorporation of radioactive ions in the crystal structure. The poor crystallinity of $YbPO_4$ and $LuPO_4$ core NPs could also increase the leakage of radionuclides [**Fig. 6-6(b)**]. The abrupt increase in leakage for both ^{85}Sr and ^{156}Eu between $EuPO_4$ and $TbPO_4$ could be attributed to the electronic peculiarities of Gd^{3+} ions commonly known as *gadolinium break* [187]. Although the leakage of ^{156}Eu from $La_{(1-x)}Eu_xPO_4$ and $LnPO_4$ core NPs was similar to the results presented in section 6.1.1.2, the high concentration of Sr cations (~15 mg/mL) in solution may have affected the retention of both ^{85}Sr and ^{156}Eu. High radionuclide purity is essential in radiochemical synthesis to increase the specific activity within each platform.

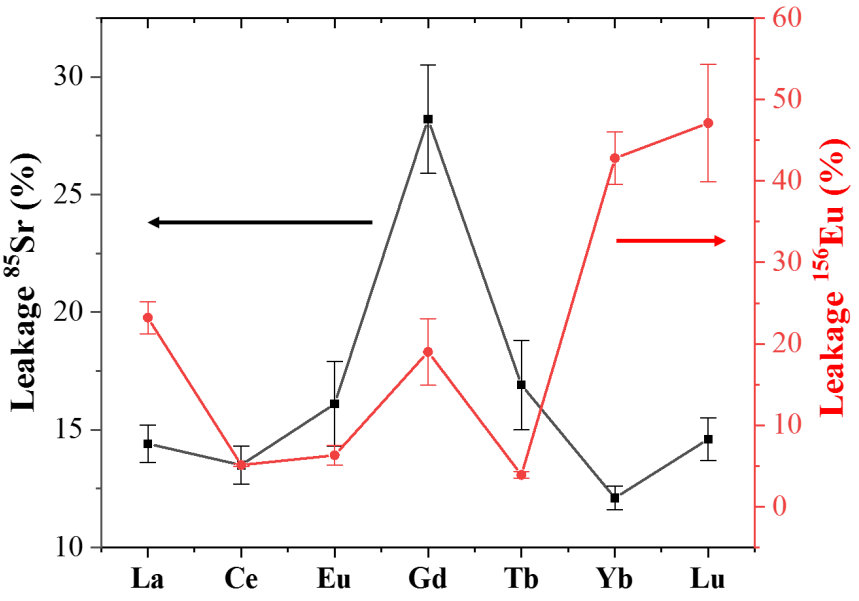

Fig. 6-8 Leakage of ^{85}Sr and ^{156}Eu from $LnPO_4$ core NPs synthesized at 90 °C for 3 hours using a 1:2 Ln:Na-TPP volume ratio.

6.2 Retention of *in vivo* α-generators ^{223}Ra, ^{225}Ac, and ^{227}Th

In this section, the retention of *in vivo* α-generators such as ^{223}Ra, ^{225}Ac, and ^{227}Th in $LnVO_4$ and $LnPO_4$ core and core-shell NPs is assessed. Adding to the proven retention capabilities of $LnPO_4$ NPs, $LaPO_4$ core and core + 2 shells NPs were tested as carriers of ^{227}Th. $GdVO_4$ and $Gd_{0.8}Eu_{0.2}VO_4$ core and core-shell NPs have been proposed as alternative carriers of ^{225}Ac, ^{223}Ra, ^{227}Th, and decay daughters, while providing multifunctional properties for multimodal molecular imaging. The results and characterization of nonradioactive NPs presented in Chapters 4 and 5 were used as a reference to develop radionuclide-doped $LnPO_4$ and $LnVO_4$ core-shell NPs, respectively. The *in vitro* retention of radionuclides was evaluated as described in section 3.4.7.

6.2.1 $GdVO_4$ and $Gd_{0.8}Eu_{0.2}VO_4$ core-shell NPs doped with ^{225}Ac

$GdVO_4$ and $Gd_{0.8}Eu_{0.2}VO_4$ core and core + 2 shells NPs were synthesized using the concentration of reagents, temperature, and heating time described in section 3.3.1. A 1:1.5 volume ratio between the core NPs suspension and the oligomeric species solution was used for core-shell synthesis (section 5.1.2). The proposed concentration of Gd and Eu cations is based on the results presented in section 5.1.3. $Gd(^{225}Ac)VO_4$ and $Gd_{0.8}Eu_{0.2}(^{225}Ac)VO_4$ core and core-shell NPs were synthesized by adding ^{225}Ac during core NPs synthesis. An aliquot containing ~50 μCi of ^{225}Ac diluted in 0.1 M HNO_3 was initially evaporated to dryness on a glass conical vial at 80 ºC. $GdCl_3$ and $EuCl_3$ were added at specific volume ratios into the vial and stirred for 5 minutes to ensure a homogeneous dispersion of ^{225}Ac cations and decay daughters. Sodium citrate and sodium orthovanadate were added under constant stirring at 0.75 volume equivalent to that of $LnCl_3$. The synthesis of core and the deposition of shells were completed as described for nonradioactive NPs (sections 3.3.1 and 5.1.2). Both $Gd(^{225}Ac)VO_4$ and $Gd_{0.8}Eu_{0.2}(^{225}Ac)VO_4$ core and core + 2 shells NPs suspensions were transferred into dialysis membranes and dialyzed against DI water to evaluate the radiochemical yield and *in vitro* retention of radionuclides over time. The crystal structure, morphology, and NPs yield were characterized for both $GdVO_4$ and $Gd_{0.8}Eu_{0.2}VO_4$ NPs. The potential application as contrast agents of $Gd_{0.8}Eu_{0.2}VO_4$ core and core-shell NPs was assessed based on their luminescence and magnetic properties, whereas $GdVO_4$ core NPs were evaluated as positive MRI contrast agents based on their longitudinal relaxivity (r_1). The results presented in this section been adapted from two manuscripts under review.

6.2.1.1 Crystal Structure

The diffraction patterns of $Gd_{0.8}Eu_{0.2}VO_4$ and $GdVO_4$ core and core-shell NPs are shown in **Fig. 6-9**. Both $Gd_{0.8}Eu_{0.2}VO_4$ and $GdVO_4$ core and core-shell NPs correspond to a zircon-type structure having a tetragonal system with space group $I4_1/amd$ of $GdVO_4$ (pdf: 00-017-0260). The

characteristic peak broadening caused by the nanometric size of the crystallites was observed for all diffraction patterns (**Fig. 6-9**). A slight decrease of the FWHM of the Bragg reflections was observed upon deposition of shells suggesting an increase of the crystallite size as described in section 0. The peak located at 25°, which corresponds to the (200) plane in the tetragonal structure, was used to calculate the crystallite size of $Gd_{0.8}Eu_{0.2}VO_4$ and $GdVO_4$ core and core-shell NPs (**Table 6-2**). As expected, the deposition of two shells resulted in an increase of the crystallite size of 0.9 nm and 0.7 nm for $Gd_{0.8}Eu_{0.2}VO_4$ and $GdVO_4$, respectively.

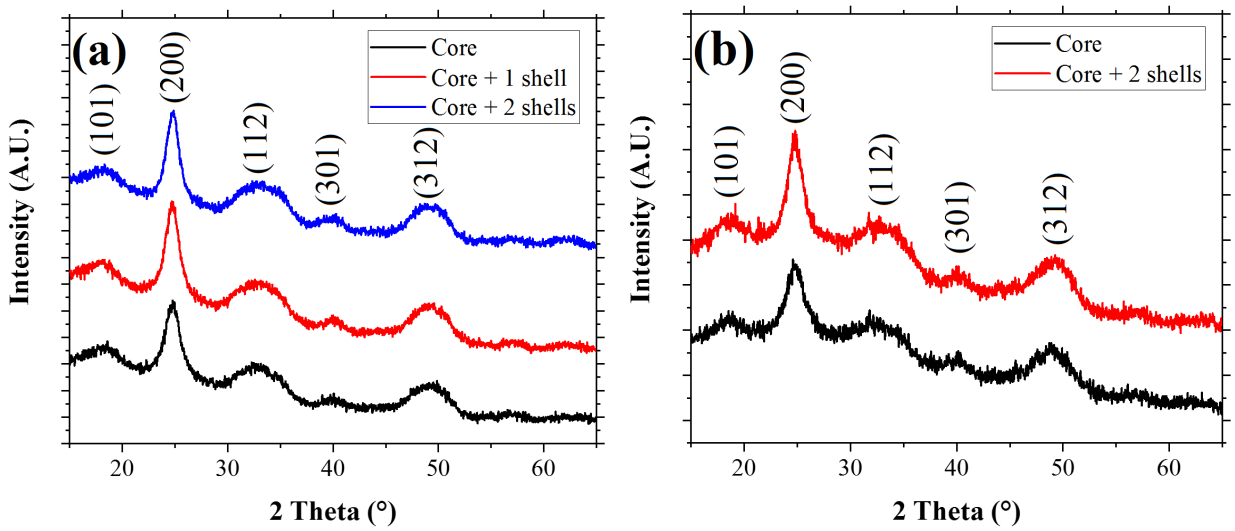

Fig. 6-9 Diffraction patterns of (a) $Gd_{0.8}Eu_{0.2}VO_4$ and (b) $GdVO_4$ core and core-shell NPs synthesized at 60 °C for 30 minutes using 1:0.75:0.75 Ln:cit:VO_4 and 1:1.5 core NPs suspension to oligomeric species solution volume ratios.

Table 6-2 Crystallite size of $Gd_{0.8}Eu_{0.2}VO_4$ and $GdVO_4$ core and core-shell NPs synthesized at 60 °C for 30 minutes using 1:0.75:0.75 Ln:cit:VO_4 and 1:1.5 core NPs suspension to oligomeric species solution volume ratios.

Crystallite size (nm)		
Sample	**$Gd_{0.8}Eu_{0.2}VO_4$**	**$GdVO_4$**
Core	4.7	4.0

Core + 1 shell	5.1	
Core + 2 shells	5.6	4.7

6.2.1.2 Morphology and Particle Size Distribution

Spherical $Gd_{0.8}Eu_{0.2}VO_4$ and $GdVO_4$ core NPs are observed in the TEM micrographs (**Fig. 6-10**). The $Gd_{0.8}Eu_{0.2}VO_4$ core NPs range from 2.0–5.1 nm with a mean particle size of 3.4 ± 0.7 nm [**Fig. 6-10(a)**], whereas a mean particle size of 3.6 ± 0.9 nm was obtained for $GdVO_4$ core NPs [**Fig. 6-10(b)**].

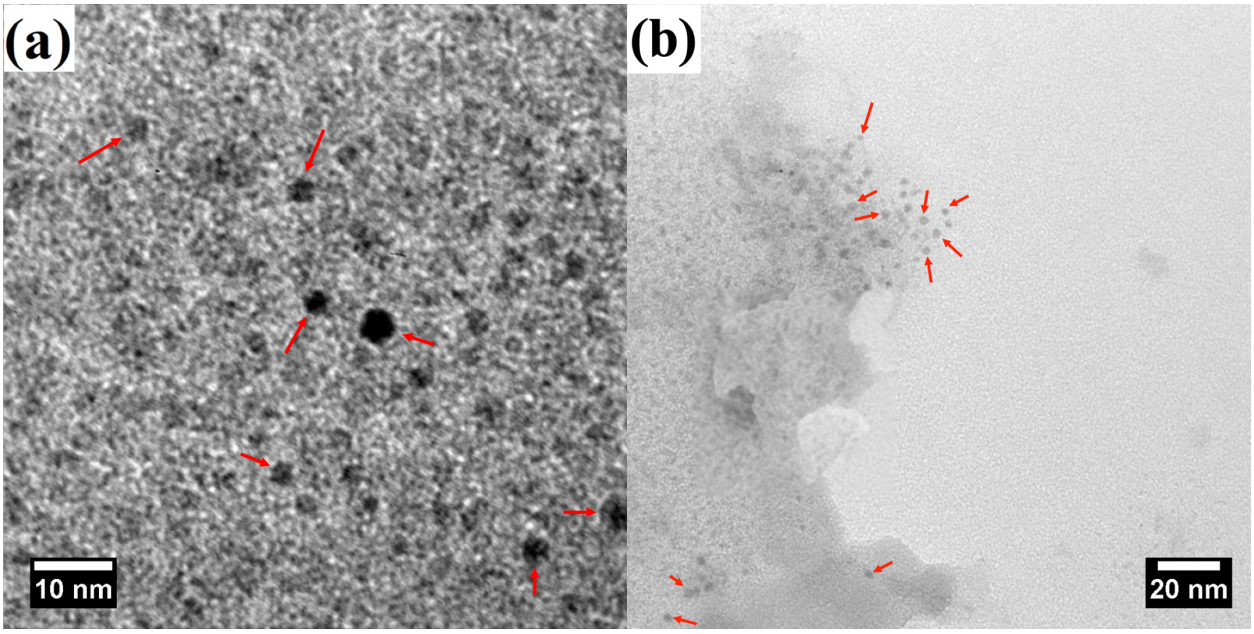

Fig. 6-10 TEM micrographs of (a) $Gd_{0.8}Eu_{0.2}VO_4$ and (b) $GdVO_4$ core NPs [indicated by arrows] synthesized at 60 °C for 30 minutes using a 1:0.75:0.75 Ln:cit:VO_4 volume ratio.

Both $Gd_{0.8}Eu_{0.2}VO_4$ and $GdVO_4$ core NPs have a narrow particle size distribution and correspond to single crystals based on the similarities between the particle size and the crystallite size (**Table 6-2**). For $GdVO_4$ core + 2 shells NPs, TEM micrographs were characterized by small aggregates of spherical and ellipsoidal NPs having a mean particle size of 4.4 ± 1.0 nm (**Fig. 6-11**).

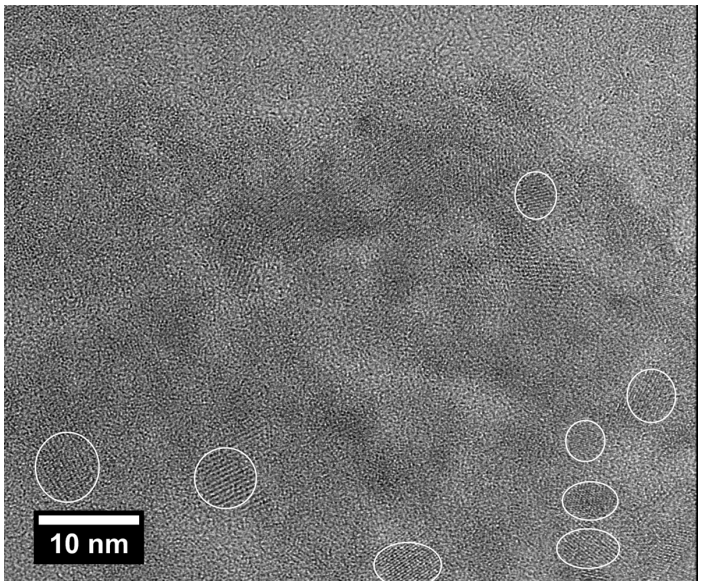

Fig. 6-11 TEM micrograph of $GdVO_4$ core + 2 shells NPs [showed in circle regions] synthesized at 60 °C for 30 minutes using 1:0.75:0.75 Gd:cit:VO_4 and 1:1.5 core NPs suspension to oligomeric species solution volume ratios.

Hydrodynamic size and particle size distributions of $Gd_{0.8}Eu_{0.2}VO_4$ and $GdVO_4$ core and core-shells NPs were characterized using as-prepared suspensions. In **Table 6-3**, the PI and mean hydrodynamic size of $Gd_{0.8}Eu_{0.2}VO_4$ core and core-shell NPs are summarized. The deposition of shells was accompanied by an increase in the PI and mean hydrodynamic size based on both particle size distributions as reported in section 5.1.2. The low PI values of both core and core + 1 shell suspensions suggest the presence of highly monodisperse NPs. In **Fig. 6-12**, narrow intensity and number distributions were obtained for $GdVO_4$ core NPs. An increase in the mean hydrodynamic size and particle size distribution was evidenced upon deposition of shells (**Fig. 6-12**). Particularly, the number particle size distribution of $GdVO_4$ core + 2 shells NPs revealed that either new core NPs were created or some of them were not covered with $GdVO_4$ shells [**Fig. 6-12(b)**].

Table 6-3 Statistics obtained from DLS of $Gd_{0.8}Eu_{0.2}VO_4$ core and core-shell NPs synthesized at 60 °C for 30 minutes using 1:0.75:0.75 Ln:cit:VO_4 and 1:1.5 core NPs suspension to oligomeric species solution volume ratios.

Sample	PI	Mean size [intensity] (nm)	Mean size [number] (nm)
Core	0.028	10.5 ± 3.6	6.2 ± 1.4
Core + 1 shell	0.053	14.5 ± 4.6	9.1 ± 2.1
Core + 2 shells	0.148	15.2 ± 3.1	12.1 ± 2.0

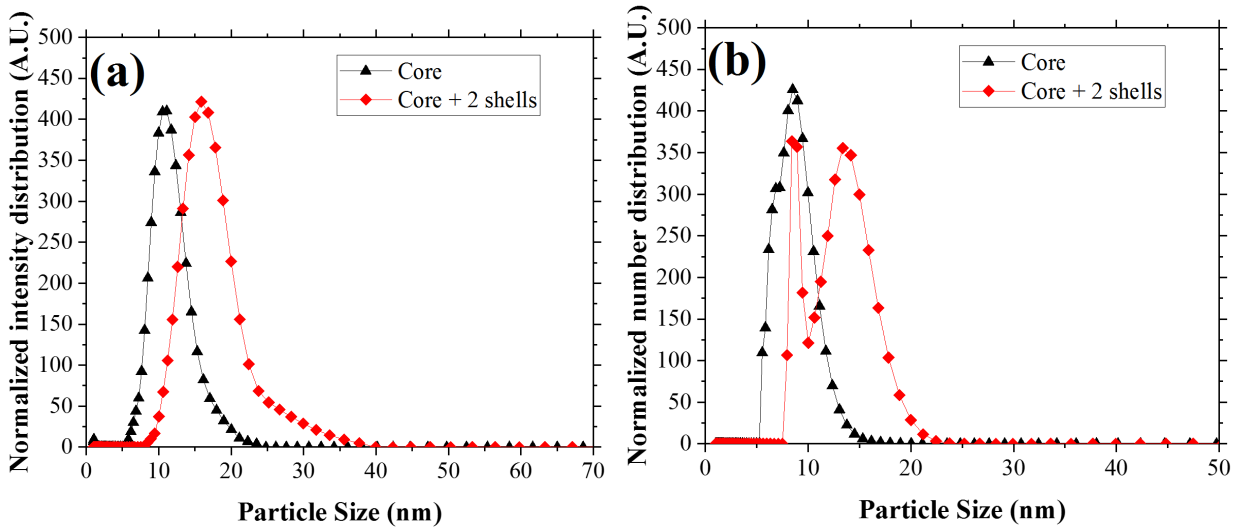

Fig. 6-12 Normalized (a) intensity and (b) number distribution of $GdVO_4$ core and core + 2 shells NPs synthesized at 60 °C for 30 minutes using 1:0.75:0.75 Ln:cit:VO_4 and 1:1.5 core NPs suspension to oligomeric species solution volume ratios.

This could be a consequence of a combined effect between the mechanism of shell growth (Ostwald ripening), the volume ratio of chemicals, and the lack of oligomeric species added during synthesis. Overall, the mean hydrodynamic size obtained from both intensity and number distributions seems to overestimate the size of $Gd_{0.8}Eu_{0.2}VO_4$ and $GdVO_4$ core and core-shell NPs based on the magnitude of crystallite size and mean particle size measured by XRD and TEM, respectively. The presence of citrate molecules on the surface or a counter ion layer in charged

surfaces will contribute to an overestimation of the particle size from both size distributions. However, the large hydrodynamic size and broad particle size distributions could also suggest the aggregation of NPs upon the deposition of shells because of a lack of complexing agents.

6.2.1.3 Nanoparticle Yield

The NPs yield is an essential parameter to assess the fraction of radioactivity lost during synthesis, while it also provides information to evaluate the proton relaxivities of MRI contrast agents and potential toxicity of using bare $LnVO_4$ NPs in biomedical applications. The as-prepared $Gd_{0.8}Eu_{0.2}VO_4$ and $GdVO_4$ core and core-shell NPs suspensions were dialyzed against DI water for 20 hours. Analysis of both dialyzed NPs suspension and dialysate was carried out. In **Table 6-4**, it is observed that the NPs yield increased upon deposition of shells for both $Gd_{0.8}Eu_{0.2}VO_4$ and $GdVO_4$ NPs. This increase is related to a higher consumption of oligomeric species caused by the continuous heating of the NPs suspension to promote the formation of core-shell structures since no intermediate cleaning was performed.

Table 6-4 Average yield of $Gd_{0.8}Eu_{0.2}VO_4$ and $GdVO_4$ core and core-shell NPs synthesized at 60 °C for 30 minutes using 1:0.75:0.75 Ln:cit:VO_4 and 1:1.5 core NPs suspension to oligomeric species solution volume ratios.

NPs yield (%)		
Sample	**$Gd_{0.8}Eu_{0.2}VO_4$**	**$GdVO_4$**
Core	41.1 ± 16.5	61.4 ± 1.6
Core + 1 shell	55.4 ± 8.0	63.4 ± 1.5
Core + 2 shells	54.8 ± 11.2	58.6 ± 3.8

6.2.1.4 Absorption, Excitation, and Emission Spectra of $Gd_{0.8}Eu_{0.2}VO_4$ core-shell NPs

The absorption spectrum of $Gd_{0.8}Eu_{0.2}VO_4$ core and core-shell NPs is represented by a broad band corresponding to the O^{2-}-V^{5+} CT band [167]. The increase in absorbance upon deposition of shells for $Gd_{0.8}Eu_{0.2}VO_4$ may be related to a higher concentration of NPs [**Fig. 6-13(a)**], which is consistent with the increase in NPs yield reported in section 6.2.1.3. An emission wavelength of 618 nm, an excitation filter between 250–395 nm, and a PMT voltage of 600 V were used to record the excitation spectra. A broad excitation band with maximum intensity ~280 nm was observed for $Gd_{0.8}Eu_{0.2}VO_4$ core NPs, whereas the excitation spectra of $Gd_{0.8}Eu_{0.2}VO_4$ core-shell NPs is characterized by two excitation bands corresponding to O^{2-}-Eu^{3+} (~280 nm) and O^{2-}-V^{5+} (~305 nm) CT [**Fig. 6-13(b)**] [168]–[170]. In addition, a red shift in the excitation spectra and an increase in the intensity of the O^{2-}-V^{5+} CT band were observed after the deposition of shells to the core NPs [**Fig. 6-13(b)**].

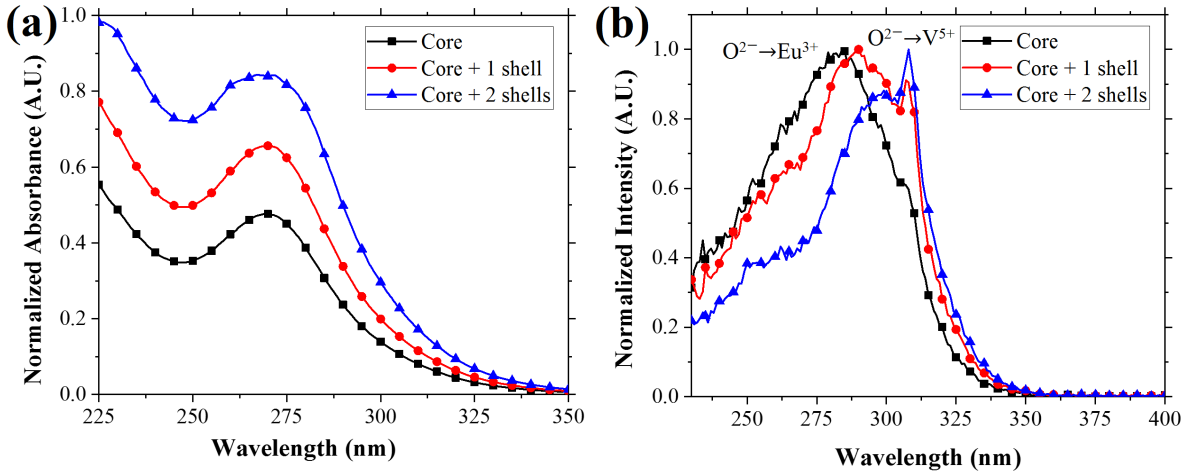

Fig. 6-13 (a) Absorption and (b) excitation (λ_{em} = 618 nm) spectra of $Gd_{0.8}Eu_{0.2}VO_4$ core and core-shell NPs synthesized at 60 °C for 30 minutes using 1:0.75:0.75 Ln:cit:VO_4 and 1:1.5 core NPs suspension to oligomeric species solution volume ratios.

The red shift implies that the core-shell structures could be excited with lower energy photons with respect to the core NPs. The increase in the O^{2-}-V^{5+} CT band suggests that the excitation of Eu^{3+} ions is more efficient through the $[VO_4]^{3-}$ units due to changes in the Eu^{3+}-O^{2-} bond elongation and/or crystal cell volume for the core-shell NPs [169], [188]. Finally, the emission spectrum was recorded using an excitation wavelength of 280 nm, an emission filter from 295–1,100 nm, and a PMT voltage of 600 V. The emission spectra of $Gd_{0.8}Eu_{0.2}VO_4$ core and core-shell NPs displayed the characteristic $^5D_0 \rightarrow {}^7F_J$ (J = 1–4) Eu^{3+} transitions (**Fig. 6-14**) [171]. The deposition of shells caused a decrease in the emission intensity, which may be related to the use of an excitation wavelength that does not correspond to the maxima intensity [**Fig. 6-13(b)**]. The changes in the excitation spectra were not considered when recording the emission spectrum since the excitation wavelength was kept at 280 nm.

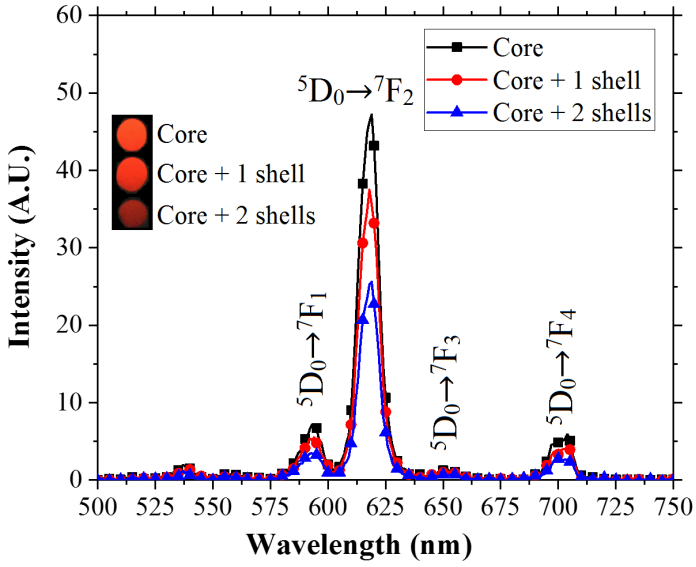

Fig. 6-14 Emission (λ_{exc} = 280 nm) spectra of $Gd_{0.8}Eu_{0.2}VO_4$ core and core-shell NPs synthesized at 60 °C for 30 minutes using 1:0.75:0.75 Ln:cit:VO_4 and 1:1.5 core NPs suspension to oligomeric species solution volume ratios. Inset corresponds to $Gd_{0.8}Eu_{0.2}VO_4$ core and core-shell suspensions NPs under UV light (λ = 254 nm).

Additionally, aggregation of NPs in both core-shell structures may have caused a decrease in the emission intensity taking into account their broader particle size distributions [188]. The inset in **Fig. 6-14** corresponds to photographs taken of aliquots from $Gd_{0.8}Eu_{0.2}VO_4$ core and core-shell NPs suspensions under UV light (λ = 254 nm).

6.2.1.5 Magnetic Susceptibilities and Relaxation Time Studies

The mass magnetization as a function of the magnetic field of $Gd_{0.8}Eu_{0.2}VO_4$ core and core-shell NPs is shown in **Fig. 6-15**. The magnetic susceptibility of $Gd_{0.8}Eu_{0.2}VO_4$ core and core-shell NPs was 56×10^{-6} emu Oe^{-1} g^{-1}, which is consistent with the constant lanthanide concentration (**Table 6-5**) and the Curie formula [equation $\chi = \frac{N\mu^2}{3k_BT}$ **4-1**].

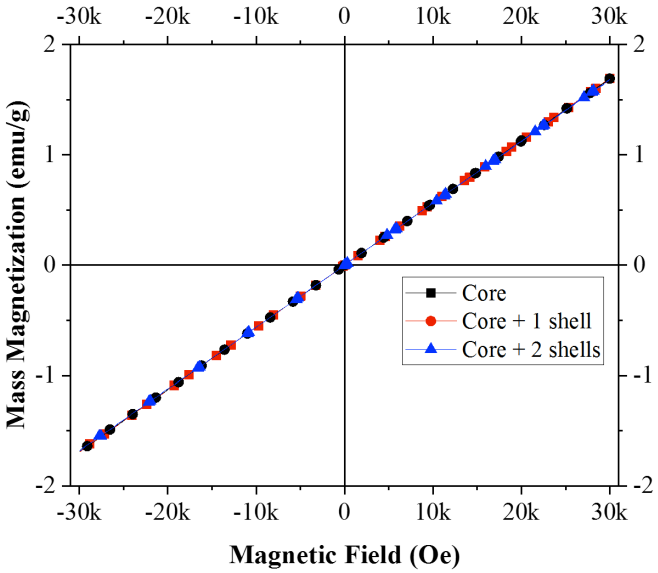

Fig. 6-15 Mass magnetization versus magnetic field of $Gd_{0.8}Eu_{0.2}VO_4$ core and core-shell NPs synthesized at 60 °C for 30 minutes using 1:0.75:0.75 Ln:cit:VO_4 and 1:1.5 core NPs suspension to oligomeric species solution volume ratios.

Table 6-5 Gadolinium and europium weight and atomic percentage in $Gd_{0.8}Eu_{0.2}VO_4$ core and core-shell NPs synthesized at 60 °C for 30 minutes using 1:0.75:0.75 Ln:cit:VO_4 and 1:1.5 core NPs suspension to oligomeric species solution volume ratios.

	Weight percentage (%)		**Atomic percentage (%)**	
Sample	**Eu**	**Gd**	**Eu**	**Gd**
Core	78.0	22.0	77.3	22.7
Core + 1 shell	78.0	22.0	77.3	22.7
Core + 2 shells	77.9	22.1	77.3	22.7

The response of $GdVO_4$ core NPs as positive-T_1 MRI contrast agents was tested using a dialyzed suspension in order to remove unreacted species, particularly Gd^{3+} ions. The phantoms used for characterization were prepared by diluting the dialyzed core NPs suspension at various concentrations (0.016-0.5 mM). Each solution was loaded into a 2 mL plastic syringe avoiding air bubbles. The phantoms were imaged in a 7T BioSpec 70/30 small animal MRI scanner (Bruker, Billerica, MA). T_1 values and T_1-weighted images were obtained using the same multi-slice and multi-echo sequence. Longitudinal relaxivity (r_1) was obtained from the slopes of the curves $1/T_1$ versus the concentration of Gd^{3+} expressed in millimoles. An increase in concentration of $GdVO_4$ core NPs resulted in an enhancement of the signal intensity, observed as brighter images [**Fig. 6-16(a)**], which is characteristic of positive (T_1) MRI contrast agents. The T_1^{-1} relaxation rate of water protons increased with higher concentration of Gd^{3+} ions as shown in **Fig. 6-16(b)**. The calculated longitudinal proton relaxivity (r_1) has a magnitude of 0.805 s^{-1} mM^{-1}, which is comparable to the longitudinal relaxivity reported for surface functionalized $Gd_{0.9}Eu_{0.1}VO_4$ nanocrystals, r_1 = 0.776 s^{-1} mM^{-1} [59]. However, Abdesselem *et al.* reported a longitudinal relaxivity for $GdVO_4$ NPs, synthesized using the same procedure, which is ~5 times higher to that obtained for the dialyzed $GdVO_4$ core NPs suspension [5].

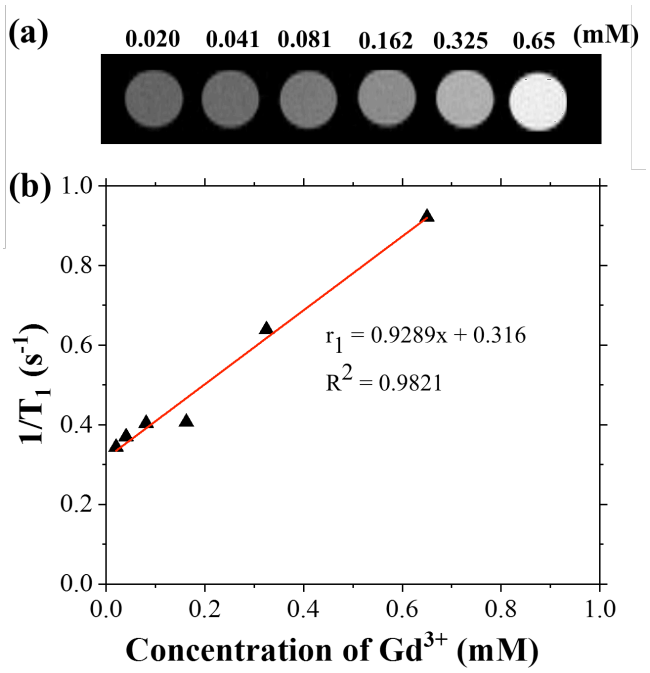

Fig. 6-16 (a) T_1-weighted images (DI water was used as a reference) and (b) longitudinal proton relaxivity (r_1) measured for different concentrations of $GdVO_4$ core NPs synthesized at 60 °C for 30 minutes using a 1:0.75:0.75 Gd:cit:VO_4 volume ratio.

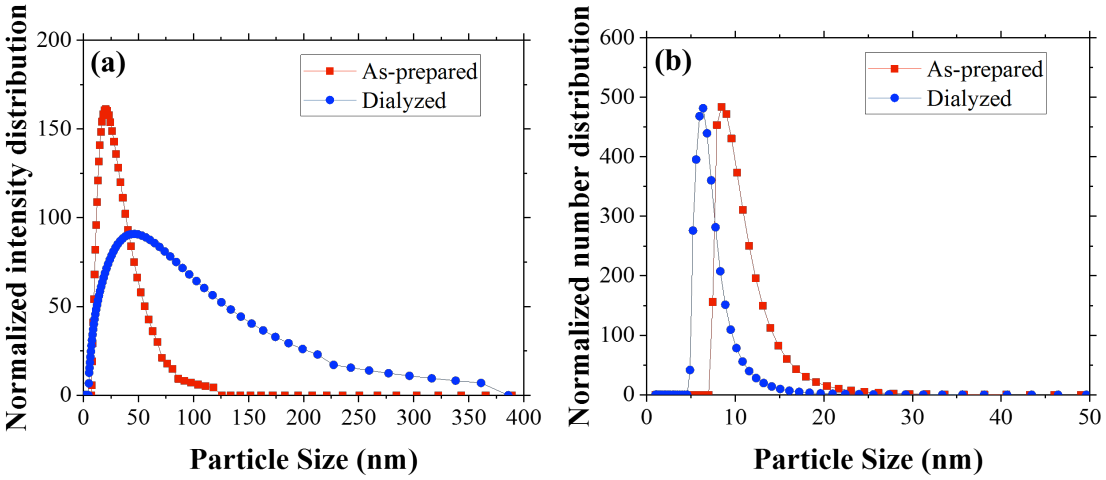

Fig. 6-17 Normalized (a) intensity and (b) number distributions of as-prepared and dialyzed $GdVO_4$ core NPs suspensions synthesized at 60 °C for 30 minutes using a 1:0.75:0.75 Gd:cit:VO_4 volume ratio.

This difference could be related to an increase in the particle size after dialysis, attributed to NPs aggregation, since significant broadening of the normalized intensity distribution was observed [**Fig. 6-17(a)**]. A reduction of the concentration of citrate groups and counter ions during dialysis could be the main reason behind the NPs aggregation based on the decrease in mean particle size observed from the normalized number distribution [**Fig. 6-17(b)**]. Overall, an increase of the particle size [22] and/or the aggregation of NPs [65] have as a consequence a decrease of the longitudinal (r_1) proton relaxivity due to lower concentration of surface Gd^{3+} ions.

6.2.1.6 In vitro Retention of ^{225}Ac and Decay Daughters

In vitro retention of ^{225}Ac and decay daughters was studied in $Gd_{0.8}Eu_{0.2}VO_4$ and $GdVO_4$ core and core + 2 shells NPs. In **Fig. 6-18**, the fraction of radioactivity (leakage) found in the dialysate from ^{225}Ac as a function of time for both $Gd_{0.8}Eu_{0.2}VO_4$ and $GdVO_4$ core and core + 2 shells NPs is presented. The activity of ^{225}Ac in the dialysate continuously increased until it reached a plateau, at which point the dialysate was replaced with fresh DI water to continue monitoring the release of ^{225}Ac (**Fig. 6-18**). After changing the dialysate, the fraction of radioactivity of ^{225}Ac built up again and reached a maximum of 25.8 ± 1.6% and 3.3 ± 0.3% after 4 weeks for $Gd_{0.8}Eu_{0.2}VO_4$ core and core + 2 shells NPs, respectively [**Fig. 6-18(a)**]. The leakage of ^{225}Ac from $GdVO_4$ core NPs reached a maximum 15.0 ± 0.9%, while the activity of ^{225}Ac increased over time for $GdVO_4$ core + 2 shells up to 2.4 ± 0.2% [**Fig. 6-18(b)**]. These results suggest that the lanthanide concentration may have an influence on the retention of ^{225}Ac within core NPs that could be related to their yield (**Table 6-4**). The activity observed in the dialysate may be related to unreacted ^{225}Ac cations that were not retained within the NPs and that remained as ^{225}Ac-cit species after synthesis. This hypothesis is supported by the continuous increase in leakage of ^{225}Ac observed for both $Gd_{0.8}Eu_{0.2}VO_4$ and $GdVO_4$ core NPs when the dialysate was replaced with fresh DI water. The continuous increase of activity could only mean that ^{225}Ac is not

a free ion but instead is in the form of a low-molecular-weight metal-citrate complex in solution or adsorbed onto the NPs surface (**Fig. 6-18**). It has been demonstrated that ^{225}Ac cations can easily form complexes with citrate ions [189], which might hinder their retention within the core NPs.

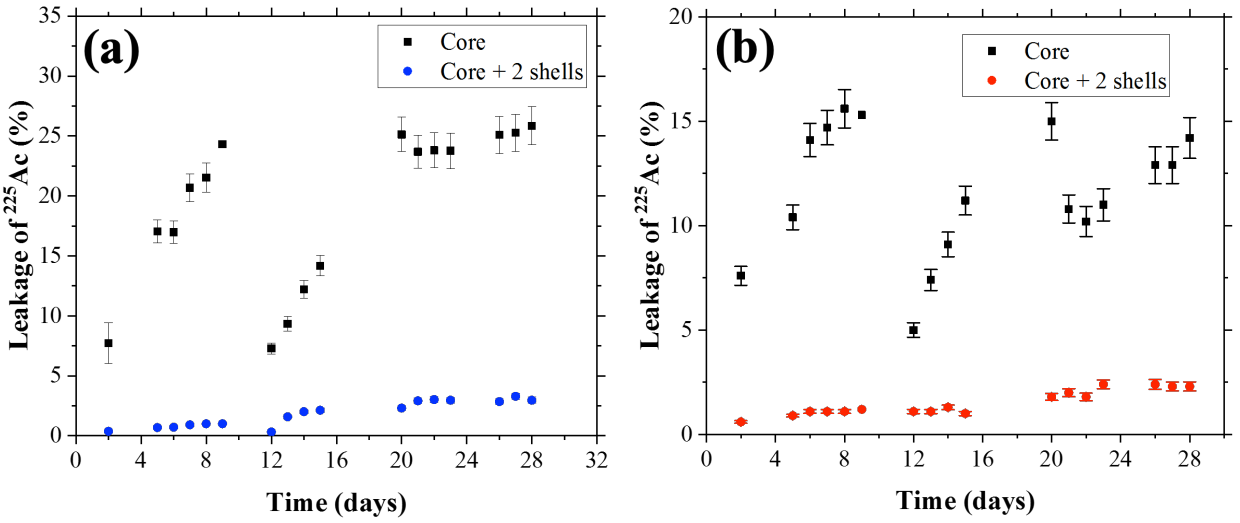

Fig. 6-18 Leakage of ^{225}Ac from (a) $Gd_{0.8}Eu_{0.2}(^{225}Ac)VO_4$ and (b) $Gd(^{225}Ac)VO_4$ core and core + 2 shells NPs synthesized at 60 °C for 30 minutes using 1:0.75:0.75 Ln:cit:VO_4 and 1:1.5 core NPs suspension to oligomeric species solution volume ratios.

A simple experiment using La cations as surrogates of ^{225}Ac was carried out to assess the difference between the leakage in dialysis of La as free ion and as a La-citrate complex. Briefly, $LaCl_3$, $LaCl_3$-cit, and $GdCl_3$-$LaCl_3$-cit solutions were dialyzed against DI water for 72 hours. Aliquots were taken after 1, 6, 24, 48, and 72 hours in dialysis and analyzed using ICP-OES to determine the La concentration. A stable concentration of La cations in the dialysate was reached between 1 to 6 hours in dialysis for $LaCl_3$, whereas La-cit and La-Gd-cit complexes required at least 48 and 24 hours, respectively [**Fig. 6-19(a)**]. The fraction of La in the dialysate was consistent with a 100% leakage for all the solutions analyzed [**Fig. 6-19(b)**]. These results endorse the fact that ^{225}Ac was in the form of a metal-citrate complex that caused a continuous increase in activity over time for core NPs. The overall enhancement in the retention of ^{225}Ac within $Gd_{0.8}Eu_{0.2}VO_4$

and $GdVO_4$ core + 2 shells NPs may be related to the reaction and consumption of the ^{225}Ac-cit complexes during the deposition of nonradioactive shells since no intermediate cleaning step was carried out after core synthesis. Therefore, a significant fraction of ^{225}Ac-cit complexes may result in the formation of new core NPs and/or retain within shells.

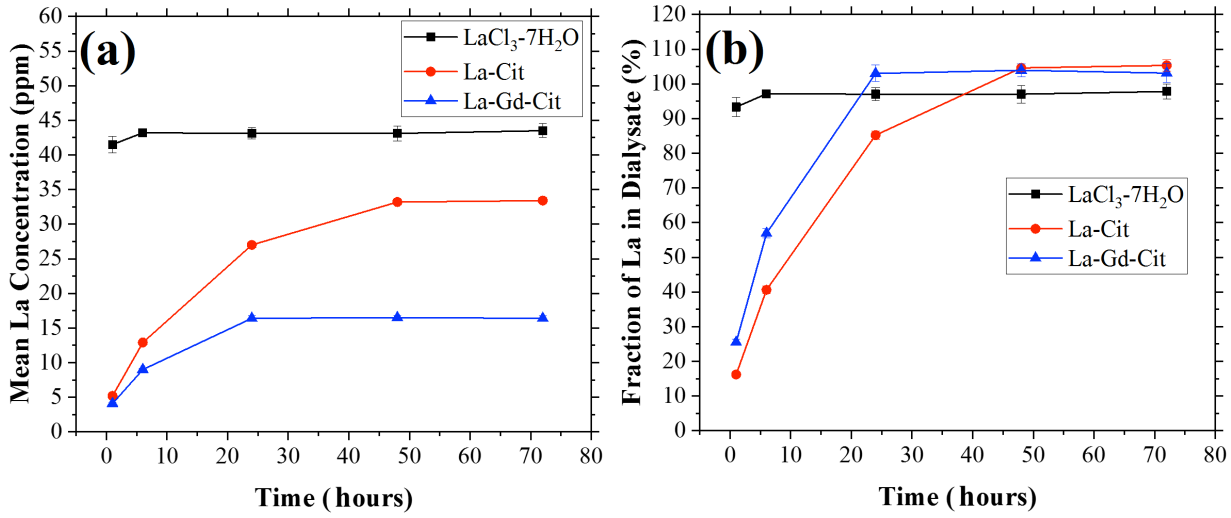

Fig. 6-19 (a) La concentration and (b) fraction of La in dialysate as a free La cation and as a La-citrate complex.

The radiochemical yield of ^{225}Ac was calculated considering the initial activity in the NPs suspensions, the activity lost in the conical vials and pipettes, and the total activity lost during dialysis. The radiochemical yield of ^{225}Ac was 43.8% and 75% for $Gd_{0.8}Eu_{0.2}VO_4$ and $GdVO_4$ core NPs, whereas an enhancement to 93.7% and 95% was obtained upon the deposition of 2 nonradioactive shells, respectively. The yield for both $Gd_{0.8}Eu_{0.2}VO_4$ and $GdVO_4$ core NPs is consistent with their NPs yield (**Table 6-4**). The ^{225}Ac radiochemical yield of $Gd_{0.8}Eu_{0.2}VO_4$ core NPs is similar to the 47 ± 5% reported for $LaPO_4$ NPs of 3–5 nm after surface modification and purification [39]. The measured yield represents a significant enhancement with respect to procedures for radiolabeling mAbs with ^{225}Ac, which have shown ~10% of radiochemical yield [190], [191]. Similarly, $GdVO_4$ core NPs had a higher radiochemical yield with respect to the

loading efficiency of polymer vesicles (67%) [113] and ^{225}Ac-DOTA-IgG (<10%) [109], whereas its magnitude is comparable to that obtained for gold-coated $LnPO_4$ core-shell NPs (76%) [42]. As discussed previously, the higher ^{225}Ac radiochemical yield of core + 2 shells NPs implies that a significant fraction of activity is retained within the two nonradioactive shells and/or in newly formed core NPs.

The leakage of ^{221}Fr was determined after subtracting the activity of ^{221}Fr being produced from ^{225}Ac in the dialysate. For $Gd_{0.8}Eu_{0.2}VO_4$ core NPs, the leakage of ^{221}Fr was 58.7 ± 3.8% within 12 days and increased to 70.9 ± 4.4% after 28 days in dialysis [**Fig. 6-20(a)**]. A similar behavior was observed for $GdVO_4$ core NPs, where the maximum leakage was 69.5 ± 4.9% [**Fig. 6-20(b)**]. Both $Gd_{0.8}Eu_{0.2}VO_4$ and $GdVO_4$ core NPs had a higher leakage of ^{221}Fr with respect to the 60% and 40% reported for $LaPO_4$ and $La_{0.5}Gd_{0.5}PO_4$ core NPs, respectively [39], [42]. The deposition of two nonradioactive shells decreased the leakage of ^{221}Fr to a maximum of 43.5 ± 3.6% and 49.2 ± 4.7% for $Gd_{0.8}Eu_{0.2}VO_4$ and $GdVO_4$, respectively (**Fig. 6-20**). This enhancement is related to the presence of a dense lattice structure which acts as a physical barrier against the leakage of radionuclides and is consistent with the 70% and 80% retention of ^{221}Fr in $La_{0.5}Gd_{0.5}PO_4$ and $LaPO_4$ core + 2 shells NPs, respectively [38], [42]. The leakage of ^{213}Bi was found to be lower to that of ^{221}Fr (**Fig. 6-21**). In addition, both $Gd_{0.8}Eu_{0.2}VO_4$ and $GdVO_4$ core NPs seem to have higher retention of ^{213}Bi with respect to core + 2 shells NPs (**Fig. 6-21**). This difference is more significant for $Gd_{0.8}Eu_{0.2}VO_4$ core-shell NPs, where the leakage of ^{213}Bi from core + 2 shells is ~10% higher with respect to core NPs [**Fig. 6-21(a)**].

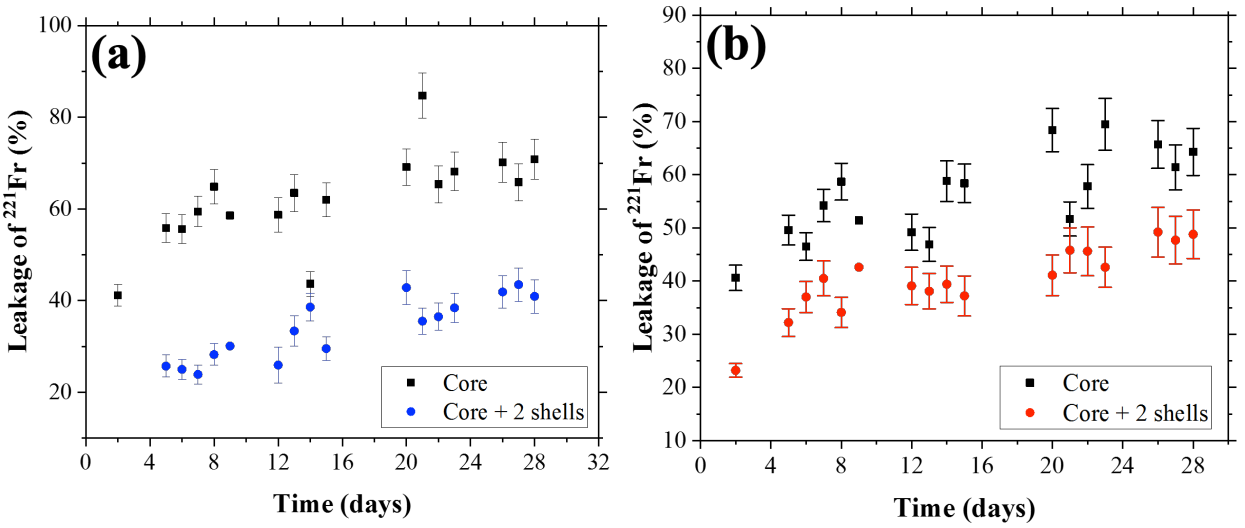

Fig. 6-20 Leakage of ^{221}Fr from (a) $Gd_{0.8}Eu_{0.2}(^{225}Ac)VO_4$ and (b) $Gd(^{225}Ac)VO_4$ core and core + 2 shells NPs synthesized at 60 °C for 30 minutes using 1:0.75:0.75 Ln:cit:VO_4 and 1:1.5 core NPs suspension to oligomeric species solution volume ratios.

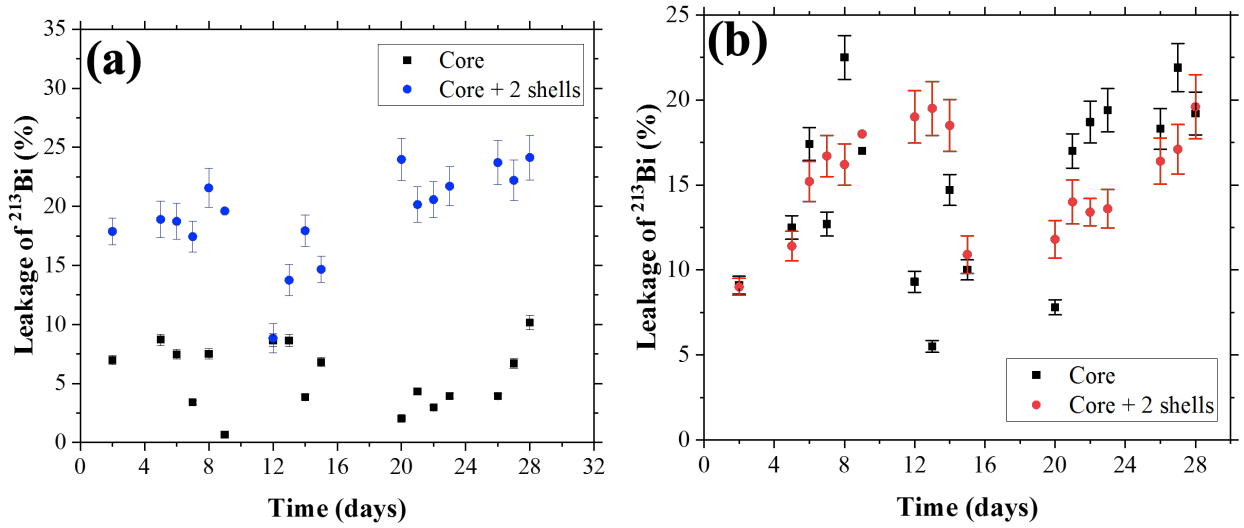

Fig. 6-21 Leakage of ^{213}Bi from (a) $Gd_{0.8}Eu_{0.2}(^{225}Ac)VO_4$ and (b) $Gd(^{225}Ac)VO_4$ core and core + 2 shells NPs synthesized at 60 °C for 30 minutes using 1:0.75:0.75 Ln:cit:VO_4 and 1:1.5 core NPs suspension to oligomeric species solution volume ratios.

The partial retention of both ^{221}Fr and ^{213}Bi in $Gd_{0.8}Eu_{0.2}VO_4$ and $GdVO_4$ core-shell NPs will cause toxicity to normal organs, particularly kidney, during *in vivo* applications [192]. It is

expected that the fraction of decay daughters leaking from the $LnVO_4$ NPs will increase because of the ^{225}Ac activity retained within the nonradioactive shells. Variation of synthesis parameters to deposit thicker shells and/or intermediate cleaning steps are expected to enhance the retention of decay daughters. A simple experiment where the $Gd(^{225}Ac)VO_4$ core NPs suspension was dialyzed before the deposition of two nonradioactive shells showed that the leakage of ^{221}Fr reached a maximum ~32% after 2 weeks, which is comparable to the results obtained with $LnPO_4$ core + 2 shells NPs [39], [42]. Overall, the partial retention of both ^{221}Fr and ^{213}Bi may be attributed to a combination of the following effects: (i) the conversion of a fraction of the recoil energy to translational energy of the NP, (ii) the intrinsic attenuation of decay daughters by the NP, or (iii) the reloading of decay daughters by adjacent NPs and/or surface groups [81], [92], [94]–[96]. The fact that inorganic $LnVO_4$ NPs are very rigid and dense suggests the possibility that a faction of the recoil energy is transferred to the translational energy of NPs. It is expected that the recoil energy will be reduced by $[m_{DD}/(m_{DD}+m_{NP})]$, where m_{DD} is atomic mass of the decay daughter and m_{NP} is the average molecular mass of NP, which is ~1000. The intrinsic attenuation of decay daughters by the NP seems unlikely due to the difference between the particle size of both core and core-shell NPs with the range of ^{221}Fr (E = 105.5 keV, ~26 nm) and ^{213}Bi (E = 132.8 keV, ~30 nm) in $GdVO_4$ ($\rho = 5.47$ g/cm^3) [81], [193]. Based on the large range of decay daughters in $GdVO_4$, a complete leakage of decay daughters would be expected in both $Gd_{0.8}Eu_{0.2}VO_4$ and $GdVO_4$ core and core + 2 shells NPs. Hence, the reloading of both decay daughters by adjacent NPs could contribute significantly to the partial retention observed in both $Gd_{0.8}Eu_{0.2}VO_4$ and $GdVO_4$ core and core-shell NPs. As observed from the DLS results, the width of the particle size distribution increased after deposition of shells because of NP aggregation (section 6.2.1.2). To illustrate, $Gd_{0.8}Eu_{0.2}VO_4$ core + 2 shells NPs displayed a particle size from 6 nm to 38 nm, while either particles or aggregates of less than ~21 nm were obtained for core NPs. In addition, it has been

observed that the width of the particle size distribution increases after dialyzing the NPs suspensions because of a reduction in the concentration of sodium citrate (**Fig. 6-17**). These results are consistent with the higher retention of ^{221}Fr in both $Gd_{0.8}Eu_{0.2}VO_4$ and $GdVO_4$ core + 2 shells NPs with respect to that in the core NPs. Therefore, it is expected that the free decay daughter will be implanted in adjacent NPs. Reloading of decay daughters by the adjacent NPs and/or surface groups, is also associated to the ion exchange characteristics of some compounds [98], [99] and the ability of surface groups to interact with free ions [94]. This effect could be responsible for the higher retention of ^{213}Bi by the core NPs with respect to that of core + 2 shells. The recoiled ^{213}Bi ions out of the NPs are thermalized quickly (within ~30 nm) and may form a complex with the citrate groups on the NPs surface. Particularly, it is expected that ^{213}Bi may be captured by the hydroxyl group, which have shown high affinity for Bi cations [94], of the citrate species that are complexed to the lanthanide ions on the NPs surface. The fact that a greater fraction of citrate species is consumed during core-shell synthesis may be responsible for the higher leakage of ^{213}Bi observed for core + 2 shells NPs with respect to that of core (**Fig. 6-21**). In summary, the partial retention of both ^{221}Fr and ^{213}Bi is due to the transfer of the recoil energy to the translation of the NP, their reloading by adjacent NPs facilitated by the formation of aggregates with sizes ~30 nm, and the interaction with hydroxyl and carboxylic groups present at the NPs surface.

6.2.2 $GdVO_4$ and $LaPO_4$ core-shell NPs Doped with ^{227}Th

$Gd(^{227}Th)VO_4$ core and core + 2 shells NPs were synthesized using a 1:0.65:0.9 volume ratio between Gd^{3+}:cit:$[VO_4]^{3-}$. This modification was done with the purpose to (i) enhance the NPs yield and (ii) increase the shell thickness based on the results obtained in section 5.1.2. An acidic solution with an initial activity of ~32 μCi of ^{227}Th was evaporated to dryness in a conical vial at 80 ºC. A 0.1 M $GdCl_3$ solution was added to the vial and stirred for 10–15 minutes for a complete dispersion of ^{227}Th and decay daughters. Sodium citrate and sodium orthovanadate

solutions were added drop-by-drop under constant stirring at the established volume ratios. This radioactive solution was heated at 60 ºC for 30 minutes to obtain Gd(^{227}Th)VO_4 core NPs. The core NPs suspension was dialyzed overnight to remove unreacted ^{227}Th ions. The deposition of nonradioactive $GdVO_4$ shells was carried out using the dialyzed Gd(^{227}Th)VO_4 core NPs suspension to prevent precipitation of unreacted ^{227}Th and decay daughters. After dialysis, the core solution was divided into two equal parts, one for retention studies and the other for core-shell synthesis. The deposition of nonradioactive shells was done by mixing the dialyzed core suspension with a solution containing oligomeric species prepared at the same volume ratio of reagents as described for the core NPs. This oligomeric species solution was added under constant stirring to the core NPs suspension in a 2:1 volume ratio (section 5.1.2). The mixture was heated at 60 ºC for 30 minutes to deposit the first shell. The process was repeated once more to synthesize Gd(^{227}Th)VO_4 core + 2 shells NPs, while keeping a 1:2 volume ratio of core NPs suspension to oligomeric species solution. The Gd(^{227}Th)VO_4 core + 2 shells NPs suspension was dialyzed against DI water to assess *in vitro* retention of ^{227}Th and decay daughter ^{223}Ra over time.

An initial activity of 12–45 µCi of ^{227}Th in 0.1 M HCl was evaporated to dryness in a conical vial at 80 ºC. $LaCl_3$ was added and stirred for 15–20 minutes before adding Na-TPP in a 1:1 volume ratio (section 3.2 and 4.2). La(^{227}Th)PO_4 core NPs were synthesized at 90 ºC for 3 hours and dialyzed overnight. The core NPs suspension was divided into two equal parts, one for retention analysis of core NPs and the other for core-shell synthesis, as carried out for Gd(^{227}Th)VO_4. Deposition of nonradioactive $LaPO_4$ shells was done as described in section 3.2, while keeping the temperature and heating time at 90 ºC and 3 hours, respectively. The radionuclide-doped core + 2 shells NPs suspensions were dialyzed against DI water to assess the retention of radionuclides over time. The crystal structure of both $GdVO_4$ and $LaPO_4$ core and core

+ 2 shells NPs was characterized as well as the morphology of $LaPO_4$ NPs. The results presented in this section have been adapted from two manuscripts under preparation.

6.2.2.1 Crystal structure

$GdVO_4$ core and core + 2 shells NPs have a tetragonal crystal system with space group $I4_1/amd$ (pdf: 00-017-0260), whereas a hexagonal crystal system with space group $P6_222$ (pdf: 01-075-1881) was obtained for $LaPO_4$ core and core + 2 shells NPs. Both $GdVO_4$ and $LaPO_4$ NPs showed an increase in the crystallite size upon deposition of two shells. An increase from 5.5 nm to 7.5 nm was observed for $GdVO_4$ NPs, while for $LaPO_4$ NPs it was from 4.2 nm to 5.2 nm. As expected from section 5.1.2, the adjustment of the volume ratio between reagents and volume of oligomeric species solution resulted in a larger increase of crystallite size for $Gd(^{227}Th)VO_4$ with respect to the results obtained for $Gd(^{225}Ac)VO_4$ in section 6.2.1.1. The increase in size between core and core + 2 shells NPs was 0.7 nm and 2.0 nm for $Gd(^{225}Ac)VO_4$ and $Gd(^{227}Th)VO_4$, respectively.

6.2.2.2 Morphology of $LaPO_4$ core and core + 2 shells NPs

$LaPO_4$ core and core + 2 shells NPs have spherical and ellipsoidal shape based on the TEM micrographs (**Fig. 6-22**). The mean particle size for core and core + 2 shells was 4.5 ± 1.2 nm and 5.4 ± 0.9 nm, respectively. The similarity between the mean particle size and crystallite size of both core and core + 2 shells suggests that the as-prepared $LaPO_4$ NPs correspond to single crystals.

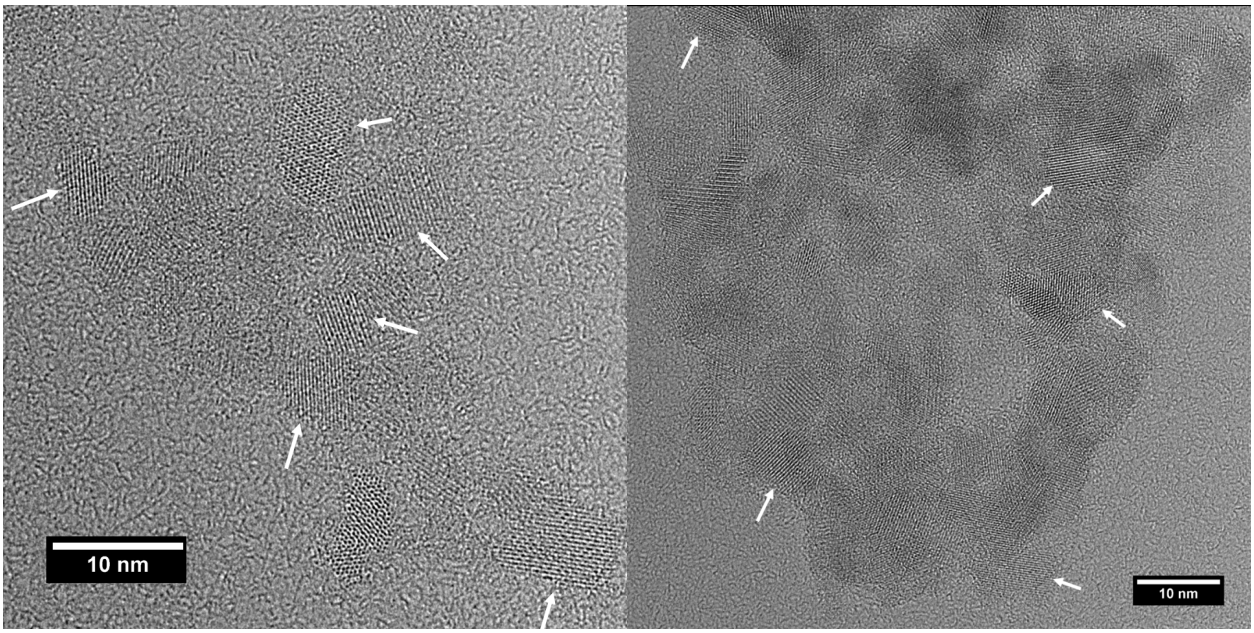

Fig. 6-22 TEM micrographs of $LaPO_4$ core (left) and core + 2 shells (right) NPs synthesized at 90 °C for 3 hours by mixing a solution of La/Na-TPP (1:2 La:Na-TPP volume ratio) with $LaPO_4$ core NPs suspension at a 1:1 volume ratio (section 3.2).

6.2.2.3 In vitro Retention of ^{227}Th and Decay Daughters

Previous studies have only involved the development of ^{227}Th radioimmunoconjugates, which cannot retain decay daughters at the target site [81], [114], [115], [194]–[197]. The synthesis of Gd(^{227}Th)VO_4 and La(^{227}Th)PO_4 core and core + 2 shells NPs may provide a partial retention of radionuclides contributing to a reduction of the radiotoxicity generated by decay daughters [195]. The leakage of ^{227}Th and ^{223}Ra from Gd(^{227}Th)VO_4 core and core + 2 shells NPs is shown in **Fig. 6-23**. The leakage of ^{227}Th from $GdVO_4$ core NPs was 3.3 ± 0.3% after 7 days and then decreased to 2.0 ± 0.5% at day 21 [**Fig. 6-23(a)**]. Although the samples were analyzed for over 30 days, the activity of ^{227}Th in the dialysate was below the detection limit of the HPGe detector. Similarly, the leakage of ^{227}Th from $GdVO_4$ core + 2 shells NPs was <1.5% in the first 12 days in dialysis, with no activity detected afterwards [**Fig. 6-23(a)**]. These results demonstrate that $^{227}Th^{4+}$

ions (i) are successfully retained within the tetragonal structure of $GdVO_4$ in comparison to $^{225}Ac^{3+}$ and (ii) do not easily form Th-cit complexes based on the results presented in section 6.2.1.6. The leakage of ^{223}Ra from $GdVO_4$ core NPs was 10 ± 0.7% after one day in dialysis, however, the fraction of activity in the dialysate increased to 39.7 ± 2.3% after 2 weeks [**Fig. 6-23(b)**]. The deposition of two nonradioactive $GdVO_4$ shells decreased the leakage of ^{223}Ra to a maximum of 25.5 ± 1.5% [**Fig. 6-23(b)**]. As discussed previously, nonradioactive shells act as a barrier against the leakage of decay daughters enhancing their retention over that of core NPs.

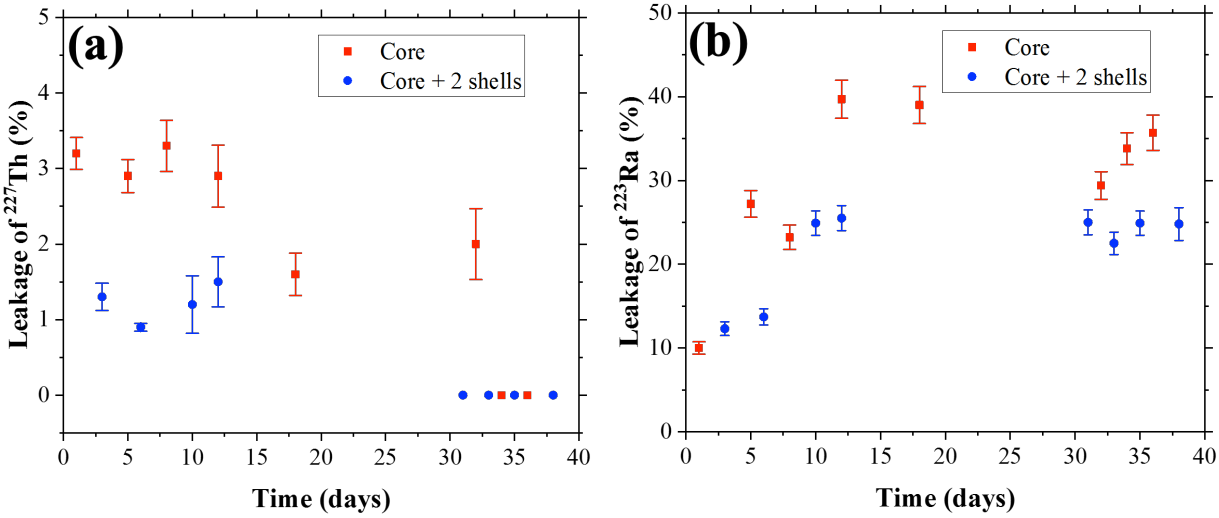

Fig. 6-23 Leakage of (a) ^{227}Th and (b) ^{223}Ra from $GdVO_4$ core and core + 2 shells NPs synthesized at 60 °C for 30 minutes using 1:0.65:0.9 Ln:cit:VO_4 and 1:2 core NPs suspension to oligomeric species solution volume ratios.

In **Fig. 6-24**, the leakage of ^{227}Th and ^{223}Ra from La(^{227}Th)PO_4 core and core + 2 shells NPs is presented. In $LaPO_4$ core NPs, the leakage of ^{227}Th had a maximum of 2.8 ± 2.8% after 6 days in dialysis and then it decreased to a minimum of 0.6 ± 0.8% [**Fig. 6-24(a)**]. The decrease in activity over time implies that the fraction of activity measured is related to surface bound ^{227}Th rather than leakage from La(^{227}Th)PO_4 core NPs. The deposition of two nonradioactive $LaPO_4$ shells decreased the leakage of ^{227}Th to <0.1% [**Fig. 6-24(b)**]. It is assumed that the lower leakage

of ^{227}Th in La(^{227}Th)PO_4 core + 2 shells is attributed to the partial removal of free radionuclides during dialysis, the consumption of unreacted species during core-shell synthesis, or both. It is expected that the longer heating times (~6 hours) used during core-shell synthesis will promote the consumption of unreacted species at the NP surface. The leakage of ^{223}Ra from $LaPO_4$ core NPs was 1.8 ± 1.7% after 6 days in dialysis and then it increased to 7.7 ± 12.5% after 23 days [**Fig. 6-24(a)**]. The retention of ^{211}Pb was quantitative in La(^{227}Th)PO_4 core NPs since almost all the activity found in the dialysate originates from ^{223}Ra and only <0.7 ± 0.9% is a consequence of ^{211}Pb leaking from the NPs. As expected, the leakage of ^{223}Ra decreased to a maximum of 0.13 ± 0.13% after deposition of two $LaPO_4$ shells [**Fig. 6-24(b)**]. Similar to core NPs, the retention of ^{211}Pb was quantitative since less than 0.16 ± 0.5% originated directly from radionuclides leaking from the NPs.

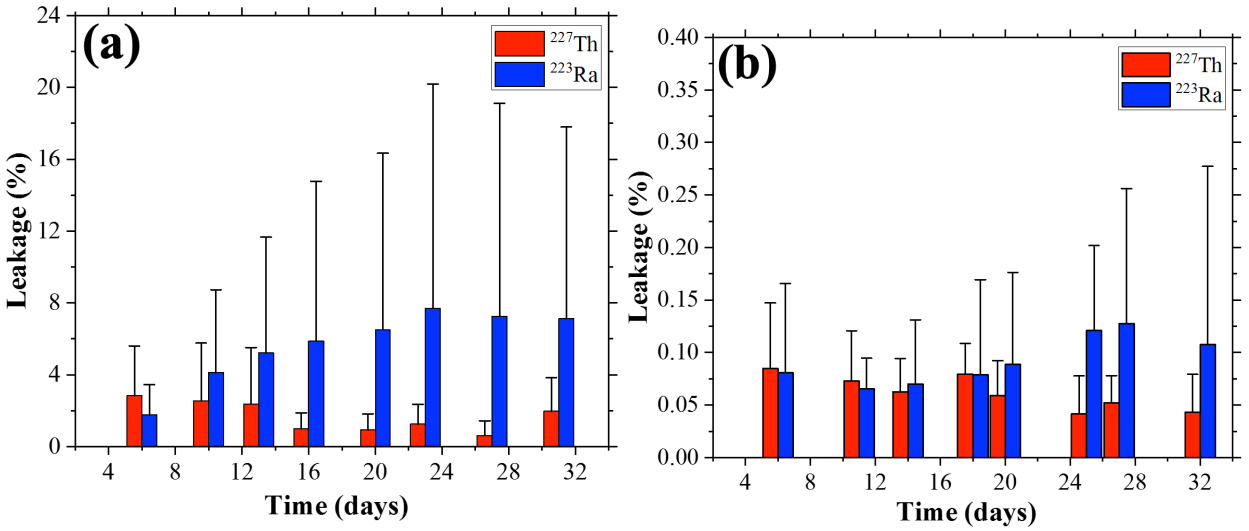

Fig. 6-24 Leakage of (a) ^{227}Th and (b) ^{223}Ra from $LaPO_4$ core and core + 2 shells NPs synthesized at 90 °C for 3 hours by mixing a solution of La/Na-TPP (1:2 La:Na-TPP volume ratio) with $LaPO_4$ core NPs suspension at a 1:1 volume ratio (section 3.2).

As discussed in section 6.2.1.6, the partial retention of ^{223}Ra and ^{211}Pb in $GdVO_4$ and $LaPO_4$ core-shell NPs is attributed to the transfer of the recoil energy to the translation of the NP,

their implantation in neighbor NPs, and adsorption by surface groups based on their recoil energy and range in $GdVO_4$ and $LaPO_4$ compounds. For example, the range of ^{223}Ra (~110 keV) in H_2O and $GdVO_4$ is ~87 nm and ~27 nm, respectively [193]. Similarly, ^{223}Ra and ^{211}Pb (~140 keV) will have a range of 27.0 nm and 32.6 nm in $LaPO_4$, with an estimated density of 5.12 g/cm^3 [193]. It is expected that the decay daughter will be attenuated by adjacent NPs as well as by water until it is implanted on another core or core + 2 shells NP. The retention of decay daughters in both $GdVO_4$ and $LaPO_4$ core + 2 shells NPs may be enhanced by the formation of aggregates, which facilitate their implantation in a neighbor NP. The difference in the *in vitro* retention of ^{227}Th and ^{223}Ra between $GdVO_4$ and $LaPO_4$ could be related to the yield or fraction of NPs in suspension. Although $GdVO_4$ core and core + 2 shells NPs had a higher leakage of ^{223}Ra, the fraction of activity released could be within the therapeutic window where acceptable myelotoxicity is caused by ^{223}Ra [198]. The retention of ~75% of ^{223}Ra activity within $GdVO_4$ core + 2 shells NPs could mitigate the myelosuppression caused by free ^{223}Ra cations, which has been observed in rodent studies using CD70 targeted ^{227}Th conjugate [115].

The radiochemical yield of ^{227}Th was 62% and 81% for Gd(^{227}Th)VO_4 core and core + 2 shells NPs, respectively. La(^{227}Th)PO_4 core and core + 2 shells NPs had a radiochemical yield of 96.7 ± 2.7% and 96.6 ± 0.4%, respectively. The yield obtained for Gd(^{227}Th)VO_4 core and core + 2 shells NPs was lower than that of targeted ^{227}Th radioimmunoconjugates (>95%), however, the partial retention of radionuclides, potential increase in specific activity, and promising multifunctional properties, make $GdVO_4$ suitable for TRT and theranostic applications. Similarly, the ability to quantitatively retain decay daughters in La(^{227}Th)PO_4 core + 2 shells NPs represents a major advantage for TRT applications. Overall, these results demonstrate the potential of both $GdVO_4$ and $LaPO_4$ core-shell NPs as carriers of ^{227}Th for TRT.

6.2.3 $GdVO_4$ NPs doped with ^{223}Ra, ^{225}Ac, and ^{227}Th

$GdVO_4$ NPs doped with ^{223}Ra, ^{225}Ac, and ^{227}Th synthesized as described in section 3.3.2 were evaluated as radionuclide carriers for TRT based on the simplicity of the synthesis route for radiochemical preparations. Prior to the synthesis of radionuclide-doped $GdVO_4$ NPs, the flexibility of the tetragonal crystal structure to host multivalent ions was assessed by using La^{3+}, Ba^{2+}, Bi^{3+}, Cs^{+}, and Pb^{2+} as surrogates of $^{225}Ac^{3+}$, $^{223}Ra^{2+}$, $^{213}Bi^{3+}$, $^{221}Fr^{+}$, and $^{211}Pb^{2+}$, respectively. Doping lanthanide-based ceramics with surrogate ions is a common practice to evaluate solid solutions for minor actinide immobilization [199], [200]. The presence of second phases was evaluated based on the diffraction patterns of the surrogate-doped $GdVO_4$ NPs. The concentration of each element found in the dialysate was determined using ICP-OES to assess the ability of $GdVO_4$ NPs to host surrogate ions.

The synthesis of surrogate-doped $GdVO_4$ NPs consisted in the mixing of aqueous solutions of $LaCl_3 \cdot 7H_2O$, CsCl, and $BiCl_3$ at 1 at.% or 10 at.% of La, Cs, and Bi ions with respect to Gd. This solution was evaporated until dryness at 80 ºC and then mixed with $GdCl_3$ (1 mmol, 0.1 M) using a vortex mixer and an ultrasonic bath. In this case, Na_3VO_4 (1 mmol, 0.1 M, pH = 12.5) was added dropwise to the aqueous solution containing Gd, La, Cs, and Bi ions under constant stirring. The modification in which $GdCl_3$ and Na_3VO_4 were mixed is based on the steps followed for the synthesis of radionuclide-doped $LnPO_4$ and $LnVO_4$ NPs as presented in previous sections. The pH of the solution was adjusted to ~11 using NaOH (1 M) after Na_3VO_4 was added and then the mixture was left under constant stirring for 30 minutes. It is expected that $GdVO_4$ NPs will be precipitated by adding Na_3VO_4 into $GdCl_3$ based on the results obtained in section 5.2.1. The turbid suspension was transferred into a dialysis membrane and dialyzed against DI water to remove unreacted ions for yield quantification. Similarly, a mixture containing $BaCl_2 \cdot 2H_2O$ and $PbCl_2$, at 1 at.% or 10 at.% of Ba and Pb ions with respect to Gd, was evaporated and mixed with $GdCl_3$.

Afterwards, the same steps described above for the synthesis and cleaning of $GdVO_4$ NPs doped with La, Cs, and Bi ions were followed.

For radiochemical synthesis, a 0.1 M HNO_3 solution containing ~4.7 µCi, 4.4 µCi, and 10.1 µCi of ^{223}Ra, ^{225}Ac, and ^{227}Th, respectively, was evaporated to dryness in a conical vial using an infrared heat lamp and a hot plate. The addition of chemicals ($GdCl_3 \cdot 6H_2O$ and Na_3VO_4), the adjustment of the pH, and stirring were carried out as described above for the surrogate-doped $GdVO_4$ NPs. Additionally, a sample of $GdVO_4$ NPs doped with ~34 µCi of ^{223}Ra was synthesized by mixing first a Na_3VO_4 solution with the radionuclides and then adding $GdCl_3$. The pH of the suspension was adjusted to ~11 using NaOH (1 M) and allowed to stir for 30 minutes before dialysis. *In vitro* retention of radionuclides over time was assessed as described in section 3.4.7. These results have been adapted from a manuscript that is under preparation.

6.2.3.1 Crystal structure

The diffraction patterns of surrogate-doped $GdVO_4$ NPs are shown in **Fig. 6-25**. $GdVO_4$ NPs doped with either 1 at.% or 10 at.% of Ba and Pb have a tetragonal system with zircon-type structure corresponding to $GdVO_4$ (pdf: 00-017-0260). Absence of additional phases in the diffraction patterns suggests that both Ba and Pb were successfully and uniformly incorporated within the $GdVO_4$ host lattice (**Fig. 6-25**). This indicates that radionuclides such as ^{223}Ra and ^{211}Pb may be retained within $GdVO_4$ NPs. $GdVO_4$ NPs doped with either 1 at.% or 10 at.% of La, Cs, and Bi are characterized by two phases, $GdVO_4$ with a tetragonal system (pdf: 00-017-0260) and BiClO with a tetragonal system and space group $P_{4/129}$ (pdf: 01-085-0861). The presence of the BiClO phase, highlighted with *, is clearly observed for 10 at.% of La, Cs, and Bi, whereas for 1 at.% only the peak ~25.8º can be seen (**Fig. 6-25**). The presence of this phase is related to the tendency of $BiCl_3$ to hydrolyze into BiClO in aqueous media and it may also suggest that Bi ions are not retained within the $GdVO_4$ lattice. BiClO is characterized by a yellowish appearance which

explains the characteristic color observed after synthesis of surrogate-doped $GdVO_4$ NPs. It is assumed that La and Cs are incorporated in the $GdVO_4$ lattice since no additional phases were observed (**Fig. 6-25**). The crystallite size of the surrogate-doped $GdVO_4$ NPs was not affected by the composition and concentration of surrogate ions since the values are between 6.9–7.9 nm.

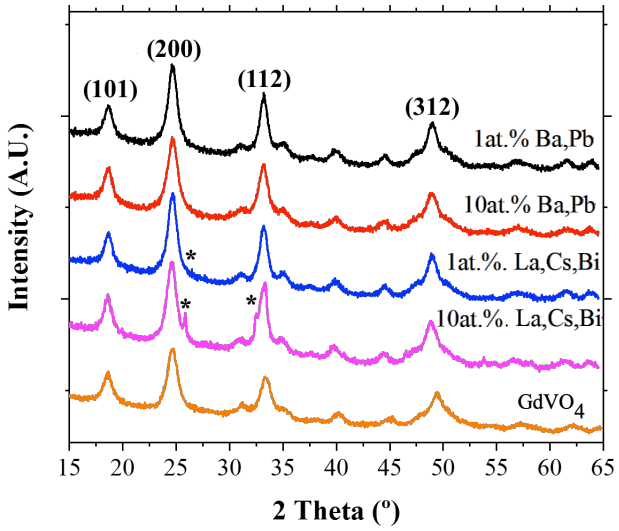

Fig. 6-25 Diffraction patterns of 1 at.% and 10 at.% surrogate-doped $GdVO_4$ NPs synthesized by adding a solution of Na_3VO_4 into $GdCl_3$, while adjusting the pH at 11.

6.2.3.2 Chemical Yield

To assess the retention of surrogate ions, surrogate-doped $GdVO_4$ NPs were dialyzed against DI water for 20 hours. The chemical yield was calculated for each element based on its concentration in the dialysate and dialyzed NPs suspension with respect to the nominal concentration. The average chemical yield and standard deviation for Gd, La, Bi, Ba, and Pb are summarized in **Table 6-6**. The chemical yield ~100% of Gd indicates that all Gd cations participated in $GdVO_4$ NPs formation. The similar chemical properties and ionic radii between La and Ac cations allow the implementation of nonradioactive La as surrogate for the characterization and evaluation of Ac-doped compounds. Herein, the chemical yield of La cations was used as a tool to assess the radiochemical yield and immobilization of Ac isotopes within $GdVO_4$ NPs.

$GdVO_4$ NPs doped with either 1 at.% or 10 at.% of La, Cs, and Bi had a chemical yield ~100% for La. These results imply that almost all Ac cations may be retained within $GdVO_4$ NPs. This is particularly relevant since ~55 Ci of ^{225}Ac and 69.5 mCi of ^{227}Ac could be retained within $GdVO_4$ NPs considering the concentration of La cations used. The evaluation of the chemical yield of Cs as surrogate of Fr isotopes was not possible because of the low concentrations used and the minimum detection limit of Cs by ICP-OES set at 3.2 ppm. The chemical yield of Bi shows an increase from 65.4 ± 137.1% to 100.0 ± 37.7% for $GdVO_4$ NPs doped with 1 at.% and 10 at.%, respectively. As evidenced from the diffraction patterns, the precipitation of BiClO could be responsible for the large standard deviation and difference between both samples and does not assure that Bi cations are retained within the NPs.

Table 6-6 Mean chemical yield and standard deviation of different elements in surrogate-doped $GdVO_4$ NPs synthesized by adding a solution of Na_3VO_4 into $GdCl_3$, while adjusting the pH at 11.

Sample	Gd (%)	La (%)	Bi (%)	Ba (%)	Pb (%)
1 at.% Ba, Pb	100.0 ± 0.5			85.1 ± 7.5	100.0 ± 64.0
10 at.% Ba, Pb	100.0 ± 2.0			59.6 ± 3.9	91.9 ± 4.4
1 at.% La, Cs, Bi	99.3 ± 0.7	100.0 ± 1.4	65.4 ± 137.1		
10 at.% La, Cs, Bi	100.0 ± 5.3	100.0 ± 5.5	100.0 ± 37.7		

Increasing the concentration of Ba and Pb from 1 at.% to 10 at.% caused a decrease of the chemical yield for both elements suggesting that Ra isotopes will be partially retained within $GdVO_4$ NPs (**Table 6-6**). The large standard deviation obtained for 1 at.% of Pb may be related to the low concentration of ions used and the detection limit for this element.

6.2.3.3 In vitro Retention of ^{223}Ra, ^{225}Ac, ^{227}Th, and Decay Daughters

In **Fig. 6-26**, the leakage of ^{223}Ra, ^{225}Ac, ^{227}Th, and decay daughters from $GdVO_4$ NPs over time is shown. The leakage of ^{225}Ac increased continuously from 17.4 ± 1.2% to 36.7 ± 2.2% after

7 days in dialysis suggesting the partial retention of this radionuclide within the $GdVO_4$ NPs [**Fig. 6-26(a)**]. This result suggests that using La as surrogates of ^{225}Ac may have its limitations since the former was homogeneously retained within $GdVO_4$ NPs based on its chemical yield (**Table 6-6**). It is expected that the difference in ionic radii between Ac and Gd as well as the ability of tetragonal structures to host mainly actinides with a tetravalent oxidation state may contribute to the leakage of ^{225}Ac observed [27]. The leakage of decay daughters, ^{221}Fr and ^{213}Bi, from $GdVO_4$ NPs is attributed to the recoil energy (100–200 keV) of both radionuclides after α-decay, which is significantly greater than the chemical bond energy [81], [201], [202]. The ~50% retention of ^{221}Fr in $GdVO_4$ NPs is comparable with the 50% and 60% obtained in $LaPO_4$ and $La_{0.5}Gd_{0.5}PO_4$ core NPs after one week [39], [42]. $GdVO_4$ NPs had a quantitative and partial retention of ^{227}Th and its decay daughter ^{223}Ra, respectively [**Fig. 6-26(b)**]. This result supports the potential use of $GdVO_4$ NPs for the retention or immobilization of long-lived thorium radionuclides such as ^{228}Th ($T_{1/2}$ = 1.9 y), ^{229}Th ($T_{1/2}$ = 7880 y), and ^{232}Th ($T_{1/2} = 1.4 \times 10^{10}$ y). The leakage of ^{223}Ra, as decay daughter of ^{227}Th, reached a maximum of 73 ± 4.0% and then decreased to 35.1 ± 2.0% [**Fig. 6-26(b)**]. As discussed previously, the leakage of decay daughters is related to their high recoil energy and large range with respect to the size of $GdVO_4$ NPs [86]. Leakage of ^{223}Ra, as parent radionuclide, from $GdVO_4$ NPs is shown in **Fig. 6-26 (c)** and **(d)**. The difference between both $GdVO_4$ NPs rely in the order in which Na_3VO_4 and $GdCl_3$ aqueous solutions were mixed with ^{223}Ra and decay daughters. In **Fig. 6-26(c)** it is shown the leakage of ^{223}Ra when a Na_3VO_4 solution was added drop-by-drop to a mixture containing Gd and radionuclides cations. $GdVO_4$ NPs showed partial retention of ^{223}Ra since ~25% of activity was found in the dialysate, which is consistent to the partial retention of Ba ions obtained from the chemical yield experiments of surrogate-doped $GdVO_4$ NPs (**Table 6-6**). The leakage of ^{223}Ra from $GdVO_4$ NPs is almost two times higher to that reported for $LaPO_4$ core NPs (12.7%) [38]. The partial retention of ^{223}Ra may be related to (i) the

difference in ionic radii between Gd and Ra, (ii) the ability of tetragonal structures to host primarily actinides with a tetravalent oxidation state, and/or (ii) the lack of electroneutrality in the $GdVO_4$ structure ($Ln^{3+} \leftrightarrow Me^{2+} + Me^{4+}$) [27]. $GdVO_4$ NPs showed a quantitative retention of ^{211}Pb since the activity found in the dialysate originates from the decay of ^{223}Ra and not from ^{211}Pb leaking. A significant difference in the retention ^{223}Ra was observed between $GdVO_4$ NPs depending in the order in which the chemical reagents were mixed with the radionuclides. The addition of Na_3VO_4 directly to ^{223}Ra and decay daughters caused a continuous increase in ^{223}Ra leakage up to 43.6 ± 2.4%, whereas ^{211}Pb was quantitatively retained [**Fig. 6-26(d)**]. It is assumed that this difference is related to the precipitation of radionuclide species in the form of hydroxides which remain in solution because of their slow interaction with $[VO_4]^{3-}$ species. Particularly, the precipitation of these species is more probable when Na_3VO_4 is added directly to the radionuclides because of its high pH (12.5). The continuous increase of ^{223}Ra activity over time suggests that this radionuclide is not present as a free ion but as a complex based on the experiments conducted with La cations (section 6.2.1.6). Radiochemical yield for ^{225}Ac-, ^{227}Th-, and ^{223}Ra-doped $GdVO_4$ NPs was 67.7%, 66.8%, and 70.8%, respectively. The ^{223}Ra-doped $GdVO_4$ NPs suspension prepared by adding Na_3VO_4 directly to the radionuclides had a radiochemical yield of 58.0%. The radiochemical yield of ^{225}Ac obtained for $GdVO_4$ is comparable to the 61% and 57.5% reported for $La(^{225}Ac)PO_4$ and $Ln(^{225}Ac)PO_4$ NPs, respectively [39], [42].

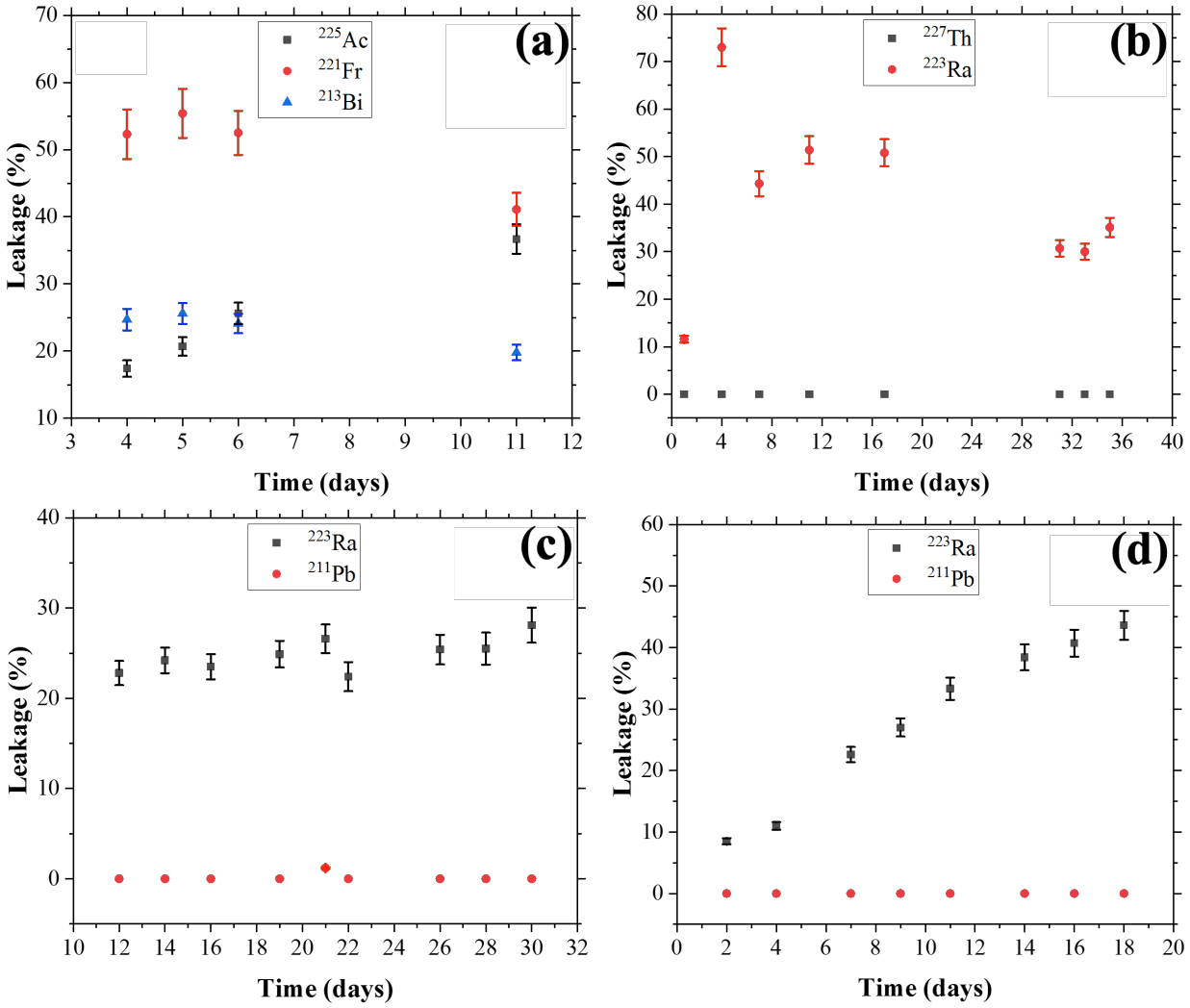

Fig. 6-26 Radionuclide leakage from (a) Gd(^{225}Ac)VO_4, (b) Gd(^{227}Th)VO_4, and (c) Gd(^{223}Ra)VO_4 NPs synthesized by adding a solution of Na_3VO_4 into $GdCl_3$ and radionuclides, while adjusting the pH at 11. (d) Gd(^{223}Ra)VO_4 NPs prepared by adding a solution of $GdCl_3$ into Na_3VO_4 and radionuclides (as reported by Huignard *et al.* [126]), while adjusting the pH at 11.

Overall, both $GdVO_4$ NPs prepared by citrate and flow synthesis displayed similar retention properties of ^{225}Ac, ^{227}Th, and decay daughters. The leakage of ^{225}Ac from the smaller NPs is related to the formation of ^{225}Ac-cit complexes, whereas either the precipitation of $Ac(OH)_3$ or dissociation of surface bound Ac cations could be responsible for the leakage from the larger NPs. The retention of ^{221}Fr was 10% higher for the larger NPs with respect to the smaller NPs

because of their large size, tendency to aggregate, and higher yield. These characteristics of the larger $GdVO_4$ may promote the implantation of decay daughters in adjacent NPs. The presence of citrate groups and hence lower NP yield may be responsible for the leakage of ^{227}Th from the smaller NPs, since a quantitative retention was observed from $GdVO_4$ prepared via flow synthesis. There was no significant difference regarding the retention of ^{223}Ra as decay daughter between both $GdVO_4$ NPs sizes, except for the higher leakage (>50%) observed from the larger NPs in the first 2 weeks [**Fig. 6-26(b)**].

6.3 Summary

In this chapter, radionuclide-doped $LnPO_4$ and $LnVO_4$ core-shell NPs were synthesized by precipitation routes to assess the *in vitro* retention of radionuclides for biomedical and engineering applications. Radionuclide-doped $LnPO_4$ and $LnVO_4$ core-shell NPs were synthesized with specific lanthanide compositions to display properties for multimodal molecular imaging. Influence of the lanthanide composition and core-shell structure on the retention of radionuclides was studied. Additionally, a comparison between the retention capabilities of $LaPO_4$ and $GdVO_4$ core-shell NPs was made based on their crystal structures. The key results obtained from the *in vitro* evaluation of radionuclide-doped $LnPO_4$ and $LnVO_4$ core-shell NPs are summarized below:

- Retention of ^{156}Eu is dependent on the composition and concentration of lanthanide ions within $LnPO_4$ core NPs. An evaluation of the retention properties of $GdPO_4$ and lanthanide-doped $GdPO_4$ core NPs revealed that the retention of ^{156}Eu decreased when Eu is used as dopant ion.
- $La_{(1-x)}Eu_xPO_4$ and $LnPO_4$ (Ln^{3+} = La, Ce, Eu, Gd, Tb, Yb, and Lu) core NPs doped with $^{85, 89}Sr$ and ^{156}Eu confirmed the influence of lanthanide composition and concentration on the retention of radionuclides, particularly ^{156}Eu. At Eu concentrations below 40% in $La_{(1-x)}Eu_xPO_4$, the leakage of ^{156}Eu was ~3 times higher than that observed from

$EuPO_4$ core NPs. The leakage of ^{156}Eu from pure $LnPO_4$ core NPs was influenced by the difference in ionic radii, where $YbPO_4$ and $LuPO_4$ displayed low retention. The retention of strontium isotopes was similar over $La_{(1-x)}Eu_xPO_4$ and $LnPO_4$ core NPs, except for $GdPO_4$ that exhibited a steep increase in leakage because of the electronic peculiarities of Gd cations. $LnVO_4$ NPs are expected to follow a similar trend to that of $LnPO_4$ based on the difference in ionic radii between radionuclides and Ln^{3+} ions. The dependence of radionuclide retention on Ln^{3+} ion composition and concentration has to be considered during the development of multifunctional platforms.

- Formation of ^{225}Ac-citrate complexes is assumed to be the main cause behind the 15–25% leakage of ^{225}Ac from $GdVO_4$ and $Gd_{0.8}Eu_{0.2}VO_4$ core NPs synthesized via the citrate route. The significant increase in ^{225}Ac retention after deposition of two nonradioactive shells is related to the consumption of ^{225}Ac-citrate complexes during the multi-step synthesis procedure. $Gd_{0.8}Eu_{0.2}VO_4$ and $GdVO_4$ core-shell NPs displayed partial retention of decay daughters (^{221}Fr and ^{213}Bi) as well as molecular imaging functionalities for FI and/or MRI. These radionuclide-doped $LnVO_4$ NPs have promising applications in biological settings as theranostic platforms.
- Retention of ^{227}Th was studied for the first time in nano-platforms such as $GdVO_4$ and $LaPO_4$ core and core + 2 shells NPs. Leakage of ^{227}Th from both core NPs was ~3%, while deposition of two nonradioactive shells increase the retention to >98% and >99.9% in $GdVO_4$ and $LaPO_4$, respectively. $LaPO_4$ core NPs retained >90% of ^{223}Ra, whereas ~40% leakage of ^{223}Ra was observed for $GdVO_4$ core NPs. Two nonradioactive shells enhanced the retention of ^{223}Ra to >99.8% and >75% in $LaPO_4$ and $GdVO_4$, respectively. Differences in decay daughter retention between $LaPO_4$ and

$GdVO_4$ may be related to either the NPs yield, surface chemistry, or particle size distribution.

- $GdVO_4$ NPs prepared via flow synthesis displayed the ability to host multivalent *in vivo* α-generators radionuclides. Quantitative retention of ^{227}Th and partial retention of ^{223}Ra and ^{225}Ac as parent radionuclides may be related to the differences in ionic radii, the electroneutrality within $GdVO_4$, and the ability of zircon-type structures to host mainly tetravalent actinides. Leakage of decay daughters ^{221}Fr and ^{223}Ra is caused by their recoil energy and range in $GdVO_4$.
- It is expected that $LnPO_4$ and $LnVO_4$ NPs could be doped with multiple radionuclides, for both diagnostic and therapeutic applications, based on the ability to host multivalent ions of their crystal structures, monoclinic and tetragonal.

7 Conclusions and Future Work

In this work, $LnVO_4$ and $LnPO_4$ NPs were synthesized in aqueous media following multi-step precipitation procedures for the preparation of core and core-shell structures. These procedures do not require specialized equipment such as autoclaves, microwave reactors, or high frequency sonicators. The simplicity of the implemented synthesis methods and the ability to obtain crystalline $LnVO_4$ and $LnPO_4$ core-shell NPs with particle size below 30 nm, different shape (spherical, trapezoidal, ellipsoidal), and good physical stability (stable in suspension) made them appealing for the development of multifunctional platforms for biomedical applications as well as for radiochemical settings. The composition and concentration of lanthanide ions can be adjusted to provide fluorescence and magnetic functionalities, whereas radionuclides can be retained within the crystal structure of both $LnVO_4$ and $LnPO_4$ NPs.

The particle size and size distribution of $LnPO_4$ was controlled by adjusting the concentration of Na-TPP, heating time, and temperature during synthesis. Although increasing the concentration of Na-TPP enhanced the physical stability and contributed to the formation of $LnPO_4$ NPs with small and uniform size, a large fraction of polyphosphate species on the NPs surface may act as luminescence quenchers. $LnPO_4$ NPs doped with Eu^{3+} and Ce^{3+}:Tb^{3+} displayed low luminescence emission as a result of their nanocrystalline nature and the large fraction of phosphate species used during synthesis. Post-annealing treatments may be considered to enhance the crystallinity and hence the luminescence emission of $LnPO_4$ NPs, however, an increase in particle size and aggregation may limit their application in biomedical settings. The retention of lanthanide and/or therapeutically relevant radionuclides within $LnPO_4$ core NPs was assessed by

using ^{156}Eu and $^{85, 89}Sr$. Retention of ^{156}Eu in $LnPO_4$ core NPs was influenced by the elemental composition and concentration of Eu cations, while the retention of strontium radionuclides was similar between the samples tested. The leakage of radionuclides observed was not related to dissolution of $LnPO_4$ NPs but rather to radionuclides bound to the NP surface or attached to the stabilizing polymeric shell formed by phosphate oligomers.

$LnVO_4$ NPs displayed small particle size (<10 nm) and narrow size distributions when using sodium citrate as complexing agent. Temperature, heating time, and reagents concentration can be adjusted to obtain the desired particle size and size distribution. Luminescence emission of europium-doped $GdVO_4$ core NPs was better than the one observed for $Gd_{(1-x)}Eu_xPO_4$ NPs because of an efficient energy transfer between $[VO_4]^{3-} \rightarrow Eu^{3+}$. $Gd_{0.8}Eu_{0.2}VO_4$ core NPs displayed the highest luminescence emission without significant concentration quenching among the different Eu^{3+} concentrations studied. $GdVO_4$ core NPs may also be used as MRI contrast agents based on their longitudinal proton relaxivity (r_1 = 0.805 s^{-1} mM^{-1}). The successful development of core-shell structures was achieved by mixing a solution containing lanthanide-citrate-vanadate complexes with the $LnVO_4$ core NPs suspensions followed by heating at the specified conditions. Larger $LnVO_4$ NPs (20–40 nm) with either trapezoidal, ellipsoidal, or anisotropic shape were precipitated by adding $LnCl_3$ into Na_3VO_4, while adjusting the pH of the solution at different values. These particles displayed both luminescence and magnetic properties and the ability to host multivalent cations within their crystal structure.

The *in vitro* retention of therapeutically relevant radionuclides ^{223}Ra, ^{225}Ac, and ^{227}Th, and decay daughters in $LaPO_4$, $Gd_{0.8}Eu_{0.2}VO_4$, and $GdVO_4$ core and core + 2 shells NPs was evaluated. The partial *in vitro* retention of radionuclides demonstrates the potential of $Gd_{0.8}Eu_{0.2}VO_4$ and $GdVO_4$ core and core + 2 shells for the development of multifunctional diagnostic and therapeutic platforms. The 15–25% leakage observed for ^{225}Ac in core NPs is caused by the presence of this

radionuclide as a metal-citrate complex in solution. A high consumption of oligomeric species during core-shell synthesis caused a significant decrease in ^{225}Ac leakage (<5%). The large fraction of ^{227}Th retained within both core and core + 2 shells exhibits a difference in the retention capabilities of $LnVO_4$ NPs based on the valence state of the radionuclides. The influence of the valence state in the retention properties of $GdVO_4$ NPs was confirmed by doping the larger particles with either ^{223}Ra, ^{225}Ac, or ^{227}Th. Based on these results it was established that tetravalent actinides (^{227}Th) may be quantitatively retained, whereas trivalent actinides (^{225}Ac) and alkaline earth metals (^{223}Ra) are partially retained. Although the deposition of shells increased the retention of both ^{221}Fr and ^{223}Ra, the high recoil energy and large range of decay daughters in $LnVO_4$ are the main reason behind radionuclide leakage from both $LnVO_4$ core and core + 2 shells NPs. $LaPO_4$ core + 2 shells NPs were able to quantitatively retain both ^{227}Th and first decay daughter ^{223}Ra as expected from previous studies regarding the *in vitro* retention of ^{225}Ac and ^{223}Ra in $LnPO_4$ core and core + 2 shells NPs. The difference in ^{223}Ra retention between $LaPO_4$ and $GdVO_4$ may be related to either the fraction of NPs in suspension, their surface chemistry, or their particle size distribution.

The suitable radiochemical synthesis, *in vitro* retention of radionuclides, fluorescence emission, and proton relaxivity encourage the use of $LnVO_4$ core-shell NPs as promising theranostic platforms for implementation in multimodal molecular imaging and TRT. Enhancement of retention capabilities of decay daughters in $LnVO_4$ NPs must be carried out to minimize the toxicity to healthy organs. Alternatives to enhance the retention of radionuclides encompass the development of multilayered structures, core-shell NPs, having shells with different compositions. A greater number of $LnVO_4$ shells will result in a thicker barrier to promote the intrinsic retention of radionuclides. The same rationale is followed by using a gold shell, which may provide the same retention properties with a smaller shell thickness owing the higher stopping

power of gold with respect to $LnVO_4$. Deposition of an inorganic shell with ion exchange characteristics may reduce the leakage of radionuclides by increasing their reloading. The deposition of shells with different composition may also decrease the toxicity of $LnVO_4$ and $LnPO_4$ NPs as well as to facilitate their functionalization and antibody conjugation for characterization and application in biological settings.

It is expected that the release of unreacted and surface bound lanthanide ions, particularly of Gd^{3+} ions, from both $LnPO_4$ and $LnVO_4$ NPs may result in *in vivo* toxicity if intended for biomedical applications [66], [203], [204]. Evaluation of efficient cleaning routes to remove unreacted species is of utmost importance to prevent unwanted toxicity. Future efforts should focus in the functionalization and bioconjugation of both $LnPO_4$ and $LnVO_4$ NPs to assess their *in vitro* and *in vivo* toxicity. Previous studies on Gd_2O_3 and $GdPO_4$ have reported significant levels of toxicity when bare NPs are used *in vivo* due to the transmetallation of Gd^{3+} ions with endogenous cations [203], [205], [206]. Surface modification of both $LnPO_4$ and $LnVO_4$ NPs will enhance their biocompatibility and prevent the release of Ln cations *in vivo* [21], [58], [205], [207]. Surface-functionalized $LnPO_4$ and $LnVO_4$ NPs doped with therapeutically relevant radionuclides should also be evaluated in biological settings to assess the response of cancer cells and tumors.

Simulation of the retention of *in vivo* α-generators radionuclides and decay daughters within $LnPO_4$ and $LnVO_4$ NPs would provide valuable information regarding the mechanism behind the retention of radionuclides. Experimental results could be compared with the simulated values as has been carried out with polymersomes. The simulation of $LnPO_4$ and $LnVO_4$ NPs doped with α-emitting radionuclides could also promote their application in nuclear waste management as nuclear waste forms. Development of radionuclide-doped $LnPO_4$ and $LnVO_4$ NPs may facilitate the fabrication of ceramic waste forms since their nanometer size would ease the densification of ceramic pellets. Besides, both $LnPO_4$ and $LnVO_4$ NPs fulfill other requirements

of nuclear waste forms such as good chemical and thermal stability, high thermal conductivity, and structural flexibility to accommodate impurities and dopant ions.

The main contributions of this dissertation are summarized below:

- Evaluation and characterization of $LnPO_4$ NPs with different compositions and concentrations of Ln^{3+} ions using a precipitation route that has been implemented for radiochemical settings. These $LnPO_4$ NPs could be doped with radionuclides towards the development of theranostic platforms for TRT and multimodal molecular imaging.
- Recommendation of a Ln:Na-TPP volume ratio that will contribute to develop $LnPO_4$ NPs with good physical stability and uniform size distribution. Additionally, heating time and temperature could be set at 2 hours and 90 °C to reduce the multistep time-consuming procedure for $LnPO_4$ core-shell NPs.
- Assessment of the *in vitro* retention of ^{227}Th and decay daughters (^{223}Ra and ^{211}Pb) in $LaPO_4$ core and core + 2 shells NPs. The quantitative retention of ^{227}Th and decay daughters is a valuable addition to previous results regarding the evaluation of ^{225}Ac and $^{223,\ 225}Ra$ in $LaPO_4$ based on the characteristics of ^{227}Th (*i.e.* half-life, production, distribution, etc).
- Development of a procedure for synthesis of $LnVO_4$ core-shell NPs based on the mixing of core NPs suspensions with a fresh lanthanide-citrate-vanadate solution.
- Evaluation of $LnVO_4$ core and core-shell NPs as radionuclide carriers (^{225}Ac, ^{223}Ra, and ^{227}Th) for TRT. The $Gd_{0.8}Eu_{0.2}VO_4$ and $GdVO_4$ core and core-shell NPs tested for the retention of radionuclides have functionalities for FI and/or MRI. Therefore, $LnVO_4$ NPs could be used as theranostic platforms for both TRT and multimodal molecular imaging.
- Suggestion of $LnVO_4$ core NPs as carriers of short-lived radionuclides (*i.e.* ^{68}Ga, $T_{1/2}$ = 68 minutes) based on the short synthesis time required to precipitate particles with characteristic morphology, physical stability, and surface chemistry.

List of References

List of References

[1] N. Sanvicens and M. P. Marco, "Multifunctional nanoparticles – properties and prospects for their use in human medicine," *Trends Biotechnol.*, vol. 26, no. 8, pp. 425–433, Aug. 2008.

[2] Y. Zhang, W. Wei, G. K. Das, and T. T. Yang Tan, "Engineering lanthanide-based materials for nanomedicine," *J. Photochem. Photobiol. C Photochem. Rev.*, vol. 20, pp. 71–96, Sep. 2014.

[3] C. Liu, Y. Hou, and M. Gao, "Are Rare-Earth Nanoparticles Suitable for In Vivo Applications?," *Adv. Mater.*, vol. 26, no. 40, pp. 6922–6932, Oct. 2014.

[4] A. Szczeszak, A. Ekner-Grzyb, M. Runowski, L. Mrówczyńska, T. Grzyb, and S. Lis, "Synthesis, photophysical analysis, and in vitro cytotoxicity assessment of the multifunctional (magnetic and luminescent) core@shell nanomaterial based on lanthanide-doped orthovanadates," *J. Nanoparticle Res.*, vol. 17, no. 3, Mar. 2015.

[5] M. Abdesselem *et al.*, "Multifunctional Rare-Earth Vanadate Nanoparticles: Luminescent Labels, Oxidant Sensors, and MRI Contrast Agents," *ACS Nano*, vol. 8, no. 11, pp. 11126–11137, Nov. 2014.

[6] T. V. Gavrilović, D. J. Jovanović, K. Smits, and M. D. Dramićanin, "Multicolor upconversion luminescence of GdVO 4 :Ln 3+ /Yb 3+ (Ln 3+ = Ho 3+ , Er 3+ , Tm 3+ , Ho 3+ /Er 3+ /Tm 3+) nanorods," *Dyes Pigments*, vol. 126, pp. 1–7, Mar. 2016.

[7] A. Escudero *et al.*, "Synthesis and functionalization of monodisperse near-ultraviolet and visible excitable multifunctional Eu^{3+}, Bi^{3+}:$REVO_4$ nanophosphors for bioimaging and biosensing applications," *Nanoscale*, vol. 8, no. 24, pp. 12221–12236, 2016.

[8] V. Muhr *et al.*, "Europium-doped GdVO 4 nanocrystals as a luminescent probe for hydrogen peroxide and for enzymatic sensing of glucose," *Sens. Actuators B Chem.*, vol. 241, pp. 349–356, Mar. 2017.

[9] T. Kim *et al.*, "Mesoporous silica-coated luminescent Eu^{3+} doped $GdVO_4$ nanoparticles for multimodal imaging and drug delivery," *RSC Adv*, vol. 4, no. 86, pp. 45687–45695, Sep. 2014.

[10] B. K. Gupta *et al.*, "Probing a Bifunctional Luminomagnetic Nanophosphor for Biological Applications: a Photoluminescence and Time-Resolved Spectroscopic Study," *Small*, vol. 7, no. 13, pp. 1767–1773, Jul. 2011.

[11] I. E. Kolesnikov, E. V. Golyeva, A. A. Kalinichev, M. A. Kurochkin, E. Lähderanta, and M. D. Mikhailov, "Nd 3+ single doped YVO 4 nanoparticles for sub-tissue heating and thermal sensing in the second biological window," *Sens. Actuators B Chem.*, vol. 243, pp. 338–345, May 2017.

[12] T. R. Senty *et al.*, "Photoluminescence spectroscopy of YVO_4:Eu^{3+} nanoparticles with aromatic linker molecules: A precursor to biomedical functionalization," *J. Appl. Phys.*, vol. 115, no. 16, p. 163107, Apr. 2014.

[13] X. Kang *et al.*, "Poly(acrylic acid) modified lanthanide-doped $GdVO_4$ hollow spheres for up-conversion cell imaging, MRI and pH-dependent drug release," *Nanoscale*, vol. 5, no. 1, pp. 253–261, 2013.

[14] Y. Liu, G. Liu, X. Dong, J. Wang, and W. Yu, "Tunable photoluminescence and magnetic properties of Dy $^{3+}$ and Eu $^{3+}$ doped GdVO $_4$ multifunctional phosphors," *Phys. Chem. Chem. Phys.*, vol. 17, no. 40, pp. 26638–26644, 2015.

[15] S. Huang, Z. Cheng, P. Ma, X. Kang, Y. Dai, and J. Lin, "Luminescent GdVO4:Eu3+ functionalized mesoporous silica nanoparticles for magnetic resonance imaging and drug delivery," *Dalton Trans.*, vol. 42, no. 18, p. 6523, 2013.

[16] T. Tegafaw *et al.*, "Dual-mode T_1 and T_2 magnetic resonance imaging contrast agent based on ultrasmall mixed gadolinium-dysprosium oxide nanoparticles: synthesis, characterization, and *in vivo* application," *Nanotechnology*, vol. 26, no. 36, p. 365102, Sep. 2015.

[17] C. Xu and X. Qu, "Cerium oxide nanoparticle: a remarkably versatile rare earth nanomaterial for biological applications," *NPG Asia Mater.*, vol. 6, no. 3, pp. e90–e90, Mar. 2014.

[18] M. L. Debasu, D. Ananias, S. L. C. Pinho, C. F. G. C. Geraldes, L. D. Carlos, and J. Rocha, "(Gd,Yb,Tb)PO4 up-conversion nanocrystals for bimodal luminescence–MR imaging," *Nanoscale*, vol. 4, no. 16, p. 5154, 2012.

[19] W. Xu *et al.*, "A T1, T2 magnetic resonance imaging (MRI)-fluorescent imaging (FI) by using ultrasmall mixed gadolinium–europium oxide nanoparticles," *New J. Chem.*, vol. 36, no. 11, p. 2361, 2012.

[20] F. Lux, L. Sancey, A. Bianchi, Y. Crémillieux, S. Roux, and O. Tillement, "Gadolinium-based nanoparticles for theranostic MRI-radiosensitization," *Nanomed.*, vol. 10, no. 11, pp. 1801–1815, Jun. 2015.

[21] H. Hifumi *et al.*, "Dextran Coated Gadolinium Phosphate Nanoparticles for Magnetic Resonance Tumor Imaging," *J. Mater. Chem.*, vol. 19, no. 35, p. 6393, 2009.

[22] H. Dong *et al.*, "Lanthanide Nanoparticles: From Design toward Bioimaging and Therapy," *Chem. Rev.*, vol. 115, no. 19, pp. 10725–10815, Oct. 2015.

[23] C. Duan, L. Liang, L. Li, R. Zhang, and Z. P. Xu, "Recent progress in upconversion luminescence nanomaterials for biomedical applications," *J. Mater. Chem. B*, vol. 6, no. 2, pp. 192–209, 2018.

[24] W. Yin *et al.*, "Lanthanide-doped GdVO4 upconversion nanophosphors with tunable emissions and their applications for biomedical imaging," *J. Mater. Chem.*, vol. 22, no. 14, p. 6974, 2012.

[25] W. Xu, K. Kattel, J. Y. Park, Y. Chang, T. J. Kim, and G. H. Lee, "Paramagnetic nanoparticle T1 and T2 MRI contrast agents," *Phys. Chem. Chem. Phys.*, vol. 14, no. 37, p. 12687, 2012.

[26] A. E. Grechanovsky, N. N. Eremin, and V. S. Urusov, "Radiation resistance of LaPO4 (monazite structure) and YbPO4 (zircon structure) from data of computer simulation," *Phys. Solid State*, vol. 55, no. 9, pp. 1929–1935, Sep. 2013.

[27] S. Neumeier *et al.*, "New insights into phosphate based materials for the immobilisation of actinides," *Radiochim Acta*, vol. 105, no. 11, pp. 961–984, 2017.

[28] M. R. Rafiuddin and A. P. Grosvenor, "Probing the effect of radiation damage on the structure of rare-earth phosphates," *J. Alloys Compd.*, vol. 653, pp. 279–289, Dec. 2015.

[29] R. T. M. de Rosales, "Potential clinical applications of bimodal PET-MRI or SPECT-MRI agents," *J. Label. Compd. Radiopharm.*, vol. 57, no. 4, pp. 298–303, Apr. 2014.

[30] A. Rahmim and H. Zaidi, "PET versus SPECT: strengths, limitations and challenges:," *Nucl. Med. Commun.*, vol. 29, no. 3, pp. 193–207, Mar. 2008.

[31] F.-M. Lu and Z. Yuan, "PET/SPECT molecular imaging in clinical neuroscience: recent advances in the investigation of CNS diseases," *Quant. Imaging Med. Surg.*, vol. 5, no. 3, pp. 433–447, Jun. 2015.

[32] B. Kharisov, O. Kharissova, and S. Berdonosov, "Radioactive Nanoparticles and their Main Applications: Recent Advances," *Recent Pat. Nanotechnol.*, vol. 8, no. 2, pp. 79–96, Jun. 2014.

[33] L. Yang *et al.*, "Intrinsically radiolabeled multifunctional cerium oxide nanoparticles for in vivo studies," *J. Mater. Chem. B*, vol. 1, no. 10, p. 1421, 2013.

[34] Y. Yang *et al.*, "Hydrothermal synthesis of NaLuF4:153Sm,Yb,Tm nanoparticles and their application in dual-modality upconversion luminescence and SPECT bioimaging," *Biomaterials*, vol. 34, no. 3, pp. 774–783, Jan. 2013.

[35] Y. Sun *et al.*, "Fluorine-18 labeled rare-earth nanoparticles for positron emission tomography (PET) imaging of sentinel lymph node," *Biomaterials*, vol. 32, no. 11, pp. 2999–3007, Apr. 2011.

[36] Y. Yin, Z. Tan, L. Hu, S. Yu, J. Liu, and G. Jiang, "Isotope Tracers To Study the Environmental Fate and Bioaccumulation of Metal-Containing Engineered Nanoparticles: Techniques and Applications," *Chem. Rev.*, vol. 117, no. 5, pp. 4462–4487, Mar. 2017.

[37] P. Padmanabhan, A. Kumar, S. Kumar, R. K. Chaudhary, and B. Gulyás, "Nanoparticles in practice for molecular-imaging applications: An overview," *Acta Biomater.*, vol. 41, pp. 1–16, Sep. 2016.

[38] J. V. Rojas, J. D. Woodward, N. Chen, A. J. Rondinone, C. H. Castano, and S. Mirzadeh, "Synthesis and characterization of lanthanum phosphate nanoparticles as carriers for 223 Ra and 225 Ra for targeted alpha therapy," *Nucl. Med. Biol.*, vol. 42, no. 7, pp. 614–620, Jul. 2015.

[39] J. Woodward *et al.*, "LaPO $_4$ Nanoparticles Doped with Actinium-225 that Partially Sequester Daughter Radionuclides," *Bioconjug. Chem.*, vol. 22, no. 4, pp. 766–776, Apr. 2011.

[40] M. F. McLaughlin, D. Robertson, P. H. Pevsner, J. S. Wall, S. Mirzadeh, and S. J. Kennel, "LnPO $_4$ Nanoparticles Doped with Ac-225 and Sequestered Daughters for Targeted Alpha Therapy," *Cancer Biother. Radiopharm.*, vol. 29, no. 1, pp. 34–41, Feb. 2014.

[41] M. F. McLaughlin *et al.*, "Gold Coated Lanthanide Phosphate Nanoparticles for Targeted Alpha Generator Radiotherapy," *PLoS ONE*, vol. 8, no. 1, p. e54531, Jan. 2013.

[42] M. F. McLaughlin, J. Woodward, R. A. Boll, A. J. Rondinone, S. Mirzadeh, and J. D. Robertson, "Gold-coated lanthanide phosphate nanoparticles for an 225Ac in vivo alpha generator," *Radiochim. Acta*, vol. 101, no. 9, pp. 595–600, 2013.

[43] N. Sobol *et al.*, "Synthesis and targeting of gold-coated ^{177} Lu-containing lanthanide phosphate nanoparticles—A potential theranostic agent for pulmonary metastatic disease," *APL Bioeng.*, vol. 2, no. 1, p. 016101, Mar. 2018.

[44] P. G. Kluetz *et al.*, "Radium Ra 223 Dichloride Injection: U.S. Food and Drug Administration Drug Approval Summary," *Clin. Cancer Res.*, vol. 20, no. 1, pp. 9–14, Jan. 2014.

[45] C. Kratochwil *et al.*, "225Ac-PSMA-617 for PSMA-Targeted α-Radiation Therapy of Metastatic Castration-Resistant Prostate Cancer," *J. Nucl. Med.*, vol. 57, no. 12, pp. 1941–1944, Dec. 2016.

[46] F. Goubard, P. Griesmar, and A. Tabuteau, "Alpha self-irradiation effects in ternary oxides of actinides elements: The zircon-like phases AmIIIVO4 and AIINpIV(VO4)2 (A=Sr, Pb)," *J. Solid State Chem.*, vol. 178, no. 6, pp. 1898–1902, Jun. 2005.

[47] A. Huignard, V. Buissette, G. Laurent, T. Gacoin, and J.-P. Boilot, "Synthesis and Characterizations of YVO $_4$:Eu Colloids," *Chem. Mater.*, vol. 14, no. 5, pp. 2264–2269, May 2002.

[48] M. Hamoudeh, M. A. Kamleh, R. Diab, and H. Fessi, "Radionuclides delivery systems for nuclear imaging and radiotherapy of cancer," *Adv. Drug Deliv. Rev.*, vol. 60, no. 12, pp. 1329–1346, Sep. 2008.

[49] R. D. Teo, J. Termini, and H. B. Gray, "Lanthanides: Applications in Cancer Diagnosis and Therapy: Miniperspective," *J. Med. Chem.*, vol. 59, no. 13, pp. 6012–6024, Jul. 2016.

[50] J. A. Barreto, W. O'Malley, M. Kubeil, B. Graham, H. Stephan, and L. Spiccia, "Nanomaterials: Applications in Cancer Imaging and Therapy," *Adv. Mater.*, vol. 23, no. 12, pp. H18–H40, Mar. 2011.

[51] J. Xie, S. Lee, and X. Chen, "Nanoparticle-based theranostic agents," *Adv. Drug Deliv. Rev.*, vol. 62, no. 11, pp. 1064–1079, Aug. 2010.

[52] C. Bouzigues, T. Gacoin, and A. Alexandrou, "Biological Applications of Rare-Earth Based Nanoparticles," *ACS Nano*, vol. 5, no. 11, pp. 8488–8505, Nov. 2011.

[53] M. Ferhi, K. Horchani-Naifer, and M. Férid, "Hydrothermal synthesis and photoluminescence of the monophosphate LaPO4:Eu(5%)," *J. Lumin.*, vol. 128, no. 11, pp. 1777–1782, Nov. 2008.

[54] T. Anfimova, Q. Li, J. O. Jensen, and N. J. Bjerrum, "Thermal Stability and Proton Conductivity of Rare Earth Orthophosphate Hydrates," *Int J Electrochem Sci*, vol. 9, p. 16, 2014.

[55] Y. Liang *et al.*, "High quality colloidal GdVO 4 :Yb,Er upconversion nanoparticles synthesized via a protected calcination process for versatile applications," *Mater. Des.*, vol. 130, pp. 190–196, Sep. 2017.

[56] M. Runowski, K. Dąbrowska, T. Grzyb, P. Miernikiewicz, and S. Lis, "Core/shell-type nanorods of Tb3+-doped LaPO4, modified with amine groups, revealing reduced cytotoxicity," *J. Nanoparticle Res.*, vol. 15, no. 11, Nov. 2013.

[57] F. Meiser, C. Cortez, and F. Caruso, "Biofunctionalization of Fluorescent Rare-Earth-Doped Lanthanum Phosphate Colloidal Nanoparticles," *Angew. Chem. Int. Ed.*, vol. 43, no. 44, pp. 5954–5957, Nov. 2004.

[58] M. F. Dumont *et al.*, "DNA Surface Modified Gadolinium Phosphate Nanoparticles as MRI Contrast Agents," *Bioconjug. Chem.*, vol. 23, no. 5, pp. 951–957, May 2012.

[59] N. O. Nuñez, S. Rivera, D. Alcantara, J. M. de la Fuente, J. García-Sevillano, and M. Ocaña, "Surface modified Eu:GdVO4 nanocrystals for optical and MRI imaging," *Dalton Trans.*, vol. 42, no. 30, p. 10725, 2013.

[60] J. Zhou, Y. Sun, X. Du, L. Xiong, H. Hu, and F. Li, "Dual-modality in vivo imaging using rare-earth nanocrystals with near-infrared to near-infrared (NIR-to-NIR) upconversion luminescence and magnetic resonance properties," *Biomaterials*, vol. 31, no. 12, pp. 3287–3295, Apr. 2010.

[61] A. Escudero *et al.*, "Rare earth based nanostructured materials: synthesis, functionalization, properties and bioimaging and biosensing applications," *Nanophotonics*, vol. 6, no. 5, pp. 881–921, Aug. 2017.

[62] T. Grzyb, A. Gruszeczka, R. J. Wiglusz, Z. Śniadecki, B. Idzikowski, and S. Lis, "Multifunctionality of GdPO4:Yb3+,Tb3+ nanocrystals – luminescence and magnetic behaviour," *J. Mater. Chem.*, vol. 22, no. 43, p. 22989, 2012.

[63] T. Grzyb *et al.*, "Comparative studies of structure, spectroscopic properties and intensity parameters of tetragonal rare earth vanadate nanophosphors doped with Eu(III)," *J. Alloys Compd.*, vol. 741, pp. 459–472, Apr. 2018.

[64] D. G. Shchukin, G. B. Sukhorukov, and H. Möhwald, "Fabrication of Fluorescent Rare Earth Phosphates in Confined Media of Polyelectrolyte Microcapsules," *J. Phys. Chem. B*, vol. 108, no. 50, pp. 19109–19113, Dec. 2004.

[65] Q. L. Vuong *et al.*, "Paramagnetic nanoparticles as potential MRI contrast agents: characterization, NMR relaxation, simulations and theory," *Magn. Reson. Mater. Phys. Biol. Med.*, vol. 25, no. 6, pp. 467–478, Dec. 2012.

[66] T. J. Fraum, D. R. Ludwig, M. R. Bashir, and K. J. Fowler, "Gadolinium-based contrast agents: A comprehensive risk assessment: Gadolinium Risk Assessment," *J. Magn. Reson. Imaging*, vol. 46, no. 2, pp. 338–353, Aug. 2017.

[67] Y. Wu *et al.*, "Lanthanide-based nanocrystals as dual-modal probes for SPECT and X-ray CT imaging," *Biomaterials*, vol. 35, no. 16, pp. 4699–4705, May 2014.

[68] S. L. Yefimova *et al.*, "GdVO 4 :Eu 3+ nanoparticles – Methylene Blue complexes for PDT: Electronic excitation energy transfer study," *J. Lumin.*, vol. 192, pp. 975–981, Dec. 2017.

[69] H. Chen *et al.*, "Nanoscintillator-Mediated X-ray Inducible Photodynamic Therapy for In Vivo Cancer Treatment," *Nano Lett.*, vol. 15, no. 4, pp. 2249–2256, Apr. 2015.

[70] L. Štefančíková *et al.*, "Effect of gadolinium-based nanoparticles on nuclear DNA damage and repair in glioblastoma tumor cells," *J. Nanobiotechnology*, vol. 14, Jul. 2016.

[71] R. Lv, G. Yang, S. Gai, Y. Dai, F. He, and P. Yang, "Multifunctional $LaPO_4$:Ce/Tb@Au mesoporous microspheres: synthesis, luminescence and controllable light triggered drug release," *RSC Adv*, vol. 4, no. 108, pp. 63425–63435, 2014.

[72] A. A. Ansari *et al.*, "Luminescent mesoporous LaVO4:Eu3+ core-shell nanoparticles: synthesis, characterization, biocompatibility and their cytotoxicity," *J. Mater. Chem.*, vol. 21, no. 48, p. 19310, 2011.

[73] R. C. Ewing, "Nuclear waste forms for actinides," *Proc. Natl. Acad. Sci.*, vol. 96, no. 7, pp. 3432–3439, Mar. 1999.

[74] A. Meldrum, L. A. Boatner, W. J. Weber, and R. C. Ewing, "Radiation damage in zircon and monazite," *Geochim. Cosmochim. Acta*, vol. 62, no. 14, pp. 2509–2520, Jul. 1998.

[75] L. Smith, Z. Kuncic, K. (Ken) Ostrikov, and S. Kumar, "Nanoparticles in Cancer Imaging and Therapy," *Journal of Nanomaterials*, 2012. [Online]. Available: https://www.hindawi.com/journals/jnm/2012/891318/. [Accessed: 14-Sep-2018].

[76] D. Kwatra, A. Venugopal, and S. Anant, "Nanoparticles in radiation therapy: a summary of various approaches to enhance radiosensitization in cancer," *Transl. Cancer Res.*, vol. 2, no. 4, p. 13, 2013.

[77] S. Sofou, "Radionuclide carriers for targeting of cancer," *Int. J. Nanomedicine*, p. 181, Jun. 2008.

[78] A. Mitra, A. Nan, B. Line, and H. Ghandehari, "Nanocarriers for Nuclear Imaging and Radiotherapy of Cancer," *Curr. Pharm. Des.*, vol. 12, no. 36, pp. 4729–4749, Dec. 2006.

[79] A. I. Kassis and S. J. Adelstein, "Radiobiologic Principles in Radionuclide Therapy," *J. Nucl. Med.*, vol. 46, no. 1 suppl, pp. 4S-12S, Jan. 2005.

[80] K. Zukotynski, H. Jadvar, J. Capala, and F. Fahey, "Targeted Radionuclide Therapy: Practical Applications and Future Prospects: Supplementary Issue: Biomarkers and their Essential Role in the Development of Personalised Therapies (A)," *Biomark. Cancer*, vol. 8s2, p. BIC.S31804, Jan. 2016.

[81] R. de Kruijff, H. Wolterbeek, and A. Denkova, "A Critical Review of Alpha Radionuclide Therapy—How to Deal with Recoiling Daughters?," *Pharmaceuticals*, vol. 8, no. 2, pp. 321–336, Jun. 2015.

[82] U. B. Hagemann *et al.*, "In Vitro and In Vivo Efficacy of a Novel CD33-Targeted Thorium-227 Conjugate for the Treatment of Acute Myeloid Leukemia," *Mol. Cancer Ther.*, vol. 15, no. 10, pp. 2422–2431, Oct. 2016.

[83] Y.-S. Kim and M. W. Brechbiel, "An overview of targeted alpha therapy," *Tumor Biol.*, vol. 33, no. 3, pp. 573–590, Jun. 2012.

[84] O. Couturier *et al.*, "Cancer radioimmunotherapy with alpha-emitting nuclides," *Eur. J. Nucl. Med. Mol. Imaging*, vol. 32, no. 5, pp. 601–614, Apr. 2005.

[85] J. A. Carrasquillo, "Alpha Radionuclide Therapy: Principles and Applications to NETs," in *Diagnostic and Therapeutic Nuclear Medicine for Neuroendocrine Tumors*, K. Pacak and D. Taïeb, Eds. Cham: Springer International Publishing, 2017, pp. 429–445.

[86] R. H. Larsen *et al.*, "Preparation of TH ^{227} -Labeled Radioimmunoconjugates, Assessment of Serum Stability and Antigen Binding Ability," *Cancer Biother. Radiopharm.*, vol. 22, no. 3, pp. 431–437, Jun. 2007.

[87] F. F. Knapp and A. Dash, "Alpha Radionuclide Therapy," in *Radiopharmaceuticals for Therapy*, New Delhi: Springer India, 2016, pp. 37–55.

[88] J. Elgqvist, S. Frost, J.-P. Pouget, and P. Albertsson, "The Potential and Hurdles of Targeted Alpha Therapy – Clinical Trials and Beyond," *Front. Oncol.*, vol. 3, 2014.

[89] S. K. Imam, "Advancements in cancer therapy with alpha-emitters: a review," *Int. J. Radiat. Oncol.*, vol. 51, no. 1, pp. 271–278, Sep. 2001.

[90] S. Gudkov, N. Shilyagina, V. Vodeneev, and A. Zvyagin, "Targeted Radionuclide Therapy of Human Tumors," *Int. J. Mol. Sci.*, vol. 17, no. 1, p. 33, Dec. 2015.

[91] G. Dancey, R. H. Begent, and T. Meyer, "Imaging in targeted delivery of therapy to cancer," *Target. Oncol.*, vol. 4, no. 3, pp. 201–217, Sep. 2009.

[92] J. Kozempel and M. Vlk, "Nanoconstructs in Targeted Alpha-Therapy," *Recent Pat. Nanomedicine*, vol. 4, no. 2, pp. 71–76, Mar. 2015.

[93] M. R. McDevitt *et al.*, "Radioimmunotherapy with alpha-emitting nuclides," *Eur. J. Nucl. Med. Mol. Imaging*, vol. 25, no. 9, pp. 1341–1351, Sep. 1998.

[94] E. Cędrowska *et al.*, "Functionalized TiO2 nanoparticles labelled with 225Ac for targeted alpha radionuclide therapy," *J. Nanoparticle Res.*, vol. 20, no. 3, Mar. 2018.

[95] R. M. de Kruijff *et al.*, "Improved 225 Ac daughter retention in InPO 4 containing polymersomes," *Appl. Radiat. Isot.*, vol. 128, pp. 183–189, Oct. 2017.

[96] U. Holzwarth, I. Ojea Jimenez, and L. Calzolai, "A random walk approach to estimate the confinement of α-particle emitters in nanoparticles for targeted radionuclide therapy," *Ejnmmi Radiopharm. Chem.*, vol. 3, no. 1, 2018.

[97] G. Henriksen, P. Hoff, and R. H. Larsen, "Evaluation of potential chelating agents for radium," *Appl. Radiat. Isot.*, vol. 56, no. 5, pp. 667–671, May 2002.

[98] A. Piotrowska, E. Leszczuk, F. Bruchertseifer, A. Morgenstern, and A. Bilewicz, "Functionalized NaA nanozeolites labeled with 224,225Ra for targeted alpha therapy," *J. Nanoparticle Res.*, vol. 15, no. 11, Nov. 2013.

[99] A. Piotrowska *et al.*, "Nanozeolite bioconjugates labeled with 223 Ra for targeted alpha therapy," *Nucl. Med. Biol.*, vol. 47, pp. 10–18, Apr. 2017.

[100] S. Sofou, J. L. Thomas, H. Lin, M. R. McDevitt, D. A. Scheinberg, and G. Sgouros, "Engineered Liposomes for Potential α-Particle Therapy of Metastatic Cancer," *J. Nucl. Med.*, vol. 45, no. 2, pp. 253–260, Feb. 2004.

[101] G. Henriksen, B. W. Schoultz, T. E. Michaelsen, Ø. S. Bruland, and R. H. Larsen, "Sterically stabilized liposomes as a carrier for α-emitting radium and actinium radionuclides," *Nucl. Med. Biol.*, vol. 31, no. 4, pp. 441–449, May 2004.

[102] O. Mokhodoeva *et al.*, "Study of 223Ra uptake mechanism by Fe3O4 nanoparticles: towards new prospective theranostic SPIONs," *J. Nanoparticle Res.*, vol. 18, no. 10, Oct. 2016.

[103] A. N. Vasiliev, A. Severin, E. Lapshina, E. Chernykh, S. Ermolaev, and S. Kalmykov, "Hydroxyapatite particles as carriers for 223Ra," *J. Radioanal. Nucl. Chem.*, vol. 311, no. 2, pp. 1503–1509, Feb. 2017.

[104] J. Kozempel *et al.*, "Prospective carriers of 223Ra for targeted alpha particle therapy," *J. Radioanal. Nucl. Chem.*, vol. 304, no. 1, pp. 443–447, Apr. 2015.

[105] S. Westrøm *et al.*, "Ra-224 labeling of calcium carbonate microparticles for internal α-therapy: Preparation, stability, and biodistribution in mice," *J. Label. Compd. Radiopharm.*, vol. 61, no. 6, pp. 472–486, May 2018.

[106] I. . Davis *et al.*, "Comparison of 225actinium chelates: tissue distribution and radiotoxicity," *Nucl. Med. Biol.*, vol. 26, no. 5, pp. 581–589, Jul. 1999.

[107] G. J. Beyer *et al.*, "Comparison of the Biodistribution of 225Ac and Radio-Lanthanides as Citrate Complexes," *Isot. Isot. Environ. Health Stud.*, vol. 26, no. 3, pp. 111–114, Jan. 1990.

[108] A. Morgenstern*, C. Apostolidis, C. Kratochwil, M. Sathekge, and L. K. and F. Bruchertseifer, "An Overview of Targeted Alpha Therapy with 225Actinium and 213Bismuth," *Current Radiopharmaceuticals*, 30-Nov-2018. [Online]. Available: http://www.eurekaselect.com/161764/article. [Accessed: 15-Sep-2018].

[109] S. Sofou, B. J. Kappel, J. S. Jaggi, M. R. McDevitt, D. A. Scheinberg, and G. Sgouros, "Enhanced Retention of the α-Particle-Emitting Daughters of Actinium-225 by Liposome Carriers," *Bioconjug. Chem.*, vol. 18, no. 6, pp. 2061–2067, Nov. 2007.

[110] L. Thijssen, D. R. Schaart, D. de Vries, A. Morgenstern, F. Bruchertseifer, and A. G. Denkova, "Polymersomes as nano-carriers to retain harmful recoil nuclides in alpha radionuclide therapy: a feasibility study," *Radiochim. Acta*, vol. 100, no. 7, pp. 473–482, Jul. 2012.

[111] R. M. de Kruijff *et al.*, "The therapeutic potential of polymersomes loaded with 225 Ac evaluated in 2D and 3D in vitro glioma models," *Eur. J. Pharm. Biopharm.*, vol. 127, pp. 85–91, Jun. 2018.

[112] M.-Y. Chang, J. Seideman, and S. Sofou, "Enhanced Loading Efficiency and Retention of ^{225} Ac in Rigid Liposomes for Potential Targeted Therapy of Micrometastases," *Bioconjug. Chem.*, vol. 19, no. 6, pp. 1274–1282, Jun. 2008.

[113] G. Wang *et al.*, "Retention studies of recoiling daughter nuclides of 225Ac in polymer vesicles," *Appl. Radiat. Isot.*, vol. 85, pp. 45–53, Feb. 2014.

[114] J. Dahle, C. Krogh, K. B. Melhus, J. Borrebæk, R. H. Larsen, and Y. Kvinnsland, "In Vitro Cytotoxicity of Low-Dose-Rate Radioimmunotherapy by the Alpha-Emitting Radioimmunoconjugate Thorium-227–DOTA–Rituximab," *Int. J. Radiat. Oncol.*, vol. 75, no. 3, pp. 886–895, Nov. 2009.

[115] U. B. Hagemann *et al.*, "Targeted alpha therapy using a novel CD70 targeted thorium-227 conjugate in *in vitro* and *in vivo* models of renal cell carcinoma," *Oncotarget*, vol. 8, no. 34, Aug. 2017.

[116] G. Henriksen, Y. S. Bruland, and R. H. Larsen, "Thorium and Actinium Polyphosphonate Compounds as Bone-seeking Alpha Particle-emitting Agents," *ANTICANCER Res.*, p. 5, 2004.

[117] J. O. Frenvik, S. Kristensen, and O. B. Ryan, "Development of separation technology for the removal of radium-223 from decayed thorium-227 in drug formulations. Material screening and method development," *Drug Dev. Ind. Pharm.*, vol. 42, no. 8, pp. 1215–1224, Aug. 2016.

[118] M. Miederer, D. A. Scheinberg, and M. R. McDevitt, "Realizing the potential of the Actinium-225 radionuclide generator in targeted alpha particle therapy applications," *Adv. Drug Deliv. Rev.*, vol. 60, no. 12, pp. 1371–1382, Sep. 2008.

[119] S. Kitson, V. Cuccurullo, A. Ciarmiello, and L. Mansi, "Targeted Therapy Towards Cancer-A Perspective," *Anticancer Agents Med. Chem.*, vol. 17, no. 3, pp. 311–317, Feb. 2017.

[120] R. A. Boll, D. Malkemus, and S. Mirzadeh, "Production of actinium-225 for alpha particle mediated radioimmunotherapy," *Appl. Radiat. Isot.*, vol. 62, no. 2005, pp. 667–679, 2005.

[121] T. Mastren *et al.*, "Simultaneous Separation of Actinium and Radium Isotopes from a Proton Irradiated Thorium Matrix," *Sci. Rep.*, vol. 7, no. 1, pp. 2–8, 2017.

[122] J. R. Griswold *et al.*, "Large scale accelerator production of 225Ac: Effective cross sections for 78– 192 MeV protons incident on 232Th targets," *Appl. Radiat. Isot. J.*, vol. 118, no. September, pp. 366–374, 2016.

[123] V. Radchenko *et al.*, "Application of ion exchange and extraction chromatography to the separation of actinium from proton-irradiated thorium metal for analytical purposes," *J. Chromatogr. A*, vol. 1380, pp. 55–63, 2015.

[124] E. Kukleva, J. Kozempel, M. Vlk, P. Mičolová, and D. Vopálka, "Preparation of 227Ac/223Ra by neutron irradiation of 226Ra," *J. Radioanal. Nucl. Chem.*, vol. 304, no. 1, pp. 263–266, 2015.

[125] V. Buissette, M. Moreau, T. Gacoin, J. P. Boilot, J. Y. Chane-Ching, and T. Le Mercier, "Colloidal synthesis of luminescent rhabdophane LaPO4:Ln 3+·xH2O (Ln = Ce, Tb, Eu; x ≈ 0.7) nanocrystals," *Chem. Mater.*, vol. 16, no. 11, pp. 3767–3773, 2004.

[126] A. Huignard, T. Gacoin, and J.-P. Boilot, "Synthesis and luminescence properties of colloidal YVO4: Eu phosphors," *Chem Mater*, vol. 12, no. 4, pp. 1090–1094, 2000.

[127] U. Holzwarth and N. Gibson, "The Scherrer equation versus the ' Debye – Scherrer equation ,'" *Nat. Nanotechnol.*, vol. 6, no. 9, p. 534, 2011.

[128] R. J. Hunter, *Zeta potential in colloid science: principles and applications*, 1st ed. 1988.

[129] B. N. L. Alejandro Sonzogni, NNDC, "Interactive Chart of Nuclides." [Online]. Available: https://www.nndc.bnl.gov/chart/reCenter.jsp?z=38&n=47. [Accessed: 12-Aug-2018].

[130] M. Toro and J. Rojas, "Influence of Synthesis Parameters on Morphology, Crystalline Structure and Colloidal Stability of Core and Core-Shell LaPO 4 Nanoparticles," in *Processing, Properties, and Design of Advanced Ceramics and Composites: Ceramic Transactions*, Hoboken, NJ, USA: John Wiley & Sons, Inc., 2016, pp. 57–69.

[131] V. Buissette, M. Moreau, T. Gacoin, and J.-P. Boilot, "Luminescent Core/Shell Nanoparticles with a Rhabdophane $LnPO_4$-xH_2O Structure: Stabilization of Ce^{3+}-Doped Compositions," *Adv. Funct. Mater.*, vol. 16, no. 3, pp. 351–355, 2006.

[132] V. Buissette, D. Giaume, T. Gacoin, and J.-P. Boilot, "Aqueous routes to lanthanide-doped oxide nanophosphors," *J. Mater. Chem.*, vol. 16, p. 529, 2006.

[133] K. Riwotzki, H. Meyssamy, H. Schnablegger, A. Kornowski, and M. Haase, "Liquid-phase synthesis of colloids and redispersible powders of strongly luminescing LaPo4:Ce,Tb nanocrystals," *Angew. Chem. - Int. Ed.*, vol. 40, no. 3, pp. 573–576, 2001.

[134] X. Wang and M. Gao, "A facile route for preparing rhabdophane rare earth phosphate nanorods," *J. Mater. Chem.*, vol. 16, no. 14, p. 1360, 2006.

[135] W. Di *et al.*, "Heat-treatment-induced luminescence degradation in Tb3+-doped CePO4 nanorods," *J. Lumin.*, vol. 130, no. 4, pp. 728–732, 2010.

[136] O. S. Wolfbeis, "An overview of nanoparticles commonly used in fluorescent bioimaging," *Chem. Soc. Rev.*, vol. 44, no. 14, pp. 4743–4768, 2015.

[137] J. D. Clogston and A. K. Patri, "Zeta Potential Measurement," in *Characterization of Nanoparticles Intended for Drug Delivery*, S. E. McNeil, Ed. Totowa, NJ: Humana Press, 2011, pp. 63–70.

[138] K. A. Gschneidner, J.-C. G. Bünzli, and V. K. Pecharsky, *Handbook on the physics and chemistry of rare earths. Vol. 39*. North Holland, 2009.

[139] S. Blundell, *Magnetism in Condensed Matter*, 1 Ed. Oxford: Oxford University Press, 2001.

[140] M. Toro-González, D. M. Clifford, R. Copping, S. Mirzadeh, and J. V. Rojas, "Synthesis and characterization of intrinsically radiolabeled lanthanide phosphate nanoparticles toward biomedical and environmental applications," *J. Nanoparticle Res.*, vol. 20, no. 9, Sep. 2018.

[141] Y. Q. Jia, "Crystal radii and effective ionic radii of the rare earth ions," *J. Solid State Chem.*, vol. 95, no. 1, pp. 184–187, 1991.

[142] N. Yaiphaba *et al.*, "Luminescence, lifetime, and quantum yield studies of redispersible Eu 3+ -doped GdPO4 crystalline nanoneedles: Core-shell and concentration effects," *J. Appl. Phys.*, vol. 107, no. 3, 2010.

[143] M. Yang *et al.*, "Morphology controllable and highly luminescent monoclinic LaPO 4:Eu3+ microspheres," *J. Alloys Compd.*, vol. 582, pp. 603–608, 2014.

[144] J. R. Lakowicz, Ed., *Principles of Fluorescence Spectroscopy*. Boston, MA: Springer US, 2006.

[145] Y. Zhang and J. Chen, "Preparation of REPO4 (RE = La–Gd) nanorods from an ionic liquid extraction system and luminescent properties of CePO4:Tb3+," *Rare Met.*, vol. 4, 2016.

[146] H. Dong, Y. Liu, P. Yang, W. Wang, and J. Lin, "Controlled synthesis and characterization of LaPO4, LaPO4:Ce3+ and LaPO4:Ce3+, Tb3+ by EDTA assisted hydrothermal method," *Solid State Sci.*, vol. 12, no. 9, pp. 1652–1660, 2010.

[147] Y. Wenyuan, L. Guanlai, and Z. Li, "Sonochemical synthesis and photoluminescence properties of rare-earth phosphate core/shell nanorods," *J. Rare Earths*, vol. 28, no. 2, pp. 171–175, 2010.

[148] S. Hachani, B. Moine, A. El-akrmi, and M. F??rid, "Luminescent properties of some ortho- and pentaphosphates doped with Gd3+-Eu3+: Potential phosphors for vacuum ultraviolet excitation," *Opt. Mater.*, vol. 31, no. 4, pp. 678–684, 2009.

[149] E. Pavitra, G. S. Rama Raju, and J. S. Yu, "Solvent interface effect on the size and crystalline nature of the GdPO4:Eu3+ nanorods," *Mater. Lett.*, vol. 156, pp. 173–176, 2015.

[150] B. Yan and X. Xiao, "Hydrothermal Synthesis, Microstructure and Photoluminescence of Eu 3+-Doped Mixed Rare Earth Nano-Orthophosphates," *Nanoscale Res. Lett.*, vol. 5, no. 12, pp. 1962–1969, 2010.

[151] H. Khajuria, J. Ladol, S. Khajuria, M. S. Shah, and H. N. Sheikh, "Surfactant mediated hydrothermal synthesis, characterization and luminescent properties of GdPO4: Ce3+/Tb3+ @ GdPO4 core shell nanorods," *Mater. Res. Bull.*, vol. 80, pp. 150–158, 2016.

[152] H. Onoda and T. Funamoto, "Synthesis and Fluorescence Properties of Europium-Lanthanum-Calcium Orthophosphates and Condensed Phosphates," *Adv. Mater. Phys. Chem.*, vol. 2, no. March, pp. 208–211, 2012.

[153] P. C. De Sousa Filho, T. Gacoin, J. P. Boilot, R. I. Walton, and O. A. Serra, "Synthesis and luminescent properties of REVO4-REPO4 (RE = Y, Eu, Gd, Er, Tm, or Yb) heteronanostructures: A promising class of phosphors for excitation from NIR to VUV," *J. Phys. Chem. C*, vol. 119, no. 42, pp. 24062–24074, 2015.

[154] G. A. Bain and J. F. Berry, "Diamagnetic Corrections and Pascal's Constants," *J. Chem. Educ.*, vol. 85, no. 4, p. 532, 2008.

[155] A. Mesbah *et al.*, "Monoclinic Form of the Rhabdophane Compounds: REEPO 4 ·0.667H 2 O," *Cryst Growth Des*, vol. 14, no. 10, pp. 5090–5098, 2014.

[156] H. Lai, A. Bao, Y. Yang, Y. Tao, and H. Yang, "Selective synthesis and luminescence property of monazite- and hexagonal-type LaPO4: Eu nanocrystals," *CrystEngComm*, vol. 11, no. 6, p. 1109, 2009.

[157] R. C. Ropp, "Phosphors Based on Rare Earth Phosphates," *J. Electrochem. Soc.*, vol. 115, no. 8, p. 841, 1968.

[158] N. Yaiphaba, R. S. Ningthoujam, N. S. Singh, R. K. Vatsa, and N. R. Singh, "Probing of inversion symmetry site in Eu 3+ -doped GdPO 4 by luminescence study: Concentration and annealing effect," *J. Lumin.*, vol. 130, pp. 174–180, 2009.

[159] P. C. De Sousa Filho and O. A. Serra, "Tripolyphosphate as precursor for REPO 4:Eu 3+ (RE = Y, La, Gd) by a polymeric method," *J. Fluoresc.*, vol. 18, no. 2, pp. 329–337, 2008.

[160] Y. Y. Fan, Z. C. Hu, J. Yang, C. Zhang, and L. Zhu, "Ultrasonic-assisted synthesis of core-shell structure CePO 4:Tb/GdPO4 and GdPO4/CePO4:Tb nanophosphors and their photoluminescence properties," *Appl. Surf. Sci.*, vol. 266, pp. 22–26, 2013.

[161] S. Rodriguez-Liviano *et al.*, "Synthesis and functionalization of biocompatible Tb:CePO4 nanophosphors with spindle-like shape," *J. Nanoparticle Res.*, vol. 15, no. 2, p. 1402, 2013.

[162] S. J. Motloung, S. K. K. Shaat, K. G. Tshabalala, and O. M. Ntwaeaborwa, "Structure and photoluminescent properties of green-emitting terbium-doped GdV1-x Px O4 phosphor prepared by solution combustion method.," *Lumin. J. Biol. Chem. Lumin.*, no. November 2015, pp. 1069–1076, 2016.

[163] C. Tang, Y. Bando, D. Golberg, and R. Ma, "Cerium phosphate nanotubes: Synthesis, valence state, and optical properties," *Angew. Chem. - Int. Ed.*, vol. 44, no. 4, pp. 576–579, 2005.

[164] A. Tymiński and T. Grzyb, "Are rare earth phosphates suitable as hosts for upconversion luminescence? Studies on nanocrystalline REPO4 (RE=Y, La, Gd, Lu) doped with Yb3+ and Eu3+, Tb3+, Ho3+, Er3+ or Tm3+ ions," *J. Lumin.*, vol. 181, pp. 411–420, Jan. 2017.

[165] G. K. Das *et al.*, "NaDyF4 Nanoparticles as T2 Contrast Agents for Ultrahigh Field Magnetic Resonance Imaging," *J. Phys. Chem. Lett.*, vol. 3, no. 4, pp. 524–529, Feb. 2012.

[166] P. W. Voorhees, "The Theory of Ostwald Ripening," *J. Stat. Phys.*, vol. 38, no. 1–2, pp. 231–252, 1985.

[167] N. Shanta Singh, R. S. Ningthoujam, G. Phaomei, S. D. Singh, A. Vinu, and R. K. Vatsa, "Re-dispersion and film formation of GdVO4 : Ln3+ (Ln3+ = Dy3+, Eu3+, Sm3+, Tm3+) nanoparticles: particle size and luminescence studies.," *Dalton Trans. Camb. Engl. 2003*, vol. 41, no. 15, pp. 4404–12, 2012.

[168] V. Singh, S. Takami, N. Aoki, D. Hojo, T. Arita, and T. Adschiri, "Hydrothermal synthesis of luminescent GdVO4:Eu nanoparticles with dispersibility in organic solvents," *J. Nanoparticle Res.*, vol. 16, no. 5, p. 2378, May 2014.

[169] A. Szczeszak *et al.*, "Structural, Spectroscopic, and Magnetic Properties of Eu 3+ -Doped GdVO 4 Nanocrystals Synthesized by a Hydrothermal Method," *Inorg. Chem.*, vol. 53, p. 12243−12252, 2014.

[170] Z. Zhou, G. Li, and P. Jia, "Molten Salt Synthesis and Luminescent Properties of GdVO4:Eu3+ Nanophosphors," *Rare Met. Mater. Eng.*, vol. 43, no. 7, pp. 1588–1593, 2014.

[171] X. Su, B. Yan, and H. Huang, "In situ co-precipitation synthesis and luminescence of GdVO4: Eu3+ and YxGd1 - XVO4: Eu 3+ microcrystalline phosphors derived from the assembly of hybrid precursors," *J. Alloys Compd.*, vol. 399, no. 1–2, pp. 251–255, 2005.

[172] K. Riwotzki and M. Haase, "Wet-Chemical Synthesis of Doped Colloidal Nanoparticles: YVO_4:Ln (Ln = Eu, Sm, Dy)," *J. Phys. Chem. B*, vol. 102, no. 50, pp. 10129–10135, Dec. 1998.

[173] R. K. Selvan, A. Gedanken, P. Anilkumar, G. Manikandan, and C. Karunakaran, "Synthesis and characterization of rare earth orthovanadate (RVO4; R = La, Ce, Nd, Sm, Eu & Gd) nanorods/nanocrystals/nanospindles by a facile sonochemical method and their catalytic properties," *J. Clust. Sci.*, vol. 20, no. 2, pp. 291–305, 2009.

[174] S. Cotton, *Lanthanide and Actinide Chemistry*, 1 Ed. Jhon Wiley & Sons, 2006.

[175] C. J. Jia, L. D. Sun, F. Luo, X. C. Jiang, L. H. Wei, and C. H. Yan, "Structural transformation induced improved luminescent properties for LaVO4: Eu nanocrystals," *Appl. Phys. Lett.*, vol. 84, no. 26, pp. 5305–5307, 2004.

[176] J. Hu and Q. Wang, "New synthesis for a group of tetragonal LnVO4 and their Luminescent properties," *Mater. Lett.*, vol. 120, pp. 20–22, 2014.

[177] Y. Liu, G. Liu, X. Dong, J. Wang, and W. Yu, "Tunable photoluminescence and magnetic properties of Dy 3+ and Eu 3+ doped GdVO 4 multifunctional phosphors," *Phys Chem Chem Phys Phys Chem Chem Phys*, vol. 17, no. 17, pp. 26638–26644, 2015.

[178] S. Tang, M. Huang, J. Wang, F. Yu, G. Shang, and J. Wu, "Hydrothermal synthesis and luminescence properties of GdVO 4:Ln 3+ (Ln = Eu, Sm, Dy) phosphors," *J. Alloys Compd.*, vol. 513, pp. 474–480, 2012.

[179] Z. Xu *et al.*, "Ln3+ (Ln = Eu, Dy, Sm, and Er) ion-doped YVO4 nano/microcrystals with multiform morphologies: Hydrothermal synthesis, growing mechanism, and luminescent properties," *Inorg. Chem.*, vol. 49, no. 14, pp. 6706–6715, 2010.

[180] D. Nayak and S. Lahiri, "Application of radioisotopes in the field of nuclear medicine I. Lanthanide series elements," *J. Radioanal. Nucl. Chem.*, vol. 242, no. 2, pp. 423–432, 1999.

[181] C. S. Cutler, C. J. Smith, G. J. Ehrhardt, T. T. Tyler, S. S. Jurisson, and E. Deutsch, "Current and Potential Therapeutic Uses of Lanthanide Radioisotopes," *Cancer Biother. Radiopharm.*, vol. 15, no. 6, pp. 531–545, 2000.

[182] L. Rosenthall, "The Role of Strontium 85 in the Detection of Bone Disease," *Radiology*, vol. 84, no. 1, pp. 75–82, 1965.

[183] G. M. Blake, M. A. Zivanovic, A. J. McEwan, and D. M. Ackery, "Sr-89 therapy: Strontium kinetics in disseminated carcinoma of the prostate," *Eur. J. Nucl. Med.*, vol. 12, no. 9, pp. 447–454, 1986.

[184] Z. Huo, Chen, D. Chu, H. Li, and Y. Li, "Systematic synthesis of lanthanide phosphate nanocrystals," *Chem. - Eur. J.*, vol. 13, no. 27, pp. 7708–7714, 2007.

[185] † Yue-Ping Fang *et al.*, "Systematic Synthesis and Characterization of Single-Crystal Lanthanide Orthophosphate Nanowires," *J. Alloys Compd.*, vol. 125, pp. 16025–16034, 2003.

[186] M. R. Rafiuddin and A. P. Grosvenor, "A Structural Investigation of Hydrous and Anhydrous Rare-Earth Phosphates," *Inorg. Chem.*, vol. 55, no. 19, pp. 9685–9695, 2016.

[187] M. Laing, "Gadolinium: Central Metal of the Lanthanoids," *J. Chem. Educ.*, vol. 86, no. 2, p. 188, 2009.

[188] N. S. Singh, R. S. Ningthoujam, N. Yaiphaba, S. D. Singh, and R. K. Vatsa, "Lifetime and quantum yield studies of Dy3+ doped GdVO4 nanoparticles: Concentration and annealing effect," *J. Appl. Phys.*, vol. 105, no. 6, p. 064303, 2009.

[189] D. A. Scheinberg and M. R. McDevitt, "Actinium-225 in Targeted Alpha-Particle Therapeutic Applications," *Curr. Radiopharm.*, vol. 4, no. 4, pp. 306–320, Oct. 2011.

[190] M. R. Mcdevitt, D. Ma, J. Simon, R. K. Frank, and D. A. Scheinberg, "Design and synthesis of 225Ac radioimmunopharmaceuticals," *Appl. Radiat. Isot.*, vol. 57, pp. 841–847, 2002.

[191] W. F. Maguire, M. R. McDevitt, P. M. Smith-Jones, and D. A. Scheinberg, "Efficient 1-step radiolabeling of monoclonal antibodies to high specific activity with 225Ac for α-particle radioimmunotherapy of cancer.," *J. Nucl. Med. Off. Publ. Soc. Nucl. Med.*, vol. 55, no. 9, pp. 1492–8, Sep. 2014.

[192] S. J. Kennel *et al.*, "Evaluation of ^{225} Ac for Vascular Targeted Radioimmunotherapy of Lung Tumors," *Cancer Biother. Radiopharm.*, vol. 15, no. 3, pp. 235–244, Jun. 2000.

[193] J. F. Ziegler, M. D. Ziegler, and J. P. Biersack, "SRIM – The stopping and range of ions in matter (2010)," *Nucl. Instrum. Methods Phys. Res. Sect. B Beam Interact. Mater. At.*, vol. 268, no. 11, pp. 1818–1823, Jun. 2010.

[194] J. Dahle *et al.*, "Targeted cancer therapy with a novel low-dose rate -emitting radioimmunoconjugate," *Blood*, vol. 110, no. 6, pp. 2049–2056, Sep. 2007.

[195] J. Dahle and R. Larsen, "Targeted Alpha-Particle Therapy with 227Th-Labeled Antibodies," *Curr. Radiopharm.*, vol. 1, no. 3, pp. 209–214, Sep. 2008.

[196] J. Dahle *et al.*, "Initial evaluation of 227Th-p-benzyl-DOTA-rituximab for low-dose rate α-particle radioimmunotherapy," *Nucl. Med. Biol.*, vol. 33, no. 2, pp. 271–279, Feb. 2006.

[197] J. Dahle, Ø. S. Bruland, and R. H. Larsen, "Relative Biologic Effects of Low-Dose-Rate α-Emitting 227Th-Rituximab and β-Emitting 90Y-Tiuexetan-Ibritumomab Versus External Beam X-Radiation," *Int. J. Radiat. Oncol. • Biol. • Phys.*, vol. 72, no. 1, pp. 186–192, Sep. 2008.

[198] R. A. A. S. LARSEN and O. A. A. S. BRULAND, "Thorium-227 for use in radiotherapy of soft tissue disease," 2006.

[199] X. Wang, Y. Teng, Y. Huang, L. Wu, and P. Zeng, "Synthesis and structure of Ce 1-x Eu x PO 4 solid solutions for minor actinides immobilization," *J. Nucl. Mater.*, vol. 451, pp. 147–152, 2014.

[200] H. Yang *et al.*, "Synthesis and crystalline phase of monazite-type Ce 1-x Gd x PO 4 solid solutions for immobilization of minor actinide curium," *J. Nucl. Mater.*, vol. 444, pp. 39–42, 2014.

[201] C.-Y. Huang, S. Guatelli, B. M. Oborn, and B. J. Allen, "Microdosimetry for Targeted Alpha Therapy of Cancer," *Comput. Math. Methods Med.*, vol. 2012, pp. 1–6, 2012.

[202] M. Essler *et al.*, "Therapeutic efficacy and toxicity of 225Ac-labelled vs. 213Bi-labelled tumour-homing peptides in a preclinical mouse model of peritoneal carcinomatosis," *Eur. J. Nucl. Med. Mol. Imaging*, vol. 39, no. 4, pp. 602–612, Apr. 2012.

[203] J. Ramalho, R. C. Semelka, M. Ramalho, R. H. Nunes, M. AlObaidy, and M. Castillo, "Gadolinium-based contrast agent accumulation and toxicity: An update," *Am. J. Neuroradiol.*, vol. 37, no. 7, pp. 1192–1198, 2016.

[204] M. Rogosnitzky and S. Branch, "Gadolinium-based contrast agent toxicity: a review of known and proposed mechanisms," *BioMetals*, vol. 29, no. 3, pp. 365–376, 2016.

[205] Q. Du *et al.*, "Facile preparation and bifunctional imaging of Eu-doped GdPO4 nanorods with MRI and cellular luminescence," *Dalton Trans*, vol. 44, no. 9, pp. 3934–3940, 2015.

[206] S. L. Ho *et al.*, "Magnetic resonance imaging, gadolinium neutron capture therapy, and tumor cell detection using ultrasmall Gd2O3nanoparticles coated with polyacrylic acid-rhodamine B as a multifunctional tumor theragnostic agent," *RSC Adv.*, vol. 8, no. 23, pp. 12653–12665, 2018.

[207] Y. Li, T. Chen, W. Tan, and D. R. Talham, "Size-dependent MRI relaxivity and dual imaging with Eu0.2Gd0.8PO4-H2O Nanoparticles," *Langmuir*, vol. 30, no. 20, pp. 5873–5879, 2014.

VITA

Miguel Toro González was born on March 9, 1991, in Medellín, Colombia. He graduated from San José de la Salle High School, Medellín, Colombia in 2008. He was accepted into the Mechanical Engineering Department at the National University of Colombia in 2009 and graduated in May 2014 with a Bachelor of Science in Mechanical Engineering. During High School and College, he was part of the state swimming team and represented his country in 2006. Miguel was a member of the Tribology and Surface Group and the Computational Mechanics Group from 2012 to 2013. During his research experience, he worked under supervision of Master's students, performed multiple experiments, and presented a talk on an international conference. In 2014, he participated in an internship as mechanical engineering and later he was hired as a project manager. In 2015, he decided to pursue doctoral studies in Mechanical and Nuclear Engineering at Virginia Commonwealth University. Miguel's research focused on the synthesis and characterization of lanthanide-based nanoparticles as radionuclide carriers for biomedical and engineering applications. He primarily studied the retention of therapeutically relevant radionuclides such as actinium-225, radium-223, and thorium-227 in lanthanide vanadate nanoparticles, which also displayed multifunctional properties for molecular imaging. The synthesis and evaluation of radionuclide-doped nanoparticles was carried out at Oak Ridge National Laboratory, where Miguel participated as a visitor researcher and as an intern in the Nuclear Engineering Science Laboratory Synthesis program between July 2017 and May 2018. In December 2018, Miguel graduated with a Ph.D. in Mechanical and Nuclear Engineering.

Publications

- **M. Toro González**, R. Copping, S. Mirzadeh, J. V. Rojas. "Multifunctional $GdVO_4$:Eu Core-Shell Nanoparticles containing ^{225}Ac for Targeted Alpha Therapy and Molecular Imaging", Journal of Materials Chemistry B, DOI: 10.1039/C8TB02173B.
- M. C. Molina, **M. Toro González**, J. V. Rojas. "Enhanced X-rays Degradation of Methylene Blue in the Presence of Gold Microspheres". Journal of Radiation Physics and Chemistry, DOI: 10.1016/j.radphyschem.2018.10.020.
- **M. Toro González**, D. M. Clifford, R. Copping, S. Mirzadeh, J. V. Rojas. "Synthesis and Characterization of Intrinsically Radiolabeled Lanthanide Phosphate Nanoparticles Toward Biomedical and Environmental Applications". Journal of Nanoparticle Research, DOI: 10.1007/s11051-018-4338-8
- J. V. Rojas, **M. Toro González**, M. C. Molina, C. E. Castano. (2016). "Facile radiolytic synthesis of ruthenium nanoparticles on graphene oxide and carbon nanotubes". Materials Science and Engineering: B, DOI: 10.1016/j.mseb.2015.12.005.
- J. Zapata, **M. Toro González**, D. Lopez. "Residual stresses in friction stir dissimilar welding of Aluminum alloys". Journal of Materials Processing Technology, DOI: 10.1016/j.jmatprotec.2015.08.026.
- J. V. Rojas, M. C. Molina, **M. Toro González**, C. E. Castano. "Single step radiolytic synthesis of iridium nanoparticles onto graphene oxide". Applied Surface Science, DOI: 10.1016/j.apsusc.2015.09.190.

Conference Proceedings

- **M. Toro González**, M. C. Molina, J. V. Rojas. "Influence of gold particle concentration and X-ray energy in radiosensitization". ANS Winter 2017 Annual Transactions, vol. 116, November 2017, pp. 33-36.
- **M. Toro González**, J. V. Rojas. "Evidence of Radiosensitization effects of $GdPO_4$ nanostructures". ANS Winter 2016 Annual Transactions, vol. 115, November 2016, pp. 26-28.
- **M. Toro González**, J. V. Rojas. "Influence of synthesis parameters on morphology, crystalline structure, and colloidal stability of core and core-shell $LaPO_4$ nanoparticles". Processing, Properties, and Design of Advanced Ceramics and Composites: Ceramic Transactions. September 2016
- P. A. Fuentes, **M. Toro González**, J. A. Isaza, J.F. Ramirez. "Roughness incidence over the coefficient of friction between stump and socket surface". Conference: Pan American Health Care Exchanges (PAHCE). December 2012.

Poster Presentations

- **M. Toro González**, J. V. Rojas. "Lanthanide vanadate nanoparticles as carriers of ^{225}Ac for targeted alpha therapy". 2017 ANS Winter Meeting and Nuclear Technology Expo, Washington, D.C.
- **M. Toro González**, M. C. Molina, J. V. Rojas. "Influence of synthesis parameters on morphology, crystalline structure, and colloidal stability of core and core-shell $LaPO_4$ nanoparticles". Material Science & Technology. October 2015
- **M. Toro González**, M. C. Molina, C. E. Castano, G. E. Hilmas, W. G. Fahrenholtz, J. V. Rojas. "Proton beam irradiation study of UHTC Zirconium Diboride (ZrB_2)". NSUF Users Meeting. July 2015

Oral Presentations

- **M. Toro González**, S. Mirzadeh, J. V. Rojas. "Lanthanide-based Nanoparticles for Multimodal Molecular Imaging and Targeted Radionuclide Therapy". MAC-AAPM 2018 Annual Meeting, Richmond, VA.
- **M. Toro González**, M. C. Molina, J. V. Rojas. "Influence of gold particle concentration and X-ray energy in radiosensitization". 2017 ANS Winter Meeting and Nuclear Technology Expo, Washington, D.C.
- **M. Toro González**, J. V. Rojas. "Evidence of Radiosensitization effects of $GdPO_4$ nanostructures". 2016 ANS Winter Meeting and Nuclear Technology Expo, Las Vegas, NV.
- **M. Toro González**, P. Fuentes, J. A. Isaza, J. F. Ramirez. "Roughness incidence over the coefficient of friction between stump and socket surface". Fifth Biomedical Engineering and Bioengineering Colombian Congress. May 2013

Awards and Fellowships

- 1st place Young Investigator's Session MAC-AAPM 2018 Annual Meeting, Richmond, VA.
- Nuclear Engineering Science Laboratory Synthesis program, Oak ridge National Laboratory, Oak Ridge, TN.
- 3rd place 2017 graduate student poster session. 2017 ANS Winter Meeting and Nuclear Technology Expo, Washington, D.C.
- 2016 Bradley-Alavi Student Fellowship Award from SNMMI
- 1st place School of Engineering Outstanding Graduate Teaching Award 2015-2016